Noise and Dynamics in Semiconductor Lasers

by

Farhan Rana

Submitted to the Department of Electrical Engineering and Computer Science
in partial fulfillment of the requirements for the degree of

Doctor of Philosophy in Electrical Engineering

at the

MASSACHUSETTS INSTITUTE OF TECHNOLOGY

January 2003

Author .....
Department of Electrical Engineering and Computer Science
October, 2002

Certified by..... .....
Rajeev J. Ram
Associate Professor
Thesis Supervisor

Accepted by .....
Arthur C. Smith
Chairman, Department Committee on Graduate Students

Noise and Dynamics in Semiconductor Lasers

by

Farhan Rana

Submitted to the Department of Electrical Engineering and Computer Science
on October, 2002, in partial fulfillment of the requirements for the degree of
Doctor of Philosophy in Electrical Engineering

Abstract

In this thesis, theoretical and experimental work on the noise and dynamics in continuous wave and mode-locked semiconductor lasers is presented. The main focus is on semiconductor cascade lasers and semiconductor mode-locked lasers.

In semiconductor cascade lasers, multiple gain stages are connected electrically in series. Each electron injected into a cascade laser is capable of producing more than one photon, and the differential quantum efficiency of cascade lasers can be much larger than that of conventional semiconductor lasers. The photon emission events in different gain stages in cascade lasers are highly positively correlated, and these correlations increase the noise in the laser output compared to a conventional laser. The work on cascade lasers has required a revision of the previous work on laser noise, and the development of self-consistent theoretical models for the current noise and the photon noise in semiconductor lasers. The current and photon noise in both interband cascade lasers and intersubband quantum cascade lasers are studied in this thesis.

The noise in optical pulses in semiconductor mode-locked lasers is also studied in this thesis. In contrast to the previous work in this field, the models presented here are fully quantum mechanical, self-consistent, and also take into account the effects of group velocity dispersion, active phase and amplitude modulation, and pulse chirp on the pulse noise. In semiconductor mode-locked lasers, as a result of the carrier density dependent refractive index, pulses are heavily chirped. The pulse noise is found to be significantly affected by the magnitude of the pulse chirp. The noise in harmonically mode-locked semiconductor lasers is also discussed, and it is shown that the correlations in the noise of different pulses inside the laser cavity can significantly affect the results when the pulse noise is measured experimentally.

Thesis Supervisor: Rajeev J. Ram
Title: Associate Professor

Acknowledgments

I am deeply indebted to Professor Rajeev Ram for his years of support and guidance. His intuition and insight in both theoretical and experimental sciences together with his remarkable personality made my research work intellectually rewarding, challenging, and also pleasant at the same time. I am very grateful to Professor Henry Smith who has been a mentor and who taught me everything I know about nano-fabrication. His passion and enthusiasm for scientific research has been a continual source of motivation and inspiration throughout my stay at MIT as a graduate student. I am also grateful to Professor Hermann Haus, Professor Erich Ippen, Professor Leslie Kolodziejski, and Professor Qing Hu with whom I had the opportunity to work at various occasions. I am grateful to the members of my thesis committee (Professor Qing Hu, Professor Franz Kaertner, and Professor Rajeev Ram) for their feedback and for reading the first draft of the thesis on a short notice. I am also thankful to all the staff at the Nano-Structures Laboratory, especially James Daley, for their generous support and help.

I would like to express my gratitude to the members of the Physical Optics and Electronics Group, Quantum Electronics and Optics Group, and the Nano-Structures Laboratory for years of help, support, and comradeship. I would especially like to mention the names of Steve Patterson (whose coming back to school after a service of ten years in the military was both astounding and inspiring), Mathew Abraham (whose wonderful dinners will always be remembered and cherished), Harry Lee (who successfully impressed upon me the importance of having concrete goals in all aspects of life), Peter Mayer (who helped me a great deal in the experimental part of the thesis and without his help this thesis could not have been completed), Kevin Pipe (who provided company when I worked through the nights and frequently treated me with his "Piper's Pies"), Erwin Lau (who helped me characterize the lasers I fabricated), Michael Lim (who helped me fabricate the lasers and without his help I would still be struggling with fabrication), Maya Farhoud (who organized the most lively and boisterous parties), Christina Manolatou (who provided company and friendship), and Jalal Khan (who has been a close friend since my undergraduate years at MIT). I am also grateful to all my other friends for making my life at MIT enjoyable. Their support and friendship has been invaluable and will always be treasured by me. I would especially like to mention the names of Babak Ayazifar, Kashif Khan, Mohammad Saeed, Aiman Shabra,

Ammar Al-Nahwi, Bilal Helal, Ihsan Djomehri, Hassan Nayfeh, Bilal Zuberi, Salal Humair, Asim Khwaja, Asad Naqvi and Tahir Mehmood. I am also grateful to all my friends in MITMSA with whom I spent many pleasant moments. There are so many of them and all so important that I must apologize to them for not being able to mention their names here.

Most of all, I am grateful to my family whose unconditional support have made it possible for me to study at MIT. Their love, their sacrifices, and their trust has been a constant driving force in my life. My feelings and sense of gratitude for them cannot be encompassed by words alone.

Farhan Rana.

Contents

List of Figures

List of Tables

Chapter 1

Introduction and Motivation

Semiconductor lasers have become the most important sources of light for optical communication systems owing to their small size, low power consumption, high efficiency, flexibility for selecting wavelengths, higher modulation speeds, and adaptability for photonic integrated circuits [1]. As optical communication systems move to higher and higher bit rates, and photonic integrated circuits become more and more dense, semiconductor lasers need to be developed that are faster, smaller, and more efficient. Large signal to noise ratios (SNRs) are also desirable in high bit rate communication systems and, therefore, low noise semiconductor lasers will also become increasingly important. The research work presented in this thesis will aim to realize novel semiconductor lasers that meet these challenges. The research will focus on both continuous wave semiconductor lasers and also mode-locked semiconductor lasers.

Continuous wave semiconductor lasers have important applications in both digital and analog optical links [1]. The research proposed here will focus specifically on continuous wave semiconductor cascade lasers. Semiconductor cascade lasers, discussed in more detail below, are highly efficient sources of light that can also provide SNRs many times larger than those obtained from conventional semiconductor lasers. In addition, intersubband cascade lasers can potentially be used to realize ultra high speed semiconductor lasers with modulation bandwidths exceeding 100 GHz. The main goals of the research on semiconductor cascade lasers presented in this thesis have been the following:

1. Development of theoretical models for the electron and photon dynamics and fluctuations in semiconductor interband and intersubband cascade lasers.

2. Fabrication of semiconductor laser devices and design of experiments to verify the theoretical models.

Semiconductor mode-locked lasers, which produce a periodic train of optical pulses, provide a compact and cheap alternative to the larger and more expensive mode-locked fiber lasers and are expected to find applications in return-to-zero (RZ) format TDM optical networks, and also in high speed optical sampling, measurements, and spectroscopy [2]. Low noise performance, specially reduced timing jitter, is critical to most of these applications. The research on semiconductor mode-locked lasers that is presented in this thesis had the following goals:

1. Development of theoretical models for the dynamics and noise in semiconductor mode-locked lasers.

2. Design of semiconductor mode-locked lasers with reduced noise and timing jitter.

The semiconductor laser devices mentioned above, and the stated research goals, are discussed in detail below.

1.1 Semiconductor Cascade Lasers

In semiconductor cascade lasers several gain stages are connected electrically in series as shown in Fig. 1-1. These gain stages may be in the same optical cavity or in different optical cavities. The fundamental difference between a semiconductor cascade laser and a conventional semiconductor laser is that in a cascade laser each electron injected into the device is recycled from one gain stage to the other and is able to produce multiple photons (see Fig. 1-3). In a conventional laser each electron injected into the device cannot produce more than one photon. Consequently, the differential quantum efficiency of a cascade laser can be much greater than 100 percent, whereas the quantum efficiency of a conventional laser is always less than 100 percent.

Directly current modulated semiconductor lasers have important applications in RF photonic links (see Fig. 1-2). The modulation response of a semiconductor laser is defined as the ratio of the small signal light output power to the small signal input current. For frequencies much less than the laser relaxation oscillation frequency, the modulation response of a conventional semiconductor laser is given by the simple expression $\eta_o \eta_i \hbar \omega_o / e$ [1], where

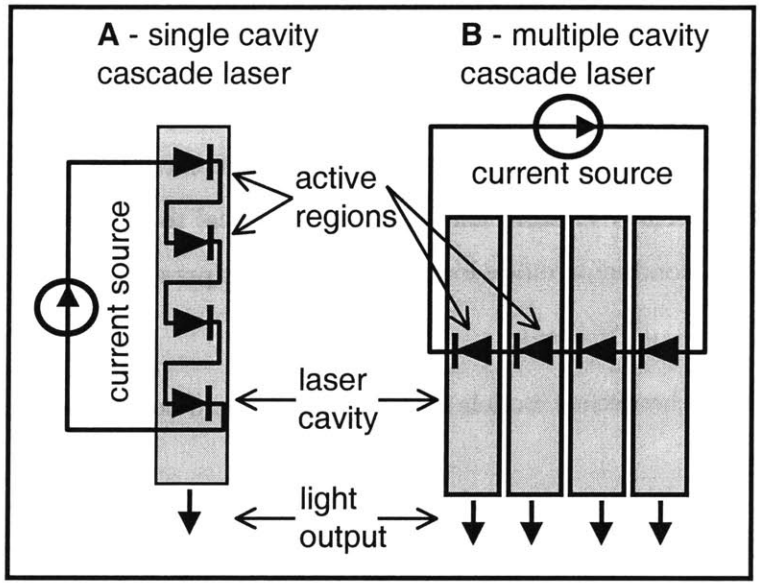

Figure 1-1: Different types of semiconductor cascade lasers.

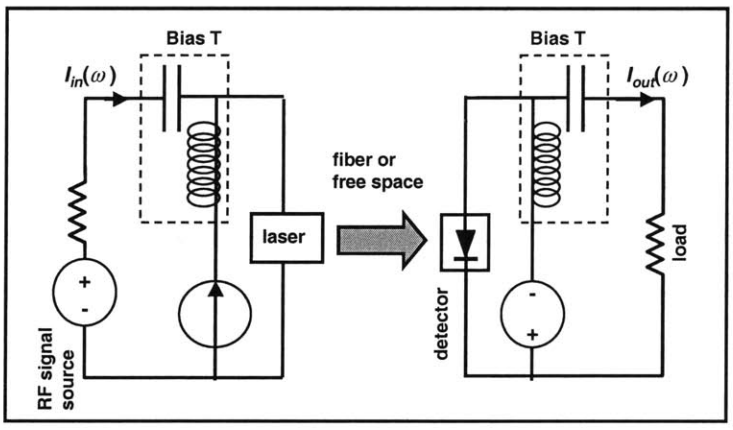

Figure 1-2: An RF photonic link

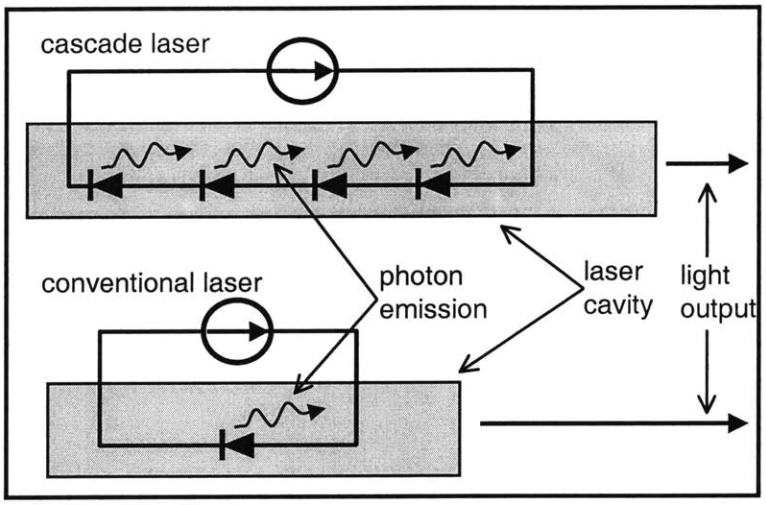

Figure 1-3: Multiple photons emitted by a single electron injected in a cascade laser.

η_o is the light output coupling efficiency, η_i is the current injection efficiency, $\hbar\Omega_o$ is energy of a single photon, and e is the charge of an electron. The modulation response of a semiconductor cascade laser with N cascaded gain stages is $\eta_o N \eta_i \hbar\Omega_o / e$. The modulation response of an N-stage cascade laser can therefore be N times larger than the modulation response of a conventional laser. Because of their large modulation response, cascade lasers are highly suitable for RF photonic links [3]. The RF power gain G of a photonic link with an N-stage cascade laser is given by the expression [3],

$$G = (\,\eta_d\, L\, \eta_o N \eta_i\,)^2\,(1-\Gamma)^2 \tag{1.1}$$

where L is the link loss, η_d is the photo-detector quantum efficiency, and Γ is the reflection coefficient which is equal to the ratio of the voltages in the RF signals reflected from and incident on the laser. Cascade lasers can be used to realize photonic links with net RF gain if N is large enough such that $L\eta_d\eta_o N\eta_q(1-\Gamma) > 1$. An important figure of merit in RF photonic links is the link Noise Figure (NF). The NF is defined as the ratio of the SNR at the input of the link to the SNR at the output of the link, and it is expressed in dB scale. It follows that,

$$NF = 10\log_{10}\left(1 + \frac{N_a}{GN_i}\right) \tag{1.2}$$

where N_i is the noise at the input of the link (typically assumed to be the thermal noise

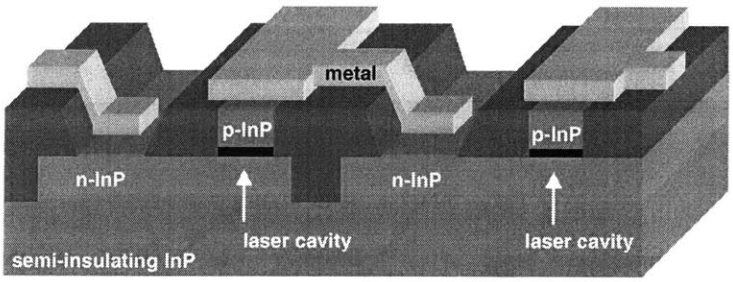

Figure 1-4: Multiple cavity interconnect coupled cascade laser (MCCL).

of a 50 Ω resistor) and N_a is the noise added by the link. In order to compute the noise added by the link, the photon noise in cascade lasers needs to be evaluated. The noise behavior of cascade lasers can be significantly different from conventional semiconductor lasers. Since all the gain stages are connected electrically in cascade lasers, the carrier density fluctuations and, consequently, the photon emission events in different gain stages are correlated. In the next two sections we briefly discuss the important and distinguishing features of semiconductor interband and intersubband cascade lasers related to high speed modulation and noise.

1.1.1 Semiconductor Interband Cascade Lasers

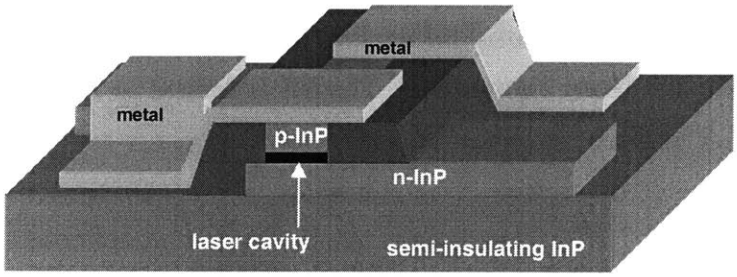

Figure 1-5: Split waveguide cascade laser (SWCL).

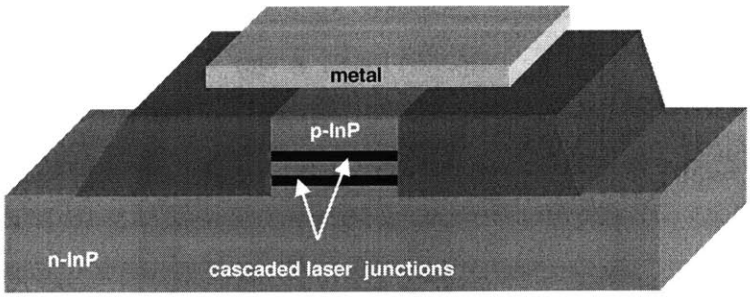

Figure 1-6: Bipolar cascade laser (BCL).

diodes inside a single optical cavity [7, 8, 9, 10, 11]. In addition, parallel laser arrays, shown in Fig. 1-7, are also considered. A property common to all these laser devices is that the gain sections are all connected electrically. While semiconductor cascade lasers in recent years have been receiving increased attention from experimentalists [3, 4, 5, 6, 7, 8, 9, 10, 11], so far very few theoretical papers have appeared in the literature.

Theoretical models have been developed as a part of this research to understand the electron and photon dynamics, noise, and correlations in semiconductor cascade lasers and semiconductor parallel laser arrays. The correlations in photon emissions in cascade lasers can be understood as follows. Suppose a photon is emitted from a gain stage in a cascade laser (see Fig. 1-3). The emission of the photon decreases the carrier density in the gain stage and this in turn decreases the potential drop across the gain stage. The potential drop across all the other gain stages and across the circuit series resistances must increase since the sum of the voltage drops across all the circuit elements in series must equal the applied voltage bias. The increase in the potential drop across the other gain stages increases the probability of photon emission in these gain stages. Therefore, the emission of a photon in one gain stage increases the probability of photon emission in all the other gain stages.

When the gain stages are connected electrically in parallel, as in a parallel laser array, the photon emission events in different gain stages are negatively correlated. The potential drops across all the gain stages connected in parallel must be equal, and the total current through all the gain stages must equal the applied current bias (see Fig. 1-7). When a photon is emitted from a gain stage and the potential drop across this gain stage decreases, extra current flows into this gain stage in order to keep the potential drop across it equal to the potential drop across all the other gain stages. Consequently, the current going into all

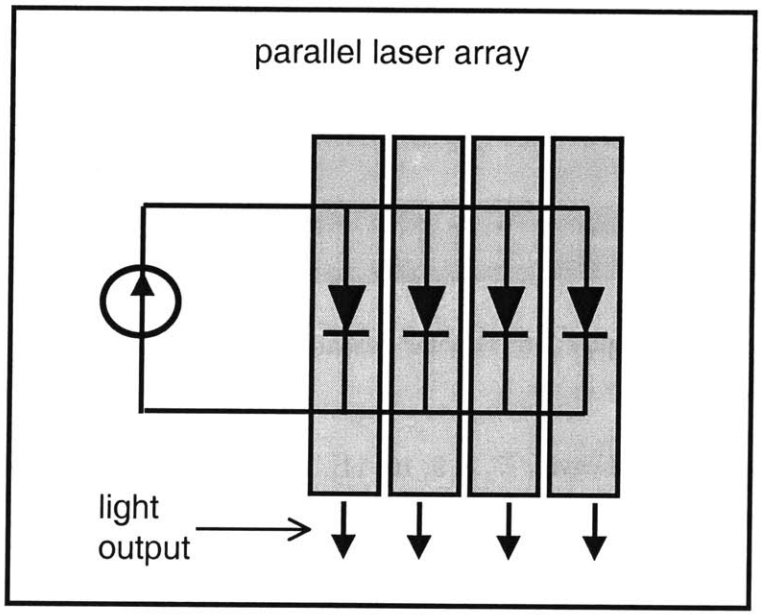

Figure 1-7: Parallel laser array (PLA).

the other gain stages decreases and the probability of photon emission in these gain stages also decreases. Theoretical modeling of photon correlations in cascade lasers requires that careful attention be paid to modeling the relationship between carrier density fluctuations, voltage fluctuations, and current fluctuations in each gain stage. The correlations in the photon noise also depend sensitively on the electrical environment in which the cascade laser device is embedded. Theoretical models for the dynamics and noise in interband cascade lasers will be presented in Chapter 3. The correlations in photon noise in multiple cavity cascade lasers and in parallel laser arrays can be measured experimentally. Experimental results on photon noise correlations are also presented in Chapter 3.

1.1.2 Semiconductor Intersubband Quantum Cascade Lasers

Unipolar quantum cascade lasers (QCLs) utilizing intersubband transitions to generate photons have become important sources of light in the mid-infrared wavelength region (5 μm - 15 μm) [12, 13, 14, 15, 16, 17, 18, 19, 20, 21, 22, 23, 24]. Recently, devices with intersubband transitions at 1.55 μm have also been reported [25] and this has opened up the possibility of realizing chirp-free intersubband lasers operating at 1.55 μm with large modulation bandwidths. The single gain stage of a typical QCL is shown in Fig. 1-8.

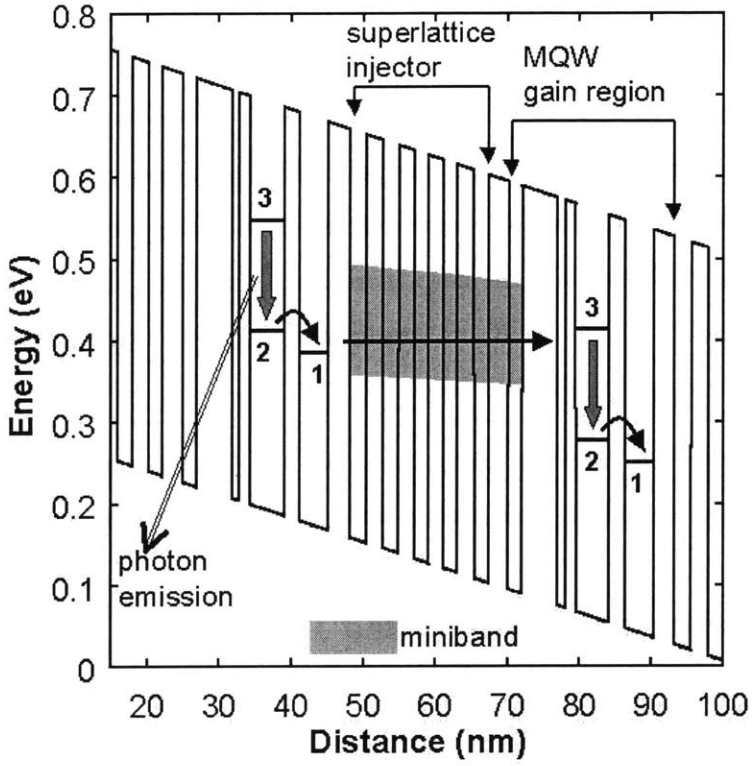

Figure 1-8: Gain stage of a Quantum Cascade Laser (QCL).

Electrons tunnel from the energy states in the injector into level 3 of the gain stage. Photons are emitted when electrons make radiative transitions from level 3 to level 2. Transitions from level 2 to level 1 occur primarily by emission of optical phonons. Electrons leave the gain stage from level 1 by tunneling out into the injector of the next stage. In addition, electrons also make non-radiative transitions from level 3 to levels 2 and 1. QCLs are different from interband semiconductor cascade lasers in two important ways which can have a significant impact on their noise properties:

1. Electron transport in QCLs takes place by tunneling between states in adjacent quantum wells. It is well known that electronic correlations in resonant tunneling in quantum well structures can suppress (or enhance) current noise by providing a negative (or positive) feedback. [26, 27, 28] High impedance suppression of the current noise in semiconductor diode lasers results in light output with squeezed photon number fluctuations. [29] It is therefore intriguing whether suppression of the current noise can also lead to squeezing in QCLs. Any model for the photon noise in QCLs must

take into account these electronic correlations self-consistently.

2. In interband lasers, the carrier density in the energy level involved in the lasing action does not increase beyond its threshold value and, therefore, the noise contributed by the non-radiative recombination and generation processes also remains unchanged beyond threshold. In QCLs, the electron densities in the upper and lower lasing states do not clamp at threshold, and keep increasing when the bias current is increased beyond threshold. As a result, non-radiative processes contribute significantly to photon noise even at high bias currents.

Theoretical models for electron transport in QCLs, laser dynamics, current noise in electron transport via tunneling, and photon noise will be presented in Chapter 4.

1.2 Semiconductor Mode-locked Lasers

Semiconductor mode-locked lasers have been used to produce sub-picosecond optical pulses with repetition rates exceeding tens of gigahertz [30, 31]. Their compact size and the ability to produce high repetition rate optical pulses make semiconductor mode-locked lasers ideal for use in high data rate (RZ format) Time Division Multiplexed (TDM) optical networks in place of the bulkier fiber mode-locked lasers. Semiconductor mode-locked lasers may also find application in spectroscopy and in optical sampling such as optical analog-to-digital (A/D) conversion [2].

Semiconductor mode-locked lasers must be able to produce short high power pulses with reduced noise and timing jitter in order to compete with other mode-locked lasers. Fig. 1-9 shows the requirements on the root mean square (RMS) timing jitter of optical pulses for optical A/D conversion [2, 32]. Fig. 1-9 shows that less than 100 femtosecond RMS jitter is required for an A/D converter with 8 bits of resolution at a sampling frequency of 10 GHz, and less than 30 femtosecond of RMS jitter is required if the desired resolution is 10 bits at 10 GHz. Very few models have been reported in the literature that describe the noise in mode-locked semiconductor lasers. Noise models for mode-locked lasers that have been reported are either geared towards fiber and solid state mode-locked lasers [33, 34], or ignore essential ingredients such as group velocity dispersion and phase modulation [35]. The models for noise developed for solid state and fiber lasers use the soliton perturbation theory in which the steady state pulse is assumed to be a soliton. An optical soliton is supported

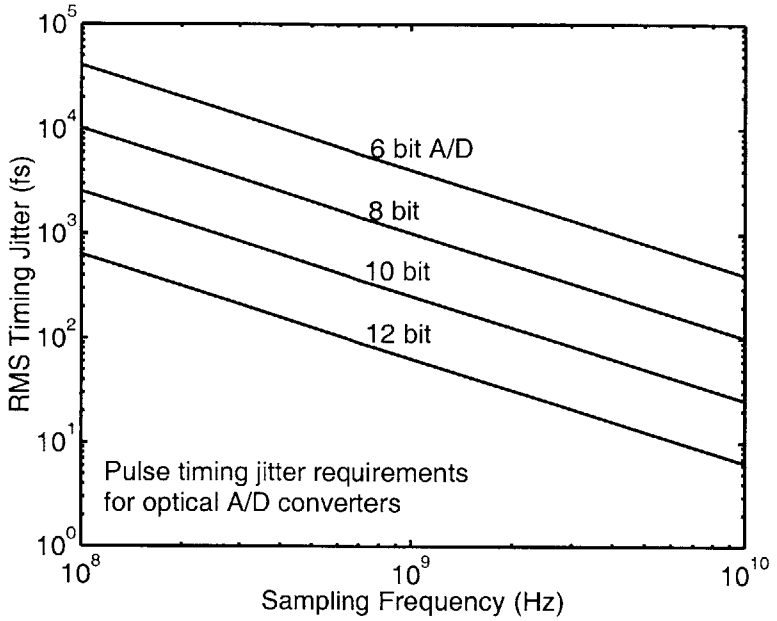

Figure 1-9: Requirements on pulse timing jitter for optical Analog-to-Digital conversion.

by the exact balance between group velocity dispersion and self-phase modulation due to the Kerr non-linearity. In semiconductor mode-locked lasers, the steady state optical pulses are not solitons. The group velocity dispersion is almost never balanced by the phase modulation, and, consequently, the pulses in semiconductor mode-locked lasers are usually highly chirped [30, 31]. Also, as a result of the carrier density refractive index in semiconductors, active gain modulation in semiconductor mode-locked lasers is always accompanied by strong active phase modulation.

As a part of this research, theoretical models were developed for the pulse noise in actively mode-locked semiconductor lasers without using the soliton perturbation theory. In Chapter 5, a model for the noise in mode-locked semiconductor lasers in the presence of group velocity dispersion and amplitude/phase modulation is presented, and it is shown that a non-zero pulse chirp significantly affects the noise in mode-locked lasers. To the best of the author's knowledge, this is the first time a model has been put forward that describes the noise in chirped mode-locked pulses. Design rules for obtaining low timing jitter in semiconductor mode-locked laser pulses are also described.

The noise in harmonically mode-locked semiconductor lasers is discussed in Chapter 6. In harmonically mode-locked lasers, the frequency of the active modulation is an integral

multiple N of the cavity roundtrip frequency. Consequently, N different optical pulses propagate in the laser cavity at the same time, and the pulse repetition frequency in the output is N times the cavity roundtrip frequency. In harmonically mode-locked lasers, the noise in the output pulses depends on the correlations in the noise in different pulses inside the laser cavity. Models for these noise correlations are also discussed in Chapter 6.

Chapter 2

Current Noise and Photon Noise in Interband Semiconductor Lasers

2.1 Introduction

In this chapter, theoretical models for the current noise and the photon noise in a standard multiple quantum well interband diode laser are presented. Noise in diode lasers has been extensively studied both theoretically and experimentally in the last two decades (see [1, 41] and references therein). However, almost all the theoretical models that have been presented in the literature ignore the current noise generated by the laser diodes. The work of Yamamoto et. al. (see [29, 42] for example) has been the exception. In Ref. [29], it was shown that diode lasers can produce amplitude squeezed light provided the noise in the pump current I_{ext} (see Fig. 2-1) is suppressed below the shot noise value. In most practical cases, the noise in the pump current does not come from the current or voltage source that biases the laser, but it is generated by the laser itself. The current noise in diode lasers is therefore closely tied with the photon noise. In the next Chapter, it will be shown that the photon emission events in different gain stages in semiconductor cascade lasers are correlated, and the magnitude of the correlation in photon emission events depends on the current noise generated by each gain stage. In order to understand the photon noise in semiconductor cascade lasers, it is necessary to accurately model the current noise in diode lasers.

The model presented for the current noise in diode lasers in Ref. [29] holds well only

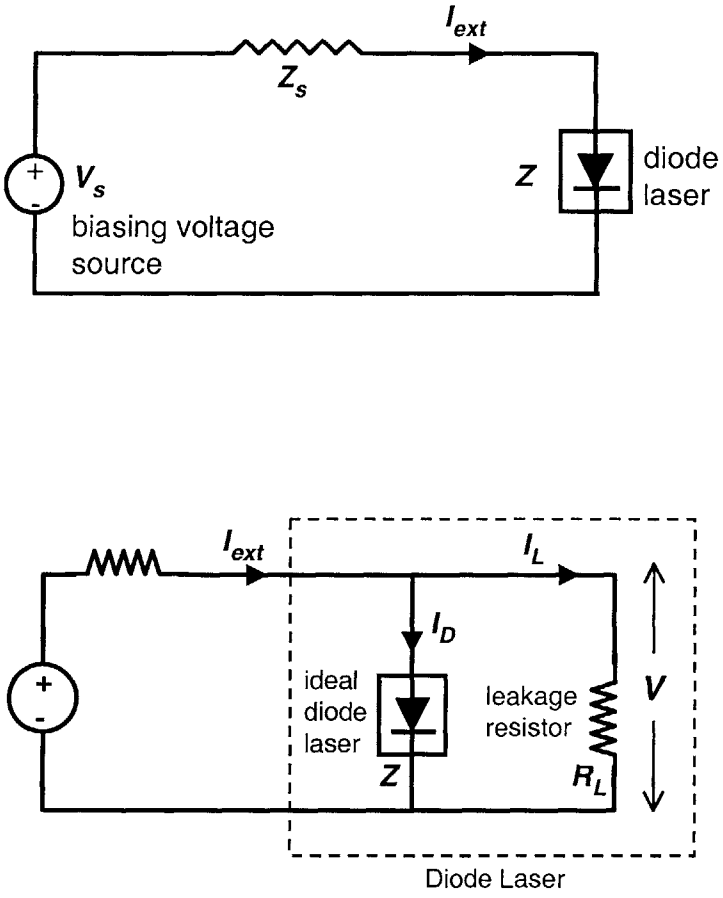

Figure 2-2: Model for current partition from Ref. [43].

for homojunction diode lasers. Even for homojunction diode lasers, the model in Ref. [29] gives results for the current noise that become infinite when the external circuit impedance Z_s (see Fig. 2-1) approaches zero. In Ref. [43], Yamamoto and Haus argued that electrical partition noise associated with current leakage in diode lasers does not contribute to the photon noise. In this chapter, it is shown that partition noise associated with current leakage in the active region of laser diodes significantly affects the photon noise and limits the maximum squeezing achievable in laser diodes. The conclusion in Ref. [43] is based on a model for current leakage in which a resistor is attached in parallel with the ideal diode, as shown in Fig. 2-2. If at any instant more current (i.e. more than the average) were to go into one branch of the parallel circuit, the potential drop V (see Fig. 2-2) will increase, and this will force extra current into the other branch of the parallel circuit ensuring that the

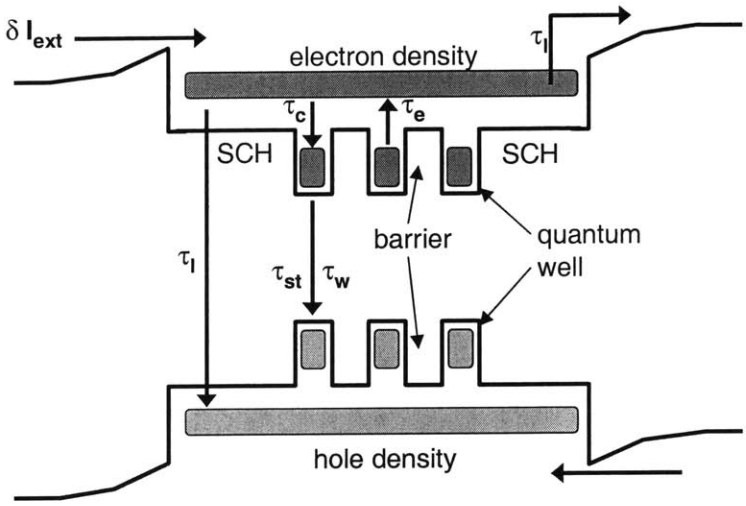

Figure 2-3: Active region of a semiconductor quantum well diode laser.

current in one branch does not increase at the expense of the current in the other branch. Also, the increase in the potential drop V will reduce the current I_{ext} being injected into the device, and this will force the currents in both the branches of the parallel circuit to return to their average values. Thus, electron partitioning at junctions in electrical circuits does not lead to current noise since deviations in the current from its average value generate voltage fluctuations that regulate the current. Since voltage fluctuations are not generated in the charge neutral active region of a diode laser, it is expected that electron partitioning associated with current leakage in the active region of a diode laser generates noise that would contribute to the photon noise. Electron partitioning in the active region of diode lasers was not considered in the model presented in Ref. [43]. In this chapter, a detailed model for the current noise in heterostructure quantum well diode lasers is presented that removes the shortcomings of the previous models.

2.2 Rate Equations for Diode Lasers

The active region of a quantum well diode laser is shown in Fig. 2-3. The carriers are injected from the leads into the separate confinement heterostructure (SCH) region either by tunneling or by thermionic emission over the hetero-barrier. The carriers in the SCH region can either go into the quantum wells or recombine non-radiatively in the SCH region.

The later contributes to current leakage. The rate equations for the carrier densities N_c and N_w in the SCH region and the quantum wells, respectively, and the photon density S_p in the laser cavity can be written as follows [1],

$$\frac{d\,N_c}{d\,t} = \frac{I_{ext}}{eV_c} - N_c\left(\frac{1}{\tau_c} + \frac{1}{\tau_l}\right) + \frac{N_w}{\tau_e}\frac{V_w}{V_c} \tag{2.1}$$

$$\frac{d\,N_w}{d\,t} = \frac{N_c}{\tau_c}\frac{V_c}{V_w} - N_w\left(\frac{1}{\tau_e} + \frac{1}{\tau_w}\right) - v_g\,g\,S_p \tag{2.2}$$

$$\frac{d\,S_p}{d\,t} = \left(\frac{V_w}{V_p}v_g\,g - \frac{1}{\tau_p}\right)S_p + \frac{V_w}{V_p}v_g\,g\frac{n_{sp}}{V_p} \tag{2.3}$$

It is assumed that the carrier density N_c in the SCH region also includes the carriers inside the quantum well barriers and also those in the quantum wells which have energy high enough to not be confined within the quantum wells (Fig. 2-3). Only those carriers which are confined within the quantum wells are included in the carrier density N_w. V_c and V_w are the volumes of the SCH region and the quantum wells, respectively. V_p is the volume of the optical mode. τ_c and τ_e are the capture and emission times for electrons going into the quantum wells from the SCH region and coming out of the quantum wells into the SCH region, respectively. τ_l is the lifetime associated with carrier leakage and recombination in the SCH region. τ_w is the non-radiative recombination time in the quantum wells. g is the optical gain per unit length in the laser cavity. n_{sp} is the spontaneous emission factor which takes into account the incomplete inversion of the active medium. v_g is the group velocity of the optical mode. τ_p is the photon lifetime inside the laser cavity. τ_p is given by the expression [1],

$$\frac{1}{\tau_p} = \frac{v_g}{L}\log\left(\frac{1}{\sqrt{R_1\,R_2}}\right) + vg\alpha_i \tag{2.4}$$

where L is the cavity length, R_1 and R_2 are the facet reflectivities, and α_i is the intrinsic loss in the cavity per unit length. Carrier leakage and recombination in the SCH region results in a less than unity efficiency for current injection into the quantum wells. The current injection efficiency η_i is,

$$\eta_i = \frac{\tau_l}{(\tau_c + \tau_l)} \tag{2.5}$$

The output power P_{out} from the laser can be written as,

$$P_{out} = \eta_o\hbar\Omega_o\frac{S_p\,V_p}{\tau_p} \tag{2.6}$$

where η_o is the laser output coupling efficiency.

The rate equations are not linear since the gain g is a function of the carrier density N_w inside the quantum wells [1]. However, some simple arguments can be used to derive an expression for the output power of the laser. As the bias current I_{ext} is increased, the carrier density in the quantum well increases, and the optical gain also increases. When I_{ext} equals the threshold bias I_{th}, the gain equals the cavity loss, and the laser starts oscillating. At threshold, the gain equals the threshold gain g_{th}, where,

$$\frac{V_w}{V_p} v_g \, g_{th} = \frac{1}{\tau_p} \tag{2.7}$$

Since in steady state operation the gain cannot exceed the loss, when the bias current is increased beyond threshold, the gain remains clamped to its value g_{th} at threshold. As a result, the carrier density N_w in the quantum wells also remains clamped to its value at threshold, and the non-radiative recombination rate, which depends on the carrier density, also remains fixed above threshold. Therefore, carriers injected into the quantum wells above the threshold injection rate recombine only by producing photons through stimulated emission. Above threshold, the rate $S_p V_p/\tau_p$ at which photons are emitted from the laser is simply $\eta_i(I_{ext} - I_{th})/e$, and the expression for the output power of the laser becomes,

$$P_{out} = \eta_o \eta_i \frac{\hbar \Omega_o}{e} (I_{ext} - I_{th}) \tag{2.8}$$

The factor $\eta_o \eta_i \, h\Omega_o/e$ is the differential slope efficiency (units: Watt/Amp) of the laser.

2.3 Langevin Rate Equations for Noise in Diode Lasers

The model for the current and photon noise in quantum well diode lasers described here follows the work published by the author in Refs. [44, 45, 46, 47]. The equations for the fluctuations δN_c and δN_w in the carrier densities in the SCH region and the quantum wells, respectively, and the fluctuations δS_p in the photon density can be obtained by linearizing the rate equations given in (2.1)-(2.3), and adding Langevin sources to model the noise,

$$\frac{d\,\delta N_c V_c}{d\,t} = \frac{\delta I_{ext}}{e} - \delta N_c V_c \left(\frac{1}{\tau_c} + \frac{1}{\tau_l} \right) + \frac{\delta N_w V_w}{\tau_e} - F_c - F_l + F_e \tag{2.9}$$

$$\frac{d\,\delta N_w V_w}{d\,t} = \frac{\delta N_c V_c}{\tau_c} - \delta N_w V_w \left(\frac{1}{\tau_e} + \frac{1}{\tau_w} + \frac{1}{\tau_{st}}\right) - \frac{V_w}{V_p} v_g\, g\, \delta S_p V_p + F_c - F_e - F_{nr} - F_R \quad (2.10)$$

$$\frac{d\,\delta S_p V_p}{d\,t} = \frac{\delta N_w V_w}{\tau_{st}} + \left(\frac{V_w}{V_p} v_g\, g - \frac{1}{\tau_p}\right) \delta S_p V_p + F_R - F_L \quad (2.11)$$

Here, τ_{st} is the differential lifetime associated with stimulated and spontaneous emission into the lasing mode. τ_{st} is given by the expression,

$$\frac{1}{\tau_{st}} = v_g \frac{dg}{dN_w} \left(S_p + \frac{n_{sp}}{V_p}\right) \quad (2.12)$$

where dg/dN_w is the differential gain. The inclusion of the rate equation for carrier density fluctuations in the SCH region is necessary to accurately model the noise associated with current partition in the SCH region. Current partition occurs because the carriers injected into the active region can either go into the quantum wells or they can contribute to leakage and recombination in the SCH region. Since the active region is charge neutral, current partition does not create charge imbalances and potential fluctuations that regulate the associated noise. F_l, F_c, and F_e in (2.9)-(2.11) are Langevin noise sources that model the noise in carrier leakage, carrier capture and carrier emission events. F_{nr} describes the noise in non-radiative recombination in the quantum wells including spontaneous emission into the non-lasing modes. F_R models the noise associated with photon emission into the lasing mode. F_L models the noise associated with photon loss from the cavity. All the non-zero correlations of the Langevin noise sources can be obtained from the methods described in Ref. [1],

$$\langle F_c(t)\, F_c(t')\rangle = \frac{N_c V_c}{\tau_c}\, \delta(t - t') \quad (2.13)$$

$$\langle F_l(t)\, F_l(t')\rangle = \frac{N_c V_c}{\tau_l}\, \delta(t - t') \quad (2.14)$$

$$\langle F_e(t)\, F_e(t')\rangle = \frac{N_w V_w}{\tau_e}\, \delta(t - t') \quad (2.15)$$

$$\langle F_{nr}(t)\, F_{nr}(t')\rangle = \frac{N_w V_w}{\tau_w}\, \delta(t - t') \quad (2.16)$$

$$\langle F_R(t)\, F_R(t')\rangle = \frac{V_w}{V_p} v_g\, g\, \left[(2n_{sp} - 1)\, S_p V_p + n_{sp}\right]\, \delta(t - t') \quad (2.17)$$

$$\langle F_L(t)\, F_L(t')\rangle = \frac{S_p V_p}{\tau_p}\, \delta(t - t') \quad (2.18)$$

The noise δP_{out} in the output power is,

$$\delta P_{out} = \eta_o \hbar\Omega_o \frac{\delta S_p V_p}{\tau_p} + F_o \tag{2.19}$$

The Langevin source F_o models the noise associated with photon partition at the output facets, and has the following correlation functions,

$$\langle F_o(t) F_o(t') \rangle = \eta_o (\hbar\Omega_o)^2 \frac{S_p V_p}{\tau_p} \delta(t - t') \tag{2.20}$$

$$\langle F_o(t) F_L(t') \rangle = \eta_o (\hbar\Omega_o) \frac{S_p V_p}{\tau_p} \delta(t - t') \tag{2.21}$$

In addition to the equations presented above, an equation is required to relate the fluctuations δI_{ext} in the current injected into the active region to the fluctuations δV in the voltage across the active region. This equation is [44, 47],

$$\frac{\delta I_{ext}}{e} = \frac{G\,\delta V}{e} - \frac{\delta N_c V_c}{\tau_G} + F_{in} \tag{2.22}$$

The conductance G relates the increase in the injection current into the SCH region to the increase in the voltage across the active region at a *fixed carrier density*. τ_G relates the decrease in the current injection rate to the increase in the carrier density in the SCH region. Approximate analytical expressions for G and τ_G in case of a conventional PN-diode are given in Ref. [42]. (2.22) shows that the carrier density fluctuations in the active region drive the current noise in the external circuit. F_{in} is the Langevin noise source associated with carrier injection into the SCH region. Since the net current injected into the active region is the difference of forward and reverse currents, i.e.,

$$I_{ext} = I_{forward} - I_{reverse} \tag{2.23}$$

F_{in} has the approximate correlation function [42],

$$\langle F_{in}(t) F_{in}(t') \rangle = \frac{I_{forward}}{e} + \frac{I_{reverse}}{e} \tag{2.24}$$

$$\approx \left(\frac{I_{ext}}{e} + 2\frac{N_c V_c}{\tau_G} \right) \delta(t - t') \tag{2.25}$$

It must be emphasized that (2.22) is sufficiently general and holds for most microscopic models for electron injection into the SCH region.

After Fourier transforming, the Langevin rate equation (2.9)-(2.11) can be put in the following matrix form,

$$\begin{bmatrix} \mathbf{D}_{11}(\omega) & \mathbf{D}_{12}(\omega) & 0 \\ \mathbf{D}_{21}(\omega) & \mathbf{D}_{22}(\omega) & \mathbf{D}_{23}(\omega) \\ 0 & \mathbf{D}_{32}(\omega) & \mathbf{D}_{33}(\omega) \end{bmatrix} \begin{bmatrix} \delta N_c(\omega) V_c \\ \delta N_w(\omega) V_w \\ \delta S_p(\omega) V_p \end{bmatrix} = \frac{\delta I_{ext}(\omega)}{e} \begin{bmatrix} 1 \\ 0 \\ 0 \end{bmatrix} + \begin{bmatrix} F_1(\omega) \\ F_2(\omega) \\ F_3(\omega) \end{bmatrix} \tag{2.26}$$

The elements of the matrix $\mathbf{D}$ are given in Appendix A.2, and the noise sources $F_1(\omega)$, $F_2(\omega)$, and $F_3(\omega)$ are as follows,

$$F_1(\omega) = -F_c(\omega) - F_l(\omega) + F_e(\omega) \tag{2.27}$$

$$F_2(\omega) = F_c(\omega) - F_e(\omega) - F_{nr}(\omega) - F_R(\omega) \tag{2.28}$$

$$F_3(\omega) = F_R(\omega) - F_L(\omega) \tag{2.29}$$

2.4 Biasing Electrical Circuits

Two electrical circuits for biasing a diode laser are shown in Fig. 2-4. In circuit A the laser, with impedance $Z(\omega)$, is biased with a voltage source V_s in series with an impedance $Z_s(\omega)$. The thermal noise originating in the impedance $Z_s(\omega)$ is modeled by adding a voltage noise source δV_s. For the sake of economy of notation it will be assumed that the impedance $Z_s(\omega)$ represents not just an external circuit impedance but the Thevenin equivalent impedance of the device ohmic contacts, external circuit resistances, and device and circuit parasitics, and the voltage noise source δV_s represents the Thevenin equivalent of their individual noise sources. Only the active region of the diode laser is not included within $Z_s(\omega)$ and is represented by the impedance $Z(\omega)$. However, $Z(\omega)$ will be loosely referred to as the impedance of the diode laser.

Direct current modulation of a diode laser can be achieved by adding an RF voltage source in series with δV_s, and this RF voltage source can also be represented by the voltage source δV_s. From the context it will be clear whether δV_s represents a RF signal source or a noise source.

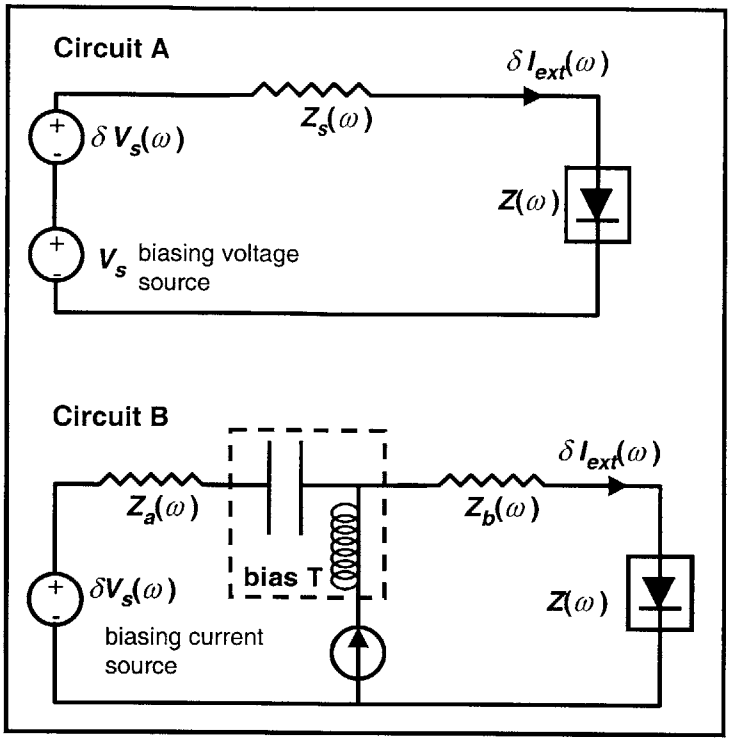

Figure 2-4: Biasing circuits for diode lasers.

Diode lasers are frequently biased as shown in circuit B in Fig. 2-4. The laser is biased with a current source in series with an ideal inductor, and it is also capacitively coupled to a voltage source δV_s with a series impedances $Z_a(\omega)$ and $Z_b(\omega)$. If at frequencies of interest the inductor and the coupling capacitor are almost open and short, respectively, then this circuit is also equivalent to circuit A. Therefore, in this paper only circuit A will be considered. In circuit A the current δI_{ext} can be expressed as,

$$\delta I_{ext}(\omega) = \frac{\delta V_s(\omega) - \delta V(\omega)}{Z_s(\omega)} \tag{2.30}$$

It is important to note here that $\delta I_{ext}(\omega)$ may not be the noise current which would be measured in an experiment. For example, suppose that the diode laser has a parasitic capacitance C_o in parallel with the actual device, as shown in Fig. 2-5. The laser is driven with a series resistor R_o and a noise voltage source $\delta V_o(\omega)$ representing the thermal noise in the resistor R_o. Fig. 2-5 shows the distinction between the noise current $\delta I_{ext}(\omega)$ defined in (2.30), and the noise current $\delta I_{meas}(\omega)$ that would be measured in an experiment. Notice

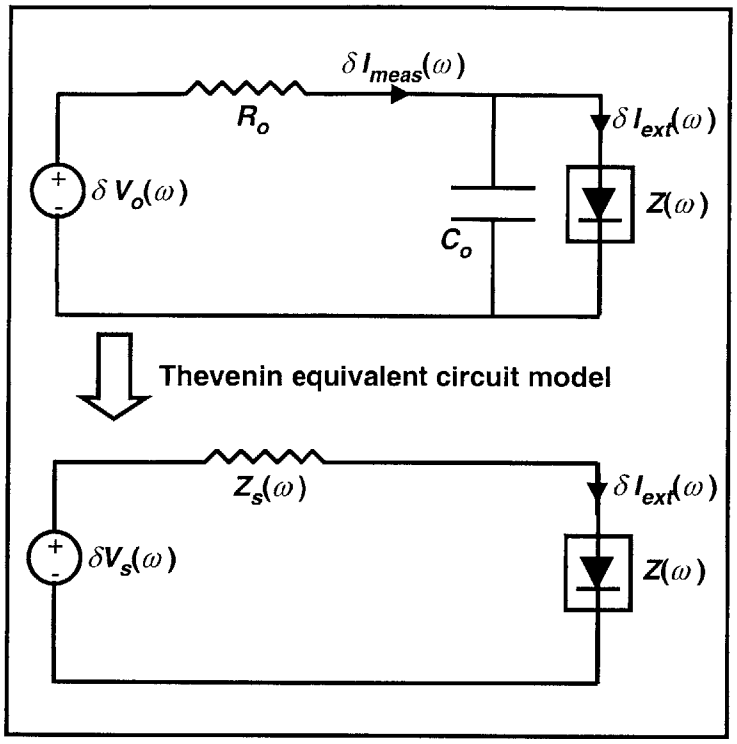

Figure 2-5: Thevenin equivalent circuit model indicating the distinction between $\delta I_{ext}(\omega)$ and $\delta I_{meas}(\omega)$.

that the Thevenin equivalent impedance $Z_s(\omega)$ is a parallel combination of the resistance R_o and the capacitance C_o. $Z_s(\omega)$ and $\delta V_s(\omega)$ are,

$$Z_s(\omega) = \frac{R_o}{(1 + j\omega\, R_o C_o)} \qquad \delta V_s(\omega) = \frac{\delta V_o(\omega)}{(1 + j\omega\, R_o C_o)} \tag{2.31}$$

and the relation between $\delta I_{ext}(\omega)$ and $\delta I_{meas}(\omega)$ is,

$$\delta I_{ext}(\omega) = \frac{\delta I_{meas}(\omega)}{(1 + j\omega\, Z(\omega) C_o)} \tag{2.32}$$

Choosing to define $Z_s(\omega)$ this way helps in formulating a noise model that is independent of the specific nature of the device parasitics.

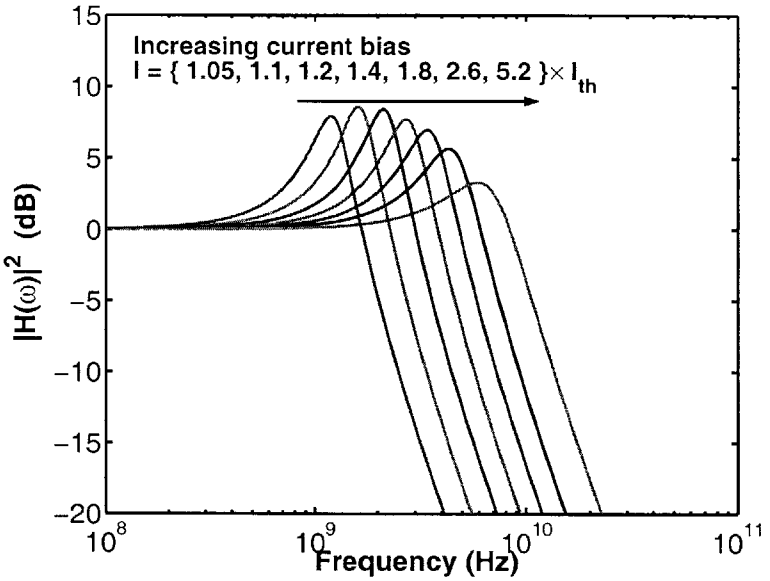

Figure 2-6: Modulation response function $|H(\omega)|^2$ for an InGaAsP/InP diode laser is plotted for different values of the bias current. The values of different parameters of the laser are given in Table 2.1.

2.5 Current Modulation Response

In this section the response $\delta P_{out}(\omega)/\delta I_{ext}(\omega)$ of diode lasers to external sinusoidal current modulation $\delta I_{ext}(\omega)$ is determined [1]. The behavior of noise in diode lasers at high frequencies is closely tied to their current modulation response. The current modulation response can be obtained from (2.26) assuming all the noise sources have been *turned off*,

$$\frac{\delta P_{out}(\omega)}{\delta I_{ext}(\omega)} = \eta_o \hbar\Omega_o \frac{\delta S_p V_p}{\tau_p} = \eta_o \frac{\hbar\Omega_o}{e} \frac{\mathbf{D}_{31}^{-1}(\omega)}{\tau_p} \tag{2.33}$$

Above threshold, and for frequencies less than the inverse of the carrier capture time τ_c, the modulation response can be put in the following form [1],

$$\frac{\delta P_{out}(\omega)}{\delta I_{ext}(\omega)} = \eta_o \eta_i \frac{\hbar\Omega_o}{e} H(\omega) \tag{2.34}$$

[1]It is assumed that $P_{out}(t) = P_{out} + \text{Real}\{\delta P_{out}(\omega)\, e^{j\,\omega t}\}$ and $I_{ext}(t) = I_{ext} + \text{Real}\{\delta I_{ext}(\omega)\, e^{j\,\omega t}\}$

where the modulation response function $H(\omega)$ is,

$$H(\omega) = \frac{\omega_R^2}{(\omega_R^2 - \omega^2 + j\omega\gamma)} \tag{2.35}$$

The relaxation oscillation frequency ω_R and the damping constant γ are,

$$\omega_R^2 = \frac{1}{\tau_{st}\,\tau_p} \tag{2.36}$$

$$\gamma = \frac{1}{\tau_w} + \frac{1-\eta_i}{\tau_e} + \frac{1}{\tau_{st}} = K\,\omega_R^2 + \gamma_o \tag{2.37}$$

where,

$$K = \tau_p \qquad \text{and} \qquad \gamma_o = \frac{1}{\tau_w} + \frac{1-\eta_i}{\tau_e} \tag{2.38}$$

Fig. 2-6 shows $|H(\omega)|^2$ plotted for different bias currents for an InGaAsP/InP diode laser. The values of laser parameters are given in Table 2.1. The peak in the modulation response is due to the laser relaxation oscillations [1]. Near threshold, when γ is small, the 3 dB bandwidth of the modulation response is given by the approximate expression,

$$\omega_{3\,\mathrm{dB}} \approx \sqrt{1+\sqrt{2}}\,\omega_R \approx 1.55\,\omega_R \tag{2.39}$$

As the bias current is increased beyond threshold, $\omega_{3\,\mathrm{dB}}$ increases until $\gamma/\sqrt{2}$ becomes equal to ω_R. When the bias current is increased beyond this point, the modulation response becomes over-damped, and $\omega_{3\,\mathrm{dB}}$ starts to decrease. The maximum achievable modulation bandwidth $\omega_{3\,\mathrm{dB}\,|\,\mathrm{max}}$ is related to the photon lifetime in the laser cavity as follows,

$$\omega_{3\,\mathrm{dB}\,|\,\mathrm{max}} \approx \frac{\sqrt{2}}{\tau_p} \tag{2.40}$$

2.6 Differential Resistance

The differential Impedance $Z(\omega)$ of a diode laser can be obtained from (2.26) using (2.22),

$$Z(\omega) = \frac{\delta V(\omega)}{\delta I_{ext}(\omega)} = \frac{1}{G}\left[1 + \frac{\mathbf{D}_{11}^{-1}(\omega)}{\tau_G}\right] \tag{2.41}$$

Table 2.1: Device Parameters for the InGaAsP/InP Diode Laser Used in Numerical Simulations

Parameter	Value
Lasing wavelength λ	1.55 μm
Operating temperature	300 K
Number of quantum wells	5
Cavity width	2.0 μm
Cavity length	600 μm
τ_p	4.1 ps
τ_c	15 ps
τ_e	101 ps
τ_g	42 ps
τ_l	90 ps
$1/\tau_w$	$2 * B * N_w + 3 * C * N_w^2$
B	10^{-10} cm^3/s
C	5×10^{-29} cm^6/s
I_{th}	21 mA

The differential resistance R_d of diode lasers, defined as $Z(\omega = 0)$, below and above threshold comes out to be,

$$R_d = \begin{cases} \dfrac{1}{G}\,(1+\theta') & (I_{ext} < I_{th}) \\ \\ \dfrac{1}{G}\,(1+\theta) & (I_{ext} > I_{th}) \end{cases} \tag{2.42}$$

θ' and θ are,

$$\theta' = \frac{1}{\tau_G}\,\frac{\tau_l\,\tau_c}{(\tau_l\,(1-\eta_e)+\tau_c)} \quad , \quad \theta = \frac{1}{\tau_G}\,\frac{\tau_l\,\tau_c}{(\tau_l+\tau_c)} \tag{2.43}$$

The carrier emission efficiency η_e is defined as $\tau_w/(\tau_e+\tau_w)$. Since τ_w is usually around 1 ns, and the value of τ_e is expected to be around 100 ps or less, η_e is close to unity. The discontinuity ΔR_d in the differential resistance at threshold follows from (2.42),

$$\Delta R_d = \frac{1}{G}\,(\theta'-\theta) = \eta_i\,\eta_e\frac{\theta'}{G} = \eta_i\,\eta_e\frac{\theta'}{1+\theta'}\,R_d\Big|_{I_{ext}\le I_{th}\text{ evaluated at }I_{ext}=I_{th}} \tag{2.44}$$

Below threshold the current-voltage characteristics of a diode laser resemble that of a plane PN diode [49],

$$I_{ext} = I_o\left[\exp\left(\frac{eV}{mK_BT}\right)-1\right] \tag{2.45}$$

where m is the diode ideality factor with values typically around 2.0. Therefore,

$$R_d\Big|_{I_{ext}\leq I_{th}} = m\frac{K_B T}{qI_{ext}} \tag{2.46}$$

and ΔR_d becomes,

$$\Delta R_d = \eta_i\,\eta_e\frac{\theta'}{1+\theta'}\,m\frac{K_B T}{qI_{th}} \tag{2.47}$$

Above threshold, the impedance $Z(\omega)$ can be expressed in terms of the modulation response $H(\omega)$,

$$Z(\omega) \approx \frac{1}{G}\left\{1+\theta\left[1+j\omega\,\tau_p\,\tau_{st}\left(\frac{1}{\tau_e}+\frac{1}{\tau_{st}}+\frac{1}{\tau_{nr}}\right)\right]H(\omega)\right\} \tag{2.48}$$

2.7 Current Noise

From Equation (2.22), it can be seen that the current noise $\delta I_{ext}(\omega)$ is driven by the carrier density fluctuations $\delta N_c(\omega)$. The carrier density fluctuations $\delta N_c(\omega)$ can be obtained by solving (2.26) in the presence of the noise sources,

$$\delta N_c(\omega)V_c = \mathbf{D}_{11}^{-1}(\omega)\frac{I_{ext}(\omega)}{e} + \sum_{k=1}^{3}\mathbf{D}_{1k}^{-1}(\omega)\,F_k(\omega) \tag{2.49}$$

The current fluctuations $I_{ext}(\omega)$ can be obtained by substituting the above expression in (2.22) and using (2.30),

$$\begin{aligned}\delta I_{ext}(\omega) \;=\; & \frac{\delta V_s(\omega)}{Z_s(\omega)+Z(\omega)} \\ & + \frac{Z(\omega)}{Z_s(\omega)+Z(\omega)}\left[\frac{e}{Z(\omega)}\,\frac{1}{G}\,F_{in}(\omega)\right. \\ & \left. -\frac{e}{Z(\omega)}\,\frac{1}{G}\sum_{k=1}^{3}\frac{\mathbf{D}_{1k}^{-1}(\omega)}{\tau_G}\,F_k(\omega)\right]\end{aligned} \tag{2.50}$$

The form of (2.50) suggests that a circuit model for the current noise can be constructed as in Fig. 2-7 where a current noise source $\delta I(\omega)$ is attached in parallel with the diode laser. $\delta I(\omega)$ is given by the expression,

$$\delta I(\omega) = \frac{e}{Z(\omega)}\,\frac{1}{G}\left[F_{in}(\omega) - \sum_{k=1}^{3}\frac{\mathbf{D}_{1k}^{-1}(\omega)}{\tau_G}\,F_k(\omega)\right] \tag{2.51}$$

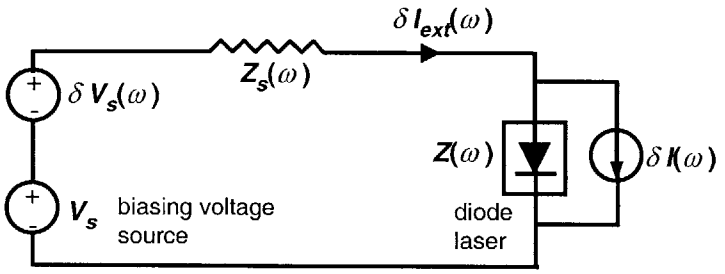

Figure 2-7: Circuit model for the current fluctuations in semiconductor diode lasers

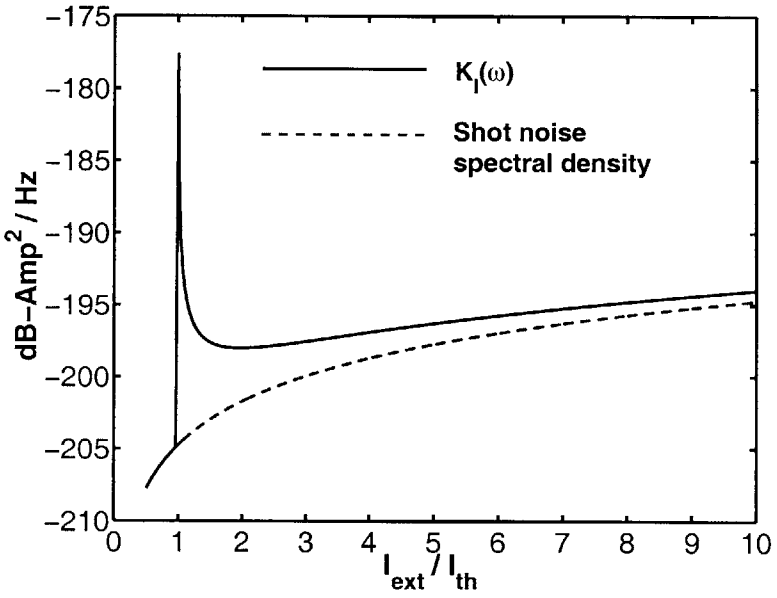

Figure 2-8: Low frequency current noise spectral density $K_I(\omega)$ ($\omega < \omega_{3\,\mathrm{dB}}$) of an InGaAsP/InP diode laser is plotted as a function of the bias current. The values of the laser parameters are given in Table 2.1.

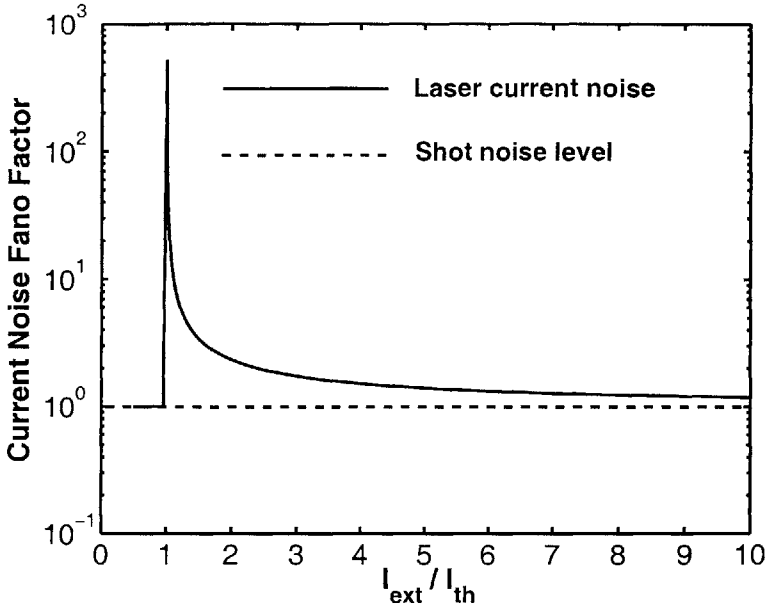

Figure 2-9: Fano Factor of the current noise of an InGaAsP/InP diode laser is plotted as a function of the bias current. The values of the laser parameters are given in Table 2.1.

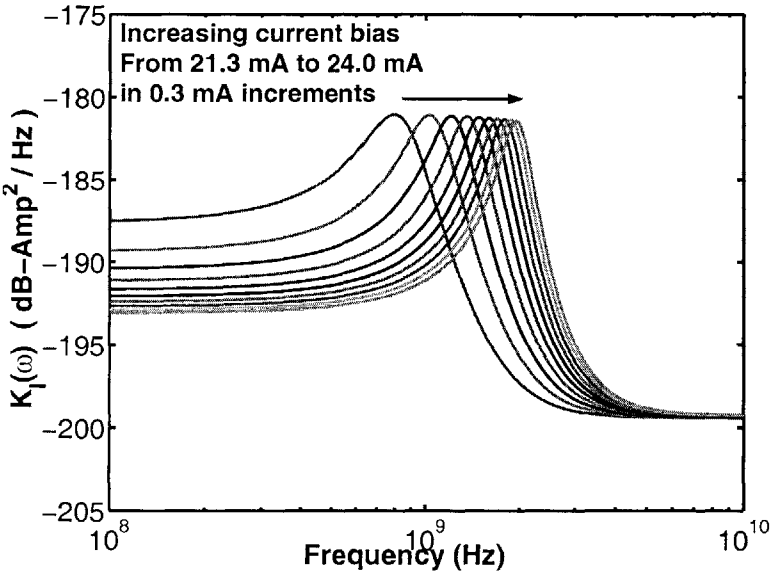

Figure 2-10: Current noise spectral density $K_I(\omega)$ of an InGaAsP/InP diode laser is plotted as a function of the frequency for different values of the bias current. The laser threshold current is 21.0 mA. The current noise spectral density shows a peak at the laser relaxation oscillation frequency ω_R. The values of laser parameters are given in Table 2.1.

Below threshold, and for frequencies less than $\omega_{3\,\mathrm{dB}}$, $\delta I(\omega)$ is,

$$\frac{\delta I(\omega)}{e} = \frac{F_{in}(\omega) + \theta'\,(1-\eta_e)\,[F_c(\omega) - F_e(\omega)] + \theta'\,F_l(\omega) + \theta'\,\eta_e\,F_{nr}(\omega)}{(1+\theta')} \tag{2.52}$$

Above threshold $\delta I(\omega)$ is,

$$\frac{\delta I(\omega)}{e} = \frac{F_{in}(\omega) + \theta\,[F_c(\omega) - F_e(\omega) + F_l(\omega)] + \theta\left(\frac{\tau_{st}}{\tau_e}\right)[F_R(\omega) - F_L(\omega)]}{(1+\theta)} \tag{2.53}$$

The spectral density $K_I(\omega)$ of the current noise $\delta I(\omega)$ follows from (2.52) and (2.53),

$$\begin{aligned} K_I\,(\omega < \omega_{3\,\mathrm{dB}}\,,\, I_{ext} < I_{th}) &= e\,I_{ext} \\ K_I\,(\omega < \omega_{3\,\mathrm{dB}}\,,\, I_{ext} > I_{th}) &= e\,I_{ext} + 2e\,\eta_e\,\eta_i\,I_{th}\,\frac{\theta'}{(1+\theta)} \\ &\quad + 2e\,n_{sp}\,\eta_i\,(I_{ext} - I_{th})\,\frac{\left(\theta\,\frac{\tau_{st}}{\tau_e}\right)^2}{(1+\theta)^2} \end{aligned} \tag{2.54}$$

Fig. 2-9 shows the Fano Factor of the current noise of an InGaAsP/InP diode laser as a function of the bias current. The values of the laser parameters are given in Table 2.1. The current noise increases dramatically near threshold and can become more than 100 times larger than the shot noise value of eI_{ext}. The increase in the current noise near threshold can be explained as follows. Below threshold, the cavity gain is less than the cavity loss and the photon density fluctuations in the cavity are strongly damped. Much above threshold, although the cavity gain equals the cavity loss, the photon density fluctuations are stabilized by negative feedback from the carrier density as a result of the strong coupling between the photon density and the carrier density above threshold. Near threshold, the cavity gain almost equals the cavity loss, but the coupling between the photon density and the carrier density is weak. Consequently, photon density fluctuations become large near threshold. Since the carrier density is weakly coupled to the photon density, the carrier density fluctuations, and consequently the current fluctuations, are also large near threshold. In the expression for the current noise spectral density above threshold given in (2.54), the last term dominates near threshold. Near threshold, the photon density S_p is small, and τ_{st}, given by the expression in (2.12), is large. It should be noted that this last term is entirely due to the Langevin noise sources present in only the rate equation for the fluctuations in the photon density.

Fig. 2-10 shows the current noise spectral density plotted as a function of the frequency for different values of the bias current. The current noise spectral density shows a resonance peak at the laser relaxation oscillation frequency ω_R. Since the carrier density fluctuations drive the current fluctuations, the relaxation oscillation peak is also present in the current noise spectral density. These relaxation oscillations peaks in the current noise spectral density can be observed experimentally, as shown in Section 2.10 of this Chapter. In the limit $\omega \rightarrow \infty$, the current noise is just the noise associated with carrier injection into the active region and has the spectral density,

$$\begin{aligned} K_I\,(\omega \rightarrow \infty\,,\, I_{ext} < I_{th}) &= e\,I_{ext}\;(1+2\,\theta') \\ K_I\,(\omega \rightarrow \infty\,,\, I_{ext} > I_{th}) &= e\,I_{ext}\;(1+2\,\theta) + e\,\eta_e\,\eta_i\,I_{th}\,\theta' \end{aligned} \tag{2.55}$$

2.7.1 Suppression of the Current Noise by Large External Impedance

The current noise $\delta I_{ext}(\omega)$ in the external circuit in the presence of an external impedance $Z_s(\omega)$ and an external voltage noise source $\delta V_s(\omega)$ is,

$$\delta I_{ext}(\omega) = \frac{\delta V_s(\omega)}{(Z(\omega)+Z_s(\omega))} + \frac{Z(\omega)}{(Z(\omega)+Z_s(\omega))}\,\delta I(\omega) \tag{2.56}$$

When $Z_s(\omega)$ is much larger than the differential impedance $Z(\omega)$ of the active region, the contribution from the noise source $\delta I(\omega)$ to the current noise in the external circuit is suppressed, and the current noise in the external circuit is just the noise contributed by the voltage noise source $\delta V_s(\omega)$. If $\delta V_s(\omega)$ represents the thermal noise originating in the impedance $Z_s(\omega)$ then,

$$\langle\,\delta V_s^*(\omega)\,\delta V_s(\omega')\,\rangle = 2K_BT\;\mathrm{Re}\,\{Z_s(\omega)\}\;\;2\pi\delta(\omega-\omega') \tag{2.57}$$

By making the impedance $Z_s(\omega)$ very large, the current noise in the external circuit can be suppressed well below the shot noise value. When $Z_s(\omega)$ is much smaller than $Z(\omega)$, the current noise in the external circuit is the noise $\delta I(\omega)$ plus the current noise contributed by the external voltage noise source $\delta V_s(\omega)$.

2.8 Photon Noise

The expression for the noise $\delta P_{out}(\omega)$ in the output power can be obtained from (2.26) using (2.19),

$$\delta P_{out}(\omega) = \eta_o \hbar\Omega_o \frac{\mathbf{D}_{31}^{-1}(\omega)}{\tau_p} \frac{\delta I_{ext}(\omega)}{e} + \eta_o \hbar\Omega_o \sum_{k=1}^{3} \frac{\mathbf{D}_{3k}^{-1}(\omega)}{\tau_p} F_k(\omega) + F_o(\omega) \tag{2.58}$$

Above threshold, and for frequencies less than $\omega_{3\,\mathrm{dB}}$, $\delta P_{out}(\omega)$ is,

$$\begin{aligned} \delta P_{out}(\omega) &= \eta_o \eta_i \hbar\Omega_o \frac{\delta I_{ext}(\omega)}{e} + \eta_o \hbar\Omega_o \Big\{ (1-\eta_i)\left[F_c(\omega) - F_e(\omega)\right] - \eta_i F_l(\omega) \\ &\quad - F_{nr}(\omega) + (\gamma\tau_{st} - 1) F_R(\omega) - \gamma\tau_{st} F_L(\omega) \Big\} + F_o(\omega) \end{aligned} \tag{2.59}$$

Note that the photon noise depends on the current noise $\delta I_{ext}(\omega)$ and not on the current noise $\delta I(\omega)$. High impedance suppression of the current noise $\delta I_{ext}(\omega)$ in the external circuit can have a profound effect on the laser intensity noise. If $\delta I_{ext}(\omega)$ is suppressed, the spectral density $K_P(\omega)$ of the intensity noise, for frequencies less than $\omega_{3\,\mathrm{dB}}$, is,

$$\begin{aligned} K_P\left(\omega < \omega_{3\,\mathrm{dB}}\,,\, I_{ext} > I_{th}\right) &= \hbar\Omega_o P_{out} \left[1 - \eta_o + 2\eta_o n_{sp} \left(\frac{1}{\tau_w} + \frac{1-\eta_i}{\tau_e}\right)^2 \tau_{st}^2\right] \\ &\quad + (\eta_o \hbar\Omega_o)^2 \left[\eta_i(1-\eta_i)\frac{I_{ext}}{e} + \eta_i \frac{I_{th}}{e}\right] \end{aligned} \tag{2.60}$$

The term proportional to I_{ext} in the above Equation is due to the current partition noise. Even if the current noise in the external circuit is suppressed, the noise due to current partition in the active region is not suppressed. If the current injection efficiency η_i is close unity, the contribution from the current partition noise to the photon noise is small. The low frequency Fano Factor $F_P(\omega)$ of the photon noise at very large bias currents is,

$$F_P\left(\omega < \omega_{3\,\mathrm{dB}}\,,\, I_{ext} \gg I_{th}\right) = 1 - \eta_o \eta_i \tag{2.61}$$

In diode lasers both η_o and η_i have typical values around 0.80 - 0.90, and therefore high impedance suppression of the current noise in the external circuit can result in more than 5 dB suppression of the laser intensity noise below the shot noise value. The laser output coupling efficiency and the current injection efficiency, therefore, set the upper limit on the photon number squeezing achievable in diode lasers. If the external impedance

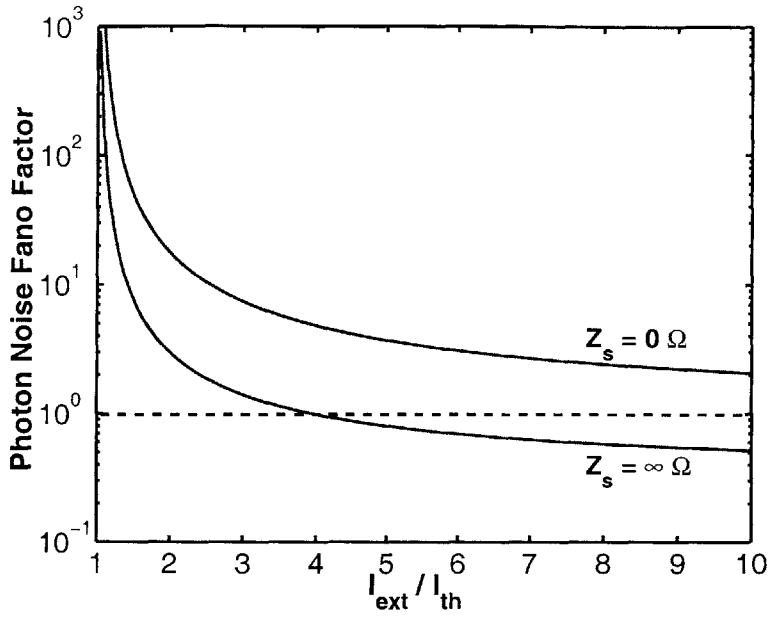

Figure 2-11: Photon noise Fano Factor of an InGaAsP/InP diode laser is plotted as a function of the bias current for different values of the external circuit impedance Z_s. Photon noise is squeezed when Z_s is very large. The values of different parameters of the laser are given in Table 2.2.

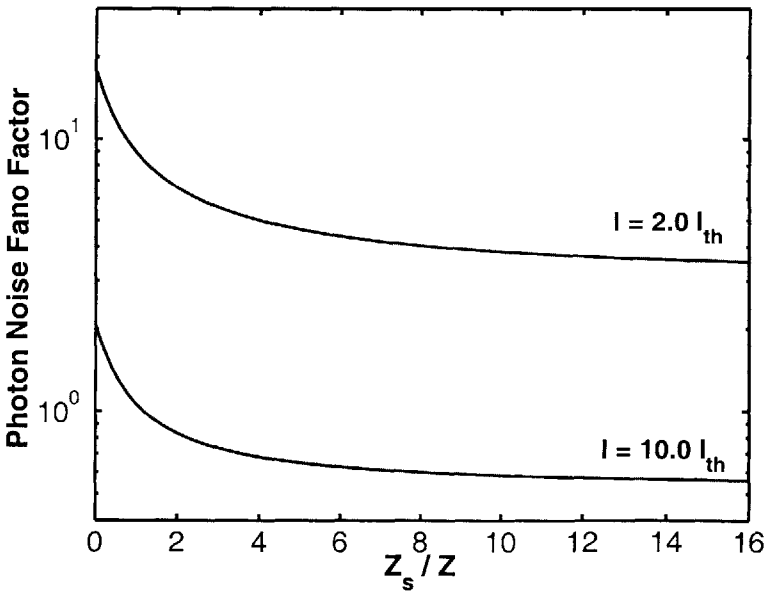

Figure 2-12: Photon noise Fano Factor of an InGaAsP/InP diode laser is plotted as a function of the ratio $Z_s(\omega)/Z(\omega)$ for two different values of the bias current. Photon noise is squeezed when Z_s is much larger than Z. The values of different parameters of the laser are given in Table 2.2.

Table 2.2: Device Parameters for the InGaAsP/InP Diode Laser Used in Numerical Simulations of Photon Noise

Parameter	Value
Lasing wavelength λ	1.55 μm
Operating temperature	300 K
Number of quantum wells	5
Cavity width	2.0 μm
Cavity length	400 μm
Cavity internal loss	9 cm^{-1}
τ_p	3.15 ps
τ_c	5 ps
τ_e	30 ps
τ_g	15 ps
τ_l	50 ps
$1/\tau_w$	$2 * B * N_w + 3 * C * N_w^2$
B	10^{-10} cm^3/s
C	5×10^{-29} cm^6/s
I_{th}	15 mA
η_i	0.90
η_o	0.75
$R_d = Z(\omega = 0)$	0.50 Ω

$Z_s(\omega)$ is much smaller than the impedance $Z(\omega)$ of the active region, current noise in the external circuit is not suppressed. In this case, it can be shown that at large bias currents the Fano Factor of the photon noise is greater than unity, and photon number squeezing is not possible. Fig. 2-11 shows the low frequency Fano Factor of the photon noise of an InGaAsP/InP diode laser as a function of the bias current for different values of the external impedance $Z_s(\omega)$. Fig. 2-12 shows the photon noise Fano Factor as a function of the ratio $Z_s(\omega)/Z(\omega)$ for two different values of the bias current. The laser parameters used in generating these Figures are given in Table. 2.2. When $Z_s \ll Z(\omega)$, the photon noise is above the shot noise value. When $Z_s \gg Z(\omega)$, the photon noise is squeezed when the bias current exceeds four times the threshold value.

Photon number squeezing in diode lasers when the current noise $\delta I_{ext}(\omega)$ in the external circuit is suppressed can be understood as follows. In the Langevin approach, the noise contribution by different transitions to the photon number noise is proportional to the average rate of the transitions. When a laser is biased much above threshold, the fastest process is carrier recombination by stimulated emission of photons. Since the average carrier density

in the quantum wells is clamped to its value at threshold, non-radiative carrier recombination is by comparison a much slower process. Also, if η_i is close to unity then current partition in the active region will also contribute little to the photon noise. Thus, much above threshold stimulated emission is by far the most important process that contributes to the photon number noise. Suppose in some small time interval photons in excess of the average rate are emitted. Immediately after the emission of photons the carrier density in the quantum wells, and the voltage drop across the active region, will be below their average values. The decrease in the carrier density will result in reduced optical gain. Consequently, the rate of stimulated emission of photons will also drop below its average value until the carrier density recovers. This negative feedback provided by the carrier density reduces the noise in photon emission and helps in photon number squeezing. If the carrier density in the quantum wells were somehow clamped to a fixed value, it would not be able to provide negative feedback to control the noise in photon emission. This is what happens when a laser is biased with a low impedance electrical circuit. Every time the carrier density drops below its average value, the circuit responds by pumping in extra current which quickly restores the carrier density to its average value. The ability of the carrier density to provide negative feedback to control the noise in photon emission is thus diminished. On the other hand, a high impedance circuit suppresses the current noise in the circuit by not allowing the circuit to respond to the carrier density fluctuations inside the laser. In addition to the mechanism described here, noise from sources external to the laser, such as thermal noise from circuit resistances, also contributes to the photon noise. Photon number squeezing in diode lasers has been experimentally observed when the lasers are biased with a high impedance circuit [50, 51]. The current noise model presented in the Section 2.7 is therefore in agreement with the experimental observation of photon number squeezing in diode lasers.

The terms in Equation (2.58) containing elements of the matrix $\mathbf{D}^{-1}$ are proportional to the modulation response function $H(\omega)$ and, therefore, for frequencies much larger than the modulation bandwidth the noise in the output power is,

$$\delta P_{out}\left(\omega \gg \omega_{3\,\mathrm{dB}}\right) = F_o(\omega) \tag{2.62}$$

Table 2.3: Device Parameters of the InGaAsP/InP Fabry-Perot Laser Used in the Experiments

Parameter	Value
Lasing wavelength λ	1.55 μm
Operating temperature	$\approx$ 300 K
Number of quantum wells	5
Quantum well thickness	60$\mathring{A}$
V_c/V_w	$\approx$ 10
Cavity width	4.0 μm
Cavity length	800 μm
V_c/V_w	$\approx$ 10
α_i	15 cm^{-1}
R_1, R_2	0.3
I_{th}	44 mA
η_o	0.25

and the spectral density of the noise in the output power equals that of shot noise,

$$K_P(\omega \gg \omega_{3\,\mathrm{dB}}) = \hbar\Omega_o P_{out} \tag{2.63}$$

2.9 Experiments for Parameter Extraction

In the previous Sections, a model for the laser noise was presented in which several different parameters, including G, τ_g, θ', θ, and τ_e established a relation between the fluctuations inside the laser and the fluctuations in the current in the external circuit. In this Section, it is shown that the values of these parameters near threshold can be extracted from experimental measurements. InGasAsP/InP Fabry-Perot laser was used in the experiments. The laser parameters are given in Table 2.3, and the SEM of the laser structure is shown in Fig. 2-13. The intrinsic cavity loss in the laser was determined by cleaving lasers of different lengths [1], and was found to be approximately 15 cm^{-1}. The output power coupling efficiency η_o of the laser (per facet), assuming facet reflectivities of 0.3, is then 0.25. Fig. 2-14 shows the output power per facet. The differential slope efficiency of the laser near threshold is measured to be 0.17 W/A. Using (2.8), the current injection efficiency η_i is found to be 0.85 near threshold. Fig. 2-15 shows the measured differential resistance of the laser. At threshold, the discontinuity in the differential resistance is 0.56 Ω. The differential resistance just above threshold is 4.4 Ω. Later in this Section, it is shown that just above threshold the

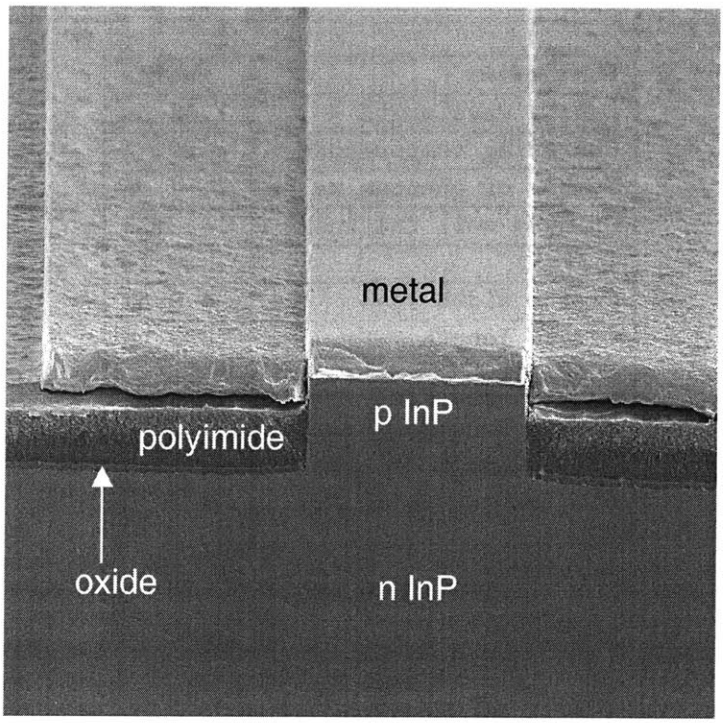

Figure 2-13: A SEM of the InGaAsP/InP Fabry-Perot laser used in the experiments.

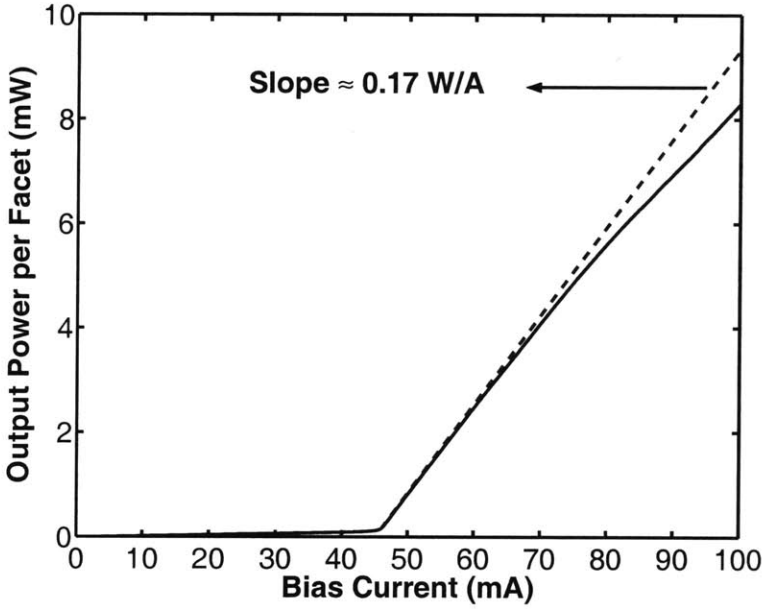

Figure 2-14: The measured output power of an InGaAsP/InP Fabry-Perot laser is plotted. The laser parameter values are given in Table 2.3. The solid line is the laser output power per facet. The dashed line indicates a differential slope of 0.17 W/A near threshold.

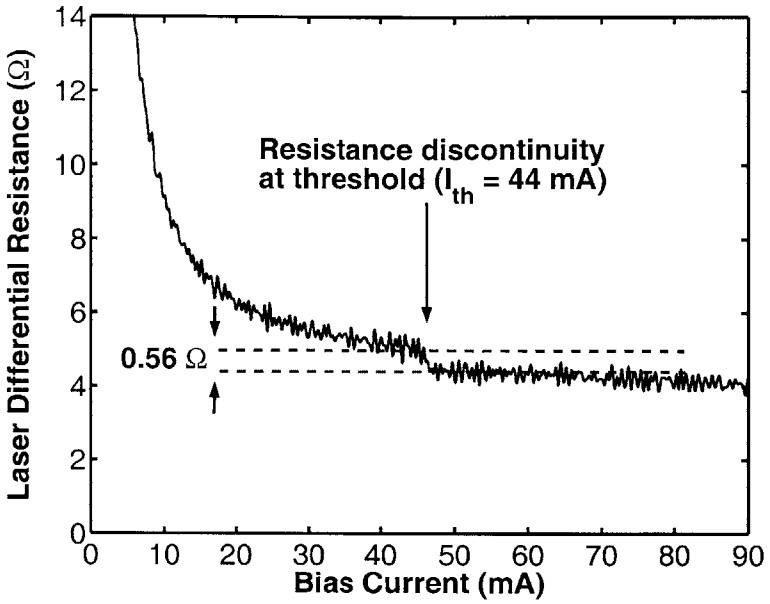

Figure 2-15: The measured differential resistance of an InGaAsP/InP Fabry-Perot laser is plotted (solid line). The laser parameter values are given in Table 2.3. The two dashed lines indicate a resistance discontinuity of 0.56 Ω at threshold. Just above threshold the differential resistance of the laser is 4.4 Ω.

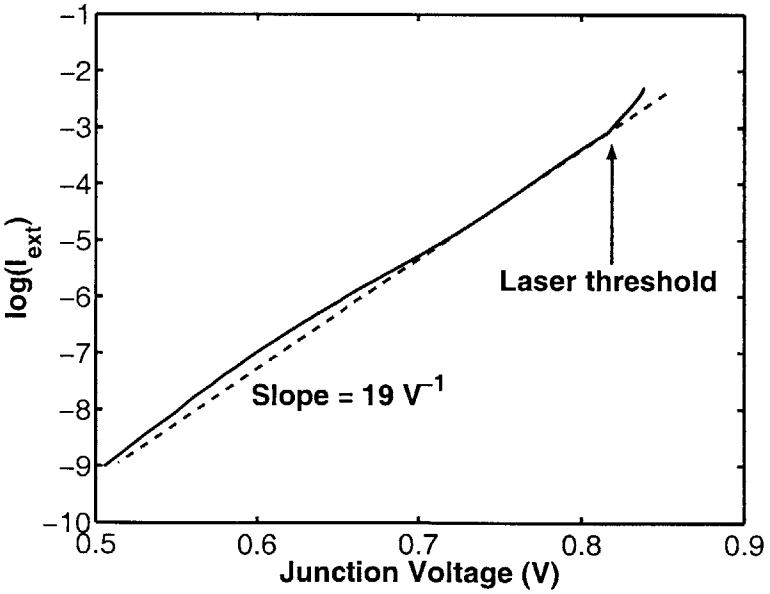

Figure 2-16: The measured value of $\log(I_{ext})$ as a function of the junction voltage V for an InGaAsP/InP Fabry-Perot laser is plotted (solid line). The laser parameter values are given in Table 2.3. The dashed line indicates a slope of 19 V^{-1} just before threshold.

differential resistance of the junction is approximately 0.65 Ω. The impedance Z_s in series with the junction is then 3.75 Ω. For any bias current, the voltage V across the junction can be estimated from the relation $V = V_s - I_{ext}\, Z_s$, where V_s is the voltage measured across the entire laser device. As discussed in Section 2.6, below threshold the laser current-voltage characteristics resemble that of a plane PN diode,

$$I_{ext} = I_o \left[\exp\left(\frac{eV}{mK_B T} \right) - 1 \right] \tag{2.64}$$

Note that V in the above Equation is the voltage across the junction. It follows that the slope of $\log(I_{ext})$ plotted as a function of the junction voltage V gives the value of e/mK_BT. This plot is shown in Fig. 2-16. The dashed line gives the slope just before threshold, and the value of e/mK_BT is found to be approximately 19 1/V. The resistance discontinuity at threshold is given by Equation (2.47),

$$\Delta R_d = \eta_i\, \eta_e \frac{\theta'}{1+\theta'}\, m \frac{K_B T}{q I_{th}} \tag{2.65}$$

The above relation can be used to obtain the value of θ' near threshold if the value of η_e is known. The value of η_e will be assumed to be 0.92 and this value will be verified later in this Section. Using (2.65), the value of θ' is found to be approximately 1.46. Since θ equals $\theta'(1 - \eta_i\, \eta_e)$, the value of θ near threshold is 0.3. Using the relation given in (2.44),

$$\Delta R_d = \frac{1}{G}(\theta' - \theta) \tag{2.66}$$

the value of G is found to be 2.1 Ω^{-1}. The differential resistance of the junction just below and just above threshold can be found using (2.42), and comes out to be 1.18 Ω and 0.65 Ω, respectively. The value of m obtained from the measured value of e/mK_BT, assuming $T \approx 300$, is approximately 2.0. The conventional theory, as formulated in Ref. [49], assumes that the current-voltage characteristics of a diode laser below threshold is given by a relation similar to (2.64), and the differential resistance of the laser above threshold is assumed to be zero. The discontinuity in the differential resistance of the laser at threshold, as predicted by the conventional theory, is therefore mK_BT/eI_{th}. For the laser used in the experiments, mK_BT/eI_{th} equals 1.18 Ω which is almost twice the value of the discontinuity in the differential resistance measured experimentally (see Fig. 2-15). The theory presented

in this Chapter agrees well with the experiments. Knowing the values of θ', θ, η_e, and η_i, the ratios τ_c/τ_g, and τ_c/τ_l can be determined and are found to be 0.357 and 0.167, respectively. The value of τ_e can be obtained from the value of G and the ratio τ_c/τ_g as follows. Below threshold, the ratio of the carrier densities N_c and N_w follow from the rate equations (2.1)-(2.3),

$$N_c V_c = N_w V_w \frac{\tau_c}{\tau_e} \frac{1}{\eta_e} \tag{2.67}$$

It is assumed that below threshold the carrier density N_c is related to the junction voltage as follows,

$$N_c V_c \propto \exp\left(\frac{eV}{mK_B T}\right) \tag{2.68}$$

Differentiating the above Equation with respect to V one obtains,

$$\frac{\delta N_c V_c}{\delta V} = \frac{e N_c V_c}{mK_B T} \tag{2.69}$$

The ratio $\delta N_c V_c/\delta V$ can also be obtained from (2.22) and (2.30) assuming that the laser is biased with a current source ($Z_s = \infty$) and the noise sources are *turned off*,

$$\frac{\delta N_c V_c}{\delta V} = \frac{\tau_g G}{e} \tag{2.70}$$

Using (2.67), (2.68) and (2.69), the value of τ_e near threshold can be estimated by the relation,

$$\frac{1}{\tau_e} = \eta_e \frac{G}{e} \left(\frac{\tau_g}{\tau_c}\right) \left(\frac{mK_B T}{e}\right) \left(\frac{1}{N_w V_w}\bigg|_{I_{ext}=I_{th}}\right) \tag{2.71}$$

At threshold, the carrier density N_w can be determined by equating the cavity gain to the cavity loss. The quantum well gain can be obtained from a model based on 6-band **k.p** theory (see [54]),

$$g = g_o \log\left(\frac{N_w}{N_{tr}}\right) \tag{2.72}$$

where $g_o = 2800$ 1/cm, and $N_{tr} = 1.5 \times 10^{18}$ 1/cm^3. The value of τ_e comes out to be approximately 101 ps. Earlier in this Section, the value of η_e was assumed to be 0.92, and this assumption can now be verified. Near threshold, the value of τ_w can be determined from values of the B and C coefficients given in Table. 2.1, and comes out to be 1.1 ns. The value of η_e, given by the expression $\tau_w/(\tau_e + \tau_w)$, is indeed 0.92. The carrier capture time τ_c cannot be obtained from the measurements presented here. It can be estimated from the

Table 2.4: Values of the Laser Parameters Extracted From Measurements

Parameter	Value
θ'	1.46
θ	0.30
G	2.10
$R_d = Z(\omega = 0)$ (below threshold)	1.18 Ω
$R_d = Z(\omega = 0)$ (above threshold)	0.62 Ω
η_i	0.857
τ_e	101 ps
τ_c	10 ps - 20 ps
τ_g	= 2.8 τ_c = 28 ps - 56 ps
τ_l	= 6.0 τ_c = 60 ps - 120 ps

theoretical result in Ref. [52],

$$\tau_c \approx 1.0\text{ps} - 2.0\text{ps} \times \frac{V_c}{V_w} \tag{2.73}$$

For the lasers used in the experiments, V_c/V_w was approximately 10, and the value of τ_c is estimated to be between 10 ps and 20 ps. Since the ratios τ_c/τ_g and τ_c/τ_l are known from the measurements, the values of τ_l and τ_g can also be estimated and are approximately $60 - 120$ ps and $28 - 56$ ps, respectively. The values of τ_c, τ_l, τ_g, τ_e, θ, θ', and G determined in this Section near the laser threshold, and given in Table 2.4, are expected to be strong functions of the temperature and the bias current.

2.10 Current Noise Experiments

The experimental setup used for measuring the current noise in diode lasers is shown in Fig. 2-17. For the experiments, InGaAsP/InP distributed feedback (DFB) diode lasers were fabricated in collaboration with Michael H. Lim and and Elisabeth Koontz. The laser structure consisted of polyimide planarized ridge optical waveguides that had negligible parasitic capacitance between the top metal contact and the substrate. The laser structure was similar to that of the Fabry-Perot laser shown in Fig. 2-13. This ensured that high frequency current noise measurements would not be affected by RC parasitics. The lasers had a side mode suppression ratio (SMSR) better than 40 dB a little above threshold, as shown in Fig. 2-18. The threshold current of 600×2 μm^2 area devices, with uncoated facets,

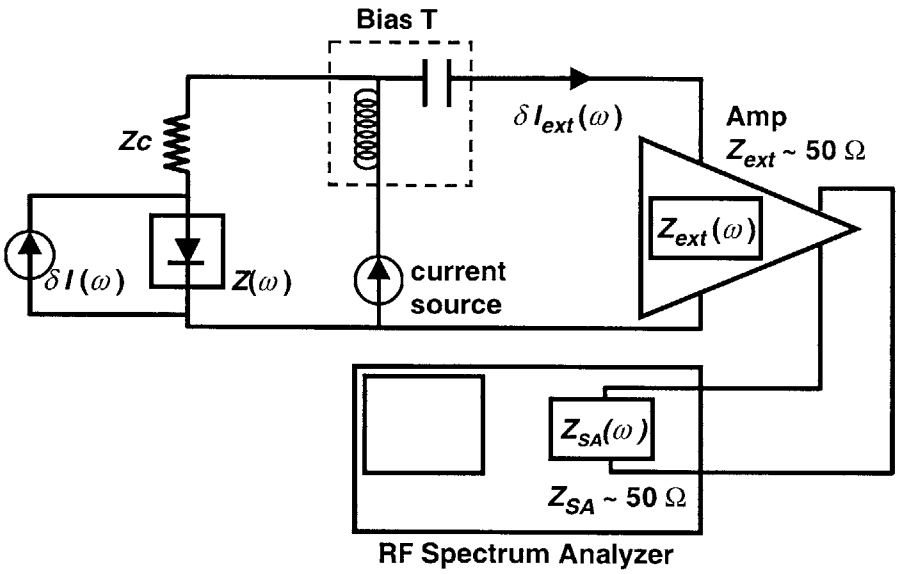

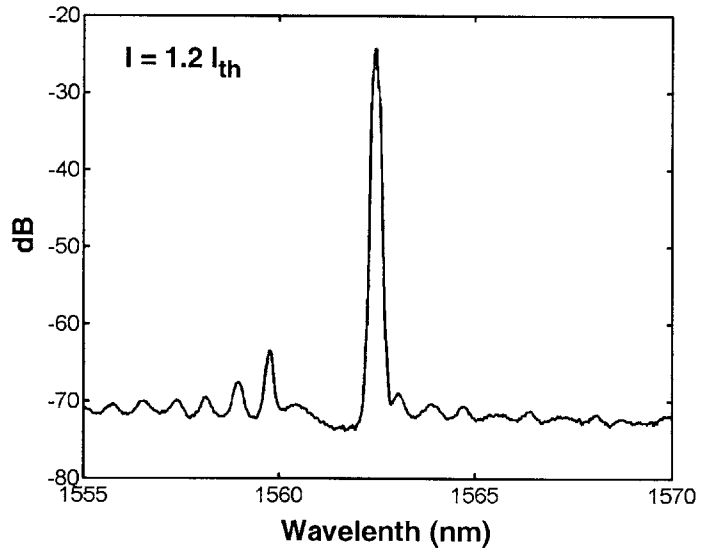

Figure 2-18: Optical spectrum for the InGaAsP/InP DFB laser structures used in the experiments. The lasers had a side mode suppression ratio of better than 40 dB a little above threshold.

Table 2.5: Device Parameters for the InGaAsP/InP DFB Laser Used in Experiments

Parameter	Value
Lasing wavelength λ	1.55 μm
Operating temperature	300 K
Number of quantum wells	5
Cavity width	2.0 μm
Cavity length	600 μm
τ_p	4.1 ps
τ_c	15 ps
τ_e	101 ps
τ_g	42 ps
τ_l	90 ps
$1/\tau_w$	$2 * B * N_w + 3 * C * N_w^2$
B	10^{-10} cm^3/s
C	5×10^{-29} cm^6/s
I_{th}	21 mA

was 21 mA. The values of the laser parameters are given in Table. 2.5. The lasers were biased with a current source through a bias tee, as shown in Fig. 2-17. The signal from the RF port of the bias tee was fed into a low noise amplifier (LNA) with a 30 dB gain over the frequency range from 200 MHz to 2 GHz, and a Noise Figure (NF) less than 1.5 dB. The LNA had a 50 Ω input impedance. The signal from the LNA was fed directly into a RF spectrum analyzer. Co-axial SMA cables were used at each stage of the setup. The large impedance mismatch between the lasers, with junction impedance typically less than 1 Ω above threshold, and the 50 Ω LNA made it difficult to couple noise power from the lasers into the LNA. A rough estimate of the noise power delivered to the RF spectrum analyzer can made as follows. As shown in Fig. 2-8, the current noise of a diode laser attains its maximum value near threshold. A little above threshold, the current noise spectral density is about -185 dB-Amp^2/Hz (see Fig. 2-10). Assuming the differential resistance of the junction to be 1 Ω near threshold, the spectral density of the current noise going into the LNA is -219 dB-Amp^2/Hz. The noise power delivered to the LNA is -172 dBm/Hz, and the noise power delivered to the RF spectrum analyzer is -142 dBm/Hz (LNA gain is 30 dB). The noise floor of the measurement setup is around -140 dBm/Hz. The noise power coupled into the RF spectrum analyzer is, therefore, very close to the noise floor.

Fig. 2-19 shows the noise power measured by the RF spectrum analyzer for different

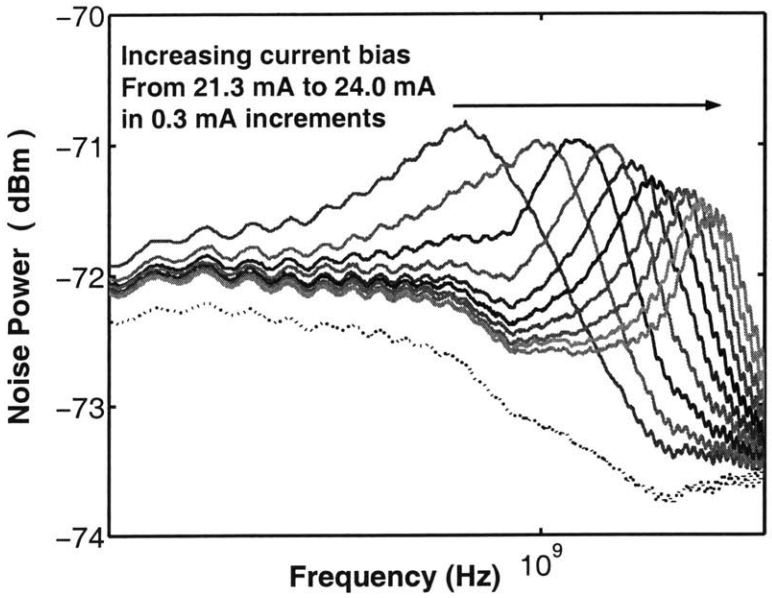

Figure 2-19: The noise power measured with the RF spectrum analyzer (units: dBm) is shown for different values of the bias current from 21.3 mA to 24.0 mA in 0.3 mA increments (solid lines). The threshold current is 21.0 mA. The dotted line shows the noise floor measured with the input to the LNA shorted. The resolution bandwidth of the RF spectrum analyzer was 3 MHz. The measured noise spectral densities show the laser relaxation oscillation peaks.

values of the laser bias current; from 21.3 mA to 24.0 mA in 0.3 mA increments. The laser relaxation oscillation peaks are clearly visible in the measured spectra. The signal measured by the RF spectrum analyzer is, as expected, close to the noise floor. The total noise power $S_N(\omega)$ (units: dBm) measured by the RF spectrum analyzer can be written as,

$$S_N(\omega) = 10 \log_{10} \left[2 K_I(\omega) \left(\frac{Z}{Z + Z_c + Z_{ext}} \right)^2 Z_{ext} \, 10^3 \, G \, R_B \; + \; N_f(\omega) \right] \tag{2.74}$$

Here, Z_c is the impedance of the diode excluding the junction impedance and was measured to be 6.0 Ω, Z is the differential resistance of the junction, Z_{ext} is the input impedance of the LNA and is assumed to be 50 Ω, G is the LNA gain and equals 10^3, R_B is the resolution bandwidth of the spectrum analyzer and equals 3 MHz, and $N_f(\omega)$ represents the noise floor. The factor of two on the right hand side in (2.74) converts from the double-sided noise spectral density $K_I(\omega)$ to the single-sided noise power $S_N(\omega)$. The dotted line in Fig. 2-19 is the noise floor (obtained by shorting the inputs to the LNA). The current noise

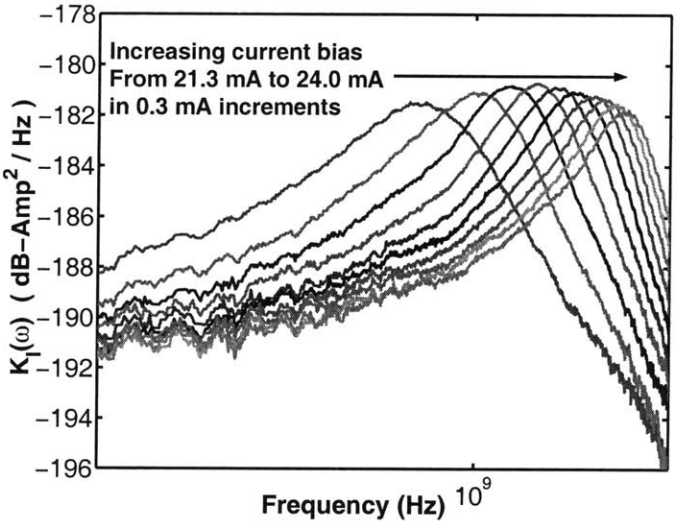

Figure 2-20: The laser current noise spectral density $K_I(\omega)$, estimated from the noise power measured with the RF spectrum analyzer, is shown for different values of the bias current from 21.3 mA to 24.0 mA in 0.3 mA increments. The measured noise spectral densities show the laser relaxation oscillation peaks. The measured current noise spectral density is in excellent agreement with the theoretical results shown in Fig. 2-21.

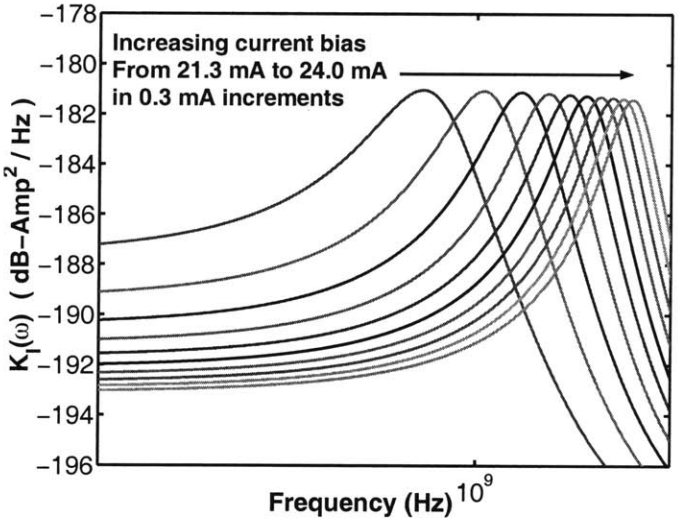

Figure 2-21: The laser current noise spectral density $K_I(\omega)$ calculated from the theory is shown for different values of the bias current from 21.3 mA to 24.0 mA in 0.3 mA increments. The values of the laser parameters are given in Table. 2.5. The calculated current noise spectral density is in excellent agreement with the measured results shown in Fig. 2-20.

spectral density $K_I(\omega)$ of the laser can be determined by inverting the relation in (2.74). Fig. 2-20 shows the measured laser current noise spectra for different values of the bias current. The theoretical results for the laser current noise spectra using the parameter values given in Table. 2.5 are shown in Fig. 2-21. The measured results agree very well with the theory. The value of the junction impedance Z in Fig. 2-20 was assumed to be 0.65 Ω in order to obtain a match with the theoretical results in Fig. 2-21. This is to our knowledge the first reported measurement of the laser current noise spectral density. The error in the measured value of $K_I(\omega)$ was estimated to be less than ± 2 dB-Amp^2/Hz. There is a good reason why the theoretical results agree so well with the measurements. Above threshold, the dominant term contributing to the laser current noise, as explained earlier, is the last term on the right hand side in (2.54),

$$2e\, n_{sp}\, \eta_i\, (I_{ext} - I_{th})\, \frac{\left(\theta\, \frac{\tau_{st}}{\tau_e}\right)^2}{Z^2\, G^2} \tag{2.75}$$

The magnitude of this term depends critically on the factor $(\theta/G\tau_e)^2$. The other factors are either known or can be estimated fairly accurately. Using (2.71), one can obtain an expression for $\theta/G\tau_e$ valid near the laser threshold,

$$\frac{\theta}{G\tau_e} = \eta_e\, \eta_i \left(\frac{mK_BT}{e}\right) \left(\frac{1}{eN_wV_w}\bigg|_{I_{ext}=I_{th}}\right) \tag{2.76}$$

The right hand side in (2.76) can be estimated accurately given that both η_e and η_i are close to unity. The laser parameters used in generating the theoretical results in Fig.2-21 (see Table 2.5) satisfy (2.76). The spectral density of the current noise in the external circuit is given by the expression in (2.75) multiplied by a current division factor which is approximately $[Z/(Z_c + Z_{ext})]^2$. So the junction impedance Z cancels out, and in the ideal case the noise power measured by the RF spectrum analyzer can be predicted fairly accurately. The junction impedance Z is needed to convert back from the noise power measured by the RF spectrum analyzer to the spectral density of the laser current noise. As mentioned above, the junction impedance was assumed to be 0.65 Ω to obtain a good match between the theory and the experimental data.

The current noise measurements, especially the observance of the relaxation oscillation peaks in the measured current noise spectra, show that the current noise in diode lasers is

driven by the carrier density fluctuations inside the active region. In the next Chapter, the theoretical models presented in this Chapter will be used to develop models for the noise in semiconductor interband cascade lasers.

Chapter 3

Noise and Correlations in Semiconductor Interband Cascade Lasers

Semiconductor cascade lasers were introduced in Chapter 1. In semiconductor cascade lasers, several gain stages are connected electrically in series as shown in Fig. 1-1 of Chapter 1. These gain stages may be in the same optical cavity or in different optical cavities. The fundamental difference between a semiconductor cascade laser and a conventional semiconductor laser is that each electron injected into a cascade laser is recycled from one gain stage to the other and is able to produce multiple photons (see Fig. 1-3). In a conventional laser, each electron injected into the device cannot produce more than one photon. Consequently, the quantum efficiency of a cascade laser can be much greater than 100 percent, whereas the quantum efficiency of a conventional laser is always less than 100 percent. In Chapter 1, it was shown that the increased quantum efficiency of cascade lasers make them highly suitable for RF photonic links. The noise behavior of cascade lasers can be significantly different from that of conventional semiconductor lasers. In cascade lasers, since all the gain stages are connected electrically, the carrier density fluctuations and, consequently, the photon emission events in different gain stages are correlated. In this Chapter, theoretical models are presented for the noise and correlations in semiconductor interband cascade lasers. Experimental results that verify the theoretical models are also presented.

In Section 3.1, interconnect-coupled multiple cavity cascade lasers, shown in Fig. 1-4

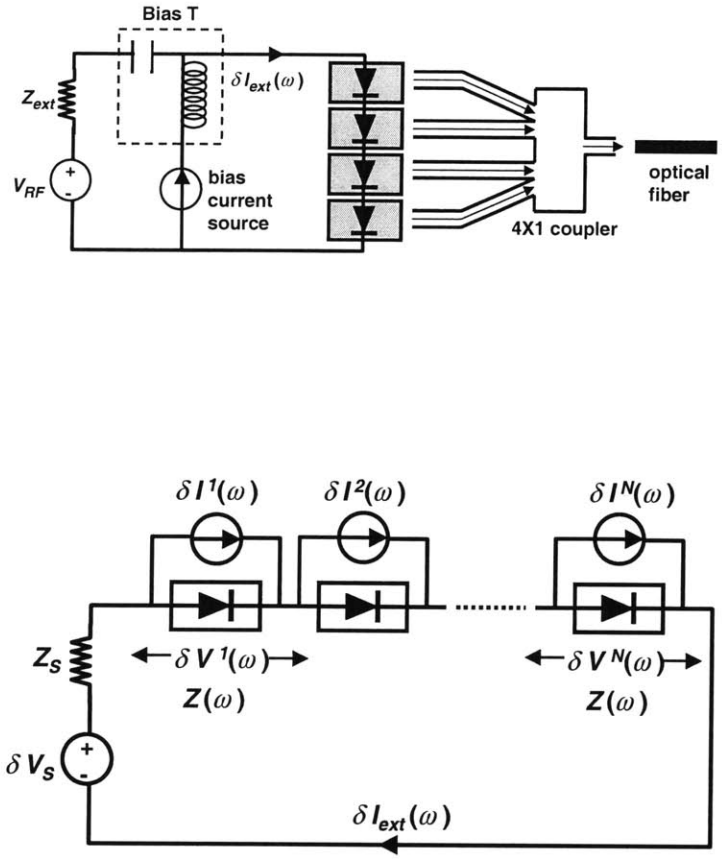

Figure 3-2: A circuit model for the current noise in a multiple cavity cascade laser (MCCL).

of Chapter 1, are discussed. Parallel laser arrays, shown in Fig.1-7 of Chapter 1, are also discussed in the same Section. Parallel laser arrays are not cascade devices, but their noise characteristics are closely related to those of multiple cavity cascade lasers. In Section 3.3, experimental results on the correlations in the photon noise in multiple cavity cascade lasers and parallel laser arrays are presented. In Section 3.4, the noise in interconnect coupled split waveguide cascade lasers, shown in Fig. 1-5 of Chapter 1, is discussed, and in Section 3.5, theoretical models for the noise in bipolar cascade lasers, shown in Fig. 1-6, are presented.

3.1 Multiple Cavity Cascade Lasers

3.1.1 Theoretical Model

In a multiple cavity cascade laser (MCCL), cascaded stages are connected electrically in series in separate optical cavities. An integrated MCCL is shown in Fig. 1-4 of Chapter 1 [3, 4]. For application in RF photonic links, light from all the optical cavities needs to be collected before it can be transmitted over an optical fiber, as shown in Fig. 3-1. The noise characteristics of MCCLs can be derived from the models of the laser current noise and photon noise presented in Chapter 2. The Langevin rate equations for the carrier and the photon densities in the j-th cascaded stage are as follows,

$$\frac{d\,\delta N_c^j V_c}{d\,t} = \frac{\delta I_{ext}}{e} - \delta N_c^j V_c \left(\frac{1}{\tau_c} + \frac{1}{\tau_l}\right) + \frac{\delta N_w^j V_w}{\tau_e} - F_c^j - F_l^j + F_e^j \tag{3.1}$$

$$\frac{d\,\delta N_w^j V_w}{d\,t} = \frac{\delta N_c^j V_c}{\tau_c} - \delta N_w^j V_w \left(\frac{1}{\tau_e} + \frac{1}{\tau_w} + \frac{1}{\tau_{st}}\right) - \frac{V_w}{V_p} v_g\, g\, \delta S_p^j V_p + F_c^j - F_e^j - F_{nr}^j - F_R^j \tag{3.2}$$

$$\frac{d\,\delta S_p^j V_p}{d\,t} = \frac{\delta N_w^j V_w}{\tau_{st}} + \left(\frac{V_w}{V_p} v_g\, g - \frac{1}{\tau_p}\right) \delta S_p^j V_p + F_R^j - F_L^j \tag{3.3}$$

The Equations above are the same as those given in (2.9)-(2.11) for a conventional semiconductor laser except for the superscript j. Since the same current flows through all the stages connected electrically in series, δI_{ext} in (3.1) does not have a superscript. The fluctuation in the output power δP_{out}^j from the j-th stage is,

$$\delta P_{out}^j = \eta_o \hbar \Omega_o \frac{\delta S_p^j\, V_p}{\tau_p} + F_o^j \tag{3.4}$$

The fluctuation δP_{out}^T in the collected output power is $\sum_{j=1}^{N} \delta P_{out}^j$, where N is the total number of cascaded stages. The current noise δI_{ext} in the external circuit can be related to the carrier density fluctuations in the j-th section as shown below,

$$\frac{\delta I_{ext}}{e} = \frac{G\,\delta V^j}{e} - \frac{\delta N_c^j V_c}{\tau_G} + F_{in}^j \tag{3.5}$$

The correlation functions of all the Langevin noise sources are given in Chapter 2. The Langevin noise sources belonging to different stages in the cascade are uncorrelated. The

condition imposed by the external circuit is given as (see Fig. 3-2),

$$\delta I_{ext}(\omega) = \frac{\delta V_s(\omega) - \sum_{j=1}^{N} \delta V^j(\omega)}{Z_s(\omega)} \tag{3.6}$$

Equations (3.1)-(3.3), together with (3.5) and (3.6), can be solved in the frequency domain to yield the circuit model shown in Fig. 3-2 in which a current noise source $\delta I^j(\omega)$ is attached in parallel with the active region of the j-th stage. The impedance $Z(\omega)$ of each active region is the same as that given in (2.41) in Chapter 2. The parasitic series resistances in all the stages are lumped in with the impedance $Z_s(\omega)$. The expression for the current noise source $\delta I^j(\omega)$ is also given by an expression identical to that in (2.51) in Chapter 2, except that all the Langevin noise sources in the expression have the superscript j,

$$\delta I^j(\omega) = \frac{e}{Z(\omega)} \frac{1}{G} \left[F_{in}^j(\omega) - \sum_{k=1}^{3} \frac{\mathbf{D}_{1k}^{-1}(\omega)}{\tau_G} F_k^j(\omega) \right] \tag{3.7}$$

The current fluctuation δI_{ext} in the external circuit is,

$$\delta I_{ext}(\omega) = \frac{\delta V_s(\omega)}{N\,Z(\omega) + Z_s(\omega)} + \left(\frac{Z(\omega)}{N\,Z(\omega) + Z_s(\omega)} \right) \sum_{j=1}^{N} \delta I^j(\omega) \tag{3.8}$$

The noise $\delta P_{out}^j(\omega)$ in the output power from the j-th cascade section follows from (2.58) in Chapter 2

$$\delta P_{out}^j(\omega) = \eta_o \frac{\hbar\Omega_o}{e} \frac{\mathbf{D}_{31}^{-1}(\omega)}{\tau_p} \delta I_{ext}(\omega) + \eta_o \hbar\Omega_o \sum_{k=1}^{3} \frac{\mathbf{D}_{3k}^{-1}(\omega)}{\tau_p} F_k^j(\omega) + F_o^j \tag{3.9}$$

$$\begin{aligned} = {} & \eta_o \frac{\hbar\Omega_o}{e} \frac{\mathbf{D}_{31}^{-1}(\omega)}{\tau_p} \frac{\delta V_s(\omega)}{N\,Z(\omega) + Z_s(\omega)} \\ & + \eta_o \frac{\hbar\Omega_o}{e} \frac{\mathbf{D}_{31}^{-1}(\omega)}{\tau_p} \left(\frac{Z(\omega)}{N\,Z(\omega) + Z_s(\omega)} \right) \sum_{q=1}^{N} \delta I^q(\omega) \\ & + \eta_o \hbar\Omega_o \sum_{k=1}^{3} \frac{\mathbf{D}_{3k}^{-1}(\omega)}{\tau_p} F_k^j(\omega) + F_o^j \end{aligned} \tag{3.10}$$

3.1.2 Correlations in the Photon Noise of Cascade Sections

Since the current noise that contributes to the photon noise of a cascade section has contributions from the noise generated in all the cascade sections, the photon noise in different cascade sections is correlated. The cross-spectral density $K_P^{jq}(\omega)$ of the noise in the output

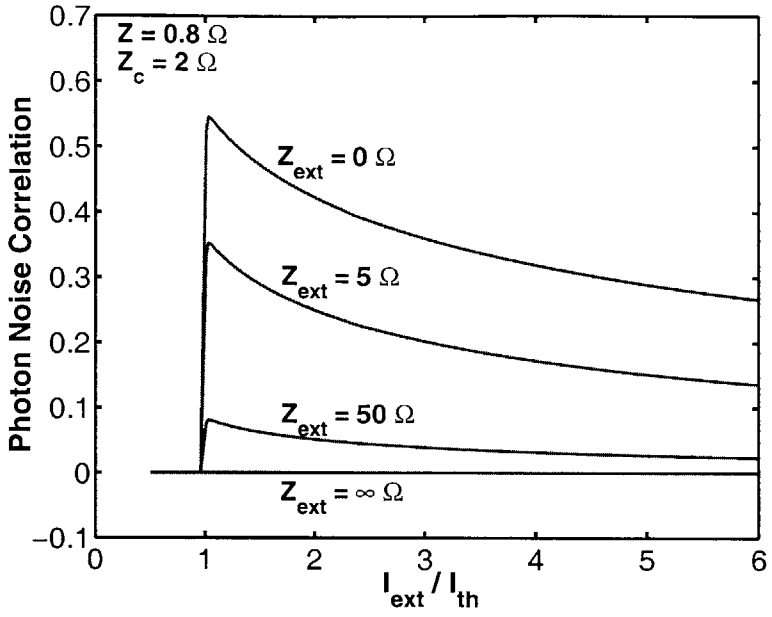

Figure 3-3: The low frequency correlation in the noise in the output powers of two different sections of a two-section multiple cavity cascade laser is plotted as a function of the bias current for different values of the circuit impedance $Z_s(\omega)$. Each laser in the cascade device is assumed to be a InGaAsP/InP diode laser operating at 1550 nm. The laser parameters are given in Table. 3.1.

powers from the j-th and the q-th cascade sections is defined as follows,

$$K_P^{jq}(\omega) = \int_{-\infty}^{\infty} d\tau \, R_P^{jq}(\tau) \, \exp\left(-j\omega\,\tau\right) \tag{3.11}$$

where the correlation function $R_P^{jq}(\tau)$ is,

$$R_P^{jq}(\tau) = \langle \delta P_{out}^{j}(t) \, \delta P_{out}^{q}(t+\tau) \rangle \tag{3.12}$$

Symmetry implies $R_P^{jq}(\tau) = R_P^{qj}(\tau)$, and symmetry with stationarity implies $R_P^{jq}(-\tau) = R_P^{jq}(\tau)$. It follows that $K_P^{jq}(-\omega) = K_P^{jq^*}(\omega) = K_P^{jq}(\omega)$. The cross-spectral density $K_P^{jq}(\omega)$ can also be calculated directly in the frequency domain (also see Appendix A.1),

$$K_P^{jq}(\omega) = \int_{-\infty}^{\infty} \frac{d\,\omega'}{2\pi} \, \langle \delta P_{out}^{j\,*}(\omega) \, \delta P_{out}^{q}(\omega+\omega') \rangle \tag{3.13}$$

In what follows, it is convenient to introduce $K_P(\omega)|_{Z_o}(\omega)$ as the spectral density of the noise in the output power of a conventional semiconductor laser when the active region of

Table 3.1: Device Parameters for the InGaAsP/InP MCCL Used in Numerical Simulations of the Correlations in the Photon Noise

Parameter	Value
Lasing wavelength λ	1.55 μm
Operating temperature	300 K
Number of quantum wells	5
Cavity width	2.0 μm
Cavity length	400 μm
Cavity internal loss	9 cm^{-1}
τ_p	3.15 ps
τ_c	5 ps
τ_e	30 ps
τ_g	15 ps
τ_l	100 ps
$1/\tau_w$	$2 * B * N_w + 3 * C * N_w^2$
B	10^{-10} cm^3/s
C	5×10^{-29} cm^6/s
I_{th}	15 mA
η_i	0.95
η_o	0.75
$R_d = Z(\omega = 0)$	0.80 Ω
$Z_c(\omega = 0)$	2.0 Ω

the laser is in series with an impedance $Z_o(\omega)$ in the *absence of any source of noise external to the active region, including thermal noise in any of the circuit impedances.* $K_P(\omega)|_{Z_o}(\omega)$ can be calculated from the formulas given in Chapter 2. $K_P^{jq}(\omega)$ can then be written in the following form,

$$\begin{aligned} K_P^{jq}(\omega) &= \left|\eta_o \frac{\hbar\Omega_o}{e} \frac{\mathbf{D}_{31}^{-1}(\omega)}{\tau_p}\right|^2 \left|\frac{1}{N\,Z(\omega) + Z_s(\omega)}\right|^2 K_{V_s}(\omega) \\ &\quad + (N-1)\left|\eta_o \frac{\hbar\Omega_o}{e} \frac{\mathbf{D}_{31}^{-1}(\omega)}{\tau_p}\right|^2 \left|\frac{Z(\omega)}{N\,Z(\omega) + Z_s(\omega)}\right|^2 K_I(\omega) \\ &\quad + K_P(\omega)|_{(N-1)Z(\omega)+Z_s(\omega)} - \left(1 - \delta^{jq}\right) K_P(\omega)|_\infty \end{aligned} \tag{3.14}$$

The normalized correlation $C_P^{jq}(\omega)$ in the photon noise of two different cascade sections is,

$$C_P^{jq}(\omega) = \frac{K_P^{jq}(\omega)}{\sqrt{K_P^{jj}(\omega)\,K_P^{qq}(\omega)}} \tag{3.15}$$

Schwartz inequality, and the fact that $K_P^{jq}(\omega)$ is real, imply that,

$$-1 \leq C_P^{jq}(\omega) \leq 1 \tag{3.16}$$

Using (3.14), one obtains,

$$C_P^{jq}(\omega) = 1 - \frac{K_P(\omega)|_\infty}{K_P^{jj}(\omega)} \tag{3.17}$$

From (3.14), and the analysis presented in Chapter 2, it follows that $K_P^{jj}(\omega)$ is always greater than $K_P(\omega)|_\infty$ for frequencies smaller than the modulation bandwidth of the laser and, therefore, at small frequencies the noise in the output power of two different cascade sections is positively correlated. At frequencies much larger than the modulation bandwidth both $K_P(\omega)|_\infty$ and $K_P^{jj}(\omega)$ approach the shot noise spectral density and the noise correlation $C_P^{jq}(\omega)$ approaches zero. The positive correlation in the photon noise of two different cascade sections at low frequencies can be understood as follows. Suppose in some time interval photons in excess of the average rate are emitted in a cascade section. As a result, the carrier density in the active region of that section, and the voltage across the active region, will drop below their average values, and the current in the circuit will become larger than its average value. The increase in the circuit current will in turn increase the chances of photon emissions in excess of the average emission rate in all the other cascade sections. Thus, photon noise in different cascade sections is positively correlated. In addition, noise sources external to the laser, such as thermal noise in the circuit resistances, also positively correlates the photon noise in different cascade sections.

The degree of the noise correlation depends sensitively on the total impedance $NZ(\omega) + Z_s(\omega)$ of the circuit. If the circuit impedance becomes large, $K_P^{jj}(\omega)$ approaches $K_P(\omega)|_\infty$, and the noise correlation approaches zero. Without loosing generality, the impedance $Z_s(\omega)$ is assumed to consist of an external circuit impedance $Z_{ext}(\omega)$ and also parasitic impedances $Z_c(\omega)$ associated with each cascade section, i.e. $Z_s(\omega) = N\, Z_c(\omega) + Z_{ext}(\omega)$. Fig. 3-3 shows the low frequency correlation in the noise in the output power of a two section MCCL as a function of the bias current for different values of the circuit impedance $Z_{ext}(\omega)$. Each cascade section is assumed to be a InGaAsP/InP diode laser operating at 1550 nm. The laser parameters are given in Table. 3.1. Fig. 3-3 shows that the correlation in the photon noise of the two cascade sections is almost 60 percent when the circuit impedance $Z_{ext}(\omega)$ is small. The maximum correlation is limited by the series impedance Z_c of each cascade

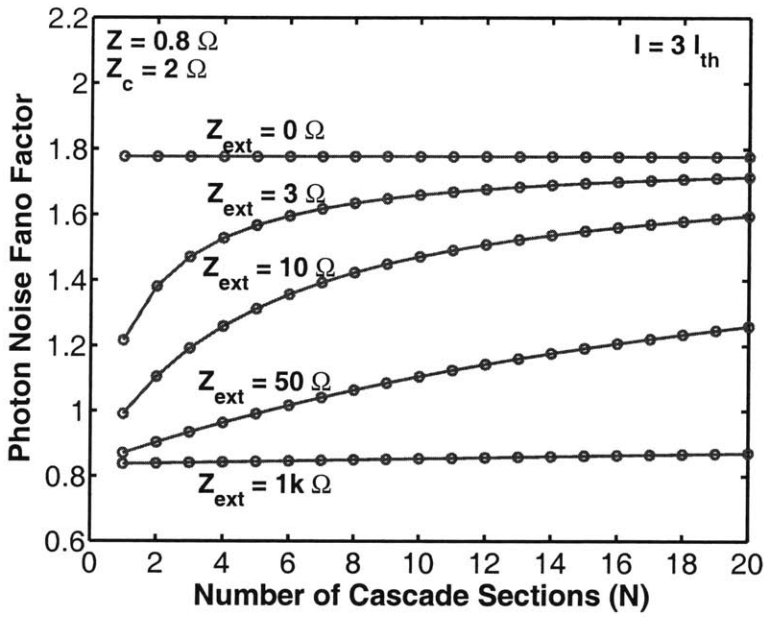

Figure 3-4: The Fano Factor of the noise in the collected output power is plotted as a function of the number of sections in a multiple cavity cascade laser for different values of the impedance $Z_{ext}(\omega)$. Each laser in the cascade device is assumed to be a InGaAsP/InP diode laser operating at 1550 nm. The laser parameters are given in Table. 3.1. The bias current is assumed to be three times the threshold bias.

section which is assumed to be 2.0 Ω in Fig. 3-3.

3.1.3 Photon Noise in the Collected Output Power

Since the photon emissions in different cascade sections are positively correlated, it is reasonable to expect that these positive correlations would increase the photon noise when light from all the cascade sections is collected. An interesting scaling relation can be derived for the noise δP_{out}^{T} in the collected output power. Summing both sides of (3.10) over the superscript j, one obtains,

$$\begin{aligned}
\delta P_{out}^{T} &= \sum_{j=1}^{N} \delta P_{out}^{j}(\omega) \\
&= \eta_o \frac{\hbar\Omega_o}{e} \frac{\mathbf{D}_{31}^{-1}(\omega)}{\tau_p} \frac{N\, V_s(\omega)}{N\, Z(\omega) + Z_s(\omega)} \\
&\quad + \sum_{q=1}^{N} \left[\eta_o \frac{\hbar\Omega_o}{e} \frac{\mathbf{D}_{31}^{-1}(\omega)}{\tau_p} \left(\frac{N\, Z(\omega)}{N\, Z(\omega) + Z_s(\omega)} \right) \delta I^{q}(\omega) \right.
\end{aligned}$$

$$+ \eta_o \hbar\Omega_o \sum_{k=1}^{3} \frac{\mathbf{D}_{3k}^{-1}(\omega)}{\tau_p} F_k^q(\omega) + F_o^q \Bigg] \tag{3.18}$$

In what follows, it will be assumed that the noise source $\delta V_s(\omega)$ represents the thermal noise associated with circuit impedances, and its spectral density $K_{V_s}(\omega)$ equals $2K_BT\,\mathrm{Re}\{Z_s\}$, where $Z_s(\omega) = NZ_c(\omega) + Z_{ext}(\omega)$. The spectral density of the noise in the collected output power depends on the average output power (or the ratio I_{ext}/I_{th}), the external circuit impedance $Z_{ext}(\omega)$, and the number N of cascade sections. The spectral density of the noise in the collected output power follows from (3.18), and it can be written in a way that explicitly shows the scaling of the noise with the number of cascade sections,

$$K_{PT}(\omega, I_{ext}/I_{th}, Z_{ext}, N) = N\,K_{PT}(\omega, I_{ext}/I_{th}, Z_{ext}/N, 1) \tag{3.19}$$

If the noise in the output power of different sections were uncorrelated, the spectral density of the noise in the collected output power would be N times the spectral density of the noise in a single section laser. The positive correlations in the photon noise of different sections results in increased noise in the collected output power. Interestingly, the increase in the noise can be expressed as a scaled external circuit impedance as shown in (3.19) above (recall from Chapter 2 that a laser biased with smaller series impedance has larger noise in the output power). When $Z_{ext}(\omega)$ is very large, the current fluctuations in the circuit, and, consequently, the positive correlations in the photon noise in different cascade sections are suppressed, and the noise in the collected output power is N times the noise in the output power of a single section laser. When $Z_{ext}(\omega)$ is zero, the spectral density of the noise in the collected output power is again N times the spectral density of the noise in a single section laser. This is because the increase in the noise due to the positive correlations in the photon noise in different cascade sections is exactly balanced by the decrease in the photon noise due to the increase in the circuit impedance seen by each cascade section with the increase in the number of cascade sections (the total impedance of the circuit, $NZ(\omega) + NZ_c(\omega) + Z_{ext}(\omega)$, increases linearly with N when $Z_{ext}(\omega)$ is zero). Fig.3-4 shows the Fano Factor of the noise in the collected output power as a function of the number of sections in a MCCL for different values of the impedance $Z_{ext}(\omega)$. Each section in the MCCL is assumed to be a InGaAsP/InP laser operating at 1550 nm. The laser parameters are given in Table. 3.1.

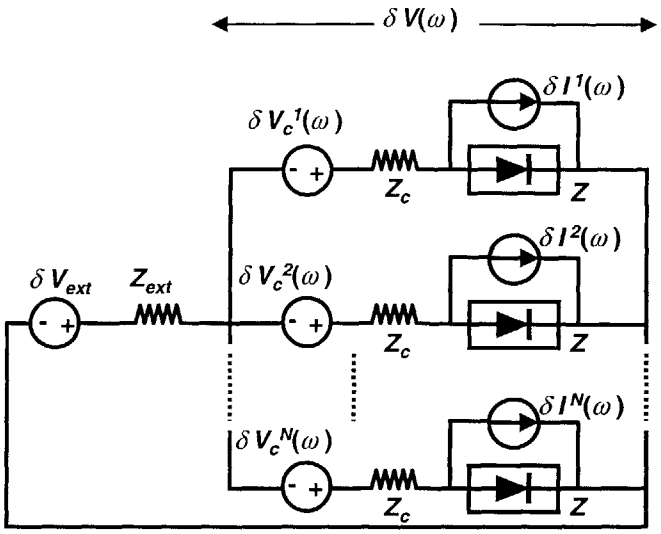

Figure 3-5: A circuit model for the current noise in a parallel laser array.

3.2 Parallel Laser Arrays

3.2.1 Theoretical Model

In a parallel laser array (PLA), laser sections are connected electrically in parallel as shown in Fig. 1-7 of Chapter 1. PLAs are not cascade devices but their noise properties bear a close relationship to cascade devices since in PLAs, like in cascade devices, the gain sections are connected electrically. The noise characteristics of PLAs can be derived using methods similar to those used for MCCL devices. In MCCLs, the current flowing through all the cascaded sections is the same. In PLAs, the potential drop across all the sections is the same since they are connected electrically in parallel. A circuit model for the noise in a PLA is shown in Fig. 3-5. A current noise source $\delta I^j(\omega)$, given by the expression in (3.7), is attached in parallel with the j-th section. In addition, a voltage noise source $\delta V_c^j(\omega)$ is also attached in series with j-th section and represents the thermal noise associated with the series impedance $Z_c(\omega)$ of each array section. The noise $\delta P_{out}^j(\omega)$ in the output power from the j-th section can be found using the methods described earlier for MCCLs,

$$\delta P_{out}^j(\omega) = \eta_o \frac{\hbar\Omega_o}{e} \frac{\mathbf{D}_{31}^{-1}(\omega)}{\tau_p} \frac{\delta V_{ext}(\omega)}{Z + Z_c + N\,Z_{ext}}$$

$$
\begin{aligned}
&+ \eta_o \frac{\hbar\Omega_o}{e} \frac{\mathbf{D}_{31}^{-1}(\omega)}{\tau_p} \left(\frac{Z}{Z+Z_c}\right) \left(\frac{Z+Z_c+(N-1)Z_{ext}}{Z+Z_c+NZ_{ext}}\right) \delta I^j(\omega) \\
&- \eta_o \frac{\hbar\Omega_o}{e} \frac{\mathbf{D}_{31}^{-1}(\omega)}{\tau_p} \left(\frac{Z}{Z+Z_c}\right) \left(\frac{Z_{ext}}{Z+Z_c+NZ_{ext}}\right) \sum_{q\neq j} \delta I^q(\omega) \\
&+ \eta_o \frac{\hbar\Omega_o}{e} \frac{\mathbf{D}_{31}^{-1}(\omega)}{\tau_p} \left(\frac{1}{Z+Z_c}\right) \left(\frac{Z+Z_c+(N-1)Z_{ext}}{Z+Z_c+NZ_{ext}}\right) \delta V_c^j(\omega) \\
&- \eta_o \frac{\hbar\Omega_o}{e} \frac{\mathbf{D}_{31}^{-1}(\omega)}{\tau_p} \left(\frac{1}{Z+Z_c}\right) \left(\frac{Z_{ext}}{Z+Z_c+NZ_{ext}}\right) \sum_{q\neq j} \delta V_c^q(\omega) \\
&+ \eta_o \hbar\Omega_o \sum_{k=1}^{3} \frac{\mathbf{D}_{3k}^{-1}(\omega)}{\tau_p} F_k^j(\omega) + F_o^j
\end{aligned} \tag{3.20}
$$

Its convenient to define impedances Z_1 and Z_2 as follows,

$$
Z_1 = (Z+Z_c)\left[\frac{Z+Z_c+NZ_{ext}}{Z+Z_c+(N-1)Z_{ext}}\right] - Z \tag{3.21}
$$

$$
Z_2 = (Z+Z_c)\left[\frac{Z+Z_c+NZ_{ext}}{Z_{ext}}\right] - Z \tag{3.22}
$$

The spectral densities $K_P^{jj}(\omega)$ and $K_P^{jq}(\omega)$ $(j \neq q)$ can then be written as,

$$
\begin{aligned}
K_P^{jj}(\omega) \;=\; & \left|\eta_o \frac{\hbar\Omega_o}{e} \frac{\mathbf{D}_{31}^{-1}(\omega)}{\tau_p}\right|^2 \left|\frac{1}{Z+Z_c+NZ_{ext}}\right|^2 K_{V_{ext}}(\omega) \\
&+ \left|\eta_o \frac{\hbar\Omega_o}{e} \frac{\mathbf{D}_{31}^{-1}(\omega)}{\tau_p}\right|^2 \left[\left|\frac{1}{Z+Z_1}\right|^2 + (N-1)\left|\frac{1}{Z+Z_2}\right|^2\right] K_{V_c}(\omega) \\
&+ \left|\eta_o \frac{\hbar\Omega_o}{e} \frac{\mathbf{D}_{31}^{-1}(\omega)}{\tau_p}\right|^2 \left[(N-1)\left|\frac{Z}{Z+Z_2}\right|^2\right] K_I(\omega) \\
&+ K_P(\omega)|_{Z_1(\omega)}
\end{aligned} \tag{3.23}
$$

$$
\begin{aligned}
K_P^{jq}(\omega) \;=\; & \left|\eta_o \frac{\hbar\Omega_o}{e} \frac{\mathbf{D}_{31}^{-1}(\omega)}{\tau_p}\right|^2 \left|\frac{1}{Z+Z_c+NZ_{ext}}\right|^2 K_{V_{ext}}(\omega) \\
&+ \left|\eta_o \frac{\hbar\Omega_o}{e} \frac{\mathbf{D}_{31}^{-1}(\omega)}{\tau_p}\right|^2 \left[\left|\frac{1}{Z+Z_1}\right|^2 + (N-1)\left|\frac{1}{Z+Z_2}\right|^2 - \left|\frac{1}{Z+Z_c}\right|^2\right] K_{V_c}(\omega) \\
&+ \left|\eta_o \frac{\hbar\Omega_o}{e} \frac{\mathbf{D}_{31}^{-1}(\omega)}{\tau_p}\right|^2 \left[\left|\frac{Z}{Z+Z_1}\right|^2 + N\left|\frac{Z}{Z+Z_2}\right|^2 - \left|\frac{Z}{Z+Z_c}\right|^2\right] K_I(\omega) \\
&- K_P(\omega)|_{Z_2(\omega)} + K_P(\omega)|_{\infty}
\end{aligned} \tag{3.24}
$$

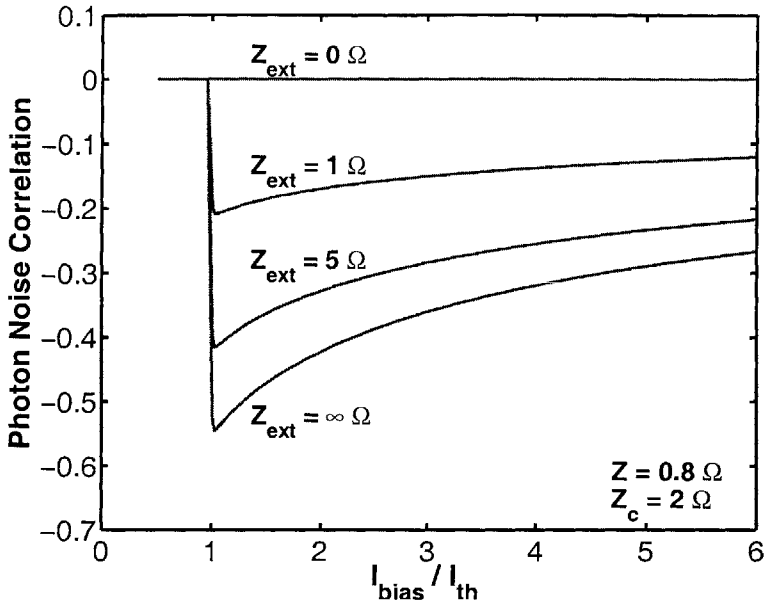

Figure 3-6: The low frequency correlation in the noise in the output powers of two different array sections of a two-section parallel laser array is plotted as a function of the bias current for different values of the circuit impedance $Z_{ext}(\omega)$. Each laser in the array is assumed to be a InGaAsP/InP diode laser operating at 1550 nm. The laser parameters are given in Table. 3.1.

3.2.2 Correlations in the Photon Noise of Array Sections

The normalized correlation $C_P^{jq}(\omega)$ in the photon noise of two different array sections can be determined using (3.23) and (3.23) with (3.15),

$$C_P^{jq}(\omega) = 1 - \frac{1}{K_P^{jj}(\omega)} \left[K_P(\omega)|_{Z_c(\omega)} + \left| \eta_o \frac{\hbar\Omega_o}{e} \frac{\mathbf{D}_{31}^{-1}(\omega)}{\tau_p} \right|^2 \left| \frac{Z}{Z+Z_1} \right|^2 K_I(\omega) + \left| \eta_o \frac{\hbar\Omega_o}{e} \frac{\mathbf{D}_{31}^{-1}(\omega)}{\tau_p} \right|^2 \left| \frac{1}{Z+Z_c} \right|^2 K_{V_c}(\omega) \right] \tag{3.25}$$

If $K_{V_{ext}}(\omega) = 0$, then $C_P^{jq}(\omega) \leq 0$ and the photon noise in any two array sections is negatively correlated at frequencies smaller than the modulation bandwidth of the laser. At frequencies much larger than the modulation bandwidth, $C_P^{jq}(\omega)$ approaches zero. The contribution to the photon noise from the voltage noise source $\delta V_{ext}(\omega)$ is positively correlated in different array sections, and if $K_{V_{ext}}(\omega)$ is large enough, $C_P^{jq}(\omega)$ can become positive at low frequencies. However, in most cases of interest, where $\delta V_{ext}(\omega)$ represents the thermal

noise in the impedance $Z_{ext}(\omega)$, $K_{V_{ext}}(\omega)$ makes only a modest contribution to the photon noise and $C_P^{jq}(\omega)$ is negative. When $N = 2$, it can be shown that $C_P^{jq}(\omega)$ for the parallel laser array with $Z_{ext}(\omega) = \infty$ and $C_P^{jq}(\omega)$ for the multiple cavity cascade laser with $Z_{ext}(\omega) = 0$ are equal in magnitude but opposite in sign. This result follows simply from the symmetry of the two problems.

The negative correlation in the photon noise of two array sections at low frequencies can be understood as follows. Suppose in some time interval photons in excess of the average rate are emitted in an array section. As a result, the carrier density in the active region of that section will drop below its average value. Since the voltage across all the array sections connected in parallel must be the same, the circuit will pump extra current in this array section in order to maintain the voltage across the section. Consequently, the current in all the other array sections will decrease and the photon emission rate in all the other sections will fall below the average emission rate. Thus, photon noise in different array sections is negatively correlated. In addition, noise sources external to the laser, such as the voltage noise sources $\delta V_c^j(\omega)$, also negatively correlates the photon noise in different array sections.

Fig. 3-6 shows the low frequency correlation in the noise in the output power of a two section PLA as a function of the bias current for different values of the impedance $Z_{ext}(\omega)$. Each array section is assumed to be a InGaAsP/InP diode laser operating at 1550 nm. The laser parameters are given in Table. 3.1. The maximum correlation is limited by the series impedance Z_c of each array section which is assumed to be 2.0 Ω in Fig. 3-6.

3.2.3 Photon Noise in the Collected Output Power

Since the photon emissions in different array sections are negatively correlated, it is reasonable to expect that these negative correlations would decrease the photon noise when light from all the cascade sections is collected. As in the case of MCCLs, a scaling relation can be derived for the spectral density of the noise δP_{out}^T in the collected output power. Summing both sides of (3.20) over the superscript j, one obtains,

$$\begin{aligned} \delta P_{out}^T &= \sum_{j=1}^{N} \delta P_{out}^j(\omega) \\ &= \eta_o \frac{\hbar\Omega_o}{e} \frac{\mathbf{D}_{31}^{-1}(\omega)}{\tau_p} \left[\frac{N\,\delta V_{ext}(\omega) + \sum_{q=1}^{N} \delta V_c^q(\omega)}{Z(\omega) + Z_c(\omega) + N Z_{ext}(\omega)} \right] \end{aligned}$$

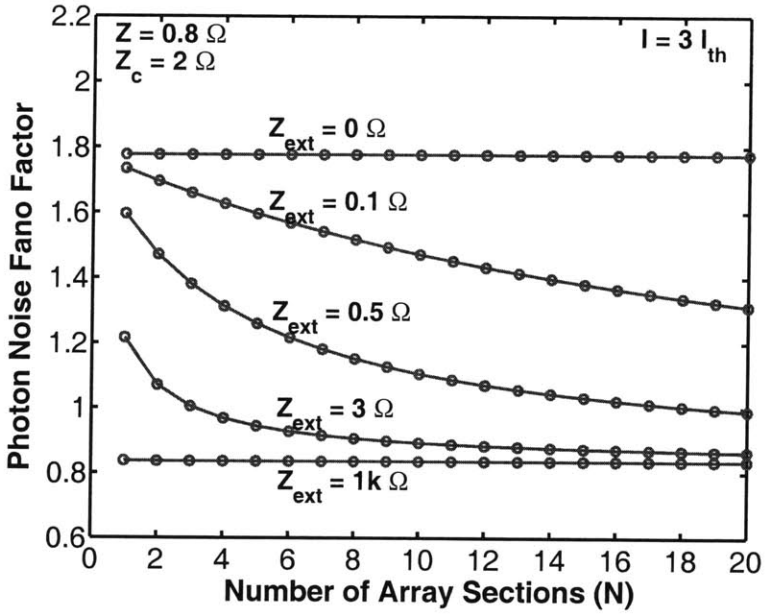

Figure 3-7: The Fano Factor of the noise in the collected output power of a parallel laser array is plotted as a function of the number of array sections for different values of the impedance $Z_{ext}(\omega)$. Each laser in the array is assumed to be a InGaAsP/InP diode laser operating at 1550 nm. The laser parameters are given in Table. 3.1. The bias current is assumed to be three times the threshold bias.

$$+\sum_{q=1}^{N}\left[\eta_o\,\frac{\hbar\Omega_o}{e}\,\frac{\mathbf{D}_{31}^{-1}(\omega)}{\tau_p}\left(\frac{Z(\omega)}{Z(\omega)+Z_c(\omega)+NZ_{ext}(\omega)}\right)\delta I^q(\omega)\right.$$
$$\left.+\,\eta_o\,\hbar\Omega_o\sum_{k=1}^{3}\frac{\mathbf{D}_{3k}^{-1}(\omega)}{\tau_p}\,F_k^q(\omega)+F_o^q\right] \tag{3.26}$$

It will be assumed that the noise sources $\delta V_{ext}(\omega)$ and $\delta V_c(\omega)$ represent the thermal noise associated with circuit impedances $Z_c(\omega)$ and $Z_{ext}(\omega)$, respectively. The spectral density $K_{PT}(\omega)$ of the noise in the collected output power depends on the average output power (or the ratio I_{bias}/I_{th} for each array section), the external circuit impedance $Z_{ext}(\omega)$, and the number N of array sections. $K_{PT}(\omega)$ follows from (3.26), and it can be written in a way that explicitly shows the scaling of the noise with the number of array sections,

$$K_{PT}(\omega, I_{bias}/I_{th}, Z_{ext}, N) = N\,K_{PT}(\omega, I_{bias}/I_{th}, NZ_{ext}, 1) \tag{3.27}$$

The negative correlations in the photon noise of different array sections decrease the noise in the collected output power, and this decrease in the noise, like in MCCLs, can be expressed

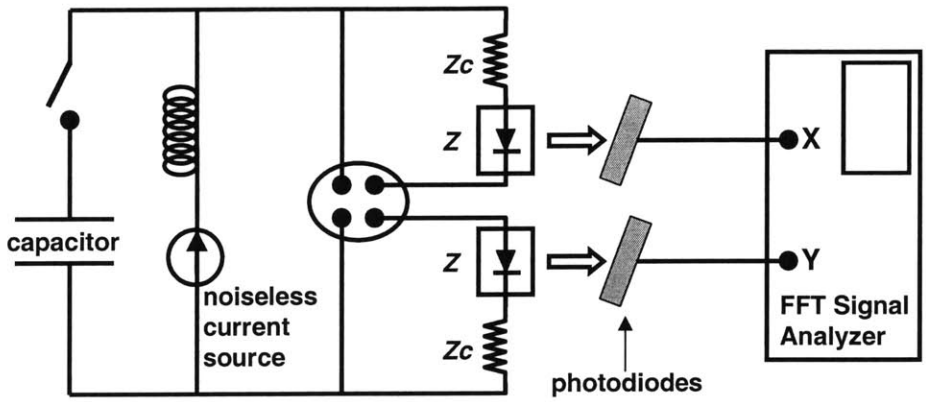

Figure 3-8: Experimental setup for measuring the photon noise correlations in diode lasers connected electrically in series or in parallel.

as a scaled external circuit impedance as shown in (3.27) above (recall from Chapter 2 that a laser biased with larger impedance has smaller noise in the output power). When $Z_{ext}(\omega)$ is very small, the current fluctuations generated by each array section do not couple into other array sections, and the photon noise in different array sections is uncorrelated. The spectral density of the noise in the collected output power is therefore N times the spectral density of the noise in a single section array. When $Z_{ext}(\omega)$ is very large, the spectral density of the noise in the collected output power is again N times the spectral density of the noise in a single section array. This is because the decrease in the photon noise Fano Factor due to the negative correlations in the photon noise in different array sections is exactly balanced by the increase in the photon noise due to the decrease in the impedance seen by each array section with the increase in the number of array sections. Fig.3-7 shows the Fano Factor of the noise in the collected output power of a PLA as a function of the number of array sections for different values of the impedance $Z_{ext}(\omega)$. Each section in the array is assumed to be a InGaAsP/InP laser operating at 1550 nm. The laser parameters are given in Table. 3.1.

Table 3.2: Device Parameters of GaAs/AlGaAs Fabry-Perot Lasers Used in Experiments.

Parameter	Value
Lasing wavelength λ	850 nm
Operating temperature	$\approx$ 300 K
Number of quantum wells	3
Quantum well thickness	$70\mathring{A}$
Cavity width	2.0 μm
Cavity length	400 μm
Facet reflectivities	0.85 and 0.10
Threshold current	15 mA
Slope efficiency	1.13 Watt/Amp

3.3 Photon Noise Correlations: Experiments

3.3.1 Experimental Setup

The theory for the noise in multiple cavity cascade lasers and parallel laser arrays presented in this Chapter predicts large positive (negative) correlations in the photon noise of lasers connected electrically in series (parallel). The experimental setup for measuring these noise correlations is shown in Fig.3-8 [56]. Two GaAs/AlGaAs Fabry-Perot lasers, part number SDL-5400-C (JDS Uniphase), operating at 850 nm were used in these experiments. The lasers were mounted such that they could be connected electrically in series or in parallel. The lasers were biased with a noiseless current source made using a lithium battery in series with a potentiometer and a large inductor. This high impedance source could be converted into a low impedance source by a large capacitor in the circuit, as shown in Fig. 3-8. At frequencies of interest, the capacitor acted like a short. The light from each laser was collected by a large area (1 cm^2) Silicon PIN photodiode, part number S3590-1 (Hamamatsu). The quantum efficiency of each photodiode was close to 80 percent (responsivity: 0.55 Amp/Watt). The photodiodes were slightly tilted with respect to the direction of incident light to avoid back reflections into the lasers. The bandwidth of the photodiode response was slightly larger than 1 MHz under a reverse bias of 40 V. The photodiode output signals were capacitively coupled into 50 Ω input channels of a dual-channel HP89410A FFT Signal Analyzer. The FFT Signal Analyzer had a measurement bandwidth of 10 MHz, and could compute the power spectral densities and the power cross-spectral density of the signals at its two input channels.

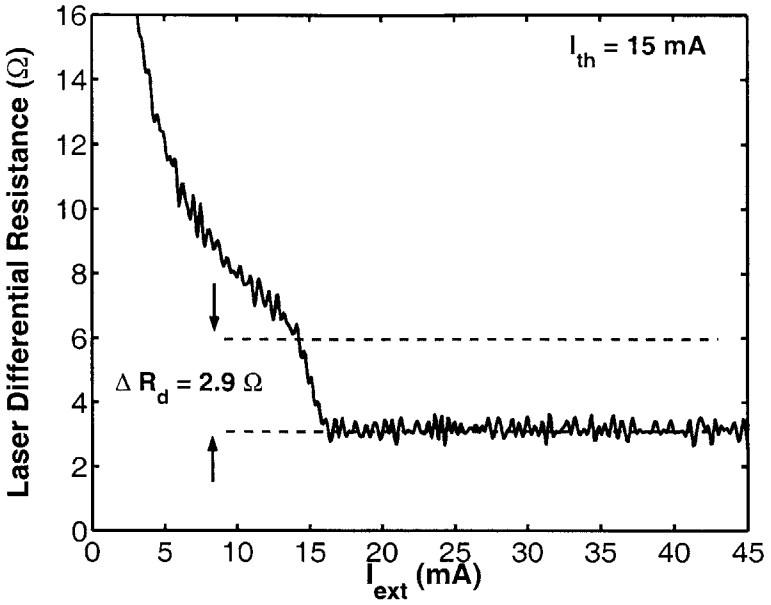

Figure 3-9: Laser differential resistance is plotted as a function of the bias current. The discontinuity in the differential resistance at threshold is 2.9 Ω.

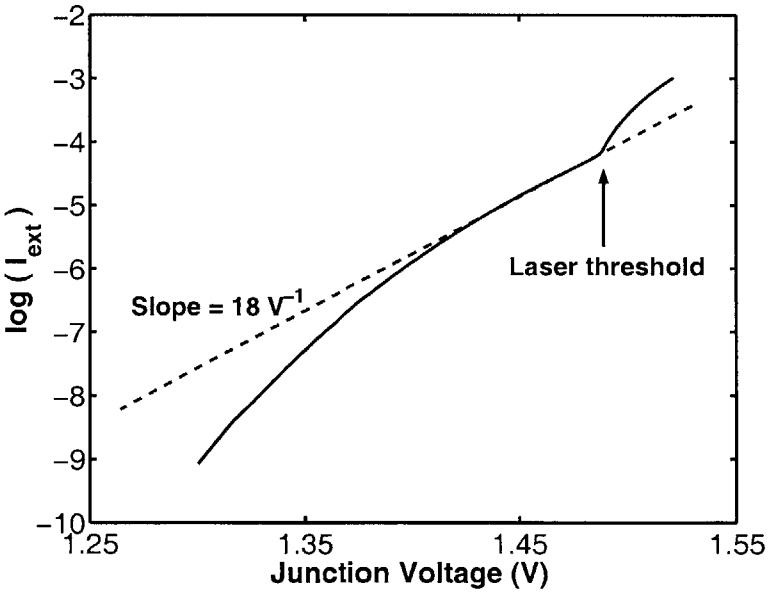

Figure 3-10: $\log(I_{ext})$ is plotted as a function of the junction voltage. The slope of the curve just before threshold is 18 V^{-1}.

Table 3.3: Values of Laser Parameters Extracted From Measurements.

Parameter	Value
External slope efficiency	1.13 Watt/Amp
η_o	0.814
η_i	0.957
Device series resistance $Z_c(\omega)$	2.3 Ω
Junction impedance $Z(\omega)$ below threshold	3.7 Ω
Junction impedance $Z(\omega)$ above threshold	0.8 Ω
τ_c	5 ps
τ_l	= 22.4 τ_c = 112 ps
τ_g	= 2.5 τ_c = 12.5 ps
τ_e	32 ps
η_e	0.972
θ'	5.44
θ	0.38
G	1.74

3.3.2 Extraction of the Laser Parameters

The lasers used in the experiments were first characterized using the methods described in Chapter 2 to extract the values of the parameters that were introduced in the theoretical model to describe the current noise and the photon noise in diode lasers. The differential slope efficiency of the lasers was measured to be approximately 1.13 Watt/Amp. The product $\eta_o \eta_i$ for the lasers was therefore 0.773. The approximate values of the laser parameters obtained from the vendor are listed in Table. 3.2. Assuming 5 cm^{-1} cavity internal loss, the value of η_o comes out to be 0.814, and η_i is therefore 0.957. The laser differential resistance is plotted in Fig. 3-9 which shows a discontinuity of 2.9 Ω in the differential resistance at threshold, and a total differential resistance (i.e. $Z + Z_c$) of 3.1 Ω above threshold. Fig. 3-10 shows $\log(I_{ext})$ plotted as a function of the junction voltage, and the slope of the curve just before threshold is approximately 18 $1/V$. From these measurements, the values of the parameters G, θ', θ, and τ_e, and the ratios τ_c/τ_g and τ_c/τ_l can be determined (see Chapter 2 for details). The values of the laser parameters determined through measurements are given in Table. 3.3. In obtaining the results in Table. 3.3, τ_c was assumed to be 5 ps, and the material gain was assumed to be related to the carrier density N_w in the quantum wells through the relation [1],

$$g = g_o \log\left(\frac{N_w + N_s}{N_{tr} + N_s}\right) \tag{3.28}$$

where $g_o = 3000\ \text{cm}^{-1}$, $N_{tr} = 1.8 \times 10^{18}\ \text{cm}^{-3}$, and $N_s = 1.2 \times 10^{18}\ \text{cm}^{-3}$. As explained in Chapter 2, the values of the laser parameters given in Table 3.3 are valid only near the laser threshold and are not expected to be valid much above threshold.

3.3.3 Results and Discussion

The FFT Signal Analyzer can measure the spectral densities $K_I^{jj}(\omega)$ and the cross-spectral density $K_I^{jq}(\omega)$ $(j \neq q)$ of the noise in the photodetector currents. The correlation $C_I^{12}(\omega)$ in the noise in the photodetector currents is given by a relation similar to (3.15),

$$C_I^{12}(\omega) = \frac{K_I^{12}(\omega)}{\sqrt{K_I^{11}(\omega)\, K_I^{22}(\omega)}} \tag{3.29}$$

The spectral densities $K_I^{jj}(\omega)$ and $K_I^{jq}(\omega)$ $(j \neq q)$ are related to the spectral densities $K_P^{jj}(\omega)$ and $K_P^{jq}(\omega)$ of the laser intensity noise as follows [1],

$$K_I^{jj}(\omega) = \left(\frac{e}{\hbar\Omega_o}\right)^2 \left[\eta^2 K_P^{jj}(\omega) + \eta\,(1-\eta)\,\hbar\Omega_o P_{out}\right] \tag{3.30}$$

$$K_I^{jq}(\omega) = \left(\frac{e}{\hbar\Omega_o}\right)^2 \left[\eta^2 K_P^{jq}(\omega)\right] \tag{3.31}$$

Here, P_{out} is the average laser output power and $\eta = \eta_d \eta_c$, where η_d is the photodetector quantum efficiency and η_c is the light collection efficiency. Since $\eta < 1$, the correlation $C_P^{12}(\omega)$ in the laser intensity noise is not equal to $C_I^{12}(\omega)$. For the lasers used in the experiments, the noise in the output power was much larger than the shot noise value. The measured photon noise Fano Factors for each laser were larger than 100 for most values of the bias current and larger than 10 for all values of the bias current [56]. Since $K_P^{jj}(\omega) \gg \hbar\Omega_o P_{out}$, and η is estimated to be at least 0.75, $C_P^{12}(\omega)$ can be safely approximated by $C_I^{12}(\omega)$. The measured value of $C_P^{12}(\omega)$ is not sensitive to the post-detection signal gains in the two channels of the FFT Spectrum Analyzer since multiplicative gain factors cancel out when $C_P^{12}(\omega)$ is computed using (3.29).

Fig. 3-11 and Fig. 3-12 show the low frequency value of $C_P^{12}(\omega)$ when the lasers are connected electrically in series and parallel, respectively, as a function of the bias current for two different values of the circuit impedance $Z_{ext}(\omega)$; 0Ω and $\infty\Omega$. The noise correlation data shown in Fig. 3-11 and Fig. 3-12 was obtained by averaging the measured value of

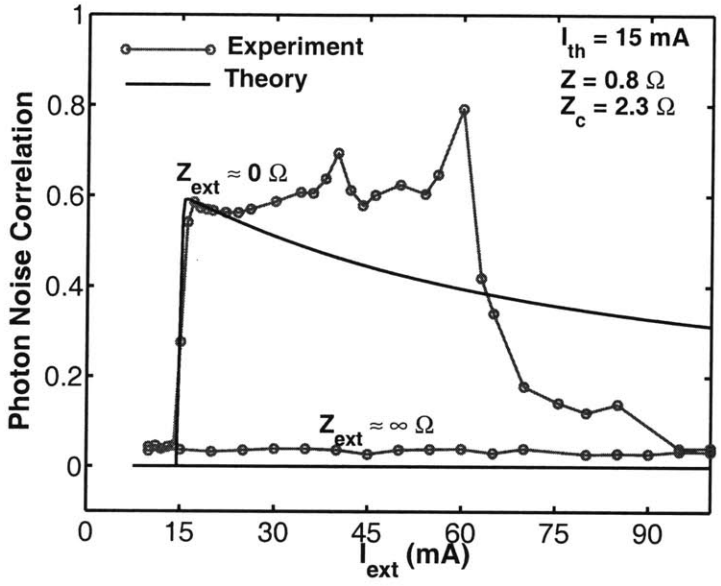

Figure 3-11: The low frequency correlation in the noise in the output powers of two lasers connected electrically in series is plotted as a function of the bias current for two different values of the circuit impedance $Z_{ext}(\omega)$. The solid lines with circles are the experimental data. The solid lines without circles are the predictions of the theoretical model using the laser parameter values given in Table. 3.3.

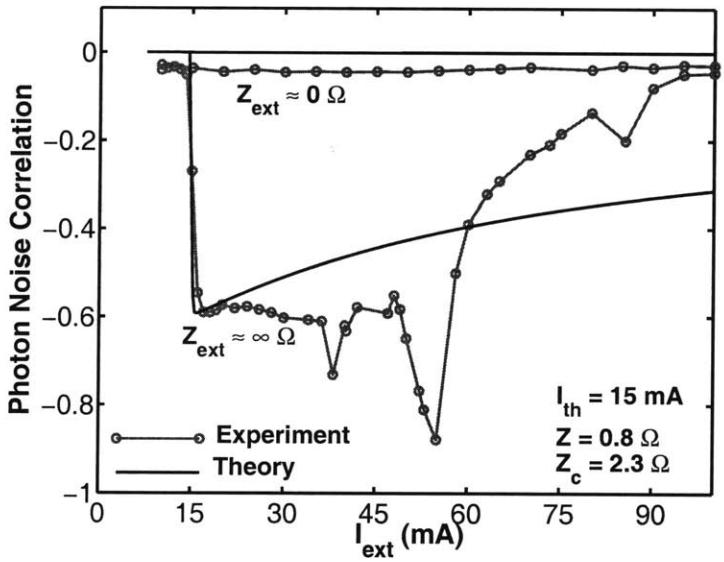

Figure 3-12: The low frequency correlation in the noise in the output powers of two lasers connected electrically in parallel is plotted as a function of the bias current for two different values of the circuit impedance $Z_{ext}(\omega)$. The solid lines with circles are the experimental data. The solid lines without circles are the predictions of the theoretical model using the laser parameter values given in Table. 3.3.

$C_P^{12}(\omega)$ over a 400 KHz wide frequency window centered at 500 KHz. $C_P^{12}(\omega)$ was found to be flat between 200 KHz and 800 KHz, and changing the center frequency of the averaging window did not affect the final results. Fig. 3-11 and Fig. 3-12 show that when the lasers are connected in series the noise in the output powers is positively correlated, and when the lasers are connected in parallel the noise is negatively correlated. The experimental results also exhibit the expected dependence of the noise correlations on the impedance $Z_{ext}(\omega)$ in both the series and the parallel configurations. The results obtained from the theoretical models using the parameter values given in Table. 3.3 are also shown in Fig. 3-11 and Fig. 3-12. The theoretical results are in good agreement with the experimental data near the laser threshold.

The laser spectrum showed multiple longitudinal modes lasing at the same time. The theoretical models for the noise correlations presented in this Chapter are based on the assumption of a single lasing mode. The photon noise in different lasing modes of a laser is negatively correlated as a result of gain competition, but, as shown in Ref. [68], the combined noise of all the lasing modes is adequately described by a single mode model. Since the noise in different lasing modes is negatively correlated, equal number of photons must be collected from all the lasing modes when making noise measurements otherwise noise in addition to that predicted by the single mode model can be introduced. Mode selective loss inside and/or outside the laser cavity can make this difficult in practice. The agreement between theoretical results and experimental data in Fig. 3-11 and Fig. 3-12 becomes poor much above threshold. This is not surprising since, as described earlier, the parameter values used in the calculations are valid only near threshold. Mode switching and mode hopping in multimode lasers can also introduce noise which may not be describable by linearized noise models such as the ones presented in this Chapter. In the lasers used in the experiments, excessive mode hopping was observed when the bias current had values between 30 mA and 60 mA.

3.4 Split Waveguide Cascade Lasers

3.4.1 Theoretical Model

A split waveguide cascade laser (SWCL) is shown in Fig. 3-13. In a SWCL, a single optical waveguide is split into sections that are connected electrically in series [5, 6]. The Langevin

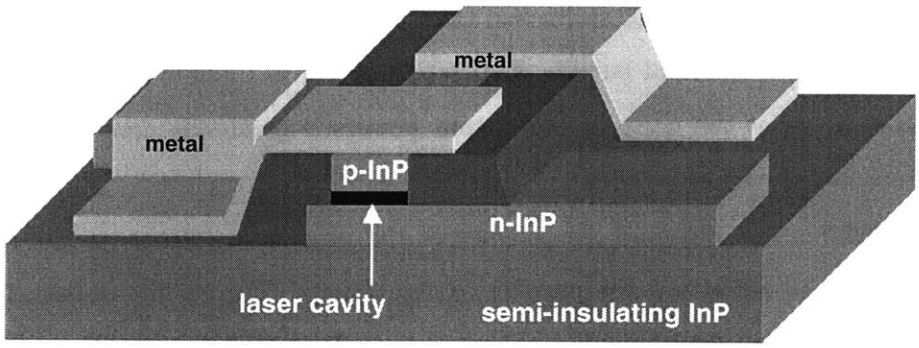

Figure 3-13: A two section split waveguide cascade laser (SWCL).

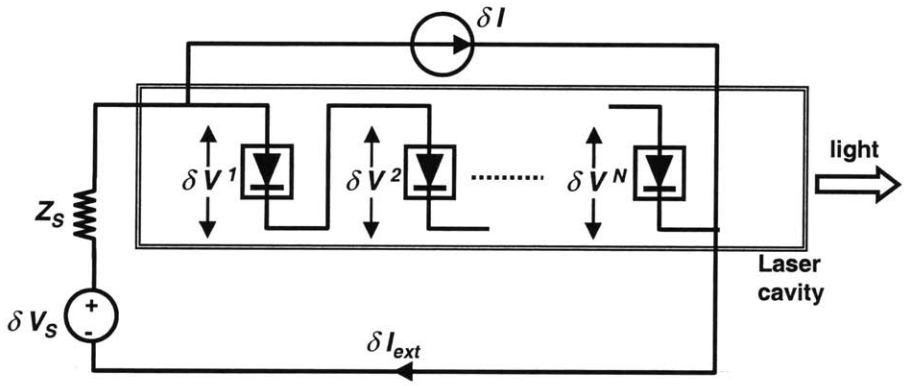

Figure 3-14: A circuit model for the noise in a split waveguide cascade laser.

rate equations for the carrier densities in the j-th section and the photon density in the optical cavity for an N section SWCL are as follows,

$$\frac{d\,\delta N_c^j V_c}{d\,t} = \frac{\delta I_{ext}}{e} - \delta N_c^j V_c \left(\frac{1}{\tau_c} + \frac{1}{\tau_l}\right) + \frac{\delta N_w^j V_w}{\tau_e} - F_c^j - F_l^j + F_e^j \tag{3.32}$$

$$\frac{d\,\delta N_w^j V_w}{d\,t} = \frac{\delta N_c^j V_c}{\tau_c} - \delta N_w^j V_w \left(\frac{1}{\tau_e} + \frac{1}{\tau_w} + \frac{1}{\tau_{st}}\right) - \frac{V_w}{V_p} v_g\, g\, \delta S_p V_p + F_c^j - F_e^j - F_{nr}^j - F_R^j \tag{3.33}$$

$$\frac{d\,\delta S_p V_p}{d\,t} = \sum_{j=1}^{N} \frac{\delta N_w^j V_w}{\tau_{st}} + \left(N \frac{V_w}{V_p} v_g\, g - \frac{1}{\tau_p}\right) \delta S_p V_p + \sum_{j=1}^{N} F_R^j - F_L \tag{3.34}$$

The Equations above are almost the same as those used for multiple cavity cascade lasers. The difference is that in SWCLs the carrier densities in all the cascade sections interact

with the same optical field. The active region volumes V_w and V_c of each cascade section are N times smaller than the active region volumes in a conventional unsplit laser. The current noise δI_{ext} in the external circuit is related to the carrier density fluctuations in the j-th section by the expression,

$$\frac{\delta I_{ext}}{e} = \frac{G\,\delta V^j}{e} - \frac{\delta N_c^j V_c}{\tau_G} + F_{in}^j \tag{3.35}$$

Since G scales with the area, G becomes N times smaller when a waveguide is split into N cascade sections. The noise in the output power is given by an expression similar to (2.19) for conventional lasers,

$$\delta P_{out} = \eta_o \hbar \Omega_o \frac{\delta S_p\, V_p}{\tau_p} + F_o \tag{3.36}$$

A circuit model for the current noise in a SWCL is shown in Fig. 3-14. The condition imposed by the external circuit is,

$$\delta I_{ext}(\omega) = \frac{\delta V_s(\omega) - \sum_{j=1}^{N} \delta V^j(\omega)}{Z_s(\omega)} \tag{3.37}$$

The condition for lasing is,

$$N \frac{V_w}{V_p} v_g\, g = \frac{1}{\tau_p} \tag{3.38}$$

The Equation above implies that the threshold carrier density in each cascade section does not scale with the number N of sections. The threshold current scales as $1/N$. The average output power P_{out} can be written as,

$$P_{out} = \eta_o \eta_i \frac{\hbar \Omega_o}{e} N\ (I_{ext} - I_{th}) \tag{3.39}$$

For the same output power, a SWCL requires N times less bias current compared to a conventional laser.

Equations (3.32)-(3.34) can be solved by summing both sides of (3.32) and (3.33) with respect to the superscript j, and after Fourier transforming one obtains the following matrix

equation,

$$\begin{bmatrix} \mathbf{D}_{11}(\omega) & \mathbf{D}_{12}(\omega) & 0 \\ \mathbf{D}_{21}(\omega) & \mathbf{D}_{22}(\omega) & \mathbf{D}_{23}(\omega) \\ 0 & \mathbf{D}_{32}(\omega) & \mathbf{D}_{33}(\omega) \end{bmatrix} \begin{bmatrix} \sum_{j=1}^{N} \delta N_c^j(\omega) V_c \\ \sum_{j=1}^{N} \delta N_w^j(\omega) V_w \\ \delta S_p(\omega) V_p \end{bmatrix} = \frac{N \delta I_{ext}(\omega)}{e} \begin{bmatrix} 1 \\ 0 \\ 0 \end{bmatrix} + \begin{bmatrix} F_1(\omega) \\ F_2(\omega) \\ F_3(\omega) \end{bmatrix} \tag{3.40}$$

For the same output power, the elements of the matrix $\mathbf{D}$ are exactly the same as the elements of the matrix $\mathbf{D}$ for a conventional laser (see Equation (2.26)). The noise sources $F_1(\omega)$, $F_2(\omega)$, and $F_3(\omega)$ are as follows,

$$F_1(\omega) = -\sum_{j=1}^{N} F_c^j(\omega) - \sum_{j=1}^{N} F_l^j(\omega) + \sum_{j=1}^{N} F_e^j(\omega) \tag{3.41}$$

$$F_2(\omega) = \sum_{j=1}^{N} F_c^j(\omega) - \sum_{j=1}^{N} F_e^j(\omega) - \sum_{j=1}^{N} F_{nr}^j(\omega) - \sum_{j=1}^{N} F_R^j(\omega) \tag{3.42}$$

$$F_3(\omega) = \sum_{j=1}^{N} F_R^j(\omega) - F_L(\omega) \tag{3.43}$$

For the same output power, the correlations of the noise sources $F_1(\omega)$, $F_2(\omega)$, and $F_3(\omega)$ are also the same as the correlations of the corresponding noise sources in a conventional laser. The total impedance $Z(\omega)$ of the active regions of all the cascade sections can be found by summing (3.35) with respect to the superscript j, and using (3.40),

$$Z(\omega) = \frac{\delta \sum_{j=1}^{N} V^j(\omega)}{\delta I_{ext}(\omega)} = \frac{N}{G} \left[1 + \frac{\mathbf{D}_{11}^{-1}(\omega)}{\tau_G} \right] \tag{3.44}$$

As described earlier, G scales as $1/N$ with the number N of cascade sections. $Z(\omega)$ therefore increases as N^2 with the number of cascade sections.

3.4.2 Current Noise

A circuit model for the current noise in SWCLs in which current noise sources are attached in parallel with each cascade section is not particularly useful since the carrier density in each cascade section interacts with the same optical field and the current noise sources of different sections become highly correlated. Current noise in a SWCL can be modeled by attaching a single current noise source $\delta I(\omega)$ in parallel with all the cascade sections, as

shown in Fig. 3-14. Defining $F_{in}(\omega)$ as $\sum_{j=1}^{N} F_{in}^{j}(\omega)$, the current noise $\delta I(\omega)$ comes out to be,

$$\delta I(\omega) = \frac{e}{Z(\omega)} \frac{1}{G} \left[F_{in}(\omega) - \sum_{k=1}^{3} \frac{\mathbf{D}_{1k}^{-1}(\omega)}{\tau_G} F_k(\omega) \right] \tag{3.45}$$

The expression in (3.45) is almost identical to the expression for the current noise in a conventional laser given in (2.51). The correlations of the noise sources $F_{in}(\omega)$, $F_1(\omega)$, $F_2(\omega)$, and $F_3(\omega)$ in (3.45) do not scale with the number N of cascade sections. The factor $Z(\omega)G$ in the denominator in (3.45) scales linearly with N. Consequently, for a fixed output power the spectral density of the current noise in a SWCL scales as $1/N^2$ with the number of cascade sections, i.e.,

$$K_I(\omega, I_{ext}/I_{th}, N) = \frac{1}{N^2} K_I(\omega, I_{ext}/I_{th}, 1) \tag{3.46}$$

This scaling of the current noise can be understood if one realizes that the current noise in the external circuit is equal to $\delta I(\omega)$ when the impedance $Z_s(\omega)$ and the voltage noise source $\delta V_s(\omega)$ are both zero. When $Zs(\omega)$ is zero, only a fraction $1/N$ of the current noise of each cascade section is able to couple into the circuit since the impedance of a single cascade section is N times smaller than the combined impedance of all the cascade sections.

3.4.3 Photon Noise

The noise in the output power can be determined by using the solution of (3.40) in (3.36),

$$\delta P_{out}(\omega) = \eta_o \frac{\hbar\Omega_o}{e} N \frac{\mathbf{D}_{31}^{-1}(\omega)}{\tau_p} \delta I_{ext}(\omega) + \eta_o \hbar\Omega_o \sum_{k=1}^{3} \frac{\mathbf{D}_{3k}^{-1}(\omega)}{\tau_p} F_k(\omega) + F_o(\omega) \tag{3.47}$$

where $\delta I_{ext}(\omega)$ is,

$$\delta I_{ext}(\omega) = \frac{\delta V_s(\omega)}{Z(\omega) + Z_s(\omega)} + \frac{Z(\omega)}{Z(\omega) + Z_s(\omega)} \delta I(\omega) \tag{3.48}$$

The impedance $Z_s(\omega)$ is assumed to consist of an external circuit impedance $Z_{ext}(\omega)$ and also a parasitic impedance $Z_c(\omega)$. Both $Z(\omega)$ and $Z_c(\omega)$ scale as N^2 with the number N of cascade sections. The spectral density of the noise in the output power can be obtained from (3.47). Assuming that the voltage noise source $\delta V_s(\omega)$ represents the thermal noise associated with the impedance $Z_s(\omega)$, the spectral density of the noise in the output power

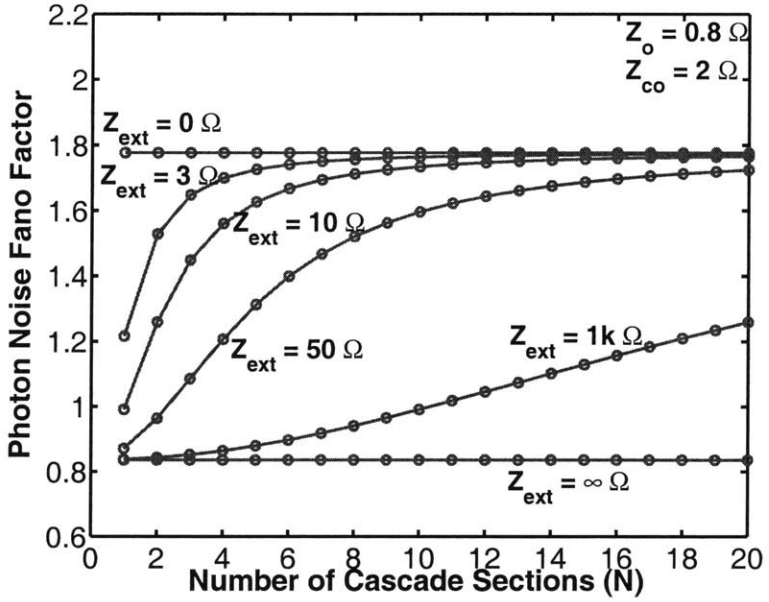

Figure 3-15: The Fano Factor of the noise in the output power in a SWCL is plotted as a function of the number N of cascade sections for different values of the impedance $Z_{ext}(\omega)$. The output power is kept fixed when N is varied by reducing the bias current. The laser parameters are given in Table. 3.1.

can be expressed as follows,

$$K_P(\omega, I_{ext}/I_{th}, Z_{ext}, N) = K_P(\omega, I_{ext}/I_{th}, Z_{ext}/N^2, 1) \tag{3.49}$$

The above Equation shows that for the same output power the spectral density of the photon noise in a N-section SWCL with an external circuit impedance $Z_{ext}(\omega)$ is equal to that in a conventional laser in which the external circuit impedance is $Z_{ext}(\omega)/N^2$. Thus, as in MCCLs, the increase in the photon noise in SWCLs due to the positive correlations in photon emissions in different cascade sections can be expressed in terms of a scaled external circuit impedance. Fig.3-15 shows the Fano Factor of the noise in the output power as a function of the number of cascade sections in a InGaAsP/InP SWCL for different values of the impedance $Z_{ext}(\omega)$. Since the threshold current in a SWCL scales as $1/N$ with the number of cascade sections, the bias currents in Fig.3-15 are also scaled to keep the output power fixed for all values of N. The laser parameters are given in Table. 3.1.

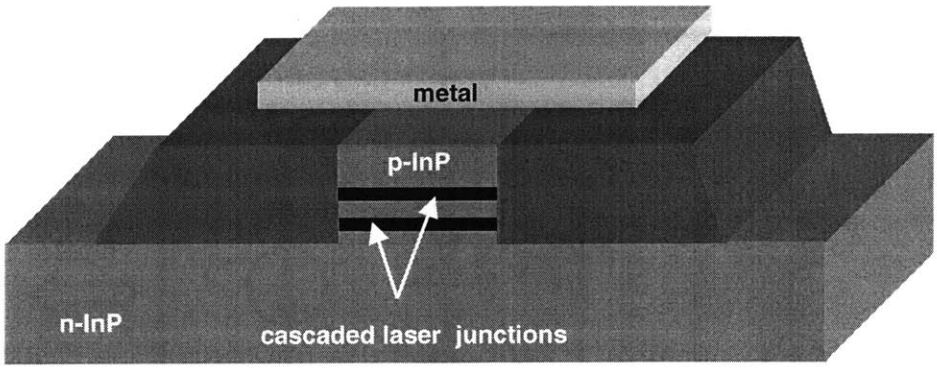

Figure 3-16: A two section bipolar cascade laser (BCL).

3.5 Bipolar Cascade Lasers

3.5.1 Theoretical Model

A bipolar cascade laser (BCL) is shown in Fig. 3-16. In BCLs, multiple gain sections are connected electrically in series within a single optical cavity by reverse biased tunnel junctions [8, 9, 10, 11]. In a BCL the mode volume V_p is assumed to scale linearly with the number of cascade sections N. The Langevin rate equations for the carrier and photon densities for a BCL have exactly the same form as Equations (3.32)-(3.34) presented in the previous section for SWCLs. The only difference is that the mode volume V_p, instead of the active region volumes V_w and V_c, scales with the number of cascade sections. The equations for the circuit current noise and the noise in the output power for BCLs are also identical to Equations (3.35) and (3.36) for SWCLs. The condition for lasing is,

$$N \frac{V_w}{V_p} v_g \, g = \frac{1}{\tau_p} \tag{3.50}$$

The threshold carrier density in each cascade section in BCLs does not scale with the number of sections. The threshold current also does not scale with the number of sections. The average output power P_{out} is given by the expression,

$$P_{out} = \eta_o \eta_i \frac{\hbar \Omega_o}{e} N \, (I_{ext} - I_{th}) \tag{3.51}$$

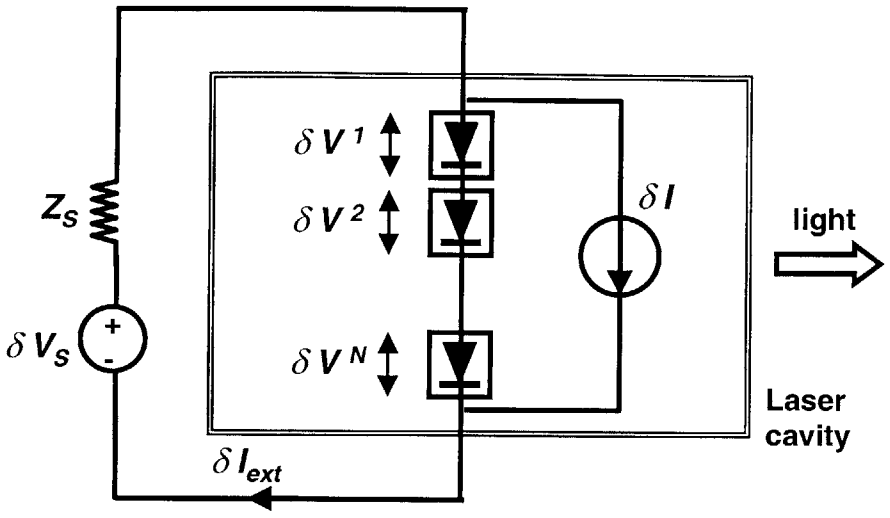

Figure 3-17: A circuit model for the noise in a bipolar cascade laser.

For a fixed bias current, the output power in BCLs scales linearly with the number N of cascade sections. Since the mode volume also increases linearly with N, the photon density in the cavity does not scale with N.

The total impedance $Z(\omega)$ of the active regions in all the cascade sections in a BCL is given by an expression identical to (3.44) for SWCLs,

$$Z(\omega) = \frac{\delta \sum_{j=1}^{N} V^j(\omega)}{\delta I_{ext}(\omega)} = \frac{N}{G}\left[1 + \frac{\mathbf{D}_{11}^{-1}(\omega)}{\tau_G}\right] \tag{3.52}$$

Since the device area does not scale with N in BCLs, G does not scale with N, and $Z(\omega)$ scales linearly with N.

3.5.2 Current Noise

Current noise in a BCL can be modeled by attaching a single current noise source $\delta I(\omega)$ in parallel with all the cascade sections, as shown in Fig. 3-17. The current noise $\delta I(\omega)$ is given by an expression identical to (3.45) for SWCLs,

$$\delta I(\omega) = \frac{e}{Z(\omega)}\frac{1}{G}\left[F_{in}(\omega) - \sum_{k=1}^{3}\frac{\mathbf{D}_{1k}^{-1}(\omega)}{\tau_G}F_k(\omega)\right] \tag{3.53}$$

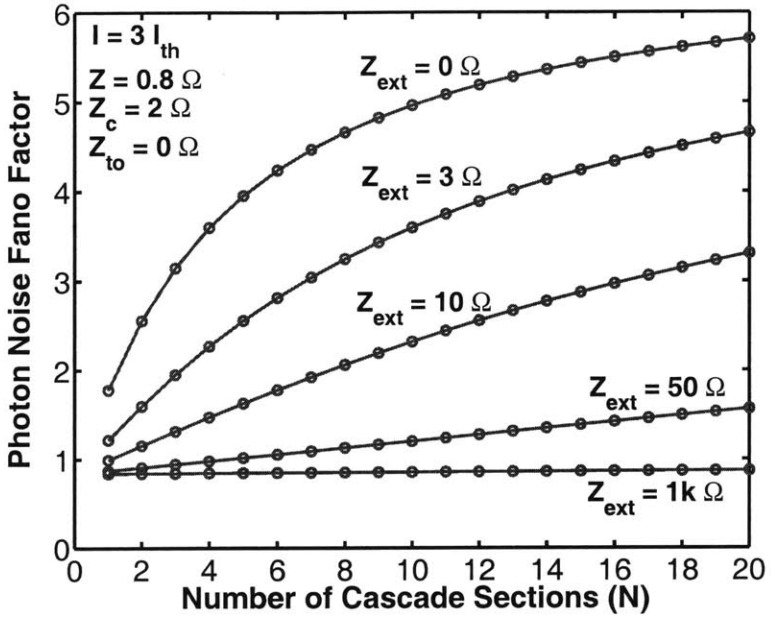

Figure 3-18: The Fano Factor of the noise in the output power in a InGaAsP/InP BCL is plotted as a function of the number N of cascade sections for different values of the impedance $Z_{ext}(\omega)$ keeping the bias current fixed. The laser parameters are given in Table. 3.1. The reverse biased tunnel junctions are assumed to have zero impedance.

The correlations of the noise sources $F_{in}(\omega)$, $F_1(\omega)$, $F_2(\omega)$, and $F_3(\omega)$ in (3.45) scale linearly with N for a fixed bias current. The factor $Z(\omega)G$ in the denominator in (3.53) also scales linearly with N. Consequently, for a fixed bias current the spectral density of the current noise scales as $1/N$, i.e.,

$$K_I(\omega, I_{ext}/I_{th}, N) = \frac{1}{N} K_I(\omega, I_{ext}/I_{th}, 1) \tag{3.54}$$

3.5.3 Photon Noise

The noise $\delta P_{out}(\omega)$ in the output power in a BCL is also given by an expression similar to (3.47) for a SWCL,

$$\delta P_{out}(\omega) = \eta_o \frac{\hbar\Omega_o}{e} N \frac{\mathbf{D}_{31}^{-1}(\omega)}{\tau_p} \delta I_{ext}(\omega) + \eta_o \hbar\Omega_o \sum_{k=1}^{3} \frac{\mathbf{D}_{3k}^{-1}(\omega)}{\tau_p} F_k(\omega) + F_o(\omega) \tag{3.55}$$

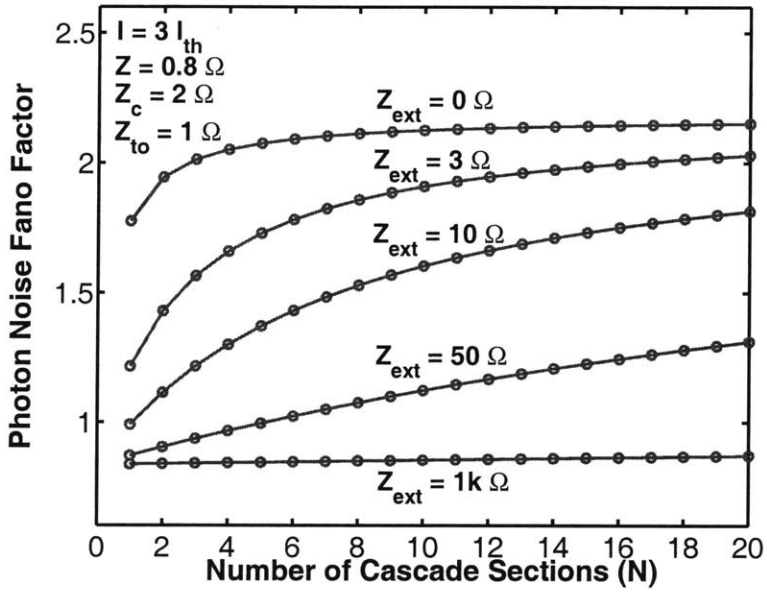

Figure 3-19: The Fano Factor of the noise in the output power in a InGaAsP/InP BCL is plotted as a function of the number N of cascade sections for different values of the impedance $Z_{ext}(\omega)$ keeping the bias current fixed. The combined impedance of the reversed biased tunnel junctions is assumed to be $(N-1)Z_{to}(\omega)$, where $Z_{to}(\omega)$ is assumed to be 1 Ω.

where $\delta I_{ext}(\omega)$ is,

$$\delta I_{ext}(\omega) = \frac{\delta V_s(\omega)}{Z(\omega) + Z_s(\omega)} + \frac{Z(\omega)}{Z(\omega) + Z_s(\omega)} \delta I(\omega) \tag{3.56}$$

The impedance $Z_s(\omega)$ consists of an external circuit impedance $Z_{ext}(\omega)$, the combined impedance $Z_t(\omega)$ of all the reverse biased tunnel junctions, and a parasitic impedance $Z_c(\omega)$. The impedance $Z_c(\omega)$, which is expected to be dominated by the resistance of the ohmic contacts, is independent of the number of cascade sections. The impedance $Z_t(\omega)$ scales linearly with the number of cascade sections, and it is convenient to write $Z_t(\omega)$ as $(N-1)Z_{to}(\omega)$, where $Z_{to}(\omega)$ is the impedance of a single reverse biased tunnel junction. The combined impedance of the active regions can also be written as $NZ_o(\omega)$, where $Z_o(\omega)$ is the impedance of the active region of a single section. The voltage noise source $\delta V_s(\omega)$ represents the thermal noise in the circuit impedances $Z_{ext}(\omega)$ and $Z_c(\omega)$. The reversed biased tunnel junctions are assumed to produce no noise. With these definitions and assumptions, the

spectral density of the noise in the output power can be written as,

$$\begin{aligned} K_P(\omega, I_{ext}/I_{th}, Z_c, Z_{ext}, N) &= N\, K_P(\omega, I_{ext}/I_{th}, Z_c/N, Z_{ext}/N + Z_{to}(N-1)/N, 1) \\ &\quad - \left| \eta_o \frac{\hbar\Omega_o}{e} N \frac{\mathbf{D}_{31}^{-1}(\omega)}{\tau_p} \right|^2 \\ &\quad \times \frac{2K_B T\, \mathrm{Re}\{Z_{to}(\omega)(N-1)\}}{|Z_o(\omega)N + Z_c(\omega) + Z_{to}(\omega)(N-1) + Z_{ext}(\omega)|^2} \end{aligned} \tag{3.57}$$

Since the reversed biased tunnel junctions are assumed to not produce thermal noise, the second term on the right hand side accounts for this by subtracting out the thermal noise contribution from the tunnel junctions which is contained in the first term. If the tunnel junctions produce thermal noise, or if $Z_{to}(\omega) = 0$, then the second term on the right hand side is not needed. The above Equation shows that for the same bias current the spectral density of the photon noise in a N-section BCL, with an external circuit impedance $Z_{ext}(\omega)$, a parasitic impedance $Z_c(\omega)$, and tunnel junction impedance $Z_{to}(\omega)$ equal to zero, is N times that in a single section laser in which the external circuit impedance is $Z_{ext}(\omega)/N$ and the parasitic impedance is $Z_c(\omega)/N$.

Fig.3-18 shows the Fano Factor of the noise in the output power as a function of the number of cascade sections in a InGaAsP/InP BCL for different values of the impedance $Z_{ext}(\omega)$ when $Z_{to}(\omega) = 0$. Fig.3-19 shows the photon noise Fano Factor when $Z_{to}(\omega) = 1$ Ω. The laser parameters are given in Table. 3.1. Since the parasitic impedance $Z_c(\omega)$ in BCLs does not scale with N, the Fano Factor of the photon noise increases with N by large amounts for small values of $Z_{ext}(\omega)$ when $Z_{to}(\omega)$ is zero. Noise in electron transport through the reversed biased tunnel junctions may also contribute to the circuit current noise and to the photon noise, and this noise has not been taken into account in the analysis presented here.

3.6 Conclusion

In this Chapter, models for the current noise and photon noise in semiconductor cascade lasers and parallel laser arrays were presented. It was shown that the photon emissions in different sections are positively correlated in cascade lasers and negatively correlated in parallel laser arrays. The correlations in the noise in the output power were measured experimentally in lasers connected electrically in series and in parallel and the results were

found to agree well with the theory. The scaling of the current and photon noise with the number of sections in cascade lasers and in parallel laser arrays were also described. The positive correlation in photon emission in different cascade sections results in an increase in the noise in the output power. It was shown that this increase in the noise in the output power could be expressed in terms of a scaled external circuit impedance.

Chapter 4

Dynamics and Noise in Semiconductor Intersubband Quantum Cascade Lasers

4.1 Introduction

In this Chapter, a comprehensive model for the dynamics and noise in QCLs is presented. QCLs are different from interband semiconductor diode lasers in three important ways which can have a significant impact on their noise properties:

1. Electron transport in QCLs takes place by tunneling between states in adjacent quantum wells. It is well known that electronic correlations in resonant tunneling in quantum well structures can suppress (or enhance) current noise by providing a negative (or positive) feedback [26, 27, 28]. High impedance suppression of the current noise in semiconductor diode lasers results in light output with squeezed photon number fluctuations [29]. It is therefore intriguing whether suppression of the current noise can also lead to squeezing in QCLs. Any model for the photon noise in QCLs must take into account these electronic correlations self-consistently.

2. In diode lasers the carrier density in the energy level involved in the lasing action does not increase beyond its threshold value and, therefore, the noise contributed by the non-radiative recombination and generation processes also remains unchanged beyond threshold. In QCLs the electron densities in the upper and lower lasing states do not

clamp at threshold, and keep increasing when the bias current is increased beyond threshold. As a result, non-radiative processes contribute significantly to photon noise even at high bias currents.

3. Since all the gain sections in a QCL are connected electrically and optically, electron density fluctuations and photon emission events in different gain sections become correlated. The effect of these correlations on the photon noise in interband cascade lasers has already been discussed in detail in Chapter 2, and the aim of this Chapter is to investigate the role of these correlations in QCLs.

Conventionally, the noise in lasers has been studied using either Langevin rate equations or Fokker-Plank equations [64]. On the other hand, the noise in electron transport in mesoscopic devices is handled using quantum mechanical scattering approaches pioneered by R. Landauer and M. Buttiker [58, 59]. Since the photon noise depends on the current noise, a technique needs to be developed for QCLs that can be used to model the photon noise as well as the noise in electron transport. In Appendix C.1. it is shown that Langevin equations can also be used to model the noise in electron transport in multiple quantum well structures. Therefore, Langevin rate equations are used to model the photon noise and the current noise in QCLs.

4.2 Outline

In section 4.4 the non-linear rate equations for the electron and photon densities in QCLs are presented. The steady state solution of these rate equations below and above threshold are described. In section 4.5 the non-linear rate equations are linearized to obtain Langevin rate equations for the fluctuations in the electron and photon densities. Electron transport in the multiple quantum well structure of QCLs is discussed in detail, and a self-consistent model for the fluctuations in the electron charge densities and the electron current density is presented. It is shown that a self-consistent description of the fluctuations in the charge and current densities can be carried out in terms of a few device parameters. Langevin noise sources are also used to model the noise associated with electron transport by tunneling. Section 4.5 is the main part of this Chapter. In section 4.6 the set of coupled linearized Langevin rate equations for the fluctuations in the electron densities in different levels of all the cascaded gain stages and the fluctuations in the photon density are solved under

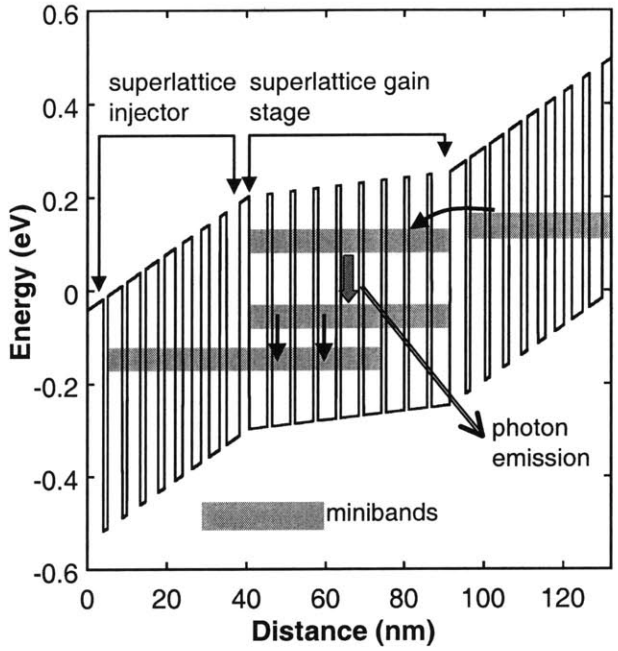

Figure 4-1: Superlattice quantum cascade laser.

the constraints imposed by the biasing electrical circuit. In addition, the direct current modulation response of QCLs is also evaluated and the maximum possible modulation bandwidth is discussed. The analytical and numerical results on the current noise and the photon noise in QCLs are presented and discussed in section 4.7 and section 4.8, respectively. In these sections the results obtained are compared with the current and photon noise in interband semiconductor diode lasers. Readers not familiar with the results on the current and photon noise in diode lasers are encouraged to read Chapter 2 before proceeding.

4.3 Types of Quantum Cascade Lasers

Many different types of QCL structures have been reported in the literature [12, 13, 14, 15, 16, 17, 18, 19, 20, 21, 22, 23, 24]. Almost all of these QCL structures can be classified into two categories:

1. *Superlattice QCLs* in which the gain stage consists of a superlattice structure and the photons are emitted when the electrons make transitions between two minibands of this superlattice. These minibands are actually clusters of closely spaced energy levels

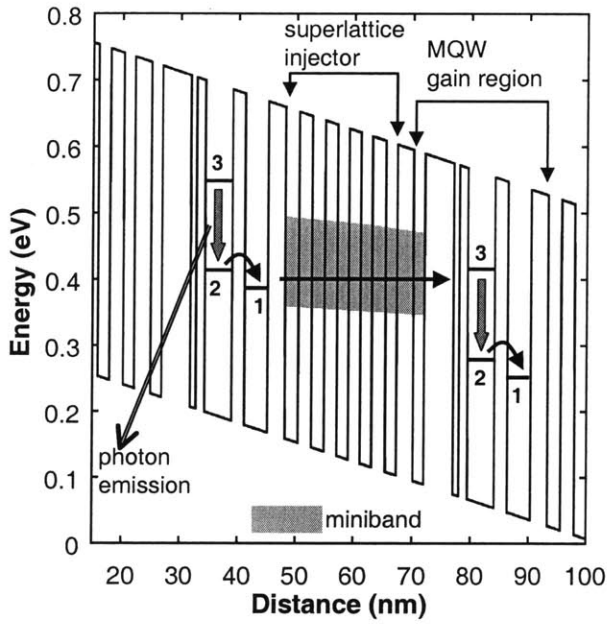

Figure 4-2: Multiple quantum well quantum cascade laser.

(Fig. 4-1) [21, 22, 23, 24].

2. *Multiple quantum well QCLs* in which the gain stage consists of multiple quantum wells (typically two or three) and the radiative electronic transitions occur between two discrete energy levels (Fig. 4-2) [12, 13, 14, 15, 16, 17].

In both types of QCLs, two successive gain stages are separated usually by a superlattice structure known as the *injector*. The superlattice injector has a mini-gap which prevents the electrons from tunneling out into the injector from the upper energy level(s) of the previous gain stage and, therefore, increases the radiative efficiency. Electrons from the lower energy level(s) of a gain stage can tunnel into the injector, and the injector injects these electrons into the upper energy level(s) of the next gain stage.

In this Chapter, photon noise and current noise in only multiple quantum well QCLs is discussed. The methods presented in this Chapter are fairly general and can be used to analyze noise and dynamics in a wide variety of QCLs including those with superlattice gain stages. The focus in this Chapter will be on the QCL structure shown in Fig. 4-2. The operation of this QCL is as follows. Electrons tunnel from the energy states in the superlattice injector into level 3 of the gain stage. Photons are emitted when electrons

make radiative transitions from level 3 to level 2. Transitions from level 2 to level 1 occur primarily by emission of optical phonons. Electrons leave the gain stage from level 1 by tunneling out into the superlattice injector of the next stage. In addition, electrons also make non-radiative transitions from level 3 to levels 2 and 1. This QCL structure is fairly general in the sense that the linearized dynamics of many different multiple quantum well QCLs can be described by a three level system with an injector state, or with an even simpler model. Therefore, with minor adjustments the model presented here can be used to study different multiple quantum well QCL structures that have been reported in the literature. For example, in the multiple quantum well QCL structure employing diagonal radiative electron transitions described in Ref. [60] level 3 is the same as the injector state, and level 1 is the same as the injector state of the next gain stage. The linearized dynamics of the QCL in Ref. [60] can be captured in the model presented here if the transition rates from the injector state into level 3 and from level 1 into the injector state of the next gain stage are made very fast.

4.4 Rate Equations and Steady State Solutions

For the multiple quantum well QCL structure shown in Fig. 4-2, the non-linear rate equations for the electron and photon densities are as follows,

$$\frac{d\,n_3^j}{d\,t} = \frac{J_{in}^j}{e} - R_{32}(n_3^j, n_2^j) - R_{31}(n_3^j, n_1^j) - \Gamma^j v_g\, g(n_3^j, n_2^j)\left(S_p + \frac{n_{sp}}{WL}\right) \tag{4.1}$$

$$\frac{d\,n_2^j}{d\,t} = R_{32}(n_3^j, n_2^j) - R_{21}(n_2^j, n_1^j) + \Gamma^j v_g\, g(n_3^j, n_2^j)\left(S_p + \frac{n_{sp}}{WL}\right) \tag{4.2}$$

$$\frac{d\,n_1^j}{d\,t} = R_{31}(n_3^j, n_2^j) + R_{21}(n_2^j, n_1^j) - \frac{J_{out}^j}{e} \tag{4.3}$$

$$\frac{d\,S_p}{d\,t} = \sum_{j=1}^{N} \Gamma^j v_g\, g(n_3^j, n_2^j)(S_p + \frac{n_{sp}}{WL}) - \frac{S_p}{\tau_p} \tag{4.4}$$

$$P_{out} = \eta_o\, \hbar\Omega_o\, \frac{WL\, S_p}{\tau_p} \tag{4.5}$$

In the above equations, n_k^j is the electron density (cm^{-2}) in the kth energy level of the jth gain stage. J_{in}^j and J_{out}^j are the electron current densities (cm^{-2}) tunneling into level 3 and tunneling out of level 1 of the jth gain stage, respectively. Only in steady state J_{in}^j equals

J^j_{out}. S_p is the photon density (cm^{-2}) inside the optical cavity. S_p is equal to the total number of photons inside the cavity divided by the width W and the length L of the cavity. v_g is the group velocity of the lasing mode and g is the optical gain (cm^{-1}) contributed by a single gain stage. Γ^j is the mode confinement factor for the jth gain stage. N is the total number of cascaded gain stages. R_{32} is the net transition rate from level 3 to level 2 through non-radiative processes and spontaneous emission into the non-lasing modes. Similarly, R_{31} and R_{21} are the net transition rates from level 3 and level 2 into level 1, respectively. n_{sp} is the spontaneous emission factor [1]. P_{out} is the output power from the laser. η_o is the power output coupling efficiency and τ_p is the photon lifetime inside the cavity. The expression for τ_p is,

$$\frac{1}{\tau_p} = v_g(\alpha_i + \alpha_m) = v_g \left[\alpha_i + \frac{1}{L}\log\left(\frac{1}{\sqrt{R_1 R_2}}\right)\right] \tag{4.6}$$

where α_i is the internal loss of the cavity, α_m is the loss from the cavity facets, and R_1 and R_2 are the facet reflectivities. The power output coupling efficiency η_o from the facet with reflectivity R_1 is,

$$\eta_o = \frac{(1-R_1)\sqrt{R_2}}{[(1-R_1)\sqrt{R_2} + (1-R_2)\sqrt{R_1}]} \frac{\alpha_m}{(\alpha_m + \alpha_i)} \tag{4.7}$$

For simplicity it is assumed that all the gain stages have the same mode confinement factor, i.e. $\Gamma^j = \Gamma$ for all j. This assumption is valid if all the cascaded gain stages are located close to the peak of the transverse profile of the optical mode where the field strength varies slowly. Even for QCLs with large number of gain stages numerical simulations show that corrections to the solution obtained by assuming all Γ^j to be equal are small. Under this assumption, the steady state electron densities n^j_k are the same in all the gain stages, and the index j may be suppressed when calculating the steady state electron densities.

4.4.1 Steady State Solutions

Below Threshold

The steady state solution to the rate equations can be found by setting all the time derivatives equal to zero, and putting $J_{in} = J_{ext}$. Below threshold, steady state carrier densities

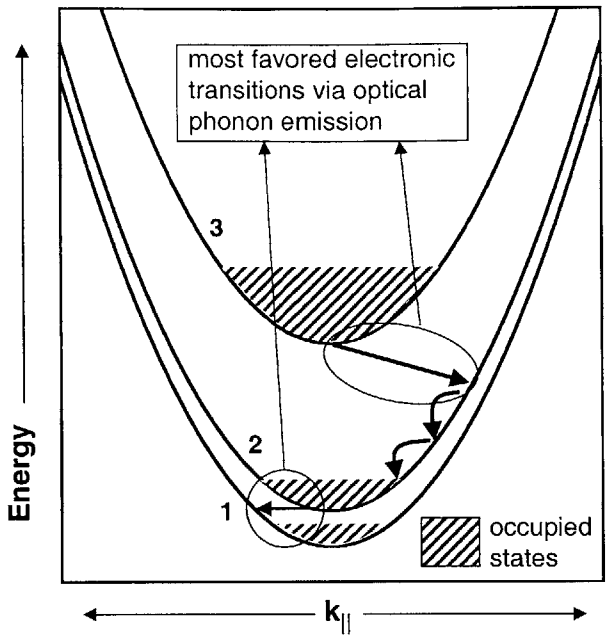

Figure 4-3: Energy subbands of the three levels of the gain stage. Most favored electronic transitions by optical phonon emission are almost horizontal in the $E(\vec{k}) - \vec{k}$ space.

can be found by putting $S_p = 0$, and solving the equations (the index j has been suppressed),

$$R_{32}(n_3, n_2) + R_{31}(n_3, n_1) = \frac{J_{ext}}{e} \tag{4.8}$$

$$R_{32}(n_3, n_2) = R_{21}(n_2, n_1) \tag{4.9}$$

The third equation can be obtained by realizing that J_{out} is also a function of n_1,

$$J_{out}(n_1) = J_{ext} \tag{4.10}$$

To proceed further, analytical expressions for the transition rates are required. These transition rates can be approximated as,

$$R_{32}(n_3, n_2) \cong \frac{n_3}{\tau_{32}} \tag{4.11}$$

$$R_{31}(n_3, n_1) \cong \frac{n_3}{\tau_{31}} \tag{4.12}$$

$$R_{21}(n_2, n_1) \cong \frac{n_2}{\tau_{21}} \tag{4.13}$$

$$\frac{J_{out}(n_1)}{e} \cong \frac{n_1}{\tau_{out}} \tag{4.14}$$

The rationale for the approximations in (4.11)-(4.13) is that optical phonons are largely responsible for intersubband transitions. As shown in Fig. 4-3, optical phonon mediated intersubband transitions that are almost horizontal in $E(\vec{k})$-$\vec{k}$ plane are more likely to occur [61]. Therefore, the transitions rates from an upper to a lower subband are not much affected by the electron density in the lower subband, as long as the electron density in the lower subband is small. More complicated expressions for these transition rates, such as,

$$R_{qk}(n_q, n_k) = \frac{n_q}{\tau_{qk}} - \frac{n_k}{\tau_{kq}} \tag{4.15}$$

may be used if necessary.

The expression for J_{out} in (4.14) does not depend upon on the electron density in the injector since electrons in the injector states are assumed to relax very quickly into the ground state of the injector which is spatially localized near the next gain stage. Using (4.11)-(4.14) in (4.8)-(4.10), expressions for the carrier densities can be obtained as a function of the current density,

$$n_3 = \frac{J_{ext}}{e} \frac{\tau_{32}\,\tau_{31}}{\tau_{32} + \tau_{31}} \tag{4.16}$$

$$n_2 = \frac{J_{ext}}{e} \frac{\tau_{21}\,\tau_{31}}{\tau_{32} + \tau_{31}} \tag{4.17}$$

$$n_1 = \frac{J_{ext}}{e}\,\tau_{out} \tag{4.18}$$

Above Threshold

Above threshold, the gain is clamped to a value determined by equating the gain with the loss,

$$\sum_{j=1}^{N} \Gamma^j v_g\, g(n_3^j, n_2^j) = N\Gamma v_g\, g(n_3, n_2) = \frac{1}{\tau_p} \tag{4.19}$$

For perfectly parabolic subbands, the expression for the gain may be approximated as,

$$g(n_3, n_2) = a\,(n_3 - n_2) \tag{4.20}$$

where a is the differential gain. In the parabolic band approximation a is [62],

$$a = \frac{1}{L_p} \frac{4\pi e^2 z_{32}^2}{\epsilon_o n_{eff} \lambda_o (2\gamma_{32})} \tag{4.21}$$

z_{32} is the optical dipole matrix element, ϵ_o is the vacuum dielectric constant, n_{eff} is the effective index of the optical mode, λ_o is the lasing wavelength, $(2\gamma_{32})$ is the full width at half maximum (FWHM) of the optical transition, and L_p is the length of a single gain stage over which the integration is performed when calculating the mode confinement factor Γ. The carrier and photon densities above threshold can be obtained by solving the equations,

$$R_{31}(n_3, n_1) + R_{21}(n_2, n_1) \cong \frac{n_3}{\tau_{31}} + \frac{n_2}{\tau_{21}} = \frac{J_{ext}}{e} \tag{4.22}$$

$$\frac{J_{out}}{e} \cong \frac{n_1}{\tau_{out}} = \frac{J_{ext}}{e} \tag{4.23}$$

$$N\Gamma v_g \, a(n_3 - n_2) = \frac{1}{\tau_p} \tag{4.24}$$

which results in,

$$n_3 = \frac{J_{ext}}{e} \frac{\tau_{21}\,\tau_{31}}{\tau_{21} + \tau_{31}} + \left(\frac{1}{N\Gamma v_g \, a\tau_p} \right) \frac{\tau_{31}}{\tau_{21} + \tau_{31}} \tag{4.25}$$

$$n_2 = \frac{J_{ext}}{e} \frac{\tau_{21}\,\tau_{31}}{\tau_{21} + \tau_{31}} - \left(\frac{1}{N\Gamma v_g \, a\tau_p} \right) \frac{\tau_{21}}{\tau_{21} + \tau_{31}} \tag{4.26}$$

$$n_1 = \frac{J_{ext}}{e} \tau_{out} \tag{4.27}$$

$$S_p = \eta_r \, N \, \frac{(J_{ext} - J_{th})}{e} \tau_p \tag{4.28}$$

$$P_{out} = \eta_o \, \eta_r \, \frac{\hbar \Omega_o}{e} \, N \, (I_{ext} - I_{th}) \tag{4.29}$$

where the threshold current density J_{th} and the radiative efficiency η_r are,

$$J_{th} = \frac{e}{N\Gamma v_g \, a\tau_p} \left(\frac{1}{\tau_{32}} + \frac{1}{\tau_{31}} \right) \frac{1}{(1 - \tau_{21}/\tau_{32})} \tag{4.30}$$

$$\eta_r = \left(1 - \frac{\tau_{21}}{\tau_{32}} \right) \frac{\tau_{31}}{(\tau_{21} + \tau_{31})} \tag{4.31}$$

The radiative efficiency η_r for a QCL is defined as that fraction of the total number of electrons injected into each gain stage per second which contribute to photon emission.

Table 4.1: Device Parameters Used in Numerical Simulations (From Ref. [16])

Parameter	Value
Lasing wavelength λ	5.0 μm
Operating temperature	20 K
Number of gain stages N	25 (unless stated otherwise)
Total confinement factor $\sum_{j=1}^{N}\Gamma^j$	$erf(0.019\,N) \approx 0.02\,N$
Cavity width W	11.7 μm
Cavity length L	3 mm
Facet reflectivities r_1, r_2	0.27
Cavity internal loss α_i	11 cm^{-1}
Mode effective index n_{eff}	3.29
Mode group index n_g	3.4
Differential gain a	$\sim 4.0 \times 10^{-9}$ cm
Length of a single gain stage L_p	45.3 nm
τ_{in}, τ_{out}, τ_3	1.0 ps
τ_2, τ_1	∞
τ_{32}	2.1 ps
τ_{31}	3.4 ps
τ_{21}	0.5 ps
C_{inj}	0.31 $\mu F/cm^2$
C_3, C_2	0.56 $\mu F/cm^2$
C_1	0.81 $\mu F/cm^2$
χ_{in}, χ_{out}	~ 1

Equations (4.25) and (4.26) show that above threshold, even though the gain is clamped to its threshold value, the electron densities keep increasing with the bias current. This is in contrast to what happens in a semiconductor diode laser in which the carrier density in the lasing state does not increase beyond its threshold value. As a result, an increase in the injected current density in QCLs does not only lead to an increase in the photon emission rate but it also leads to an increase in the rate of non-radiative transitions. For this reason, QCLs tend to have radiative efficiencies η_r significantly smaller than unity. If the lifetime τ_{21} of the electrons in the lower lasing state is much smaller than both the non-radiative lifetimes, τ_{32} and τ_{31}, then the electron densities in levels 3 and 2 would not increase much beyond threshold, and the radiative efficiency η_r would be close to unity. As will be shown later, the value of η_r has a significant impact on the noise properties of QCLs.

Fig. 4-4 shows the electron densities n_3 and n_2 plotted as a function of the bias current. The values of the various device parameters used in generating Fig. 4-4 belong to the QCL

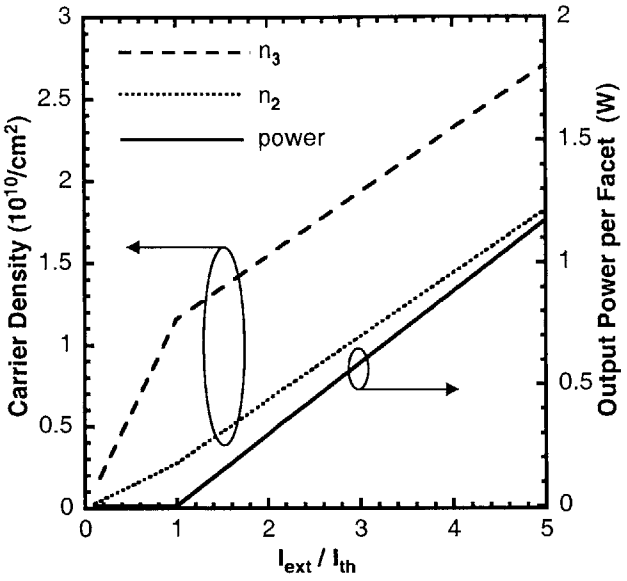

Figure 4-4: Electron densities in level 3 and level 2 of the gain stage, and the output power per facet are plotted as a function of the bias current. There is a discontinuity in the rate of increase of the electron densities with the bias current at threshold. For values of the QCL parameters see Table 4.1.

reported in Ref. [16], and these values are given in Table 4.1. Fig. 4-4 shows that the rate of change of electron densities in levels 3 and 2 with the bias current exhibits discontinuities at threshold. This can be confirmed by comparing Equations (4.25) and (4.26) with Equations (4.16) and (4.17). As will be shown later in this Chapter, these discontinuities in the rate of increase of electron densities with the bias current result in a discontinuity in the value of the differential resistance of the laser at threshold.

4.5 Noise and Fluctuations

The model for the noise presented here consists of a set of coupled self-consistent Langevin rate equations for the fluctuations in the electron density in different energy levels of a gain stage. Fluctuations in the electron density are caused by radiative and non-radiative scattering processes, electron tunneling processes and also by fluctuations in the current injected into the gain stage. Fluctuations in the current are a relaxational response to electron scattering and tunneling events occurring inside all the gain stages of the QCL,

and they are also caused by sources external to the laser which include thermal noise sources associated with circuit resistances. Photon density fluctuations are also modeled by Langevin rate equations. Electron density fluctuations in different gain stages are all coupled to the photon density fluctuations and also to the fluctuations in the current which flows through all the gain stages connected in series. The system of equations obtained this way can easily be solved analytically or numerically to give the spectral density of the photon number fluctuations and the current fluctuations.

4.5.1 Linearized Langevin Rate Equations for Electron and Photon densities

The non-linear rate equations can be linearized around any bias point to obtain rate equations for the fluctuations. Linearized Langevin rate equations for these fluctuations are as follows,

$$\begin{aligned}\frac{d\,\delta n_3^j}{d\,t} &= \frac{\delta J_{in}^j}{e} - \frac{\delta n_3^j}{\tau_{32}} - \frac{\delta n_3^j}{\tau_{31}} - \Gamma^j v_g \left[a\left(\delta n_3^j - \delta n_2^j\right)\left(S_p + \frac{n_{sp}}{WL}\right) + g(n_3^j, n_2^j)\delta S_p\right] \\ &\quad -f_{32}^j - f_{31}^j - f_{RN}^j \end{aligned} \tag{4.32}$$

$$\frac{d\,\delta n_2^j}{d\,t} = \frac{\delta n_3^j}{\tau_{32}} - \frac{\delta n_2^j}{\tau_{21}} + \Gamma^j v_g \left[a\left(\delta n_3^j - \delta n_2^j\right)\left(S_p + \frac{n_{sp}}{WL}\right) + g(n_3^j, n_2^j)\delta S_p\right] + f_{32}^j - f_{21}^j + f_{RN}^j \tag{4.33}$$

$$\frac{d\,\delta n_1^j}{d\,t} = \frac{\delta n_3^j}{\tau_{31}} + \frac{\delta n_2^j}{\tau_{21}} + f_{31}^j + f_{21}^j - \frac{\delta J_{out}^j}{e} \tag{4.34}$$

$$\frac{d\,\delta S_p}{d\,t} = \sum_{j=1}^{N} \Gamma^j v_g \left[a\left(\delta n_3^j - \delta n_2^j\right)\left(S_p + \frac{n_{sp}}{WL}\right) + g(n_3^j, n_2^j)\delta S_p\right] - \frac{\delta S_p}{\tau_p} - F_L + \sum_{j=1}^{N} f_{RS}^j \tag{4.35}$$

$$\delta P_{out} = \eta_o\, \hbar\Omega_o \frac{WL\,\delta S_p}{\tau_p} + F_o \tag{4.36}$$

Equations (4.11)-(4.13) have been used above for approximating the transition rates R_{qk}. f_{32}, f_{31}, and f_{21} are Langevin sources which model the noise associated with the non-radiative intersubband transitions and also the radiative transitions into the non-lasing

modes. f_{RN} and f_{RS} are Langevin sources which model the noise in photon emission and absorption from the lasing mode. F_L and F_o describe the noise associated with photon loss from the cavity [1]. All the Langevin noise sources have a white spectral density. All the non-zero correlations among the noise sources are given in Appendix C.2.

4.5.2 Linearized Electron Transport, Coulomb Correlations and Noise

In order to determine δJ_{in}^{j} and J_{out}^{j}, the electron transport through the active region needs to be looked at in detail. Self-consistent modeling of electron transport in multiple quantum well structures poses a significant challenge, and the steady state current-voltage characteristics of QCLs are difficult to compute accurately. On the other hand, a self-consistent analysis for the fluctuations in the electron current density and the electron charge density can be carried out in terms of only a few device parameters. The values of these parameters can either be determined experimentally or computed theoretically from more detailed self-consistent transport models.

The expression for the direct sequential tunneling current density from the injector state into level 3 of the gain stage can be written as [63],

$$\begin{aligned} J_{in} &= J_{in-forward} - J_{in-backward} \\ &= 2e \int \frac{d^2\vec{k}}{(2\pi)^2} \int \frac{d^2\vec{k}'}{(2\pi)^2} \frac{2\pi}{\hbar} \left|T_{\vec{k},\vec{k}'}\right|^2 \int_{-\infty}^{\infty} dE\, A\left(E - E_{inj}(\vec{k})\right) A\left(E - E_3(\vec{k}')\right) \times \\ &\qquad \left[f\left(E - \mu_{inj}\right) - f\left(E - \mu_3\right)\right] \end{aligned} \tag{4.37}$$

where the forward and backward components of the injection current are,

$$\begin{aligned} J_{in-forward} &= 2e \int \frac{d^2\vec{k}}{(2\pi)^2} \int \frac{d^2\vec{k}'}{(2\pi)^2} \frac{2\pi}{\hbar} \left|T_{\vec{k},\vec{k}'}\right|^2 \int_{-\infty}^{\infty} dE\, A\left(E - E_{inj}(\vec{k})\right) A\left(E - E_3(\vec{k}')\right) \times \\ &\qquad f\left(E - \mu_{inj}\right) \left[1 - f\left(E - \mu_3\right)\right] \end{aligned} \tag{4.38}$$

$$\begin{aligned} J_{in-backward} &= 2e \int \frac{d^2\vec{k}}{(2\pi)^2} \int \frac{d^2\vec{k}'}{(2\pi)^2} \frac{2\pi}{\hbar} \left|T_{\vec{k},\vec{k}'}\right|^2 \int_{-\infty}^{\infty} dE\, A\left(E - E_{inj}(\vec{k})\right) A\left(E - E_3(\vec{k}')\right) \times \\ &\qquad f\left(E - \mu_3\right) \left[1 - f\left(E - \mu_{inj}\right)\right] \end{aligned} \tag{4.39}$$

$T_{\vec{k},\vec{k}'}$ is the coupling constant, and its related to the transmission probability. $E_{inj}(\vec{k})$

and $E_3(\vec{k})$ are the energies of electrons in the injector state and level 3 of the gain stage, respectively. $A(E)$ is a normalized Lorentzian function with FWHM equal to the broadening of the energy levels, and $f(E-\mu)$ is the Fermi-Dirac distribution function with a chemical potential μ. Expressions similar to (4.37) can also be written for the phonon assisted tunneling current density. The analysis presented in this paper is independent of the specific nature of the electron tunneling mechanisms. In what follows, E_{inj} and E_3 will stand for $E_{inj}(\vec{k}=0)$ and $E_3(\vec{k}=0)$, respectively. The tunneling current in (4.37) depends upon the following three quantities,

- The difference $(\mu_{inj} - E_{inj})$ between the injector chemical potential and the energy of the injector state.
- The difference $(\mu_3 - E_3)$ between the chemical potential and the energy of level 3 of the gain stage.
- The relative difference $(E_{inj} - E_3)$ between the energies of the injector state and level 3 of the gain stage.

The current can change if the number of electrons in the injector level or in level 3 of the gain stage changes. The current can also change if the energy of the injector level shifts with respect to the energy of level 3. δJ_{in} can be written as,

$$\begin{aligned}
\delta J_{in}^j &= \frac{\delta J_{in}/\delta(\mu_{inj}-E_{inj})}{\delta n_{inj}/\delta(\mu_{inj}-E_{inj})}\,\delta n_{inj}^j + \frac{\delta J_{in}/\delta(\mu_3-E_3)}{\delta n_3/\delta(\mu_3-E_3)}\,\delta n_3^j \\
&\quad + \frac{\delta J_{inj}}{\delta(E_{inj}-E_3)}\,(\delta E_{inj}^j - \delta E_3^j) + e f_{in}^j \qquad (4.40) \\
&= \frac{\delta J_{in}}{\delta n_{inj}}\,\delta n_{inj}^j + \frac{\delta J_{in}}{\delta n_3}\,\delta n_3^j + \frac{\delta J_{inj}}{\delta(E_{inj}-E_3)}\,(\delta E_{inj}^j - \delta E_3^j) + e f_{in}^j \qquad (4.41)
\end{aligned}$$

f_{in} is a Langevin noise source which models the noise in electron tunneling. As shown in Appendix C.1, noise in electron transport by sequential tunneling in multiple quantum well structures can be described with Langevin noise sources. In Ref. [26], the current noise in double barrier resonant tunneling structures is evaluated using a quantum mechanical scattering approach. It can be shown that Langevin rate equations yield results identical to those presented in Ref. [26] for the current noise in double barrier resonant tunneling devices (see Appendix C.1). A linearized analysis based on Langevin rate equations may become invalid for highly non-linear devices. The correlation function for the noise source

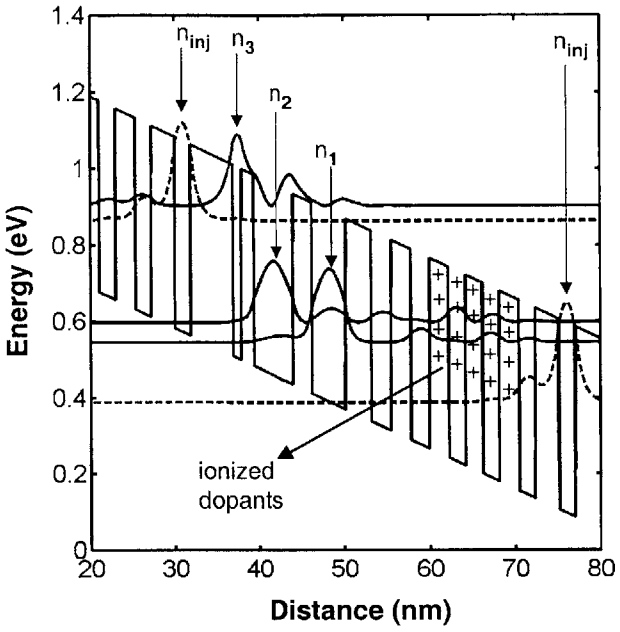

Figure 4-5: Charge densities associated with the electron densities δn_{inj}, δn_3, δn_2, and δn_1 are shown. The electron charge densities are imaged on the positively charged ionized dopants present in the superlattice injector of the subsequent stage.

f_{in} is,

$$WL\,\langle f_{in}^{j}(t)\, f_{in}^{k}(t')\rangle = \frac{1}{e}\left(J_{in-forward} + J_{in-backward}\right)\delta_{jk}\,\delta(t-t') \tag{4.42}$$

$$\approx \frac{J_{in}}{e}\,\chi_{in}\,\delta_{jk}\,\delta(t-t') \tag{4.43}$$

The factor χ_{in} relates the sum of the forward and backward tunneling currents to their difference which is the total injection current J_{in}. At low temperatures χ_{in} is expected to be close to unity since Pauli's exclusion would restrict the available phase space for the backward tunneling current [28]. For the same reason, χ_{in} is expected to be close to unity for large values of the injection current J_{in}. At high temperatures and small values of the injection current, χ_{in} can be larger than unity. Although the expression in (4.41) for the change in current density is derived for direct sequential tunneling, it also holds for phonon assisted tunneling. Even if the energy distribution of electrons inside each energy level in the steady state were not a Fermi-Dirac distribution with a well defined chemical potential, (4.41) would still hold.

It is assumed that the superlattice injector is doped in regions not close to the gain stage. Electric field lines from electron density fluctuations δn_{inj}^j, δn_3^j, δn_2^j, and δn_1^j are imaged on the ionized dopants in the injector layer of the $(j+1)$th gain stage, as shown in Fig. 4-5. Therefore, the fluctuation δV^j in the potential difference across the jth gain stage can be written as,

$$\delta V^j = \frac{e\delta n_{inj}^j}{C_{inj}} + \frac{e\delta n_3^j}{C_3} + \frac{e\delta n_2^j}{C_2} + \frac{q\delta n_1^j}{C_1} \tag{4.44}$$

C_{inj}, C_3, C_2, and C_1 are capacitances which relate the incremental change in the potential difference across a gain stage to the changes in the electron densities in different energy levels. Using first order quantum mechanical perturbation theory, $\delta E_{inj}^j - \delta E_3^j$ can be related to the fluctuation in the average potential difference between the injector level and level 3 of the gain stage. The fluctuation in the average potential difference between these two levels can also be expressed in terms of capacitances. Therefore, the expression for $\delta E_{inj}^j - \delta E_3^j$ becomes,

$$\delta E_{inj}^j - \delta E_3^j = \frac{e^2\delta n_{inj}^j}{C'_{inj}} - \frac{e^2\delta n_3^j}{C'_3} - \frac{e^2\delta n_2^j}{C'_2} - \frac{e^2\delta n_1^j}{C'_1} \tag{4.45}$$

Using (4.44) and (4.45), (4.41) can be put in the form,

$$\frac{\delta J_{in}^j}{e} = \left(\frac{1}{t_{in}} + \frac{G_{in}}{C'_{inj}}\right)\delta n_{inj}^j - \left(\frac{1}{t_3} + \frac{G_{in}}{C'_3}\right)\delta n_3^j - \left(\frac{G_{in}}{C'_2}\right)\delta n_2^j - \left(\frac{G_{in}}{C'_1}\right)\delta n_1^j + f_{in}^j \tag{4.46}$$

$$\begin{aligned} &= \left(\frac{C_{inj}}{t_{in}} + \frac{C_{inj}}{C'_{inj}}G_{in}\right)\frac{\delta V^j}{e} - \left[\left(\frac{1}{t_{in}} + \frac{G_{in}}{C'_{inj}}\right)\frac{C_{inj}}{C_3} + \left(\frac{1}{t_3} + \frac{G_{in}}{C'_3}\right)\right]\delta n_3^j \\ &\quad - \left[\left(\frac{1}{t_{in}} + \frac{G_{in}}{C'_{inj}}\right)\frac{C_{inj}}{C_2} + \left(\frac{G_{in}}{C'_2}\right)\right]\delta n_2^j - \left[\left(\frac{1}{t_{in}} + \frac{G_{in}}{C'_{inj}}\right)\frac{C_{inj}}{C_1} + \left(\frac{G_{in}}{C'_1}\right)\right]\delta n_1^j \\ &\quad + f_{in}^j \end{aligned} \tag{4.47}$$

In (4.47), G_{in}, t_{in}, and t_3 are given by,

$$G_{in} = e\frac{\delta J_{in}}{\delta(E_{inj} - E_3)} \quad , \quad \frac{1}{t_{in}} = \frac{1}{e}\frac{\delta J_{in}}{\delta n_{inj}} \quad , \quad \frac{1}{t_3} = -\frac{1}{e}\frac{\delta J_{in}}{\delta n_3} \tag{4.48}$$

More generally, there may be more than just one energy level in the injector from which electrons get injected into level 3 of the gain stage. (4.46) can be modified appropriately to take into account the contributions from all the energy levels inside the injector. However,

if the values of t_{in} are roughly the same for all such states in the injector then the final form of (4.46) will remain unchanged, but δn_{inj} will then represent the total electron density in all the injector states.

Similarly, the fluctuation δJ^j_{out} in the tunneling current density from level 1 of the gain stage into the injector is given by the expression,

$$\delta J^j_{out} = \frac{\delta J_{out}/\delta(\mu_1 - E_1)}{\delta n_1/\delta(\mu_1 - E_1)}\,\delta n^j_1 + \frac{\delta J_{out}}{\delta(E_1 - E'_{inj})}\,(\delta E^j_1 - \delta E'^j_{inj}) + e f^j_{out} \tag{4.49}$$

$$= \frac{\delta J_{out}}{\delta n_1}\,\delta n^j_1 + \frac{\delta J_{out}}{\delta(E_1 - E'_{inj})}\,(\delta E^j_1 - \delta E'^j_{inj}) + e f^j_{out} \tag{4.50}$$

The Langevin noise source f^j_{out} has the correlation function,

$$WL\,\langle f^j_{out}(t)\, f^k_{out}(t')\rangle = \frac{1}{e}\,(J_{out-forward} + J_{out-backward})\,\delta_{jk}\,\delta(t-t') \tag{4.51}$$

$$\approx \frac{J_{out}}{e}\,\chi_{out}\,\delta_{jk}\,\delta(t-t') \tag{4.52}$$

In a well designed QCL, the backward tunneling current from the injector of the next stage into level 1 of the gain stage is small, and χ_{out} is expected to be close to unity. E'^j_{inj} is the energy of the injector level of the next stage into which electrons tunnel from level 1 of the gain stage. $\delta E^j_1 - \delta E'^j_{inj}$, as before, can be expressed in terms of capacitances,

$$\delta E^j_1 - \delta E'^j_{inj} = \frac{e^2\delta n^j_{inj}}{C''_{inj}} + \frac{e^2\delta n^j_3}{C''_3} + \frac{e^2\delta n^j_2}{C''_2} + \frac{e^2\delta n^j_1}{C''_1} \tag{4.53}$$

Using (4.44) and (4.53), δJ^j_{out} becomes,

$$\frac{\delta J^j_{out}}{e} = \left(\frac{C_{inj}}{C''_{inj}}G_{out}\right)\frac{\delta V^j}{e} - \left(\frac{G_{out}}{C''_{inj}}\frac{C_{inj}}{C_3} - \frac{G_{out}}{C''_3}\right)\delta n^j_3 - \left(\frac{G_{out}}{C''_{inj}}\frac{C_{inj}}{C_2} - \frac{G_{out}}{C''_2}\right)\delta n^j_2$$
$$- \left[\frac{G_{out}}{C''_{inj}}\frac{C_{inj}}{C_1} - \left(\frac{1}{t_{out}} + \frac{G_{out}}{C''_3}\right)\right]\delta n^j_1 + f^j_{out} \tag{4.54}$$

where t_{out} and G_{out} are,

$$\frac{1}{t_{out}} = \frac{1}{e}\frac{\delta J_{out}}{\delta n_1} \quad , \quad G_{out} = e\frac{\delta J_{out}}{\delta(E_1 - E'_{inj})} \tag{4.55}$$

In (4.49), it is assumed that electrons in the injector relax into the ground state of the injector sufficiently fast so that electron occupation in the injector levels do not effect the

electron escape rate out of level 1 of the gain stage. Note that G_{in} and G_{out} can be positive or negative depending upon the relative alignment of the energy levels E_{inj} and E_3 in the steady state. The scheme used in deriving (4.47) and (4.54) is fairly general and can be used to derive self-consistent linearized transport equations for a variety of QCL structures. Approximations can be made to simplify (4.47) and (4.54). Expression for δJ_{in}^j can also be written as,

$$\frac{\delta J_{in}^j}{e} = \frac{1}{\tau_{in}}\delta n_{inj}^j - \frac{1}{\tau_3}\delta n_3^j - \frac{1}{\tau_2}\delta n_2^j - \frac{1}{\tau_1}\delta n_1^j + f_{in}^j \tag{4.56}$$

$$= \left(\frac{C_{inj}}{\tau_{in}}\right)\frac{\delta V^j}{e} - \left(\frac{1}{\tau_{in}}\frac{C_{inj}}{C_3} + \frac{1}{\tau_3}\right)\delta n_3^j - \left(\frac{1}{\tau_{in}}\frac{C_{inj}}{C_2} + \frac{1}{\tau_2}\right)\delta n_2^j - \left(\frac{1}{\tau_{in}}\frac{C_{inj}}{C_1} + \frac{1}{\tau_1}\right)\delta n_1^j + f_{in}^j \tag{4.57}$$

For the sake of economy of notation, new parameters have been introduced in the above Equation,

$$\frac{1}{\tau_{in}} = \frac{1}{t_{in}} + \frac{G_{in}}{C'_{inj}} \quad , \quad \frac{1}{\tau_3} = \frac{1}{t_3} + \frac{G_{in}}{C'_3} \quad , \quad \frac{1}{\tau_2} = \frac{G_{in}}{C'_2} \quad , \quad \frac{1}{\tau_1} = \frac{G_{in}}{C'_1} \tag{4.58}$$

Simple electrostatic arguments can be used to show that τ_2 and τ_1 will be large, and can be assumed to be infinite.

The injector is assumed to have a large number of closely spaced energy levels. J_{out} is, therefore, largely insensitive to the relative shifts in E_1 and E'_{inj}. This implies that terms containing G_{out} in the expression for δJ_{out}^j may be neglected, and the simplified expression for δJ_{out}^j becomes,

$$\frac{\delta J_{out}^j}{e} = \frac{1}{\tau_{out}}\delta n_1^j + f_{out}^j \tag{4.59}$$

where τ_{out} is just t_{out}. (4.57) and (4.59) show that in addition to the parameters given in the electron and photon density rate equations (Equations (4.32)-(4.35)), the only other parameters necessary for describing electron transport through the gain stage are C_{inj}, C_3, C_2, C_1, τ_{in}, τ_3, τ_2, and τ_1.

4.5.3 Displacement Currents

The noise current δJ_{ext}, which flows in the external circuit, is not equal to δJ_{in}^{j} or δJ_{out}^{j}. δJ_{ext} also includes displacement currents and is given by the expression,

$$\delta J_{ext} = \delta J_{in}^{j} + e\frac{d\,\delta n_{inj}^{j}}{d\,t} \tag{4.60}$$

Since all the gain stages are connected electrically in series, the same current δJ_{ext} flows through all the gain stages. The second term on the right hand side in (4.60) is the contribution to δJ_{ext} from displacement currents. Differentiating both sides of Equation (4.44) with respect to time, and rearranging yields,

$$q\frac{d\,n_{inj}^{j}}{d\,t} = C_{inj}\frac{d\delta\,V^{j}}{d\,t} - \sum_{k=1}^{3} e\frac{C_{inj}}{C_k}\frac{d\,\delta n_k^{j}}{d\,t}$$

Using the above Equation, the expression for δJ_{ext} becomes,

$$\begin{aligned}
\delta J_{ext} &= \delta J_{in}^{j} + C_{inj}\frac{d\delta\,V^{j}}{d\,t} - \sum_{k=1}^{3} e\frac{C_{inj}}{C_k}\frac{d\,\delta n_k^{j}}{d\,t} && (4.61)\\
&= \delta J_{out}^{j} + C_{inj}\frac{d\,\delta V^{j}}{d\,t} + \sum_{k=1}^{3} e\left(1 - \frac{C_{inj}}{C_k}\right)\frac{d\,\delta n_k^{j}}{dt} && (4.62)
\end{aligned}$$

(4.62) follows from (4.61) using the particle number conservation equation,

$$\sum_{k=1}^{3} e\,\frac{d\,\delta n_k^{j}}{dt} = \delta J_{in}^{j} - \delta J_{out}^{j}$$

(4.61) and (4.62) satisfy the Ramo-Shockley theorem [66].

4.5.4 Differential Resistance

Below threshold, the total differential resistance R_d of all the gain stages can be calculated by using (4.16)-(4.18) in (4.57),

$$\begin{aligned}
R_d &= \frac{N}{WL}\frac{\tau_{in}}{C_{inj}}\left[1 + \left(\frac{1}{\tau_{in}}\frac{C_{inj}}{C_3} + \frac{1}{\tau_3}\right)\frac{\tau_{32}\tau_{31}}{\tau_{32}+\tau_{31}}\right.\\
&\quad \left. + \left(\frac{1}{\tau_{in}}\frac{C_{inj}}{C_2} + \frac{1}{\tau_2}\right)\frac{\tau_{21}\tau_{31}}{\tau_{32}+\tau_{31}} + \left(\frac{1}{\tau_{in}}\frac{C_{inj}}{C_1} + \frac{1}{\tau_1}\right)\tau_{out}\right] && (4.63)\\
&= \frac{N}{WL}\frac{\tau_{in}}{C_{inj}}\left(1 + \theta_3' + \theta_2' + \theta_1\right) && (4.64)
\end{aligned}$$

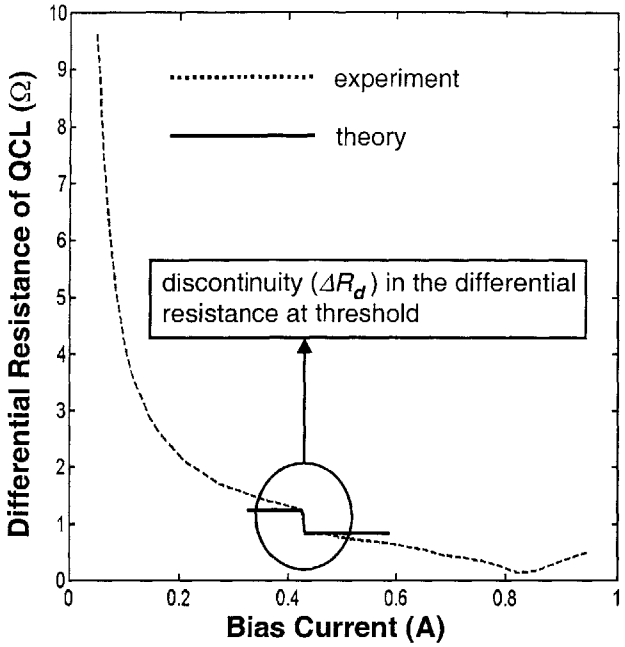

Figure 4-6: Differential Resistance of a QCL is shown as a function of the bias current. The experimentally measured discontinuity in the differential resistance at threshold is about 0.3 Ω. The theoretical model reproduces the discontinuity exactly. The experimental data is taken from [16].

Above threshold, the differential resistance can be computed by using (4.25)-(4.27) in (4.57),

$$R_d = \frac{N}{WL}\frac{\tau_{in}}{C_{inj}}\left[1+\left(\frac{1}{\tau_{in}}\frac{C_{inj}}{C_3}+\frac{1}{\tau_3}\right)\frac{\tau_{21}\tau_{31}}{\tau_{21}+\tau_{31}} + \left(\frac{1}{\tau_{in}}\frac{C_{inj}}{C_2}+\frac{1}{\tau_2}\right)\frac{\tau_{21}\tau_{31}}{\tau_{21}+\tau_{31}}+\left(\frac{1}{\tau_{in}}\frac{C_{inj}}{C_1}+\frac{1}{\tau_1}\right)\tau_{out}\right] \quad (4.65)$$

$$= \frac{N}{WL}\frac{\tau_{in}}{C_{inj}}\left(1+\theta_3+\theta_2+\theta_1\right) \quad (4.66)$$

Expressions for the parameters θ_3, θ_3', θ_2, θ_2', and θ_1 are given in Appendix C.3. Notice the similarity between the expressions in (4.64) and (4.66), and the expression in (2.42) for the differential resistance of interband semiconductor diode lasers given in Chapter 2. Unlike the active regions of diode lasers, the active regions of unipolar QCLs are not charge neutral, and as a result various capacitances appear in the expression for the differential resistance of QCLs.

The discontinuity ΔR_d in the differential resistance at threshold for an N stage QCL is,

$$\begin{aligned}\Delta R_d &= \frac{N}{WL}\frac{\tau_{in}}{C_{inj}}\left[\left(\frac{1}{\tau_{in}}\frac{C_{inj}}{C_3}+\frac{1}{\tau_3}\right)\left(\frac{\tau_{32}\tau_{31}}{\tau_{32}+\tau_{31}}-\frac{\tau_{21}\tau_{31}}{\tau_{21}+\tau_{31}}\right)\right. \\ &\quad \left.+\left(\frac{1}{\tau_{in}}\frac{C_{inj}}{C_2}+\frac{1}{\tau_2}\right)\left(\frac{\tau_{21}\tau_{31}}{\tau_{32}+\tau_{31}}-\frac{\tau_{21}\tau_{31}}{\tau_{21}+\tau_{31}}\right)\right] \qquad (4.67) \\ &= \frac{N}{WL}\frac{\tau_{in}}{C_{inj}}\left[(\theta_3'-\theta_3)+(\theta_2'-\theta_2)\right] \qquad (4.68)\end{aligned}$$

The Incremental change in the potential drop across a gain stage is related to the incremental changes in electron densities through (4.44). Therefore, the discontinuity in the differential resistance at threshold results from the discontinuity at threshold in the rate of change of electron densities in levels 3 and 2 of the gain stage with the bias current. Fig. 4-6 shows the calculated and measured differential resistance of a QCL as a function of the bias current. The experimental data is taken from [16]. The values of the various device parameters are given in Table 4.1. Values of τ_{21}, τ_{31} and τ_{32} are taken from [16]. Values of all the capacitances that are given in Table 4.1 are estimated for the QCL structure described in Ref. [16]. Values of τ_{in}, τ_3, and τ_{out} are estimated from (4.48) and (4.55). The total resistance of the ohmic contacts and the superlattice injectors is assumed to be approximately 0.3 Ω at threshold. The experimentally observed discontinuity in the differential resistance at threshold is exactly reproduced in the calculated results without the use of any fitting parameters. This agreement suggests that the self-consistent model for the linearized electron transport presented in this paper adequately captures the essential ingredients.

Diode lasers also exhibit a discontinuity in the differential resistance at threshold. As shown in Chapter 2, the discontinuity in the differential resistance of diode lasers at threshold is K_BT/eI_{th} times a factor of the order of unity, which can be compared with the more complicated expression given in (4.67) for QCLs.

4.5.5 Electron Transport in the Superlattice Injector

In this Chapter, no attention has been given to modeling the electron transport through the superlattice injector. In the absence of any bias current, the energy levels in the injector are not suitably aligned to facilitate electron transport, and the resistance of the injector region is large. As the bias current is gradually increased, electrons pile up in different quantum

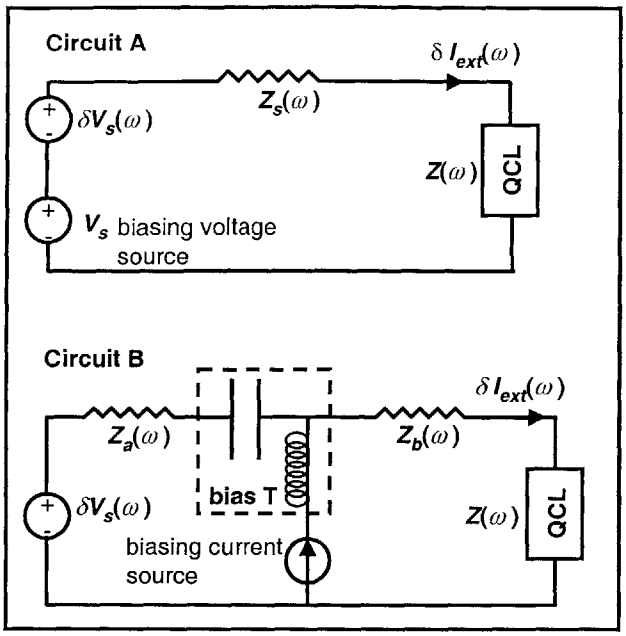

Figure 4-7: Circuits used for biasing QCLs.

wells until their presence modifies the potential profile and aligns the energy levels such that the electron current can flow. Once the injector has been *turned on* in this fashion, the differential resistance of the injector region is negligible, and the only bottleneck for electron transport is the gain stage. As a result of the small differential resistance of the injector region, any current noise originating in the injector region will not couple well into the external circuit. Therefore, electron transport in the injector region may be ignored when modeling noise. If necessary, the impedance of the superlattice injectors can be modeled with a lumped element, and the current noise generated inside the injector regions can be modeled with a voltage source in series (or a current source in parallel) with that element, as shown below. A detailed discussion of the current noise in superlattice structures is beyond the scope of this paper.

4.5.6 Biasing Electrical Circuits

Two electrical circuits for biasing QCLs are shown in Fig. 4-7. In circuit A the QCL, with an impedance $Z(\omega)$, is biased with a voltage source V_s in series with an impedance $Z_s(\omega)$. The thermal noise originating in the impedance $Z_s(\omega)$ is modeled by adding a voltage noise

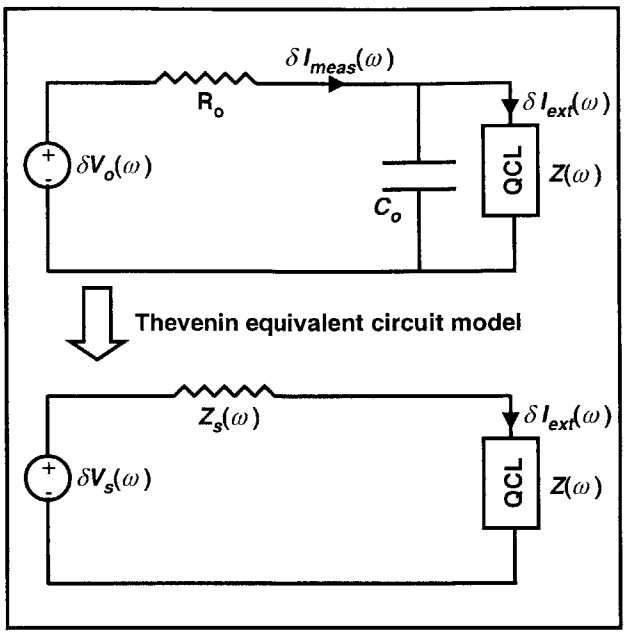

Figure 4-8: Thevenin equivalent circuit model indicating the distinction between $\delta I_{ext}(\omega)$ and $\delta I_{meas}(\omega)$.

source δV_s. The differential impedance of the superlattice injector and the current noise generated by the injector can also be modeled with an impedance and a voltage noise source in series (or a current noise source in parallel) with that impedance. For the sake of economy of notation it will be assumed that the impedance $Z_s(\omega)$ represents not just an external circuit impedance but the Thevenin equivalent impedance of the superlattice injectors, device ohmic contacts, external circuit resistances, and device and circuit parasitics, and the voltage noise source δV_s represents the Thevenin equivalent of their individual noise sources. Only the gain stages inside the QCL are not included within $Z_s(\omega)$ and they are represented by the impedance $Z(\omega)$. However, $Z(\omega)$ will be loosely referred to as the impedance of the QCL. The current noise generated by the gain stages can also be modeled by adding a current noise source in parallel with $Z(\omega)$, as shown in later sections.

Direct current modulation of the QCL can be achieved by adding an RF voltage source in series with V_s, and this RF voltage source can also be represented by the voltage source δV_s. From the context it will be clear whether δV_s represents a RF signal source or a noise source.

Semiconductor lasers are frequently biased as shown in circuit B in Fig. 4-7. The laser is biased with a current source in series with an ideal inductor, and it is also capacitively coupled to a voltage source δV_s with a series impedances $Z_a(\omega)$ and $Z_b(\omega)$. If at frequencies of interest the inductor and the coupling capacitor are almost open and short, respectively, then this circuit is also equivalent to circuit A. Therefore, in this Chapter only circuit A will be considered. In circuit A, the current δI_{ext} can be expressed as,

$$\delta I_{ext}(\omega) = \delta J_{ext}(\omega)\, WL = \frac{\delta V_s(\omega) - \sum_{j=1}^{N} \delta V^j(\omega)}{Z_s(\omega)} \tag{4.69}$$

It is important to note here that $\delta I_{ext}(\omega)$ may not be the noise current which would be measured in an experiment. For example, suppose that the QCL has a parasitic capacitance C_o in parallel with the actual device, as shown in Fig. 4-8. The QCL is driven with a series resistor R_o and a noise voltage source $\delta V_o(\omega)$ representing the thermal noise in the resistor R_o. Fig. 4-8 shows the distinction between the noise current $\delta I_{ext}(\omega)$ defined in (4.69), and the noise current $\delta I_{meas}(\omega)$ that would be measured in an experiment. Notice that the Thevenin equivalent impedance $Z_s(\omega)$ is a parallel combination of the resistance R_o and the capacitance C_o. $Z_s(\omega)$ and $\delta V_s(\omega)$ are,

$$Z_s(\omega) = \frac{R_o}{(1 + j\omega\, R_o C_o)} \qquad \delta V_s(\omega) = \frac{\delta V_o(\omega)}{(1 + j\omega\, R_o C_o)} \tag{4.70}$$

and the relation between $\delta I_{ext}(\omega)$ and $\delta I_{meas}(\omega)$ is,

$$\delta I_{ext}(\omega) = \frac{\delta I_{meas}(\omega)}{(1 + j\omega\, Z(\omega) C_o)} \tag{4.71}$$

Choosing to define $Z_s(\omega)$ this way helps in formulating a noise model that is independent of the specific nature of the device parasitics.

4.6 Solution of the Coupled Equations: Modulation Response and Noise

4.6.1 Current Modulation Response

In this section the response $\delta P_{out}(\omega)/\delta I_{ext}(\omega)$ of QCLs to external sinusoidal current modulation $\delta I_{ext}(\omega)$ is determined [1]. The frequency dependence of the photon noise spectral density of semiconductor lasers is directly related to the frequency dependence of the current modulation response. It is therefore instructive to look at the modulation response of QCLs. The modulation response can be found by solving (4.32)-(4.36), together with (4.57) and (4.59), and setting all the noise sources equal to zero. The external circuit constraints expressed in (4.61) and (4.69) must also be enforced. Equations (4.32)-(4.34) for each gain stage are coupled to the same set of equations for all the other gain stages through Equations (4.35) and (4.61). Such a large system of coupled equations can be solved only numerically. A numerical approach, although simple to implement, is not very instructive. With the approximation that all gain stages have the same confinement factor Γ, a significant portion of the work can be done analytically. This approach will be followed here. All equations, unless stated otherwise, will be expressed in the frequency domain.

The relationship between the current density $\delta J_{ext}(\omega)$, which flows in the external circuit, and the total potential drop $\delta V(\omega)$ across all the gain section can be obtained by using (4.57) in (4.61), and summing over the index j,

$$\frac{C_{inj}}{\tau_{in}}\frac{\delta V(\omega)}{e} = \frac{N}{(1+j\omega\,\tau_{in})}\frac{\delta J_{ext}(\omega)}{e} + \sum_{k=1}^{3}\left[\frac{1}{\tau_{in}}\frac{C_{inj}}{C_k} + \frac{1}{\tau_k\,(1+j\omega\,\tau_{in})}\right]\delta N_k(\omega) \qquad (4.72)$$

The following new symbols have been introduced in (4.72),

$$\delta N_k(\omega) = \sum_{j=1}^{N}\delta n_k^j(\omega) \qquad \{\text{where } k=1,2,3\} \qquad \text{and} \qquad \delta V(\omega) = \sum_{j=1}^{N}\delta V^j(\omega)$$

Using (4.57), (4.59) and (4.72) in (4.32)-(4.35), summing over the index j, and arranging

[1] It is assumed that $P_{out}(t) = P_{out} + \text{Real}\{\delta P_{out}(\omega)\,e^{j\,\omega t}\}$ and $I_{ext}(t) = I_{ext} + \text{Real}\{\delta I_{ext}(\omega)\,e^{j\,\omega t}\}$

the resulting equations in a matrix form gives,

$$\begin{bmatrix} \mathbf{D}_{11} & \mathbf{D}_{12} & \mathbf{D}_{13} & 0 \\ 0 & \mathbf{D}_{22} & \mathbf{D}_{23} & \mathbf{D}_{24} \\ \mathbf{D}_{31} & \mathbf{D}_{32} & \mathbf{D}_{33} & \mathbf{D}_{34} \\ 0 & \mathbf{D}_{42} & \mathbf{D}_{43} & \mathbf{D}_{44} \end{bmatrix} \begin{bmatrix} \delta N_1(\omega) \\ \delta N_2(\omega) \\ \delta N_3(\omega) \\ \delta S_p(\omega) \end{bmatrix} = \frac{N}{(1+j\omega\,\tau_{in})} \frac{\delta J_{ext}(\omega)}{e} \begin{bmatrix} 0 \\ 0 \\ 1 \\ 0 \end{bmatrix} \tag{4.73}$$

The coefficients of the matrix $\mathbf{D}$ can be found from (4.32)-(4.35), and they are given in Appendix C.4. The solution of (4.73) can be written as,

$$\begin{bmatrix} \delta N_1(\omega) \\ \delta N_2(\omega) \\ \delta N_3(\omega) \\ \delta S_p(\omega) \end{bmatrix} = \begin{bmatrix} \mathbf{D}_{13}^{-1}(\omega) \\ \mathbf{D}_{23}^{-1}(\omega) \\ \mathbf{D}_{33}^{-1}(\omega) \\ \mathbf{D}_{43}^{-1}(\omega) \end{bmatrix} \frac{N}{(1+j\omega\,\tau_{in})} \frac{\delta J_{ext}(\omega)}{e} \tag{4.74}$$

The coefficients of the matrix $\mathbf{D}^{-1}$ are given in Appendix C.5. (4.74) can be used in (4.72) to calculate the total impedance $Z(\omega)$ of all the gain stages,

$$Z(\omega) = \frac{N}{WL} \frac{\tau_{inj}}{C_{inj}} \frac{1}{(1+j\omega\,\tau_{in})} \left[1 + \sum_{k=1}^{3} \left(\frac{1}{\tau_{in}} \frac{C_{inj}}{C_k} + \frac{1}{\tau_k\,(1+j\omega\,\tau_{in})} \right) \mathbf{D}_{k3}^{-1}(\omega) \right] \tag{4.75}$$

$Z(\omega = 0)$ is just the differential resistance R_d of the QCL given earlier in (4.63) and (4.65). Finally, from (4.36) and (4.74), the current modulation response can be written as,

$$\frac{\delta P_{out}(\omega)}{\delta I_{ext}(\omega)} = \eta_o \frac{\hbar\Omega_o}{e} \frac{N}{\tau_p} \frac{\mathbf{D}_{43}^{-1}(\omega)}{(1+j\omega\,\tau_{in})} \tag{4.76}$$

In QCLs that have been reported in the literature the photon lifetime τ_p is usually much longer than any other relevant time constant of the laser. Therefore, it is expected that the bandwidth of the modulation response in QCLs will be limited by the inverse photon lifetime. Above threshold, an analytical approximation for the modulation response valid for values of ω smaller than $1/\tau_{in}$, $1/\tau_{st}$, and $1/\tau_{21}$ can be found in the limit $\{\tau_2\,,\,\tau_1\} \to \infty$ (see Appendix C.5),

$$\frac{\delta P_{out}(\omega)}{\delta I_{ext}(\omega)} = \eta_o\,\eta_r \frac{\hbar\Omega_o}{e} N \frac{\omega_R^2}{(\omega_R^2 - \omega^2 + j\omega\gamma)} \tag{4.77}$$

where η_r is the radiative efficiency defined in (4.31), and the relaxation oscillation frequency ω_R and the damping constant γ are,

$$\omega_R^2 = \frac{\dfrac{1}{\tau_p \tau_{st}} \left(1 + \dfrac{\tau_{21}}{\tau_{31}}\right)}{\left[1 + \dfrac{\tau_{21}}{\tau_{31}} + \dfrac{\tau_{21}}{\tau_{32}} + \dfrac{\tau_{in}}{\tau_3} + \dfrac{\tau_{21}}{\tau_{st}} \left(2 + \dfrac{\tau_{in}}{\tau_3}\right)\right]} \tag{4.78}$$

$$\gamma = \frac{\left[\dfrac{1}{\tau_{st}} \left(1 + \dfrac{\tau_{21}}{\tau_{31}}\right) + \dfrac{1}{\tau_{31}} + \dfrac{1}{\tau_{32}} + \dfrac{\tau_{21}}{\tau_p \tau_{st}} \left(2 + \dfrac{\tau_{in}}{\tau_3}\right)\right]}{\left[1 + \dfrac{\tau_{21}}{\tau_{31}} + \dfrac{\tau_{21}}{\tau_{32}} + \dfrac{\tau_{in}}{\tau_3} + \dfrac{\tau_{21}}{\tau_{st}} \left(2 + \dfrac{\tau_{in}}{\tau_3}\right)\right]} \tag{4.79}$$

In the above expressions, τ_{st} is the differential lifetime associated with stimulated and spontaneous photon emission into the lasing mode, and is given by the relation,

$$\frac{1}{\tau_{st}} = \Gamma v_g a \left(S_p + \frac{n_{sp}}{WL}\right) \tag{4.80}$$

(4.77) has the standard form used for semiconductor diode lasers (see Chapter 2 and [1]). The damping constant γ can be related to ω_R,

$$\gamma = K \omega_R^2 + \gamma_o \tag{4.81}$$

where,

$$K = \tau_p \tag{4.82}$$

$$\gamma_o = \frac{\left[\dfrac{1}{\tau_{31}} + \dfrac{1}{\tau_{32}} + \dfrac{\tau_{21}}{\tau_p \tau_{st}} \left(2 + \dfrac{\tau_{in}}{\tau_3}\right)\right]}{\left[1 + \dfrac{\tau_{21}}{\tau_{31}} + \dfrac{\tau_{21}}{\tau_{32}} + \dfrac{\tau_{in}}{\tau_3} + \dfrac{\tau_{21}}{\tau_{st}} \left(2 + \dfrac{\tau_{in}}{\tau_3}\right)\right]} \tag{4.83}$$

The K-factor describes the damping of the QCL modulation response at high photon densities. γ_o has a weak dependence on the photon density through τ_{st}, and it approaches $1/\tau_p$ at large photon densities.

If the condition $\omega_R < \gamma/2$ is satisfied, then (4.77) describes a second order over-damped system. For QCLs that have been reported in the literature, this condition holds true above threshold. Using the values of device parameters from Table 4.1, ω_R and γ can be calculated. If the output power of the laser is assumed to be around 150 mW, then from (4.6) and (4.80) τ_p and τ_{st} are approximately 7 ps and 2.8 ps, respectively. The resulting value of

γ is more than three times larger than that of ω_R. The internal time constants in QCLs are usually smaller than the photon lifetime τ_p, and therefore the modulation response of QCLs is over-damped. An over-damped modulation response implies the absence of relaxation oscillations. In contrast, the current modulation response of semiconductor diode lasers is under-damped, and becomes over-damped only at very large bias currents when τ_{st} becomes small [1].

For QCLs the 3 dB frequency, which is defined to be the frequency at which the square modulus of the laser modulation response becomes one half of its value at zero frequency, can be found from the simplified expression for the modulation response in (4.77),

$$\omega_{3\,\mathrm{dB}}^2 = \sqrt{(\frac{\gamma^2}{2} - \omega_R^2)^2 + \omega_R^4} \; - (\frac{\gamma^2}{2} - \omega_R^2) \tag{4.84}$$

As the photon density inside the laser cavity increases, the 3 dB frequency also increases but it asymptotically approaches an upper limit $\omega_{3\,\mathrm{dB}\,|\,\mathrm{max}}$. This maximum attainable 3 dB bandwidth can be calculated from (4.84), and comes out to be,

$$\omega_{3\,\mathrm{dB}\,|\,\mathrm{max}} \approx \frac{1}{\tau_p} \tag{4.85}$$

(4.85) confirms the intuition that a laser cannot be modulated much faster than the inverse of the photon lifetime inside the laser cavity. As long as the photon lifetime τ_p is much longer than τ_{in}, τ_{st}, and τ_{21}, the approximations made in deriving (4.77) are justified. Otherwise, the exact expression given in (4.76) must be evaluated numerically. As shown in Chapter 2, in diode lasers the value of $\omega_{3\,\mathrm{dB}\,|\,\mathrm{max}}$ equals $\sqrt{2}/\tau_p$. The difference of a factor of $\sqrt{2}$ comes from the fact that in diode lasers the modulation response is under-damped (see Chapter 2).

As in diode lasers, the photon lifetime imposes a fundamental limit on how fast QCLs can be modulated. It is not uncommon to find predictions of THz modulation bandwidths for QCLs in literature [67]. However, for all the QCLs reported in the literature so far, the photon lifetime is the longest of all the time constants and it is the dominant factor that would limit the modulation bandwidth of these QCLs to tens of GHz instead of THz. It remains to be seen if QCL structures can be designed in which the photon lifetime is not the bottleneck for the modulation bandwidth.

Fig. 4-9 shows the calculated modulation response of a QCL as a function of the fre-

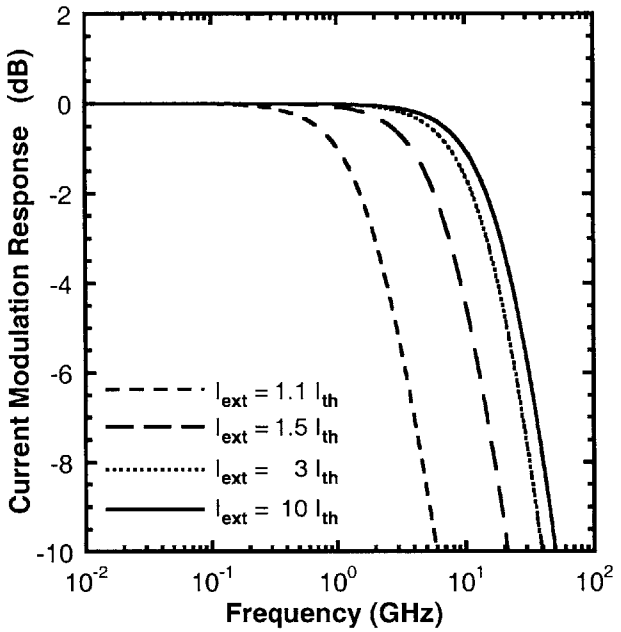

Figure 4-9: Absolute value squared of the direct current modulation response is plotted as a function of the frequency for different bias currents. Modulation response shown in the figure has been normalized w.r.t its value at zero frequency. For values of the QCL parameters see Table 4.1.

quency for different values of the bias current. The values of the different parameters of the QCL are taken from [16] and are given in Table 4.1. In the numerical calculations, values of all the device time constants (except τ_{st}) were assumed to be independent of the bias. Fig. 4-9 shows that at low bias currents the 3 dB frequency increases with the bias current, and at high bias currents the 3 dB frequency saturates to a value which is well approximated by $1/(2\pi\tau_p) = 21$ GHz. The analysis carried out in this paper does not take into account device heating which may also be important in limiting the modulation bandwidth of QCLs at large bias currents.

Fig. 4-10 shows the impedance $Z(\omega)$ of the QCL plotted as a function of the frequency for different bias currents. The peaks in the values of $Z(\omega)$ are not due to relaxation oscillations since, as already pointed out earlier, the modulation response of the QCL is over-damped. The peaks are due to the fact that the smallest zero of $Z(\omega)$ is at a frequency which is smaller than the frequency of its smallest pole. Impedance measurements can therefore provide valuable information about the time scales associated with electron dynamics in

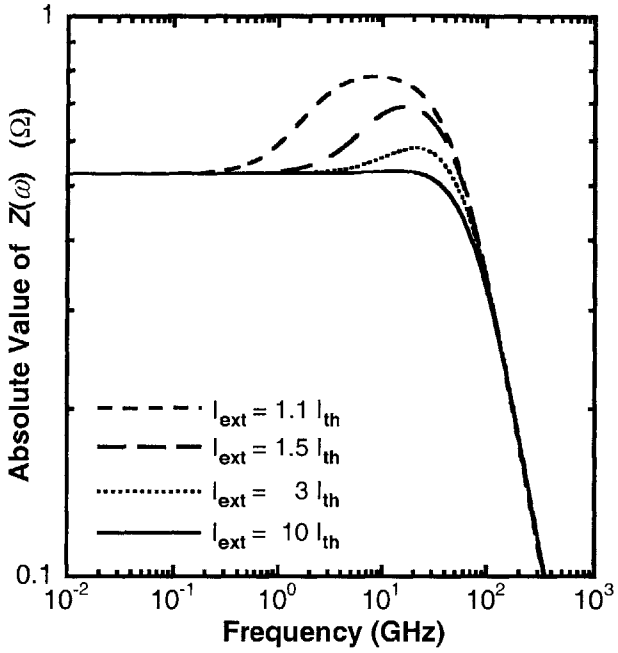

Figure 4-10: Absolute value of the impedance $Z(\omega)$ is plotted as a function of the frequency for different bias currents. The peaks in the values of $Z(\omega)$ are not because of relaxation oscillations, since the modulation response of the QCL is over-damped, but because the smallest zero of $Z(\omega)$ is smaller than its smallest pole. For values of the QCL parameters see Table 4.1.

QCLs.

4.6.2 Current Noise and Photon Noise

In this section, the current noise in the external circuit and the photon noise in the output power from QCLs is calculated. In the Langevin equation formalism noise is added through the Langevin noise sources which were introduced in (4.32)-(4.36) and also in (4.57) and (4.59). In addition, any noise originating in the external circuit and in the superlattice injectors can also contribute to the current noise and the photon noise, and as already explained earlier, this noise can be represented by the voltage source δV_s. Here, it is assumed that δV_s represents the thermal noise originating in the series impedance $Z_s(\omega)$, and its correlation function is,

$$\langle \delta V_s(\omega)\, \delta V_s(\omega') \rangle = 2K_B T\ \mathrm{Real}\{Z_s(\omega)\}\, 2\pi\, \delta(\omega - \omega') \tag{4.86}$$

By assuming the above correlation function for the noise source δV_s, noise that is contributed by the superlattice injectors is being ignored.

Including the Langevin noise sources, (4.73) can be written as,

$$\begin{bmatrix} \mathbf{D}_{11} & \mathbf{D}_{12} & \mathbf{D}_{13} & 0 \\ 0 & \mathbf{D}_{22} & \mathbf{D}_{23} & \mathbf{D}_{24} \\ \mathbf{D}_{31} & \mathbf{D}_{32} & \mathbf{D}_{33} & \mathbf{D}_{34} \\ 0 & \mathbf{D}_{42} & \mathbf{D}_{43} & \mathbf{D}_{44} \end{bmatrix} \begin{bmatrix} \delta N_1(\omega) \\ \delta N_2(\omega) \\ \delta N_3(\omega) \\ \delta S_p(\omega) \end{bmatrix} = \frac{N}{(1+j\omega\,\tau_{in})} \frac{\delta J_{ext}(\omega)}{e} \begin{bmatrix} 0 \\ 0 \\ 1 \\ 0 \end{bmatrix} + \begin{bmatrix} F_1(\omega) \\ F_2(\omega) \\ F_3(\omega) \\ F_4(\omega) \end{bmatrix} \tag{4.87}$$

The expressions for the noise sources F_1, F_2, F_3, and F_4 are,

$$F_1(\omega) = \sum_{j=1}^{N} F_1^j = \sum_{j=1}^{N} \left[f_{31}^j(\omega) + f_{21}^j(\omega) - f_{out}^j(\omega) \right] \tag{4.88}$$

$$F_2(\omega) = \sum_{j=1}^{N} F_2^j = \sum_{j=1}^{N} \left[f_{32}^j(\omega) - f_{21}^j(\omega) + f_{RN}^j(\omega) \right] \tag{4.89}$$

$$F_3(\omega) = \sum_{j=1}^{N} F_3^j = \sum_{j=1}^{N} \left[f_{in}^j(\omega) \frac{j\omega\,\tau_{in}}{(1+j\omega\,\tau_{in})} - f_{32}^j(\omega) - f_{31}^j(\omega) - f_{RN}^j(\omega) \right] \tag{4.90}$$

$$F_4(\omega) = \sum_{j=1}^{N} F_4^j = \sum_{j=1}^{N} \left[f_{RS}^j(\omega) - \frac{F_L(\omega)}{N} \right] \tag{4.91}$$

The solution of (4.87) can be written as,

$$\begin{bmatrix} \delta N_1(\omega) \\ \delta N_2(\omega) \\ \delta N_3(\omega) \\ \delta S_p(\omega) \end{bmatrix} = \begin{bmatrix} \mathbf{D}_{13}^{-1}(\omega) \\ \mathbf{D}_{23}^{-1}(\omega) \\ \mathbf{D}_{33}^{-1}(\omega) \\ \mathbf{D}_{43}^{-1}(\omega) \end{bmatrix} \frac{N}{(1+j\omega\,\tau_{in})} \frac{\delta J_{ext}(\omega)}{e} + \begin{bmatrix} \sum_{l=1}^{4} \mathbf{D}_{1l}^{-1}(\omega)\, F_l(\omega) \\ \sum_{l=1}^{4} \mathbf{D}_{2l}^{-1}(\omega)\, F_l(\omega) \\ \sum_{l=1}^{4} \mathbf{D}_{3l}^{-1}(\omega)\, F_l(\omega) \\ \sum_{l=1}^{4} \mathbf{D}_{4l}^{-1}(\omega)\, F_l(\omega) \end{bmatrix} \tag{4.92}$$

$\delta J_{ext}(\omega)$ in (4.92) still needs to be determined. Using (4.57) in (4.61), summing over the index j, and making use of (4.92) yields,

$$\begin{aligned} \delta V(\omega) \;=\; & Z(\omega)\,\delta I_{ext}(\omega) \\ & - e\,\frac{\tau_{in}}{C_{inj}} \left[\frac{F_{in}(\omega)}{(1+j\omega\,\tau_{in})} \right. \\ & \left. - \sum_{k=1}^{3} \sum_{l=1}^{4} \left(\frac{1}{\tau_{in}} \frac{C_{inj}}{C_k} + \frac{1}{\tau_k(1+j\omega\,\tau_{in})} \right) \mathbf{D}_{kl}^{-1}(\omega)\, F_l(\omega) \right] \end{aligned} \tag{4.93}$$

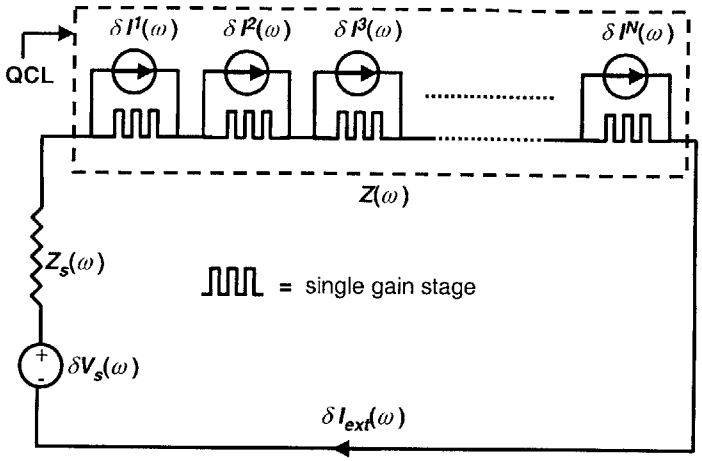

Figure 4-11: Circuit model for the current fluctuations.

where $F_{in} = \sum_{j=1}^{N} f_{in}^{j}$. Substituting the value of $\delta V(\omega)$ from (4.69) in (4.93), the final expression for the current fluctuations $\delta I_{ext}(\omega)$ in the external circuit is obtained,

$$\begin{aligned}\delta I_{ext}(\omega) &= \frac{\delta V_s(\omega)}{(Z(\omega)+Z_s(\omega))} + \frac{e}{(Z(\omega)+Z_s(\omega))}\frac{\tau_{in}}{C_{inj}}\left[\frac{F_{in}(\omega)}{(1+j\omega\,\tau_{in})}\right. \\ &\quad \left. - \sum_{k=1}^{3}\sum_{l=1}^{4}\left(\frac{1}{\tau_{in}}\frac{C_{inj}}{C_k} + \frac{1}{\tau_k(1+j\omega\,\tau_{in})}\right)\mathbf{D}_{kl}^{-1}(\omega)\,F_l(\omega)\right] \qquad (4.94)\end{aligned}$$

The fluctuation $\delta P_{out}(\omega)$ in the output power can be obtained by substituting (4.94) in (4.92), and using (4.36),

$$\begin{aligned}\delta P_{out}(\omega) &= \eta_o \frac{\hbar\Omega_o}{e}\frac{N}{\tau_p}\frac{\mathbf{D}_{43}^{-1}(\omega)}{(1+j\omega\,\tau_{in})}\,\delta I_{ext}(\omega) \\ &\quad + \eta_o \frac{\hbar\Omega_o}{e}\frac{WL}{\tau_p}\left[e\sum_{l=1}^{4}\mathbf{D}_{4l}^{-1}(\omega)\,F_l(\omega)\right] + F_o(\omega) \qquad (4.95)\end{aligned}$$

4.7 Current Noise: Results and Discussion

4.7.1 Circuit Models for the Current Noise

A circuit model for the current fluctuations can be constructed by attaching a current noise source $\delta I^j(\omega)$ in parallel with the jth gain stage, as shown in Fig. 4-11. But current noise sources belonging to two different gain stages are not independent but are correlated. This

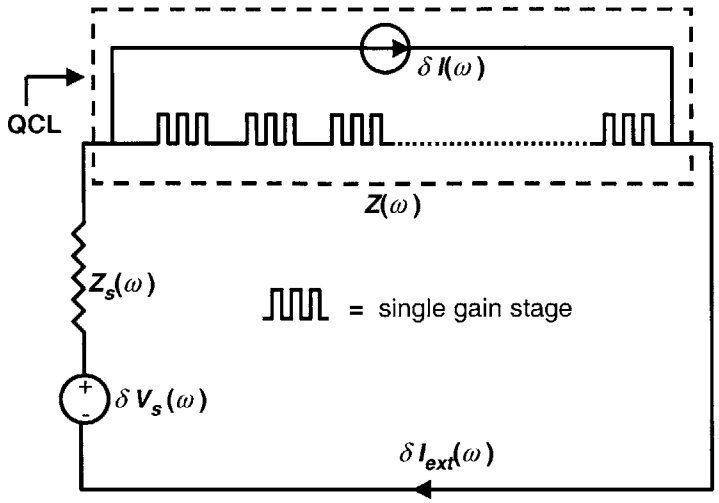

Figure 4-12: A simplified circuit model for the current fluctuations.

is because electron densities in different gain stages interact with the same optical field. A simpler approach, more relevant from the experimental point of view, will be followed in this paper. Equation (4.94) for the current fluctuations in the external circuit can be written as,

$$\delta I_{ext}(\omega) = \frac{\delta V_s(\omega)}{(Z(\omega) + Z_s(\omega))} + \frac{Z(\omega)}{(Z(\omega) + Z_s(\omega))}\,\delta I(\omega) \tag{4.96}$$

Expression for $\delta I(\omega)$ is,

$$\delta I(\omega) = \frac{e}{Z(\omega)}\,\frac{\tau_{in}}{C_{inj}}\left[\frac{F_{in}(\omega)}{(1+j\omega\,\tau_{in})} - \sum_{k=1}^{3}\sum_{l=1}^{4}\left(\frac{1}{\tau_{in}}\,\frac{C_{inj}}{C_k} + \frac{1}{\tau_k(1+j\omega\,\tau_{in})}\right)\mathbf{D}_{kl}^{-1}(\omega)\,F_l(\omega)\right] \tag{4.97}$$

It follows that a circuit model for the current fluctuations can be constructed by attaching a single current noise source $\delta I(\omega)$ in parallel with all the gain stages of the QCL, as shown in Fig. 4-12. (4.96) shows that the current noise $\delta I(\omega)$ is equal to the current noise $\delta I_{ext}(\omega)$ in the external circuit if $\delta V_s(\omega)$ and $Z_s(\omega)$ are both zero. This is also obvious from Fig. 4-12. The characteristics of the noise source $\delta I(\omega)$ are explored next.

4.7.2 Spectral Density and Fano Factor of the Current Noise

The spectral density $K_I(\omega)$ of the noise source $\delta I(\omega)$ can be calculated from (4.97). Most of the numerical results presented in this paper, unless stated otherwise, are for the QCL

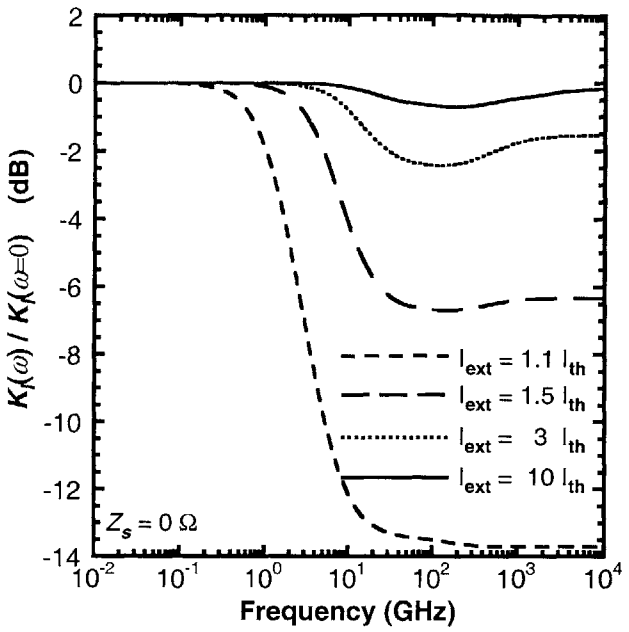

Figure 4-13: Spectral density $K_I(\omega)$ of the current noise is plotted as a function of the frequency. The noise spectral density has been normalized w.r.t. its value at zero frequency. For values of the QCL parameters see Table 4.1.

described in Ref. [16]. The device parameters for this QCL are given in the Table 4.1. In the numerical calculations, values of all the device time constants (except τ_{st}) were assumed to be independent of bias. The values of χ_{in} and χ_{out} were assumed to be unity (see the discussion in section 4.5.2). Fig. 4-13 shows the frequency dependence of $K_I(\omega)$ for different values of the bias current. As expected, $K_I(\omega)$ rolls over near the 3 dB frequency ($\omega_{3\,\mathrm{dB}}$) for the laser modulation response. Fig. 4-15 shows the Fano Factor (see Appendix A.1) for the low frequency fluctuations of the current noise source $\delta I(\omega)$ as a function of the bias current. Near the laser threshold, the current fluctuations are very large. Below threshold, the photon number fluctuations inside the laser cavity are damped by the photon loss from the cavity. Above threshold, the photon number fluctuations are damped by negative feedback from the electron density in the lasing levels. Near the laser threshold, both these damping mechanisms are small and therefore photon number fluctuations and, consequently, the electron density fluctuations become large. Since, as discussed in detail below, the current fluctuations are driven by the electron density fluctuations, the current noise is also large near the laser threshold. Away from the laser threshold, the current noise is suppressed far

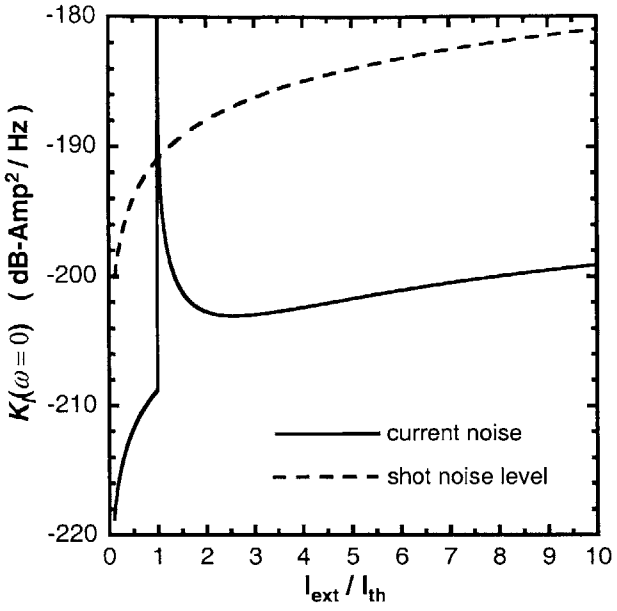

Figure 4-14: Low frequency spectral density $K_I(\omega = 0)$ of the current noise is plotted as a function of the bias current. For values of the QCL parameters see Table 4.1.

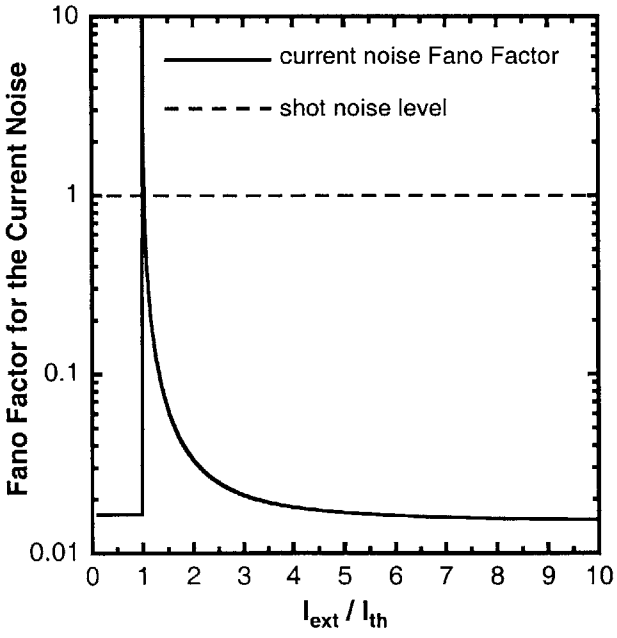

Figure 4-15: Fano Factor for the low frequency current fluctuations is plotted as a function of the bias current. For values of the QCL parameters see Table 4.1.

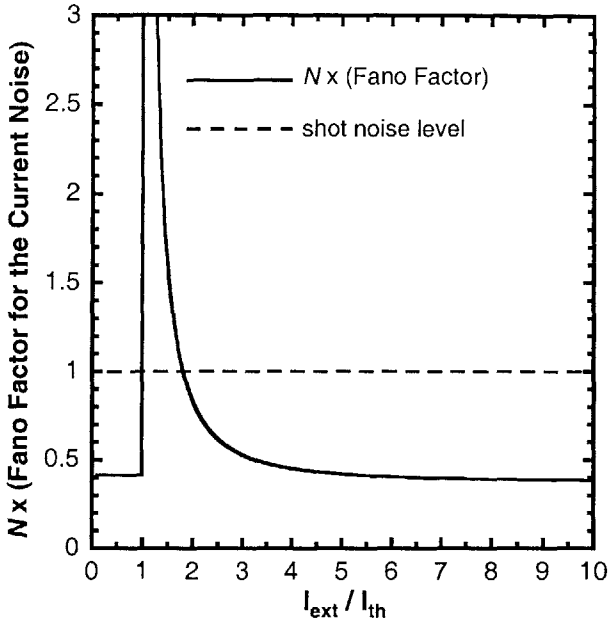

Figure 4-16: N times the Fano Factor for the low frequency current fluctuations is plotted as a function of the bias current. For values of the QCL parameters see Table 4.1.

below the shot noise value.

For frequencies less than $\omega_{3\,\mathrm{dB}}$, analytical expression for $K_I(\omega)$ can be found using the expressions for the elements of the matrix $\mathbf{D}^{-1}$ given in Appendix C.5,

$$\begin{aligned} K_I\left(\omega < \omega_{3\,\mathrm{dB}}\,,\, I_{ext} < I_{th}\right) &= e\frac{I_{ext}}{N}\,\frac{\left(\chi_{in}^2 + (\theta_3')^2 + (\theta_2')^2\,\left(1 + 2\,\frac{\tau_{32}}{\tau_{31}}\right) + (\theta_1\,\chi_{out})^2\right)}{\left(1 + \theta_3' + \theta_2' + \theta_1\right)^2} \\ K_I\left(\omega < \omega_{3\,\mathrm{dB}}\,,\, I_{ext} > I_{th}\right) &= e\frac{I_{ext}}{N}\,\frac{\left(\chi_{in}^2 + (\theta_3 + \theta_2)^2 + (\theta_1\,\chi_{out})^2\right)}{\left(1 + \theta_3 + \theta_2 + \theta_1\right)^2} \\ &\quad + 2en_{sp}\,\eta_r\frac{(I_{ext} - I_{th})}{N}\,\frac{\left(\theta_3\,\frac{\tau_{st}}{\tau_{21}} - \theta_2\,\frac{\tau_{st}}{\tau_{31}}\right)^2}{\left(1 + \theta_3 + \theta_2 + \theta_1\right)^2} \end{aligned} \tag{4.98}$$

Expressions for the parameters θ_3, θ_3', θ_2, θ_2' and θ_1 are given in Appendix C.3. The expression for $K_I(\omega)$ above threshold is valid provided,

$$N\Gamma v_g\,g - \frac{1}{\tau_p} \approx 0 \quad \text{and} \quad S_p \gg \frac{n_{sp}}{WL} \tag{4.99}$$

It is insightful to compare the expression for the current noise in (4.98) to the current noise in interband semiconductor diode lasers. Using the model presented in Chapter 2, one gets

for diode lasers (see Chapter 2 for details),

$$\begin{aligned} K_I\left(\omega < \omega_{3\,\mathrm{dB}}\,,\, I_{ext} < I_{th}\right) &= e\, I_{ext} \\ K_I\left(\omega < \omega_{3\,\mathrm{dB}}\,,\, I_{ext} > I_{th}\right) &= e\, I_{ext} + 2e\, I_{th}\, \frac{(\theta' - \theta)}{(1+\theta)} \\ &\quad + 2e n_{sp}\, \eta_i\, (I_{ext} - I_{th})\, \frac{\left(\theta\, \frac{\tau_{st}}{\tau_e}\right)^2}{(1+\theta)^2} \end{aligned} \tag{4.100}$$

where η_i is the current injection efficiency, θ' is a number of the order of unity, and θ is much less than unity (see Chapter 2). Comparing (4.98) and (4.100), it is seen that below threshold and also much above threshold (when $\tau_{st} \rightarrow 0$ and $I \gg I_{th}$) the current noise approaches the shot noise value in diode lasers, whereas in QCLs the current noise can be suppressed much below the shot noise value. The mechanisms responsible for the suppression of the current noise in QCLs are discussed below.

Effect of Small Differential Impedance of a Single Gain Stage

The total differential impedance of all the gain stages in a N-stage QCL is larger than the differential impedance of a single gain stage by a factor of N. This reduces the total noise power of the current fluctuations by a factor of N, and therefore $K_I(\omega)$ has an explicit $1/N$ dependence in (4.98).

Effect of Electronic Correlations

The expression for the current fluctuations $\delta I(\omega)$ given in (4.97), for frequencies less than $\omega_{3\,\mathrm{dB}}$, can also be written as,

$$\frac{N\,\delta I(\omega)}{e\,W L} = \sum_{j=1}^{N} \left[f_{in}^{j}(\omega) - \sum_{k=1}^{3} \left(\frac{1}{\tau_{in}} \frac{C_{inj}}{C_k} + \frac{1}{\tau_k} \right) \delta n_k^j(\omega) \right] \tag{4.101}$$

The expression in (4.101), which is almost identical to that in (2.22) given in Chapter 2 for semiconductor diode lasers, shows that fluctuations in the electron density in different levels of the gain stage causes fluctuations in the current. The sign of the current fluctuations is such as to restore the electron density to its average value, thus providing a negative feedback. The physical mechanisms responsible for this negative feedback are discussed below. On one hand these *electronic correlations* suppress the current noise associated with

electron injection into the gain stage by providing negative feedback, and on the other hand they are also responsible for generating current noise in response to electron density fluctuations caused by noise sources internal to the gain stage. Various physical mechanisms which contribute to these electronic correlations are described below:

1. *Coulomb Correlations*: If the electron density changes in any level of the gain stage then the electrostatic potential energy of level 3 also changes because of coulomb interactions. As a result, the energy level separation $\delta E_{inj} - \delta E_3$ also changes, and consequently the total electron current from the injector into the gain stage also changes. Usually QCLs are not biased in the negative differential regime and the value of the conductance G_{in}, given in (4.48), is positive. Therefore, the change in the current will be such as to restore the electron density in the levels of the gain stage to its steady state value. Coulomb correlations provide negative feedback to regulate electron density fluctuations. If a QCL is biased in the negative differential regime, in which the coulomb correlations provide positive feedback (negative G_{in}), the fluctuations may increase substantially and the linearized noise analysis presented in this paper may not be applicable. In the model presented here, the effect of coulomb correlations was introduced through the parameters G_{in}/C'_k in (4.47).

2. *Pauli's Exclusion and Backward Tunneling Current*: If the electron density increases in level 3 of the gain stage then this reduces the phase space available for additional electrons to tunnel into level 3 from the injector due to Pauli's exclusion, and consequently the forward tunneling current from the injector into level 3 decreases from its average value. In addition, an increase in electron density in level 3 also increases the backward tunneling current from level 3 into the injector and this also reduces the net current from the injector into level 3 (recall from (4.37) that the net current is the difference of the forward and backward tunneling currents). In model presented in this Chapter, both these effects were introduced through the parameter t_3^{-1} in (4.47). The readers are reminded that later in (4.56) and (4.57), t_3^{-1} and G_{in}/C'_3 were absorbed in the definition of τ_3^{-1}, and G_{in}/C'_2 and G_{in}/C'_3 were relabeled as τ_2^{-1} and τ_1^{-1}, respectively. Therefore, coulomb correlations, Pauli's exclusion and backward tunneling current account for the presence of the terms $\delta n_k^j(\omega)/\tau_k$ in (4.101).

3. *Injector Electron Density Response*: Here, the presence of the terms $(C_{inj}/\tau_{in}\, C_k)\, \delta n_k^j(\omega)$ in (4.101) is explained. Recall that the current fluctuations $\delta I(\omega)$ can be evaluated by looking at the current fluctuations $\delta I_{ext}(\omega)$ in the external circuit when $Z_s(\omega)$ is zero, and all external voltage sources are incrementally shorted, and the sum of the fluctuations in voltage across all the gain stages (i.e. $\sum_{j=1}^{N} \delta V^j$) is, therefore, also zero. Under these conditions, the relationship between the fluctuations in the carrier densities, expressed earlier in (4.44), becomes,

$$\sum_{j=1}^{N} \delta n_{inj}^j(\omega) = -\sum_{j=1}^{N} \sum_{k=1}^{3} \frac{C_{inj}}{C_k}\, \delta n_k^j(\omega) \tag{4.102}$$

(4.102) can be used to write (4.101) as,

$$\frac{N\, \delta I(\omega)}{e\, W L} = \sum_{j=1}^{N} \left[\frac{1}{\tau_{in}}\, \delta n_{inj}^j(\omega) - \sum_{k=1}^{3} \left(\frac{1}{\tau_k}\, \delta n_k^j(\omega) \right) + f_{in}^j(\omega) \right] \tag{4.103}$$

(4.103) shows that the current fluctuations are proportional to the total fluctuations in the electron density in the injector states of all the stages. Since $\sum_{j=1}^{N} \delta V^j(\omega) = 0$, a net increase in the electron density in different levels of all the gain stages must result in a net decrease of the electron density in all the injector states, and consequently, the current being injected into the gain stages must also decrease. This effect is captured through the terms $(C_{inj}/\tau_{in}\, C_k)\, \delta n_k^j(\omega)$ appearing in (4.101).

As a result of the electronic correlations described above, the current noise associated with electron injection into the gain stages, which is described by the noise sources $f_{in}^j(\omega)$, is suppressed. Electron density fluctuations caused by sources internal to the gain stage contribute more strongly towards the current fluctuations because of the same correlations. To see this in a more transparent fashion, it is best to write (4.101) in terms of all the noise sources. Below threshold, (4.101) is,

$$\begin{aligned} \frac{N\, \delta I(\omega)}{e\, W L} \;=\; & \frac{1}{(1 + \theta_3' + \theta_2' + \theta_1)} \sum_{j=1}^{N} \Big[f_{in}^j(\omega) + \theta_1 f_{out}^j(\omega) + (\theta_3' + \theta_2')\, f_{31}^j(\omega) \\ & + \theta_2' \left(1 + \frac{\tau_{32}}{\tau_{31}} \right) f_{21}^j(\omega) + \left(\theta_3' - \theta_2' \frac{\tau_{32}}{\tau_{31}} \right) f_{32}^j(\omega) \Big] \end{aligned} \tag{4.104}$$

Above threshold $\delta I(\omega)$ is,

$$\frac{N\,\delta I(\omega)}{e\,W\,L} = \frac{1}{(1+\theta_3+\theta_2+\theta_1)} \sum_{j=1}^{N} \Big[f_{in}^{j}(\omega) + \theta_1 f_{out}^{j}(\omega) + (\theta_3+\theta_2)\left(f_{31}^{j}(\omega) + f_{21}^{j}(\omega)\right) + \left(\theta_3 \frac{\tau_{st}}{\tau_{21}} - \theta_2 \frac{\tau_{st}}{\tau_{31}}\right)\left(f_{RS}^{j}(\omega) - \frac{F_L(\omega)}{N}\right)\Big] \quad (4.105)$$

Note that the strength of the electronic correlations depends on the values of the parameters θ_3, θ_3', θ_2, θ_2' and θ_1 (Appendix C.3). From (4.104) and (4.105), it is clear that larger values of these parameters will result in stronger electronic correlations, larger suppression of the current noise associated with electron injection into the gain stage, and also larger contribution to the current noise from the noise sources internal to the gain stage. The reader is encouraged to compare (4.104) and (4.105) with the corresponding expressions for semiconductor diode lasers given in (2.52) and (2.53) in Chapter 2.

A quantitative measure of the role played by the electronic correlations in suppressing the current noise can be obtained by multiplying the Fano Factor of the current noise by N. It has been mentioned earlier that a factor of $1/N$ appears in (4.98) because the total differential impedance of all the gain stages is larger than the differential impedance of a single gain stage by a factor of N. Therefore, multiplying the current noise Fano Factor by N removes this explicit $1/N$ dependence in the current noise, and the resulting expression can only be less than unity because of electronic correlations. Fig. 4-16 shows the current noise Fano Factor from Fig. 4-15 multiplied by N. Below threshold, and also much above threshold, N times the current noise Fano Factor is less than 0.5. This implies that electronic correlations are responsible for suppressing the current noise by a factor greater than 2. Using (4.98), expression for the current noise Fano Factor F_I can be written as,

$$N \times F_I\,(\omega < \omega_{3\,\mathrm{dB}}) = \begin{cases} \dfrac{\left(\chi_{in}^2 + (\theta_3')^2 + (\theta_2')^2\left(1 + 2\,\frac{\tau_{32}}{\tau_{31}}\right) + (\theta_1\,\chi_{out})^2\right)}{(1+\theta_3'+\theta_2'+\theta_1)^2} & (I_{ext} < I_{th}) \\ \dfrac{\left(\chi_{in}^2 + (\theta_3+\theta_2)^2 + (\theta_1\,\chi_{out})^2\right)}{(1+\theta_3+\theta_2+\theta_1)^2} & (I_{ext} \gg I_{th}) \end{cases} \quad (4.106)$$

For semiconductor diode lasers, using (4.100), one gets,

$$F_I\,(\omega < \omega_{3\,\mathrm{dB}}) = 1 \qquad (I_{ext} < I_{th} \quad \text{and} \quad I_{ext} \gg I_{th}) \quad (4.107)$$

At frequencies much higher than the inverse of the smallest time constant of the QCL the current noise $\delta I(\omega)$ is just the capacitive response to the various electronic transitions which occur inside the gain stages. In the limit $\omega \rightarrow \infty$, $K_I(\omega)$ is given by the expression,

$$\begin{aligned} K_I\left(\omega \rightarrow \infty\,,\, I_{ext} < I_{th}\right) &= e\frac{I_{ext}}{N}\left[\left(1-\frac{C_{inj}}{C_3}\right)^2 \chi_{in}^2 + \left(\frac{C_{inj}}{C_1}\right)^2 \chi_{out}^2\right] \\ &+ \frac{e^2 WL}{N}\left[R_{31}\left(\frac{C_{inj}}{C_3}-\frac{C_{inj}}{C_1}\right)^2 + R_{21}\left(\frac{C_{inj}}{C_2}-\frac{C_{inj}}{C_1}\right)^2\right. \\ &\left. + R_{32}\left(\frac{C_{inj}}{C_3}-\frac{C_{inj}}{C_2}\right)^2\right] \end{aligned} \tag{4.108}$$

Above threshold an extra term,

$$e(2n_{sp}-1)n_r\frac{(I_{ext}-I_{th})}{N}\left(\frac{C_{inj}}{C_3}-\frac{C_{inj}}{C_2}\right)^2 \tag{4.109}$$

is added to the above equation to account for the stimulated transitions. Semiconductor diode lasers on the other hand are charge neutral. Therefore, in the limit $\omega \rightarrow \infty$, the current noise in diode lasers is just the noise associated with carrier injection into the active region (see Chapter 2),

$$K_I\left(\omega \rightarrow \infty\right) = \begin{cases} e\,I_{ext}\,\left(1+2\,\theta'\right) & \left(I_{ext} < I_{th}\right) \\ e\,I_{ext}\,\left(1+2\,\theta\right) + 2e\,I_{th}\,\left(\theta'-\theta\right) & \left(I_{ext} > I_{th}\right) \end{cases} \tag{4.110}$$

4.7.3 Scaling of the Current Noise with the Number of Cascade Stages

In QCLs, the spectral density $K_I(\omega)$ of the current noise obeys a simple scaling relation with respect to the number of cascaded gain stages N, and this relation can be determined from (4.97),

$$N^2 K_I(\omega, I_{ext}/I_{th}, N) = N'^2 K_I(\omega, I_{ext}/I_{th}, N') \tag{4.111}$$

According to the above Equation, the spectral density of the current noise, for a fixed value of I_{ext}/I_{th} (i.e. for a fixed value of the output power), scales as $1/N^2$. This scaling relation for $K_I(\omega)$ holds provided the transition rates $R_{jk}(n_j, n_k)$ and the material gain $g(n_3, n_2)$ are linear functions of the electron densities and the total mode confinement factor also scales linearly with the number of cascade stages N.

4.7.4 Spectral density of the Current Noise in the External Circuit

Equation (4.95) shows that the quantity which affects the photon noise is not the current noise $\delta I(\omega)$, but the current noise in the external circuit $\delta I_{ext}(\omega)$. When $Z_s(\omega) \neq 0\ \Omega$, which is usually the case, then $K_{I_{ext}}(\omega)$ is not the same as $K_I(\omega)$. Expression for $K_{I_{ext}}(\omega)$ can be obtained from (4.96),

$$\begin{aligned} K_{I_{ext}}(\omega) &= \frac{K_{V_s}(\omega)}{|Z(\omega)+Z_s(\omega)|^2} + \left|\frac{Z(\omega)}{Z(\omega)+Z_s(\omega)}\right|^2 K_I(\omega) \\ &= \frac{2K_BT\,\mathrm{Real}\{Z_s(\omega)\}}{|Z(\omega)+Z_s(\omega)|^2} + \left|\frac{Z(\omega)}{Z(\omega)+Z_s(\omega)}\right|^2 K_I(\omega) \end{aligned} \tag{4.112}$$

(4.112) shows that in the presence of a large impedance $Z_s(\omega)$, the current fluctuations in the external circuit are suppressed. The total differential impedance of a QCL is usually less than 1 Ω. Therefore, for even a moderately large impedance $Z_s(\omega)$ the current noise in the external circuit can be dominated by the thermal noise from the impedance $Z_s(\omega)$. Experimental measurement of the current noise would therefore require a relatively sensitive measurement scheme. High impedance suppression of the current noise in the external circuit can influence the photon noise, as shown in the following section.

4.8 Photon Noise: Results and Discussion

4.8.1 Spectral Density and Fano Factor of the Photon Noise

The spectral density $K_P(\omega)$ of the photon noise can be calculated from (4.95). The Fano Factor for the low frequency fluctuations in the laser output power is plotted as a function of the bias current in Fig. 4-17. The numerical results presented here are for the QCL structure described in Ref. [16] (see Table 4.1). The Relative Intensity Noise (RIN) is plotted in Fig. 4-18. In each Figure, the respective shot noise limit is also shown. It is assumed that the light coming out from both the facets of the laser is collected before the noise is evaluated. This is equivalent to assuming that the output coupling efficiency η_o, defined earlier in (4.7), is,

$$\eta_o = \frac{\alpha_m}{(\alpha_m + \alpha_i)} \tag{4.113}$$

In practice this can be achieved by HR/AR coating the laser facets so that that most of the light comes out from only one facet of the laser. When the value of the external impedance

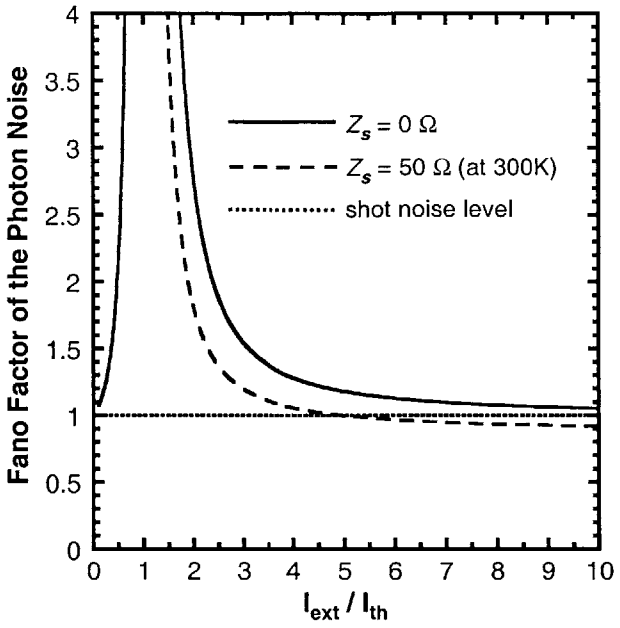

Figure 4-17: Fano Factor for the (low frequency) photon noise is plotted as a function of the bias current. For values of the QCL parameters see Table 4.1.

Z_s is 0 Ω, the photon noise remains above the shot noise limit. Even at high bias levels, no amplitude squeezing is observed despite the fact that the current noise is suppressed much below the shot noise value as shown earlier in Fig. 4-15. When $Z_s = 50\ \Omega$, and the current noise in the circuit is further suppressed, a very small amount of squeezing is observed at high bias levels (less than 0.4 dB at $I_{ext} = 10\, I_{TH}$).

Fig. 4-20 shows the RIN as a function of the frequency for different values of the bias current assuming $Z_s(\omega) = 0$. The RIN also rolls over at the frequency $\omega_{3\,\mathrm{dB}}$. Fig. 4-21 shows that the Fano Factor of the photon noise as a function of the frequency. As in all other lasers, at frequencies much higher than the inverse of the photon lifetime inside the cavity, the RIN is dominated by the noise from photon partition at the output facet. Therefore,

$$K_P\,(\omega \gg 1/\tau_p) = \hbar\Omega_o\, P_{out} \tag{4.114}$$

In this paper careful attention has been given to modeling the current fluctuations in the external circuit. The question arises if such detailed modeling of the current fluctuations is necessary for calculating the photon noise. In (4.95), the current noise $\delta I_{ext}(\omega)$ is included

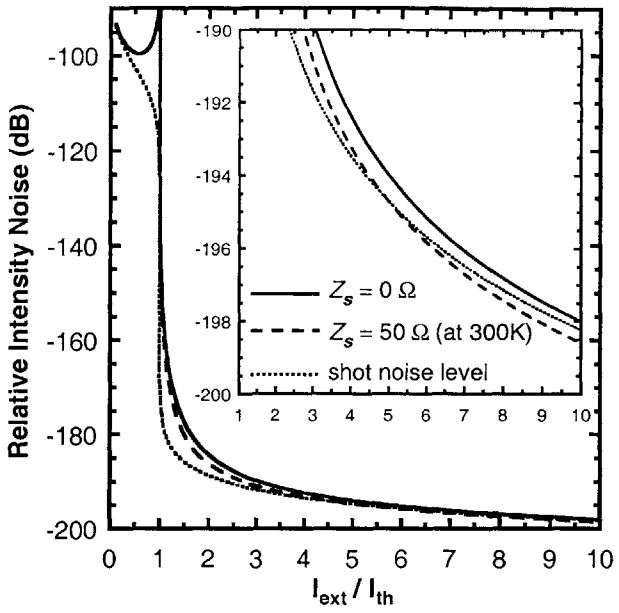

Figure 4-18: Low frequency Relative Intensity Noise (RIN) is plotted as a function of the bias current. Very small amount of squeezing (less than 0.4 dB) is exhibited at high bias levels even when the circuit current fluctuations are suppressed with a 50 Ω impedance. For values of the QCL parameters see Table 4.1.

in the first term on the right hand side. It should be noted here that the first and the second term on the right hand side in (4.95) are correlated, and the spectral density of the photon noise cannot be obtained by a simple addition of the spectral densities of these two terms. In Fig. 4-22, the ratio of the low frequency spectral density of the photon noise obtained by ignoring the term containing $\delta I_{ext}(\omega)$ in (4.95) to the actual spectral density of the photon noise is plotted as a function of the bias current for different values of the impedance Z_s. When the laser is biased a little above threshold, the fluctuations in the current are large, and the error incurred by ignoring the term containing $\delta I_{ext}(\omega)$ in (4.95) is also large. Also, when Z_s is much larger than the total differential impedance of the QCL, the current fluctuations in the circuit are suppressed, and the term containing $\delta I_{ext}(\omega)$ can be ignored in (4.95).

Above threshold and for large $Z_s(\omega)$, analytical expression can be obtained for the spectral density of the low frequency photon noise using the expressions for the elements of

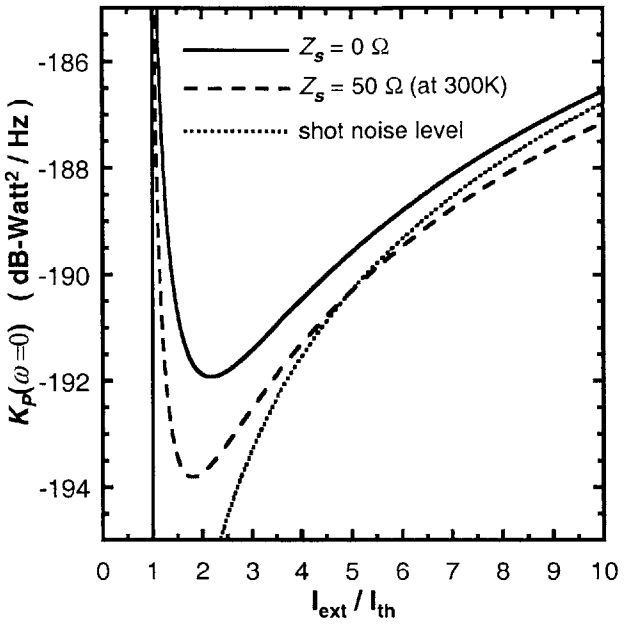

Figure 4-19: Low frequency Spectral density $K_P(\omega = 0)$ of the photon noise is plotted as a function of the bias current. When Z_s is large (50 Ω) small amount of squeezing is seen at high bias levels. For values of the QCL parameters see Table 4.1.

the matrix $\mathbf{D}^{-1}$ in Appendix C.5,

$$K_P\left(\omega < \omega_{3\,\mathrm{dB}}\,,\, I_{ext} > I_{th}\right) = \hbar\Omega_o\, P_{out}\left[1 - \eta_o + 2\eta_o\, n_{sp}\left(\frac{\tau_{31}}{\tau_{21}+\tau_{31}}\right)^2\left(\frac{1}{\tau_{31}}+\frac{1}{\tau_{32}}\right)^2\tau_{st}^2\right] + (\eta_o\,\hbar\,\Omega_o)^2\, N\, W\, L\left[R_{32} + \eta_r^2\, R_{31} + (1-\eta_r)^2\, R_{21}\right] \quad (4.115)$$

$$= \hbar\Omega_o\, P_{out}\left[1 - \eta_o + 2\eta_o\, n_{sp}\left(\frac{\tau_{31}}{\tau_{21}+\tau_{31}}\right)^2\left(\frac{1}{\tau_{31}}+\frac{1}{\tau_{32}}\right)^2\tau_{st}^2\right] + (\eta_o\,\hbar\,\Omega_o)^2\, N\left[\alpha\,\frac{I_{ext}}{e} + \beta\,\frac{I_{th}}{e}\right] \quad (4.116)$$

η_r in the above Equation is the radiative efficiency defined in (4.31). The constants α and β are,

$$\alpha = \eta_r\,(1-\eta_r) + 2\,(1-\eta_r)\,\frac{\tau_{31}}{\tau_{21}+\tau_{31}}\left(\frac{\tau_{21}}{\tau_{32}}\right) \quad (4.117)$$

$$\beta = \eta_r - 2\eta_r\,(1-\eta_r)\,\frac{\tau_{32}}{\tau_{31}+\tau_{32}} \quad (4.118)$$

The above expression for $K_P(\omega)$ is valid for frequencies smaller than $\omega_{3\,\mathrm{dB}}$, and when the laser is biased above threshold when the conditions given by (4.99) are satisfied. The

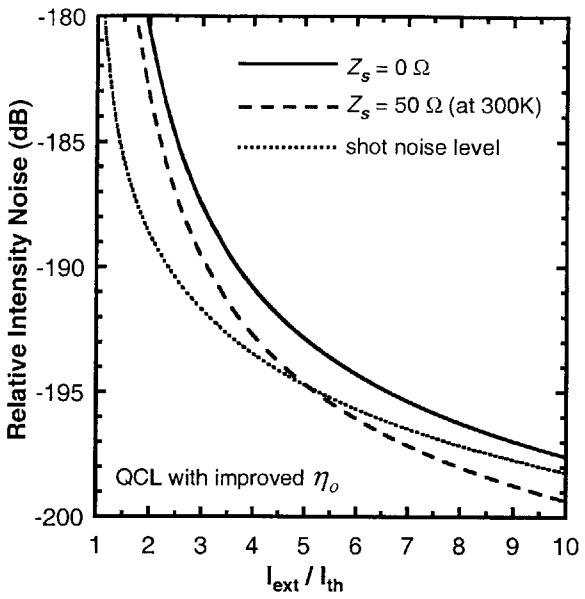

Figure 4-20: Relative Intensity Noise (RIN) is plotted as a function of the frequency for different bias currents ($Z_s = 0\ \Omega$). At high frequencies the RIN reaches the shot noise value. For values of the QCL parameters see Table 4.1.

expression given in (4.116) is almost identical to the expression for $K_P(\omega)$ for semiconductor diode lasers (when the later are also biased with a high impedance current source). Using the model presented in Chapter 2 one gets for diode lasers (see Chapter2 2 for details),

$$K_P\left(\omega < \omega_{3\,\mathrm{dB}}\,,\, I_{ext} > I_{th}\right) = \hbar\Omega_o\, P_{out}\left[1 - \eta_o + 2\eta_o\, n_{sp}\left(\frac{1}{\tau_w} + \frac{1-\eta_i}{\tau_e}\right)^2 \tau_{st}^2\right] + (\eta_o\,\hbar\Omega_o)^2\left[\eta_i(1-\eta_i)\frac{I_{ext}}{e} + \eta_i\frac{I_{th}}{e}\right] \quad (4.119)$$

η_i in the above equation is the current injection efficiency into the quantum wells [1].

The contributions from the non-radiative electronic transitions to the photon noise in QCLs and diode lasers are proportional to the terms inside the second square bracket in (4.115) and (4.119), respectively. The contributions to the photon noise from the photon loss from the laser cavity and from the radiative transitions in QCLs and diode lasers are proportional to the terms inside the first square bracket in (4.115) and (4.119), respectively. Two important differences emerge when (4.115) is compared with (4.119), and both these differences make it harder to achieve photon number squeezing in QCLs compared to diode

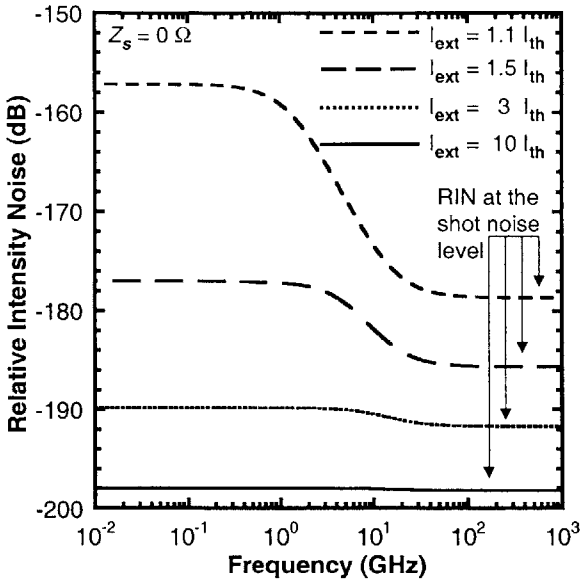

Figure 4-21: Fano Factor of the photon noise is plotted as a function of the frequency ($Z_s = 0\ \Omega$). The photon noise at frequencies much higher than the inverse of the photon lifetime in the cavity is dominated by the photon partition noise at the output facet. For values of the QCL parameters see Table 4.1.

lasers. These differences are discussed in detail below.

Contribution of Non-Radiative Transitions to Photon Noise

The contribution to the photon noise from the non-radiative recombination in diode lasers is constant above threshold and it has been expressed in terms of the threshold current in (4.119). As shown earlier, in QCLs above threshold the electron densities in different energy levels of a gain stage do not remain fixed at their threshold values. The electron densities keep increasing when the bias current is increased beyond threshold. As a result, the contribution of non-radiative electronic transitions to the photon noise also keeps increasing with the bias current. Since only a fraction η_r of the electrons injected in level 3 of the gain stage end up producing photons, a multiplicative factor η_r^2 appears with the transition rate R_{31} in (4.115). A fraction $1-\eta_r$ of the vacancies left by removing electrons from level 2 get filled by radiative transitions from level 3 to level 2, and therefore a factor $(1-\eta_r)^2$ appears with R_{21}. All the electrons taken out of level 2 and injected into level 3 will end up producing photons (since $1-\eta_r+\eta_r=1$) and, therefore, R_{32} has no multiplicative factor

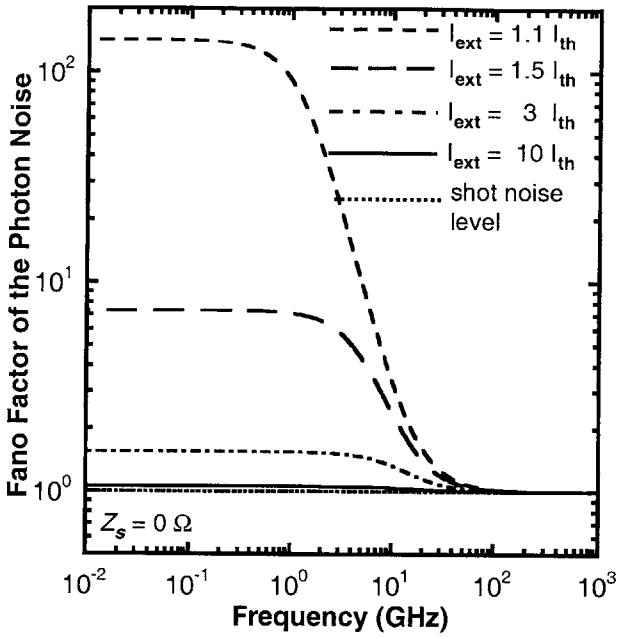

Figure 4-22: Ratio of the low frequency photon noise spectral density obtained by ignoring the term containing the current fluctuations in (4.95) to the actual spectral density is plotted as a function of the bias current for different values of the impedance Z_s. The current fluctuations are suppressed when Z_s is large and the error incurred in calculating the spectral density is, therefore, small. For values of the QCL parameters see Table 4.1.

in (4.115).

The noise associated with the electron transitions from level 1 into the injector of the next stage does not directly contribute to photon noise at low frequencies. These transitions contribute to the current noise in the external circuit, which can in turn contribute to the photon noise. But in (4.115), it is assumed that $Z_s(\omega)$ is large and the current fluctuations are suppressed. Similarly, the noise associated with the electron transitions from the injector into level 3 of the gain stage is also suppressed at low frequencies when $Z_s(\omega)$ is large.

In diode lasers, since the current injection efficiency η_i is less than unity, the partition noise associated with carrier leakage from the SCH region contributes a term to the photon noise which increases linearly with the bias current even beyond the laser threshold, as shown in (4.119). Since η_i is usually close to unity in well designed diode lasers [1], the contribution of this term to the photon noise is small.

Contributions of Photon Loss and Radiative Transitions to Photon Noise

The most important contribution to the photon noise from the photon loss from the laser cavity and from the radiative transitions is given by the term proportional to τ_{st}^2 in (4.115) and (4.119). Just above threshold, the photon density is small, and τ_{st}, which is inversely proportional to the photon density, is large. Consequently, just above threshold the term proportional to τ_{st}^2 dominates all the other terms in (4.115) and (4.119). As the bias current is increased, and the photon density becomes large, τ_{st} becomes small. It is evident from (4.115) and (4.119) that photon number squeezing can only be achieved if the ratio $(\tau_{st}/\tau_{nr})^2$, where τ_{nr} is the total non-radiative lifetime for the carrier density interacting with the photons, becomes smaller than unity. The appearance of this ratio is related to the carrier density and the photon density dynamics in response to sudden radiative transition events or photon loss events which temporarily move the carrier density and the photon density away from their steady state values. In diode lasers τ_{nr}, given by,

$$\frac{1}{\tau_{nr}} = \frac{1}{\tau_w} + \frac{1-\eta_i}{\tau_e} \qquad \text{Diode Lasers} \tag{4.120}$$

is around 0.5 ns to 1 ns (see [1]). In QCLs, τ_{nr} is the non-radiative lifetime of the difference carrier density $(n_3 - n_2)$ that interacts with the photons, and is given by the expression,

$$\frac{1}{\tau_{nr}} = 2\frac{\tau_{31}}{\tau_{21}+\tau_{31}}\left(\frac{1}{\tau_{31}} + \frac{1}{\tau_{32}}\right) \qquad \text{QCLs} \tag{4.121}$$

The factor of 2 in the above equation does not show up in (4.115) because the differential stimulated emission lifetime of the difference carrier density is $\tau_{st}/2$, and the factor of 2 cancels out. In deriving the above Equation, the sum carrier density $(n_3 + n_2)$, which does not interact with the photons, was adiabatically eliminated from the rate equations. In QCLs, the value of $(2\tau_{nr})$ is usually around a few picoseconds. In the QCL structure described in Ref. [16], $(2\tau_{nr})$ equals 1.5 ps (see Table 4.1). Therefore, for photon number squeezing to be possible the value of τ_{st} in QCLs must be a few hundred times less than the value of τ_{st} is diode lasers (assuming both have equal values for η_o and n_{sp}). For the same photon density and the mode group velocity, the ratio of τ_{st} in QCLs and diode lasers depends on their respective differential gains (see (4.80) and (2.12)). For the QCL described

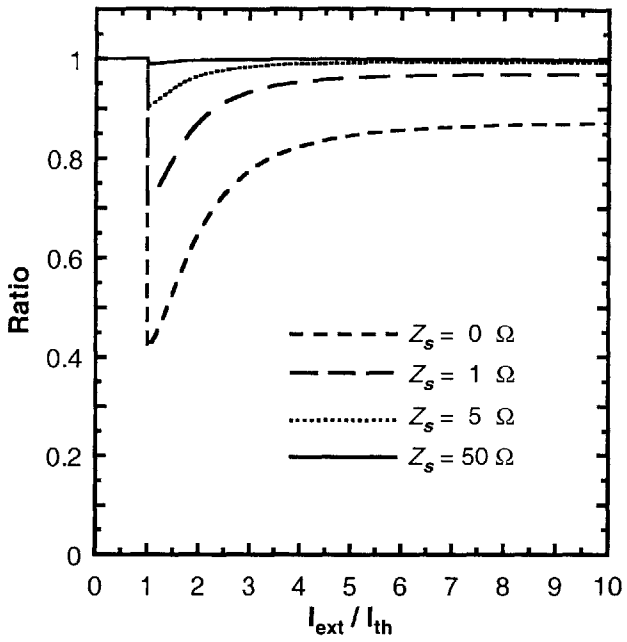

Figure 4-23: Relative Intensity Noise (RIN) for the QCL with improved η_o (= 0.84) is shown. Only 1.2 dB of squeezing is seen at high bias levels and when $Z_s = 50\ \Omega$.

in Ref. [16],

$$\frac{1/\tau_{st}\,(\text{QCL})}{1/\tau_{st}\,(\text{Diode Lasers})} = \frac{a\ L_p}{dg/dN_w} \sim 15 \tag{4.122}$$

In the above Equation, the differential gain dg/dN_w of diode lasers is assumed to be around 1.0-1.5 $\times 10^{-15}$ cm^2 [1]. Note that the ratio in (4.122) is independent of any geometrical factors and depends only on the properties of the material gain of the lasers. The expression above implies that the photon density in the active region of QCLs must be at least an order of magnitude larger than the photon density in diode lasers to make squeezing possible. This does not seem to be a formidable obstacle to achieving photon number squeezing in QCLs since QCLs with output powers exceeding 1.0 Watt have been demonstrated [16]. However, in QCLs, in contrast to diode lasers, it will be difficult to achieve squeezing with only a few tens of milli-Watts of output power. In QCLs, since both τ_{nr} and τ_{st} depend on the spatial overlap of the wavefunctions of the upper and lower lasing states, it may not be possible to change the value of the ratio (τ_{st}/τ_{nr}) by engineering the wavefunction overlap.

The output coupling efficiency η_o of QCLs that have been reported in the literature is much smaller than those of typical diode lasers. But even if that were not the case,

squeezing is expected to be less in QCLs than in diode lasers for the reasons discussed above. The QCL, whose characteristics are shown in Fig. 4-17 and Fig. 4-18, has a 3 mm long cavity, a waveguide loss of 11 cm^{-1}, and an output coupling efficiency of only 28%. Consider a QCL with a 500 μm long cavity, a waveguide loss of 5 cm^{-1}, and an output coupling efficiency of 84%, which is comparable to that of good diode lasers [1]. The values of all the other parameters of this QCL are identical to those given in Table 4.1. Fig. 4-23 shows the relative intensity noise when this QCL is driven with a 50 Ω resistor in series. Only about 1.2 dB of squeezing is observed even at very large bias levels ($I_{ext} \approx 10\, I_{TH}$).

The Fano factors for the photon noise much above threshold (when $\tau_{st} \rightarrow 0$ and $I_{ext} \gg I_{th}$) in QCLs and diode lasers can be calculated from (4.116) and (4.119),

$$F_P(\omega)\Big|_{(\omega < \omega_{3\,\mathrm{dB}}\ ,\ I_{ext} \gg I_{th})} = \begin{cases} 1 - \eta_o \eta_r + 2\eta_o \dfrac{(1-\eta_r)}{\eta_r} \dfrac{\tau_{31}}{\tau_{21}+\tau_{31}} \left(\dfrac{\tau_{21}}{\tau_{32}}\right) & \text{QCLs} \\ 1 - \eta_o \eta_i & \text{Diode Lasers} \end{cases} \tag{4.123}$$

(4.123) gives the maximum photon number squeezing which is asymptotically achievable in QCLs and in diode lasers at very large output power levels. In real devices, the squeezing will be always less than that predicted in (4.123). In diode lasers, η_i and η_o can be larger than 0.9 and 0.85, respectively [1], and the photon noise in diode lasers can be maximally suppressed more than 6 dB below the shot noise value. For the QCL whose parameters are listed in Table 4.1, η_r and η_o have the values 0.66 and 0.28, respectively, and, consequently, the maximum possible squeezing is only 0.6 dB. Even if the output coupling efficiency η_o of this QCL is increased to 0.85, the maximum squeezing predicted by (4.123) is only 2.0 dB.

The maximum squeezing achievable in QCLs can be increased by decreasing the lifetime τ_{21} of electrons in level 2 of the gain stage, and increasing the lifetimes τ_{31} and τ_{32} associated with the non-radiative electronic transitions out of level 3. This will reduce the rate of increase of the electron density above threshold in levels 3 and 2 with the bias current, increase the radiative efficiency η_r, and reduce the contribution of the non-radiative electronic transitions to the photon noise.

4.8.2 Scaling of the Photon Noise with the Number of Cascade Stages

The spectral density of the photon noise in QCLs is a function of the output power (or I_{ext}/I_{th}), the circuit impedance $Z_s(\omega)$, and the number of cascaded stages N. In Chapter 3,

it was shown that the effect of the positive correlations in photon emissions in different cascade sections on the photon noise in semiconductor interband cascade lasers can be expressed simply in terms of a scaled circuit impedance. A similar relation holds for QCLs and can easily be derived from (4.95),

$$K_P(\omega, I_{ext}/I_{th}, Z_s(\omega), N) = K_P(\omega, I_{ext}/I_{th}, Z_s(\omega)\, N'/N, N') \tag{4.124}$$

The scaling relation for $K_p(\omega)$ holds provided that the transition rates $R(n_j, n_q)$ and the material gain $g(n_3, n_2)$ are linear functions of electron densities and the total mode confinement factor also scales linearly with the number of cascaded stages N. In Ref. [62], it is shown that the total mode confinement factor scales with the number of cascaded stages according to the expression $\sim erf(0.019N)$, which is almost linear in N for $N < 40$.

4.9 Conclusion

A model for noise and fluctuations in intersubband quantum cascade lasers has been presented. The current noise exhibited by QCLs is much below the shot noise value. Suppression of the current noise in QCLs is largely due to the small differential resistance of individual gain stages compared to the total differential resistance of all the cascaded gain stages. In addition, electronic correlations also suppress the current noise. However, unlike semiconductor diode lasers, current noise suppression does not lead to significant photon number squeezing in QCLs. In QCLs the contribution to the photon noise coming from the non-radiative electronic transitions keeps increasing with bias beyond the laser threshold, and this reduces the amount of photon number squeezing achievable in QCLs compared to semiconductor diode lasers. It has also been shown that photon noise in QCLs is squeezed at photon densities much larger than those in diode lasers.

The current modulation response of QCLs has also been investigated. It has been found that the direct current modulation response of many QCLs that have been reported in the literature is over-damped since, in contrast to diode lasers, the photon lifetime inside the optical cavity in QCLs is usually the longest time constant. The modulation bandwidth is also limited by the inverse photon lifetime. At present, in the wavelength region of interest only quantum well infrared photodetectors (QWIPs) have bandwidths wide enough that they could be used to study the modulation response of QCLs. However, the current noise

provides an alternate way of studying the high speed dynamics of QCLs, and as shown in this paper, the modulation bandwidth of QCLs can be found by looking at the spectral density of the current noise in the external circuit.

Although in this paper the emphasis has been on a specific multiple quantum well QCL structure, the theoretical methods and techniques presented in this paper can be used to study a variety of QCLs that have been reported in the literature.

Chapter 5

Quantum Noise in Actively Mode-Locked Semiconductor Lasers

5.1 Introduction

Mode-locked lasers have important applications in electro-optic sampling, optical analog-to-digital conversion, optical communication systems, and ultra-fast optical measurements [69]. Low noise performance of mode-locked lasers, especially reduced amplitude noise and timing jitter, is critical to most of these applications. Semiconductor mode-locked lasers, by virtue of their small size and high repetition rates, are potential candidates for replacing bulkier solid state and fiber mode-locked lasers. Semiconductor mode-locked lasers have been used to produce sub-picosecond optical pulses with repetition rates exceeding hundreds of gigahertz [30, 31]. Semiconductor mode-locked lasers must be able to produce short high power pulses with reduced noise and timing jitter in order to compete with other mode-locked lasers. Fig. 1-9 of Chapter 1 shows the requirements on the root mean square (RMS) timing jitter of optical pulses for optical A/D conversion [2, 32]. Less than 100 femtosecond RMS jitter is required for an A/D converter with 8 bits of resolution at a sampling frequency of 10 GHz, and less than 30 femtosecond of RMS jitter is required if the desired resolution is 10 bits at 10 GHz.

Very few theoretical models have been reported in the literature that describe the noise

in mode-locked semiconductor lasers. Models for the noise in mode-locked solid state and fiber lasers have been developed by Haus et. al. [33, 34]. These models use the soliton perturbation theory [70], and assume that the group velocity dispersion and the Kerr non-linearity in the laser cavity balance each other so that the steady state optical pulse is a soliton. Optical pulses in semiconductor mode-locked lasers are not solitons since the non-resonant Kerr non-linearity in semiconductors is negligible compared to the resonant non-linearities, such as dynamic gain saturation and dynamic self-phase modulation [36]. Also, in semiconductor mode-locked lasers the group velocity dispersion in the laser cavity is generally not balanced by either the self-phase modulation or by active phase modulation, and, consequently, the steady state optical pulses are almost always chirped [30, 31]. Theoretical models presented in the literature for the noise in semiconductor mode-locked lasers have either used the soliton perturbation approach (which assumes unchirped pulses) [71], or have completely ignored phase modulation and group velocity dispersion [35]. Soliton perturbation theory, as presented in Refs. [33, 34, 71], treats active phase modulation only perturbatively and a self-consistent solution is not known. Therefore, to the best of author's knowledge, a theoretical model that can describe the noise in chirped optical pulses in mode-locked lasers has never been presented in the literature. Accounting for active phase modulation in the theoretical model is important since active gain (or amplitude) modulated mode-locked semiconductor lasers are also strongly phase modulated as a result of the carrier density dependent refractive index in semiconductors [1].

In this Chapter, a theoretical model for the noise in semiconductor mode-locked lasers is presented that for the first time accounts for group velocity dispersion and phase modulation without relying on the soliton perturbation theory. It is shown here that a non-zero pulse chirp significantly affects the noise in mode-locked semiconductor lasers. The model presented here is linear, and non-linearities, such as dynamic gain saturation and dynamic self-phase modulation, are ignored. In semiconductor mode-locked lasers, these non-linearities become important only at large pulse energies, and at low pulse energies a linear theory is adequate [36]. The model presented in this Chapter is fairly general and can be used to model the noise in a wide variety of mode-locked lasers (not necessarily semiconductor mode-locked lasers) with amplitude modulation, phase modulation, and/or group velocity dispersion.

5.2 Effect of Phase Modulation and/or Group Velocity Dispersion on the Pulse Noise

The noise in an optical pulse in a mode-locked laser can be determined by a perturbative expansion in terms of the eigenmodes of the linear operator that describes the slow time evolution of the pulse fluctuations [33, 34, 72]. In most mode-locked semiconductor lasers, this operator is not Hermitian (i.e. not self-adjoint) or even normal (i.e. does not commute with its adjoint). This operator can be non-Hermitian in the presence of a number of different factors, such as group velocity dispersion, active phase modulation, and/or dynamic self-phase modulation. The eigenmodes of a non-normal operator are not mutually orthogonal [73]. It is well known that the non-orthogonality of the eigenmodes significantly affects the noise in non-Hermitian and non-normal optical systems and, in most cases, generates excess noise [74, 75, 76, 77]. In this Chapter, it is shown that the non-orthogonality of the eigenmodes result in excess noise in the pulse photon number, phase, frequency, and timing fluctuations. In this Chapter, quantum mechanical operators are constructed for the pulse photon number, phase, timing, and frequency noise, and it is shown that as a result of the non-orthogonality of the eigenmodes, these noise operators have significant contributions from the noise in all the higher order eigenmodes. In the presence of active phase modulation and/or dispersion, the magnitude of the frequency chirp of the steady state pulse is a good measure of the degree of non-normality of the operator that governs the slow time evolution of the pulse fluctuations, or the degree of non-orthogonality of the eigenmodes of this operator. The excess noise in the pulse can be related to the chirp in the steady state pulse. It is shown that when the magnitude of the pulse chirp exceeds a critical value (≈ 0.577), the perturbative expansion for the pulse noise diverges exponentially as more eigenmodes are included in the expansion. A modified perturbative expansion is developed that converges. The origin of the excess noise in linear systems with non-orthogonal eigenmodes is explained in Appendix D.1, and readers are strongly encouraged to browse through this Appendix before proceeding.

5.3 Theoretical Model

5.3.1 Master Equation for Actively Mode-Locked Lasers

The model presented here uses the time domain perturbation theory for optical pulses developed in Refs. [33, 34, 72]. The quantum field operator for the optical pulse inside the laser cavity is assumed to be $\widehat{\phi}(t,T)\exp(-j\,\Omega_o t)$, where $\widehat{\phi}(t,T)$ describes the slowly varying envelope of the optical pulse and Ω_o is the pulse center frequency. The additional time variable T describes the evolution of the pulse over time scales larger than the cavity round trip time T_R. The operator $\widehat{\phi}(t,T)$ is normalized such that $\langle\widehat{\phi}^{\dagger}(t,T)\,\widehat{\phi}(t,T)\rangle$ equals the photon number flux (units: number/sec). The angled brackets $\langle\ldots\rangle$ stand for averaging with respect to the quantum mechanical density operator which describes the state of the optical pulse at time T. $\widehat{\phi}(t,T)$ obeys the quantum mechanical commutation relation [34],

$$\left[\widehat{\phi}(t,T),\widehat{\phi}^{\dagger}(t',T)\right]=\delta(t-t') \tag{5.1}$$

The master equation that describes the slow time evolution of the optical pulse inside the laser cavity is [33, 34, 72],

$$\begin{aligned}\frac{d\,\widehat{\phi}(t,T)}{dT} &= j\frac{\nu}{T_R}\,\widehat{\phi}(t,T)+\frac{1}{2}\left(G-\frac{1}{\tau_p}\right)\widehat{\phi}(t,T)+O(t)\,\widehat{\phi}(t,T)\\ &\quad+\widehat{F}_{SP}(t,T)+\widehat{F}_V(t,T)\end{aligned} \tag{5.2}$$

where the operator $O(t)$ is,

$$O(t)=(B-jD)\,\frac{1}{2}\frac{\partial^2}{\partial\,t^2}+\frac{1}{2}(A_M+jP_M)\,\left[\cos\left(\omega_R\,t\right)-1\right] \tag{5.3}$$

Here, G is the cavity gain (units: 1/sec). τ_p is the photon lifetime in the laser cavity. B describes the effect of the finite gain bandwidth. D is the dispersion (units: sec). A_M and P_M are the modulation depths for amplitude and phase modulation, respectively. ω_R is the frequency of the active modulation and it is assumed to be equal to $2\pi/T_R$. ν is a phase shift accumulated by the pulse in one round trip. G, B and D are given by the expressions,

$$G=\frac{1}{T_R}\oint dz\,g(z) \tag{5.4}$$

$$B = -\frac{1}{2T_R} \oint dz \, \frac{\partial^2 g(z)}{\partial \Omega^2} \tag{5.5}$$

$$D = \frac{1}{T_R} \oint dz \, \beta_2(z) \tag{5.6}$$

where $g(z)$ and β_2 are the position dependent power gain (units: 1/cm) and dispersion (units: $\sec^2$/cm) in the cavity, and the integrals $\oint dz$ are over one complete roundtrip in the cavity. In semiconductor mode-locked lasers the phase modulation depth P_M is related to the amplitude modulation depth A_M by the semiconductor α-parameter,

$$P_M = -\alpha \, A_M \tag{5.7}$$

The α-parameter relates the changes in the real part of the gain with carrier density to the changes in the imaginary part of the gain (or the refractive index), and has values typically between 3.0 and 5.0. $\widehat{F}_{SP}(t,T)$ and $\widehat{F}_V(t,T)$ in (5.2) are Langevin noise operators which represent the noise in spontaneous emission and photon loss (or vacuum fluctuations), respectively, and have the following correlation functions,

$$\langle \widehat{F}^\dagger_{SP}(t,T) \, \widehat{F}_{SP}(t',T') \rangle = n_{sp} \left[G + O(t) + O^\dagger(t) \right] \, \delta(t-t') \, \delta(T-T') \tag{5.8}$$

$$\langle \widehat{F}_{SP}(t,T) \, \widehat{F}^\dagger_{SP}(t',T') \rangle = (n_{sp} - 1) \left[G + O(t) + O^\dagger(t) \right] \, \delta(t-t') \, \delta(T-T') \tag{5.9}$$

$$\langle \widehat{F}^\dagger_{V}(t,T) \, \widehat{F}_{V}(t',T') \rangle = \frac{n_{th}}{\tau_p} \, \delta(t-t') \, \delta(T-T') \tag{5.10}$$

$$\langle \widehat{F}_{V}(t,T) \, \widehat{F}^\dagger_{V}(t',T') \rangle = \frac{(n_{th}+1)}{\tau_p} \, \delta(t-t') \, \delta(T-T') \tag{5.11}$$

where n_{sp} is the spontaneous emission factor that takes into account incomplete inversion of the gain medium [1]. n_{th} is the thermal occupation number for photons at the frequency Ω_o, and is close to zero since the photon energy $\hbar\Omega_o$ is usually much greater than the thermal energy at room temperature. The noise operators obey the quantum mechanical commutation relations,

$$\left[\widehat{F}_{SP}(t,T), \widehat{F}^\dagger_{SP}(t',T') \right] = -\left[G + O(t) + O^\dagger(t) \right] \, \delta(t-t') \, \delta(T-T') \tag{5.12}$$

$$\left[\widehat{F}_{V}(t,T), \widehat{F}^\dagger_{V}(t',T') \right] = \frac{1}{\tau_p} \, \delta(t-t') \, \delta(T-T') \tag{5.13}$$

Carrier number fluctuations in the gain medium will be included in the master equation later in this Chapter. A linear quantum theory for optical pulses, such as the one presented in this Chapter, gives almost the same results as the corresponding classical theory in which the operator $\widehat{\phi}(t,T)$ is replaced by a classical field $\phi(t,T)$, and $\widehat{\phi}^{\dagger}(t,T)$ by $\phi^{*}(t,T)$. In the classical theory the noise sources acquire an unphysical character, e.g. the correlation function $\langle F_{sp}^{*}(t,T)\, F_{sp}(t',T')\rangle$ no longer equals $\langle F_{sp}(t',T')\, F_{sp}^{*}(t,T)\rangle$. To avoid this problem, a fully quantum mechanical model is presented. It should be noted that the master equation (5.2) describes the pulse only over time scales longer than the cavity round trip time. The master equation is valid provided the pulse does not change significantly as it travels in the laser cavity.

5.3.2 Steady State Solution

The steady state solution of the master equation (5.2) is obtained by *turning off* the noise sources and setting the right hand side of the master equation (5.2) equal to zero. The solution is much simpler if the term $[\cos(\omega_R(t) - 1]$ is approximated by $-\omega_R^2 t^2/2$ [72]. The eigenfunctions $A_k(t)$ of the operator $O(t)$ are complex Hermite-Gaussians, and the corresponding complex eigenvalues are λ_k. It follows that,

$$O(t)\, A_k(t) = \lambda_k\, A_k(t) \tag{5.14}$$

where $\lambda_k = (2k+1)\,\lambda_0$, and,

$$\lambda_0 = -\frac{1}{2}\sqrt{\frac{(A_M + jP_M)\,(B - jD)}{2\,\omega_R^2}} \tag{5.15}$$

The master equation (5.2) is valid only if $|\lambda_0| \ll 1/T_R$. In actively mode-locked semiconductor lasers, $|\lambda_0|$ is usually two or three orders of magnitude smaller than $1/T_R$ [36, 78, 79, 80]. The approximation $|\lambda_0| \ll 1/T_R$ will be used frequently in this Chapter. The eigenfunctions $A_k(t)$ are normalized such that $\int dt\, |A_k(t)|^2 = 1$. The steady state pulse is given by the eigenfunction $A_0(t)$ of the smallest (in magnitude) eigenvalue λ_0, where,

$$A_0(t) = \frac{1}{(\sqrt{\pi}\,\tau)^{1/2}}\, \exp\left[-\frac{t^2}{2\tau^2}(1 + j\beta)\right] \tag{5.16}$$

The pulse chirp parameter β and the pulse width τ are given by the relations,

$$\tan^{-1}(\beta) = \frac{1}{2}\left[\tan^{-1}(P_M/A_M) + \tan^{-1}(D/B)\right] \tag{5.17}$$

$$\tau^2 = \sqrt{1+\beta^2}\sqrt{\frac{2}{\omega_R^2}\left(\frac{B^2+D^2}{A_M^2+P_M^2}\right)^{1/2}} \tag{5.18}$$

In terms of the pulse width τ the eigenvalue λ_0 is,

$$\lambda_0 = -\frac{(1-j\beta)}{(1+\beta^2)}\frac{\omega_R^2\,\tau^2\,(A_M+jP_M)}{4} \tag{5.19}$$

The expectation value of the field operator $\widehat{\phi}(t,T)$ with respect to the quantum mechanical state of the optical pulse is,

$$\langle\widehat{\phi}(t,T)\rangle = \sqrt{n_o}\,A_0(t) \tag{5.20}$$

where n_o is the number of photons in the steady state pulse. For stable pulse operation the real and imaginary parts of the eigenvalue λ_0 must satisfy the equations,

$$G - \frac{1}{\tau_p} + 2\lambda_0^r = 0 \tag{5.21}$$

$$\lambda_0^i + \frac{\nu}{T_R} = 0 \tag{5.22}$$

The gain G is assumed to be a decreasing function of the number of photons n_o in the optical pulse as a result of gain saturation. The details of the relationship between G and n_o are not important for the purposes of this Chapter. However, it should be noted that (5.21) fixes the number of photons in the steady state pulse. In semiconductor lasers, mode-locking with pure phase modulation can be done by using an external modulator. When pure phase modulation is used (i.e. when $A_M = 0$), the pulse can be at the crest or trough of the sinusoidal modulation signal where the phase modulation has opposite signs. Using (5.15) with (5.21) and assuming $P_M > 0$, it can be shown that when $D < 0$, the threshold gain is lower if the pulse is at the crest, and when $D > 0$, the threshold gain is lower if the pulse is at the trough.

5.3.3 Non-orthogonal Eigenfunctions

The operator $O(t)$, in the presence of dispersion and/or phase modulation, is not Hermitian (or not self-adjoint) and also not normal (i.e. it does not commute with its adjoint). Consequently, the eigenfunctions of the adjoint operator $O^\dagger(t)$. The eigenfunctions of the operator $O^\dagger(t)$ are complex conjugates of the corresponding eigenfunctions of the operator $O(t)$,

$$O^\dagger(t)\, A_k^*(t) = \lambda_k^*\, A_k^*(t) \tag{5.23}$$

The orthogonality relation is then $\int dt\, A_q(t)\, A_k(t) \propto \delta_{qk}$. The cross-product matrix M_{kq} is defined as,

$$M_{qk} = M_{kq}^* = \int dt\, A_q^*(t) A_k(t) \tag{5.24}$$

If the eigenfunctions were orthogonal then M_{kq} would equal δ_{kq}. In Appendix D.2, it is shown that M_{kq} depends only on the pulse chirp β. The larger the magnitude of β, the larger the magnitude of M_{kq}. Therefore, the degree of non-orthogonality of the eigenfunctions increases with the increase in the magnitude of the pulse chirp. When $\beta = 0$, the eigenfunctions are all orthogonal and $M_{kq} = \delta_{kq}$. Also, M_{kq} is non-zero only if $A_k(t)$ and $A_q(t)$ have the same parity (i.e. if k and q are both even or both odd). Properties of the complex Hermite-Gaussian functions, and expressions for the elements of the matrix M_{kq}, are given in Appendix D.2. The eigenfunctions $A_k(t)$ form a complete basis set and satisfy the completeness relation,

$$\sum_{k=0}^{\infty} \frac{A_k(t)\, A_k(t')}{\int dt\, A_k^2(t)} = \delta(t - t') \tag{5.25}$$

5.4 Solution in the Presence of Noise

5.4.1 Eigenfunction Expansion

In the presence of noise, the field operator $\widehat{\phi}(t, T)$ can be written as a sum of a classical field, which describes the steady state pulse, and a quantum operator which describes the noise and also preserves the field commutation relations [34, 70],

$$\widehat{\phi}(t, T) = \sqrt{n_o}\, A_0(t) + \widehat{\psi}(t, T) \tag{5.26}$$

where,

$$\langle \widehat{\psi}(t,T) \rangle = 0 \tag{5.27}$$

$$\left[\widehat{\psi}(t,T), \widehat{\psi}^{\dagger}(t',T) \right] = \delta(t-t') \tag{5.28}$$

The operator $\widehat{\psi}(t,T)$ can be expanded in terms of the eigenfunctions of the operator $O(t)$,

$$\psi(t,T) = \sqrt{n_o} \sum_{k=0}^{\infty} \widehat{c}_k(T)\, A_k(t) \tag{5.29}$$

where $\widehat{c}_k(T)$ is a quantum mechanical annihilation operator. The operators $\widehat{c}_k(T)$ obey the commutation relation,

$$\left[\widehat{c}_k(T), \widehat{c}_q^{\dagger}(T) \right] = \frac{1}{n_o} \left[\frac{M_{qk}}{\int dt\, A_q^{*2}(t) \int dt\, {A_k}^2(t)} \right] \tag{5.30}$$

If the eigenfunctions were orthogonal, the terms inside the square bracket in (5.30) would equal δ_{kq}. The operator $\widehat{c}_k^{\dagger}(T)$ creates a photon in the mode $A_k^*(t)$ and not in the mode $A_k(t)$. This can be shown as follows. The temporal *wave-function* of the photon created by the operator $\widehat{c}_k^{\dagger}(T)$ can be obtained by looking at the probability amplitude when the state is destroyed by $\widehat{\psi}(t,T)$,

$$\widehat{\psi}(t,T)\, \widehat{c}_k^{\dagger}(T)\, |0\rangle = \left[\widehat{\psi}(t,T), \widehat{c}_k^{\dagger}(T) \right] |0\rangle = \frac{A_k^*(t)}{\sqrt{n_0} \int dt\, A_k^{*2}(t)} |0\rangle \tag{5.31}$$

In many cases the quantities of interest are the pulse photon number, phase, timing, and frequency fluctuations. If the eigenmode expansion for the operator $\widehat{\psi}(t,T)$ in (5.29) is restricted to only the first two eigenfunctions, $A_0(t)$ and $A_1(t)$, then one obtains [33, 34, 70],

$$\begin{aligned} \widehat{\psi}(t,T) = \sqrt{n_o} \Bigg[\left(\frac{\delta \widehat{N}_p(T)}{2n_o} + j\, \delta\widehat{\Theta}(T) \right) A_o(t) - \delta \widehat{J}(T)\, \frac{\partial A_o(t)}{\partial t} - j\, \delta\widehat{\Omega}(T)\, t\, A_o(t) \Bigg] \\ + \{ \text{ terms containing higher order eigenfunctions } \} \end{aligned} \tag{5.32}$$

The operators $\delta \widehat{N}_p(T)$, $\delta\widehat{\Theta}(T)$, $\delta \widehat{J}(T)$, and $\delta\widehat{\Omega}(T)$ describe the pulse photon number, phase, timing, and frequency fluctuations, respectively, and are given as follows,

$$\delta \widehat{N}_p(T) = n_o\, \widehat{c}_0(T) + h.c \tag{5.33}$$

$$\delta\widehat{\Theta}(T) = \frac{1}{2j}\,\widehat{c}_0(T) + h.c \tag{5.34}$$

$$\delta\widehat{J}(T) = \frac{\tau}{\sqrt{2}}\frac{(1+j\beta)^{1/2}}{(1+\beta^2)^{1/4}}\,\widehat{c}_1(T) + h.c \tag{5.35}$$

$$\delta\widehat{\Omega}(T) = \frac{j}{\sqrt{2}\,\tau}\frac{(1+\beta^2)^{3/4}}{(1+j\beta)^{1/2}}\,\widehat{c}_1(T) + h.c \tag{5.36}$$

The operators $\delta\widehat{N}_p(T)$, $\delta\widehat{\Theta}(T)$, $\delta\widehat{J}(T)$, and $\delta\widehat{\Omega}(T)$ describe only those perturbations that do not *distort* the shape of the pulse. The non-zero commutation relations among the operators $\delta\widehat{N}_p(T)$, $\delta\widehat{\Theta}(T)$, $\delta\widehat{J}(T)$, and $\delta\widehat{\Omega}(T)$, and the corresponding uncertainty relations, are given below,

$$\left[\delta\widehat{N}_p(T), \delta\widehat{\Theta}(T)\right] = j\left(1+\beta^2\right)^{1/2} \qquad \langle\Delta\widehat{N}_p^2(T)\rangle\,\langle\delta\widehat{\Theta}^2(T)\rangle \geq \frac{1}{4}\left(1+\beta^2\right) \tag{5.37}$$

$$\left[\delta\widehat{\Omega}(T), \delta\widehat{J}(T)\right] = \frac{j}{n_o}\left(1+\beta^2\right)^{3/2} \qquad \langle\delta\widehat{\Omega}^2(T)\rangle\,\langle\delta\widehat{J}^2(T)\rangle \geq \frac{1}{4}\frac{\left(1+\beta^2\right)^3}{n_o^2} \tag{5.38}$$

If both $\langle\widehat{c}_1(T)\,\widehat{c}_1(T)\rangle$ and $\langle\widehat{c}_1^{\dagger}(T)\,\widehat{c}_1^{\dagger}(T)\rangle$ vanish then,

$$\langle\delta\widehat{\Omega}^2(T)\rangle = \frac{\langle\delta\widehat{J}^2(T)\rangle}{\tau^4}\left(1+\beta^2\right) \tag{5.39}$$

The expansion in (5.32) has been used in the literature [33, 34, 70]. The problem with the expansion in (5.32) is that when the eigenfunctions are not orthogonal, the perturbations given by the higher order eigenfunctions are no longer orthogonal to the perturbations described by the first two eigenfunctions. Consequently, the operators for the pulse photon number, phase, timing, and frequency fluctuations given in (5.33)-(5.36) are not valid, and do not correspond to the quantities that are measured in experiments, when the eigenfunctions are not orthogonal (see Section 5.9 for details). In the next Section, operators are constructed that describe the pulse photon number, phase, timing, and frequency fluctuations when the eigenfunctions of the operator $O(t)$ are not orthogonal.

5.4.2 Pulse Fluctuation Operators

The total number of photons in the pulse at time T is given by the operator,

$$\int dt\;\widehat{\phi}^{\dagger}(t,T)\widehat{\phi}(t,T) \tag{5.40}$$

The operator $\Delta\widehat{N}_p(T)$ for the fluctuations in the pulse photon number can be obtained by using (5.26) in (5.40) and keeping only the terms first order in $\widehat{\psi}(t,T)$,

$$\Delta\widehat{N}_p(T) = \sqrt{n_o}\int dt\, A_0^*(t)\widehat{\psi}(t,T) + h.c \tag{5.41}$$

The operator $\Delta\widehat{\Theta}(T)$ for the pulse phase fluctuations, which is also conjugate to $\Delta\widehat{N}_p(T)$, is,

$$\Delta\widehat{\Theta}(T) = \frac{1}{\sqrt{n_o}}\int dt\,\frac{1}{2j}A_0^*(t)\widehat{\psi}(t,T) + h.c \tag{5.42}$$

The commutation relation between $\Delta\widehat{N}_p(T)$ and $\Delta\widehat{\Theta}(T)$ follow from the commutation relation between $\widehat{\psi}(t,T)$ and $\widehat{\psi}^\dagger(t',T)$,

$$\left[\Delta\widehat{N}_p(T), \Delta\widehat{\Theta}(T)\right] = j \tag{5.43}$$

The resulting uncertainty relation is,

$$\langle\Delta\widehat{N}_p^2(T)\rangle\,\langle\Delta\widehat{\Theta}^2(T)\rangle \geq \frac{1}{4} \tag{5.44}$$

The operator for the pulse position in time is,

$$\int dt\ \widehat{\phi}^\dagger(t,T)\, t\, \widehat{\phi}(t,T) \tag{5.45}$$

It follows that the operator $\Delta\widehat{J}(T)$ for the fluctuations in the pulse timing is,

$$\Delta\widehat{J}(T) = \frac{1}{\sqrt{n_o}}\int dt\, t\, A_0^*(t)\,\widehat{\psi}(t,T) + h.c \tag{5.46}$$

The operator $\Delta\widehat{\Omega}(T)$ for the pulse frequency fluctuations, which is also conjugate to $\Delta\widehat{J}(T)$, is,

$$\Delta\widehat{\Omega}(T) = \frac{1}{\sqrt{n_o}}\int dt\,\frac{1}{j}\frac{\partial A_0^*(t)}{\partial t}\,\widehat{\psi}(t,T) + h.c \tag{5.47}$$

The commutation relation between $\Delta\widehat{\Omega}(T)$ and $\Delta\widehat{J}(T)$ is,

$$\left[\widehat{\Omega}(T), \widehat{J}(T)\right] = \frac{j}{n_o} \tag{5.48}$$

and it implies the uncertainty relation,

$$\langle \Delta\widehat{\Omega}^2(T) \rangle \, \langle \Delta\widehat{J}^2(T) \rangle \geq \frac{1}{4\, n_o^2} \tag{5.49}$$

An important relation can be derived between the mean square frequency and timing fluctuations by comparing (5.46) and (5.47). If $\langle \widehat{\psi}(t,T)\, \widehat{\psi}(t',T) \rangle = \langle \widehat{\psi}^{\dagger}(t,T)\, \widehat{\psi}^{\dagger}(t',T) \rangle = 0$, which is most often the case, then,

$$\langle \Delta\widehat{\Omega}^2(T) \rangle = \frac{\langle \Delta\widehat{J}^2(T) \rangle}{\tau^4} \left(1 + \beta^2\right) \tag{5.50}$$

It can be shown that other than the commutation relations given in (5.43) and (5.48), all other commutators between $\Delta\widehat{N}_p(T)$, $\Delta\widehat{\Theta}(T)$, $\Delta\widehat{J}(T)$, and $\Delta\widehat{\Omega}(T)$ vanish. Using the eigenfunction expansion for $\widehat{\psi}(t,T)$, the expressions for the pulse fluctuation operators become,

$$\Delta\widehat{N}_p(T) = n_o \sum_{k=0}^{\infty} M_{0k}\, \widehat{c}_k(T) + h.c \tag{5.51}$$

$$\Delta\widehat{\Theta}(T) = \frac{1}{2j} \sum_{k=0}^{\infty} M_{0k}\, \widehat{c}_k(T) + h.c \tag{5.52}$$

$$\Delta\widehat{J}(T) = \frac{\tau}{\sqrt{2}} \frac{(1+j\beta)^{1/2}}{(1+\beta^2)^{1/4}} \sum_{k=0}^{\infty} M_{1k}\, \widehat{c}_k(T) + h.c \tag{5.53}$$

$$\Delta\widehat{\Omega}(T) = \frac{j}{\sqrt{2}\,\tau} \frac{(1+\beta^2)^{3/4}}{(1+j\beta)^{1/2}} \sum_{k=0}^{\infty} M_{1k}\, \widehat{c}_k(T) + h.c \tag{5.54}$$

Equations (5.51)-(5.54) show that when the eigenfunctions $A_k(t)$ are not orthogonal, the noise in all the higher order eigenfunctions contributes to the pulse photon number, phase, timing, and frequency fluctuations. If the eigenfunction expansions for the operators $\Delta\widehat{N}_p(T)$, $\Delta\widehat{\Theta}(T)$, $\Delta\widehat{J}(T)$, and $\Delta\widehat{\Omega}(T)$, given in (5.51)-(5.54), are terminated after the second eigenfunction $A_1(t)$, then the operators $\delta\widehat{N}_p(T)$, $\delta\widehat{\Theta}(T)$, $\delta\widehat{J}(T)$, and $\delta\widehat{\Omega}(T)$, given in (5.33)-(5.36), are obtained. In Section 5.9, it will be shown that the experimentally measured pulse fluctuations correspond to the operators $\Delta\widehat{N}_p(T)$, $\Delta\widehat{\Theta}(T)$, $\Delta\widehat{J}(T)$, $\Delta\widehat{\Omega}(T)$ and not to $\delta\widehat{N}_p(T)$, $\delta\widehat{\Theta}(T)$, $\delta\widehat{J}(T)$, $\delta\widehat{\Omega}(T)$. Note that only the even numbered eigenfunctions contribute to the pulse photon number and phase noise, and only the odd numbered eigenfunctions contribute to the pulse timing and frequency noise. In Appendix D.3, it is shown that the expansion for the operator $\widehat{\psi}(t,T)$, in terms of the operators $\Delta\widehat{N}_p(T)$, $\Delta\widehat{\Theta}(T)$, $\Delta\widehat{J}(T)$, and $\Delta\widehat{\Omega}(T)$,

can be written in a form similar to (5.32),

$$\widehat{\psi}(t,T) = \sqrt{n_o}\left[\left(\frac{\Delta\widehat{N}_p(T)}{2n_o} + j\,\Delta\widehat{\Theta}(T)\right) A_o(t) - \Delta\widehat{J}(T)\,\frac{\partial A_o(t)}{\partial t} - j\,\Delta\widehat{\Omega}(T)\,t\,A_o(t)\right] + \{\text{ terms containing orthogonal perturbations }\} \tag{5.55}$$

The difference between (5.55) and (5.32) is that the additional terms in (5.55) consist of only perturbations that are orthogonal to those described by the operators $\Delta\widehat{N}_p(T)$, $\Delta\widehat{\Theta}(T)$, $\Delta\widehat{J}(T)$, and $\Delta\widehat{\Omega}(T)$. In the next Section, the dynamical equations for the operators $\widehat{c}_k(T)$ are derived.

5.5 Noise Dynamics and Excess Noise

The dynamical equation for the operator $\widehat{c}_k(T)$ can be found by substituting the eigenfunction expansion in (5.29) in the master equation (5.2), and using the eigenfunction $A_k^*(t)$ of the adjoint operator $O^\dagger$ to project out the equation for $\widehat{c}_k(T)$,

$$\frac{d\,\widehat{c}_k(T)}{dT} = (\lambda_k - \lambda_0)\,\widehat{c}_k(T) + \frac{\int dt\,\left[\widehat{F}_{SP}(t,T) + \widehat{F}_V(t,T)\right] A_k(t)}{\sqrt{n_o}\int dt\,A_k^2(t)} \tag{5.56}$$

$$= 2\,k\,\lambda_0\,\widehat{c}_k(T) + \widehat{F}_k(T) \tag{5.57}$$

The commutation relations given in (5.12) and (5.13) for the noise sources, $\widehat{F}_{SP}(t,T)$ and $\widehat{F}_V(t,T)$, preserve the commutation relations for the operators $\widehat{c}_k(T)$ during time evolution. The equation for the operator $\widehat{c}_0(T)$ is not damped. Carrier number fluctuations (or gain fluctuations) must be included in the model to damp the fluctuations in $\widehat{c}_0(T)$ and this will be done later in this Chapter. For $k \neq 0$, (5.57) can be integrated directly to yield,

$$\widehat{c}_k(T) = \int_{-\infty}^{T} dT'\,\exp\left[2\,k\,\lambda_0\,(T-T')\right] F_k(T') \tag{5.58}$$

The expectation values for the operators $\widehat{c}_k(T)$ can be calculated using the expression above, and for $k, q \neq 0$ one obtains,

$$\langle\widehat{c}_k(T)\rangle = \langle\widehat{c}_k^\dagger(T)\rangle = \langle\widehat{c}_k(T)\,\widehat{c}_q(T)\rangle = \langle\widehat{c}_k^\dagger(T)\,\widehat{c}_q^\dagger(T)\rangle = 0 \tag{5.59}$$

$$\langle \widehat{c}_k^{\dagger}(T)\, \widehat{c}_q(T) \rangle = \frac{\dfrac{1}{\tau_p}\left(n_{th}+n_{sp}\right) + \left(2k\lambda_0^* + 2q\lambda_0\right) n_{sp}}{-\left(2k\lambda_0^* + 2q\lambda_0\right)\ n_o} \left[\frac{M_{kq}}{\int dt\, A_k^{*2}(t)\ \int dt\, A_q{}^2(t)}\right] \tag{5.60}$$

$$\langle \widehat{c}_q(T)\, \widehat{c}_k^{\dagger}(T) \rangle = \frac{\dfrac{1}{\tau_p}\left(n_{th}+n_{sp}\right) + \left(2k\lambda_0^* + 2q\lambda_0\right) \left(n_{sp}-1\right)}{-\left(2k\lambda_0^* + 2q\lambda_0\right)\ n_o} \left[\frac{M_{kq}}{\int dt\, A_k^{*2}(t)\ \int dt\, A_q{}^2(t)}\right] \tag{5.61}$$

The terms in (5.60) and (5.61) proportional to $(2k\lambda_0^* + 2q\lambda_0)$ in the numerator can be ignored if $|\lambda_0| \ll 1/\tau_p$. Since τ_p is usually of the order of T_R, the condition $|\lambda_0| \ll 1/\tau_p$ is also satisfied if $|\lambda_0| \ll 1/T_R$. Since the master equation (5.2) is valid only if $|\lambda_0| \ll 1/T_R$, these terms will be ignored in this Chapter. If the eigenfunctions were orthogonal, the terms inside the square bracket in (5.60) and (5.61) would equal δ_{kq} and there would be no correlation in the noise in different eigenfunctions. The expectation values $\langle \widehat{c}_k(T)\, \widehat{c}_k^{\dagger}(T) \rangle$ and $\langle \widehat{c}_k^{\dagger}(T)\, \widehat{c}_k(T) \rangle$ are proportional to the factor $1/\left|\int dt\, A_k^2(t)\right|^2$, which is the excess noise factor. The excess noise factor appears as a result of the non-orthogonality of the eigenmodes and would have been absent if the eigenfunctions $A_k(t)$ were orthogonal. The excess noise factor is similar to the Petermann's K-factor that describes the excess noise in optical amplifiers and oscillators with non-orthogonal optical modes [74, 75, 76, 77]. Readers are referred to Appendix D.1 for a general discussion of the excess noise in linear systems with non-orthogonal eigenmodes. It needs to be emphasized here that the excess noise does not disappear if, instead of the eigenfunction basis, any orthonormal basis, such as the one introduced in Appendix D.3, is used to expand the operator $\widehat{\psi}(t,T)$. The excess noise is intimately tied to the non-normality of the operator $O(t)$ itself, irrespective of the basis set used to study noise. It can be shown that (see Appendix D.2),

$$\frac{1}{\left|\int dt\, A_k^2(t)\right|^2} = \left|\sqrt{1+j\beta}\ P_k\left(\sqrt{1+\beta^2}\right)\right|^2 \tag{5.62}$$

where $P_k(.)$ is the k-th Legendre polynomial, and $P_0(x) = 1$ and $P_1(x) = x$. The excess noise depends on the degree of non-orthogonality of the eigenfunctions (or on the degree of non-normality of the operator $O(t)$). The larger the magnitude of the pulse chirp, the more non-orthogonal the eigenfunctions, and the larger the excess noise.

As stated earlier, the fluctuations associated with the even numbered eigenfunctions do not contribute to the pulse timing and frequency fluctuations. Therefore, the discussion of the dynamical equation for the operator $\widehat{c}_0(T)$ is postponed, and proceed to study the pulse

timing and frequency fluctuations in the next Section.

5.6 Timing and Frequency Fluctuations

In section 5.4.2, it was pointed out that the when the eigenfunctions are not orthogonal the operators $\Delta\widehat{J}(T)$ and $\Delta\widehat{\Omega}(T)$, and not $\delta\widehat{J}(T)$ and $\delta\widehat{\Omega}(T)$, describe the timing and frequency noise in an optical pulse. However, it is instructive to first look at $\delta\widehat{J}(T)$ and $\delta\widehat{\Omega}(T)$. The mean square value of $\delta\widehat{J}(T)$ can be obtained using (5.60) and (5.61) with (5.35),

$$\langle \delta\widehat{J}^2(T)\rangle = \frac{\tau^2}{2}\left[\langle \widehat{c}_1(T)\,\widehat{c}_1^{\dagger}(T)\rangle + \langle \widehat{c}_1^{\dagger}(T)\,\widehat{c}_1(T)\rangle\right] \tag{5.63}$$

$$= \frac{\tau^2}{2\,n_o}\left[\frac{2n_{sp}+(2n_{sp}-1)\,(2\lambda_0+2\lambda_0^*)\,\tau_p}{(-2\lambda_0-2\lambda_0^*)\,\tau_p}\right]\frac{1}{\left|\int dt\,{A_1}^2(t)\right|^2} \tag{5.64}$$

$$\approx \left(\frac{n_{sp}}{n_o}\right)\frac{(1+\beta^2)^{5/2}}{\tau_p\,\omega_R^2\,(A_M+\beta\,P_M)} \tag{5.65}$$

The mean square value of $\delta\widehat{\Omega}(T)$ can be obtained from the mean square value of $\delta\widehat{J}(T)$ using (5.39),

$$\langle \delta\widehat{\Omega}^2(T)\rangle = \frac{\langle \delta\widehat{J}^2(T)\rangle}{\tau^4}\left(1+\beta^2\right) \tag{5.66}$$

$$\approx \left(\frac{n_{sp}}{n_o}\right)\frac{(1+\beta^2)^{7/2}}{\tau_p\,\omega_R^2\,\tau^4\,(A_M+\beta\,P_M)} \tag{5.67}$$

The term $1/\left|\int dt\,{A_1}^2(t)\right|^2 = (1+\beta^2)^{3/2}$ in (5.64) is the excess noise factor and it can be much greater than unity when the pulse chirp β is large. In Section 5.5, it was shown that the noise in different eigenfunctions is correlated. $\Delta\widehat{J}(T)$ and $\Delta\widehat{\Omega}(T)$ contain noise contributions from all the odd numbered eigenfunctions. Therefore, one may expect that the presence of these correlations would affect the mean square fluctuations $\langle\Delta\widehat{J}^2(T)\rangle$ and $\langle\Delta\widehat{\Omega}^2(T)\rangle$. Using (5.53), (5.60), and (5.61), $\langle\Delta\widehat{J}^2(T)\rangle$ becomes,

$$\langle \Delta\widehat{J}^2(T)\rangle = \frac{\tau^2}{2}\sum_{k,q=0}^{\infty} M_{1k}\,M_{q1}\left[\langle \widehat{c}_k(T)\,\widehat{c}_q^{\dagger}(T)\rangle + \langle \widehat{c}_q^{\dagger}(T)\,\widehat{c}_k(T)\rangle\right] \tag{5.68}$$

$$= \frac{\tau^2}{2\,n_o}\sum_{k,q=0}^{\infty}\frac{M_{1k}\,M_{qk}\,M_{q1}}{(-2k\lambda_0-2q\lambda_0^*)\,\tau_p}\,\frac{\left[2n_{sp}+(2n_{sp}-1)\,(2k\lambda_0+2q\lambda_0^*)\,\tau_p\right]}{\int dt\,A_q^{*2}(t)\,\int dt\,{A_k}^2(t)} \tag{5.69}$$

$$\approx \left(\frac{n_{sp}}{n_o}\right)\frac{\tau^2}{\tau_p}\sum_{k,q=0}^{\infty}\frac{M_{1k}\,M_{qk}\,M_{q1}}{(-2k\lambda_0-2q\lambda_0^*)}\,\frac{1}{\int dt\,A_q^{*2}(t)\,\int dt\,{A_k}^2(t)} \tag{5.70}$$

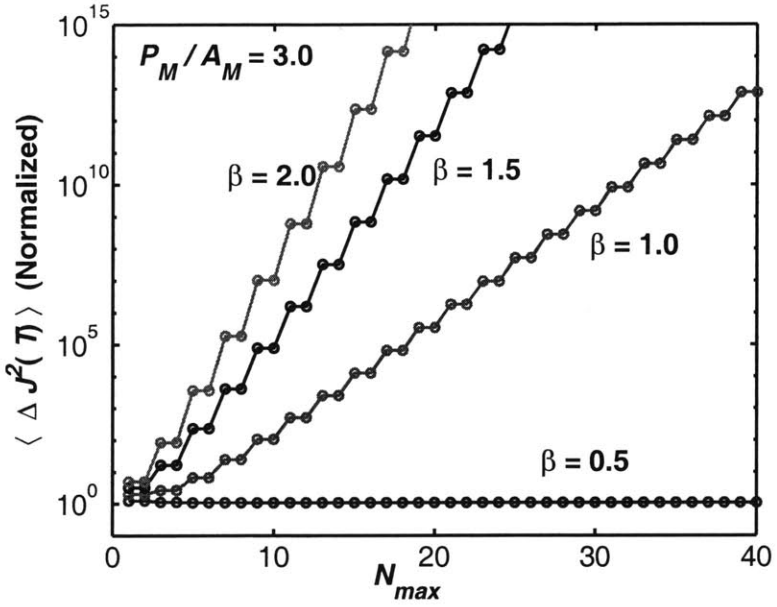

Figure 5-1: Mean square timing noise $\langle \Delta \widehat{J}^2(T) \rangle$ calculated using (5.70), normalized to the value of $\langle \delta \widehat{J}^2(T) \rangle$ in (5.65), is plotted as a function of the number N_{max} of eigenfunctions used in the expansion. The perturbative expansion diverges exponentially when the pulse chirp $|\beta|$ becomes larger than $1/\sqrt{3} \approx 0.577$. The steps appear because only the odd numbered eigenfunctions contribute to the timing noise.

The first non-zero term ($k = q = 1$) of the series in (5.70) equals $\langle \delta \widehat{J}^2(T) \rangle$ given in (5.64). Fig. 5-1 shows the mean square timing noise $\langle \Delta \widehat{J}^2(T) \rangle$ calculated using (5.70) as a function of the number of eigenfunctions N_{max} used in the expansion (i.e. when only terms with $k, q < N_{max}$ are included in the summation in (5.70)). When the magnitude of the pulse chirp β is larger than $1/\sqrt{3} \approx 0.577$, the series in (5.70) does not converge and diverges exponentially. The perturbative expansion for the pulse frequency noise also diverges in the same way. Later in this Chapter, it is shown that the perturbative expansions for the pulse photon number noise and phase noise also diverge. The divergence of the perturbative expansion is analyzed in detail in Appendix D.4, and it is shown that in general a series of the form,

$$\sum_{k,q=0}^{\infty} F_{qk} \frac{M_{pk}\, M_{qk}\, M_{qp}}{\int dt\, A_q^{*2}(t) \int dt\, A_k{}^2(t)} \tag{5.71}$$

where F_{qk} $(= F_{kq}^*)$ decays only algebraically as k, q become large, diverges exponentially when $|\beta| > 1/\sqrt{3}$. The divergence is not physical and can be removed by an appropriate

resummation. In Appendix D.4, the following result is established,

$$\sum_{k,q=0}^{\infty} F_{qk} \frac{M_{pk}\, M_{qk}\, M_{qp}}{\int dt\, A_q^{*2}(t)\, \int dt\, A_k{}^2(t)} = \lim_{N_{max}\to\infty} \left| \int dt\, A_p^2(t) \right|^2 \sum_{k,q=0}^{N_{max}-1} F_{qk}\, M_{kp}^{-1}\, M_{qk}\, M_{pq}^{-1} \quad (5.72)$$

The series on the right hand side in the above Equation converges for all values of the pulse chirp β as N_{max} becomes large. Using (5.70) and (5.72), one obtains,

$$\begin{aligned} \langle \Delta \widehat{J}^2(T) \rangle &= \frac{\tau^2}{2\, n_o\, (1+\beta^2)^{3/2}} \sum_{k,q=0}^{N_{max}-1} \frac{M_{k1}^{-1}\, M_{qk}\, M_{1q}^{-1}}{(-2k\lambda_0 - 2q\lambda_0^*)\, \tau_p} [\, 2n_{sp} \\ &\quad + (2n_{sp}-1)\, (2k\lambda_0 + 2q\lambda_0^*)\, \tau_p\,] \qquad (5.73) \\ &\approx \left(\frac{n_{sp}}{n_o}\right) \frac{\tau^2}{\tau_p\, (1+\beta^2)^{3/2}} \sum_{k,q=0}^{N_{max}-1} \frac{M_{k1}^{-1}\, M_{qk}\, M_{1q}^{-1}}{(-2k\lambda_0 - 2q\lambda_0^*)} \qquad (5.74) \end{aligned}$$

The series above converges for all values of P_M/A_M and chirp β that satisfy (5.18) to a value which may be approximated (with less than five percent error) by the expression,

$$\langle \Delta \widehat{J}^2(T) \rangle \approx \left(\frac{n_{sp}}{n_o}\right) \frac{(1+\beta^2)^{3/2}}{\tau_p\, \omega_R^2\, (A_M + \beta\, P_M)} \quad (5.75)$$

Fig. 5-2 shows $\langle \Delta \widehat{J}^2(T) \rangle$ calculated using (5.74) and normalized to the approximate expression given in (5.75) as a function of N_{max} for $P_M/A_M = 3.0$. The expression in (5.75) can be written as,

$$\langle \Delta \widehat{J}^2(T) \rangle \approx \sigma_A^2 \frac{(1+\beta^2)^{3/2}}{(\, 1+\beta\, P_M/A_M\,)} \quad (5.76)$$

where σ_A^2, given by the expression,

$$\sigma_A^2 = \left(\frac{n_{sp}}{n_o}\right) \frac{1}{\tau_p\, \omega_R^2\, A_M} \quad (5.77)$$

is the mean square timing noise in the absence of group velocity dispersion and phase modulation. The factor,

$$\frac{(1+\beta^2)^{3/2}}{(\, 1+\beta\, P_M/A_M\,)} \quad (5.78)$$

captures the effect of dispersion and phase modulation on the mean square timing jitter. Pulse stability with respect to timing perturbations require that $(1+\beta\, P_M/A_M\,) > 0$. Using (5.17), it can be shown that the stability condition is always satisfied for all values of D/B and P_M/A_M. Fig. 5-3 shows $\langle \Delta \widehat{J}^2(T) \rangle$, normalized to σ_A^2, plotted as a function of the ratio

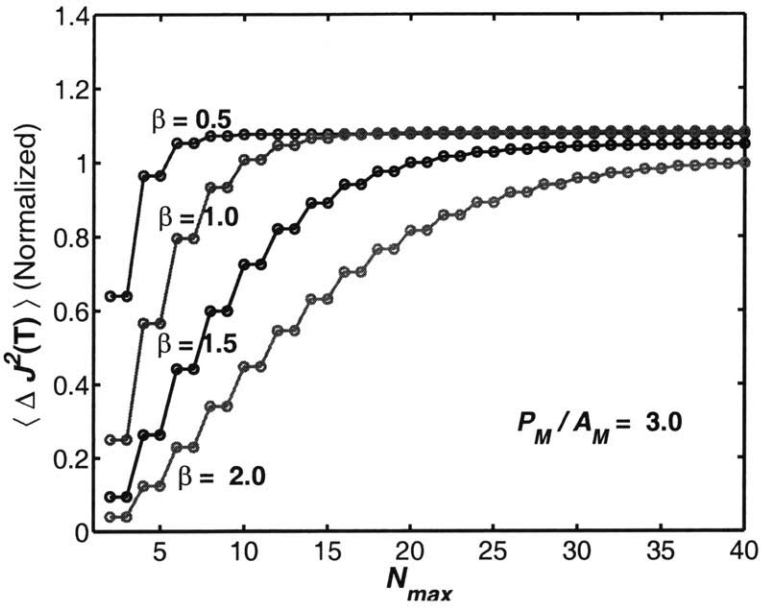

Figure 5-2: Mean square timing noise $\langle \Delta \widehat{J}^2(T) \rangle$, calculated using (5.74) and normalized to the expression given in Equation (5.75), is plotted as a function of the number N_{max} of eigenfunctions used in the perturbative expansion. The series in (5.74) converges for all values of the pulse chirp.

D/B for different values of the ratio P_M/A_M. The corresponding values of the pulse chirp are shown in Fig. 5-4. In the presence of dispersion and phase modulation, keeping A_M fixed, the mean square timing noise is minimized when,

$$4\beta \frac{P_M}{A_M} = \sqrt{9 + 8\left(\frac{P_M}{A_M}\right)^2} - 3 \tag{5.79}$$

In the presence of phase modulation, the minimum timing noise always occurs for a non-zero value of the pulse chirp, as shown in Fig. 5-3 and Fig. 5-4. If pure phase modulation is used (i.e. if $A_M = 0$) then,

$$\langle \Delta \widehat{J}^2(T) \rangle \approx \sigma_P^2 \, \frac{(1+\beta^2)^{3/2}}{\beta} \tag{5.80}$$

where σ_P^2 is,

$$\sigma_P^2 = \left(\frac{n_{sp}}{n_o}\right) \frac{1}{\tau_p \, \omega_R^2 \, P_M} \tag{5.81}$$

In this case, pulse stability with respect to timing perturbations requires that $\beta P_M > 0$ which, using (5.17), can be shown to be satisfied for all values of D/B. Fig. 5-5 shows $\langle \Delta \widehat{J}^2(T) \rangle$, normalized to σ_P^2, plotted as a function of the ratio D/B. The corresponding

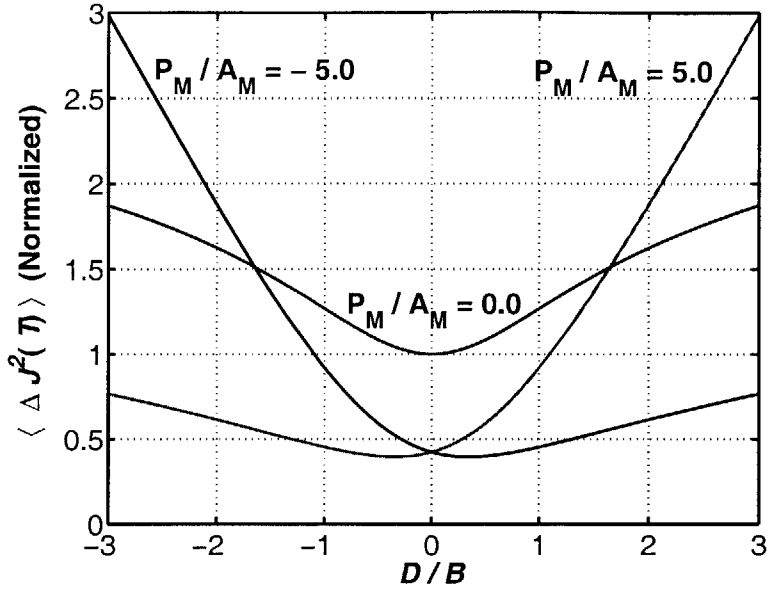

Figure 5-3: Mean square timing noise $\langle \Delta \widehat{J}^2(T) \rangle$, normalized to σ_A^2 (see Equation (5.77), is plotted as a function of the ratio D/B for different values of the ratio P_M/A_M.

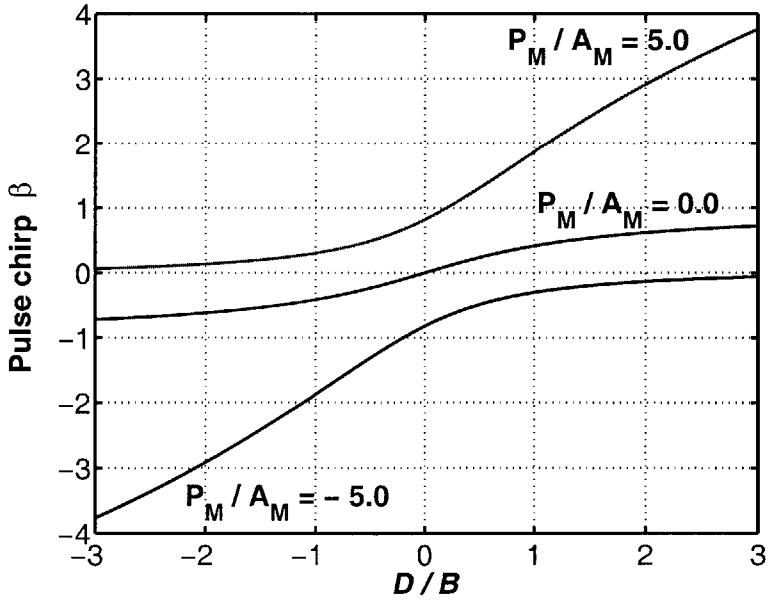

Figure 5-4: Pulse chirp β is plotted as a function of the ratio D/B for different values of the ratio P_M/A_M.

values of the pulse chirp are shown in Fig. 5-6. In case of pure phase modulation, assuming P_M is fixed, the mean square timing noise is minimized when $\beta^2 = 1/2$ (and $\beta P_M > 0$).

$\langle \Delta\widehat{\Omega}^2(T) \rangle$ can be determined using the result in (5.50),

$$\begin{aligned} \langle \Delta\widehat{\Omega}^2(T) \rangle &= \frac{\langle \widehat{J}^2(T) \rangle}{\tau^4} \left(1 + \beta^2\right) \\ &\sim \left(\frac{n_{sp}}{n_o}\right) \frac{\left(1 + \beta^2\right)^{5/2}}{\tau_p \, \omega_R^2 \, \tau^4 \, \left(A_M + \beta \, P_M\right)} \end{aligned} \tag{5.82}$$

Comparing (5.75) and (5.82) with (5.65) and (5.67), it is seen that $\langle \Delta\widehat{J}^2(T) \rangle$ and $\langle \Delta\widehat{\Omega}^2(T) \rangle$ are smaller by a factor $(1 + \beta^2)$ compared to $\langle \delta\widehat{J}^2(T) \rangle$ and $\langle \delta\widehat{\Omega}^2(T) \rangle$, respectively. Since the noise in different eigenfunctions is correlated, when contribution to the pulse timing and frequency noise from all the eigenfunctions is taken into account, the excess noise factor is reduced by a factor $(1 + \beta^2)$.

The external cavity semiconductor mode-locked laser, shown in Fig. 5-7, is considered next for obtaining numerical results on the timing jitter. The lengths L_G and L_M of the gain and the modulator sections are assumed to be 500 μm, and 100 μm, respectively. The operating wavelength is 1.55 μm. The cavity round trip time T_R is 0.1 ns, and corresponds to a cavity roundtrip frequency of 10 GHz. The value of the gain bandwidth parameter B is such that $BT_R = 2500$ fs^2 [36], and this corresponds to an actual gain bandwidth of approximately 2.0 THz. The spontaneous emission factor n_{sp} equals 2.0. The pulse energy $\hbar\Omega_o \, n_o$ is assumed to be 0.15 pJ, and the modulation strength A_M is assumed to be $0.1/\tau_p$. As explained earlier in this Chapter, P_M equals $-\alpha \, A_M$ in gain modulated semiconductor mode-locked lasers. Fig. 5-8 shows the root mean square (RMS) timing jitter as a function of the dispersion parameter DT_R for different values of the α-parameter. Fig. 5-9 shows the corresponding values of the pulse chirp. It can be seen that RMS timing jitter less than 50 fs can be achieved in semiconductor mode-locked lasers at a repetition rate of 10 GHz. Lower timing jitter can be achieved by increasing the pulse energy or by increasing the modulation strength A_M. The pulse energy in semiconductor mode-locked lasers is limited by dynamic gain saturation to less than 0.15 pJ for conventional waveguide structures [36]. Higher pulse energies may be obtained by designing waveguide structures with larger mode areas. Note that for non-zero values of the α-parameter, the minimum values of the timing jitter are obtained at non-zero values of the dispersion and the pulse chirp. The material dispersion in the active region of semiconductor lasers is expected to be negative, with values ranging

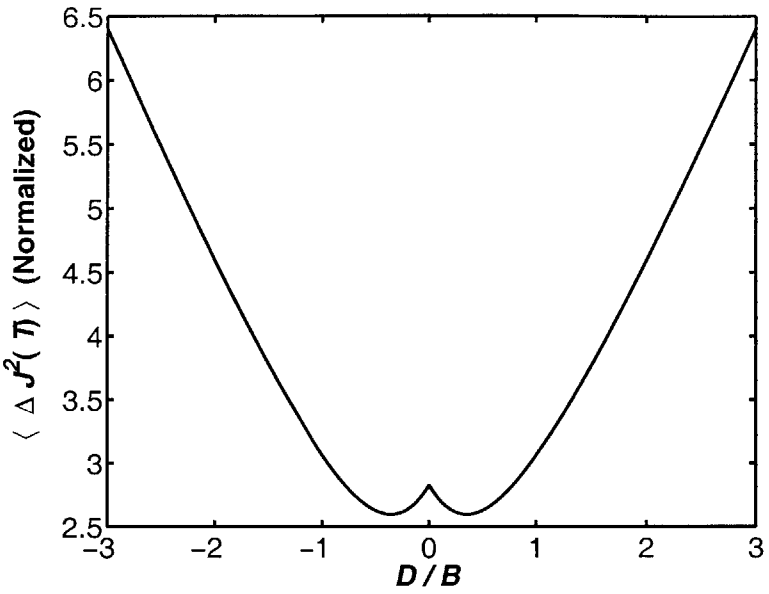

Figure 5-5: Mean square timing noise $\langle \Delta \hat{J}^2(T) \rangle$, normalized to σ_P^2 (see Equation (5.81), is plotted as a function of the ratio D/B when pure phase modulation is used.

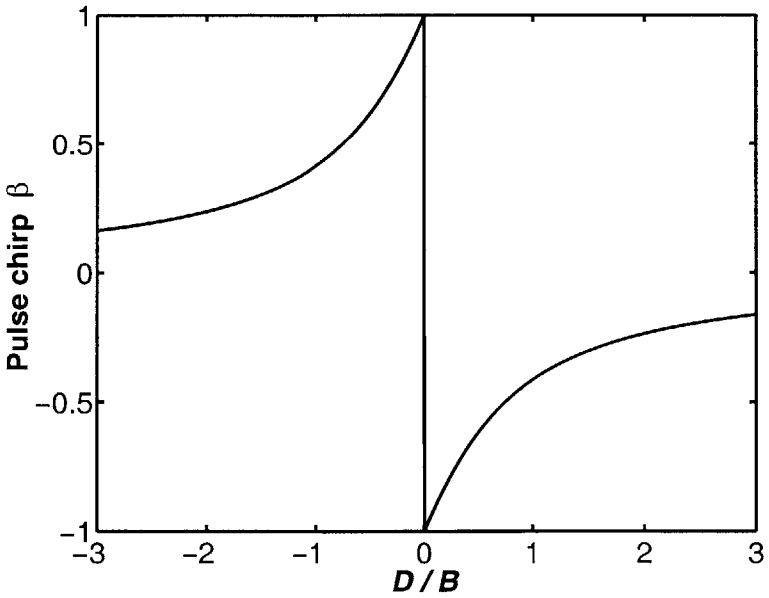

Figure 5-6: Pulse chirp β is plotted as a function of the ratio D/B when pure phase modulation is used.

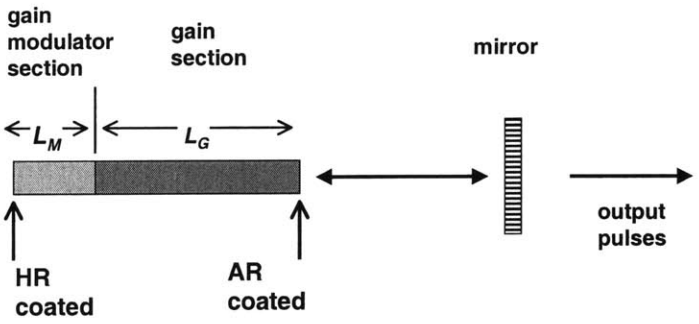

Figure 5-7: An external cavity actively mode-locked semiconductor laser structure used in the numerical simulations is shown. For the laser parameters, see text.

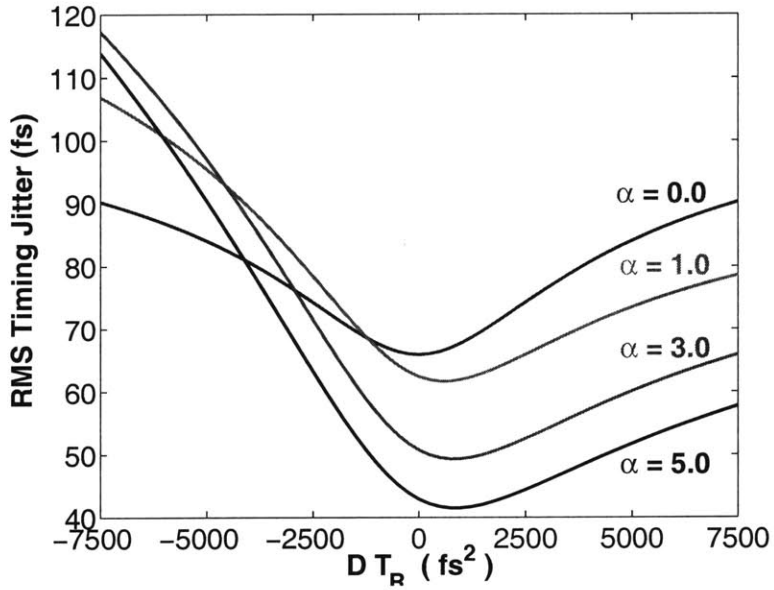

Figure 5-8: The RMS timing jitter in an actively mode-locked semiconductor laser is plotted as a function of the dispersion parameter DT_R for different values of the α-parameter for the laser structure shown in Fig. 5-7. The minimum jitter for non-zero values of α is obtained at a non-zero value of the dispersion and the pulse chirp. The pulse energy is assumed to be 0.15 pJ. The amplitude modulation strength A_M is assumed to $0.1/\tau_p$.

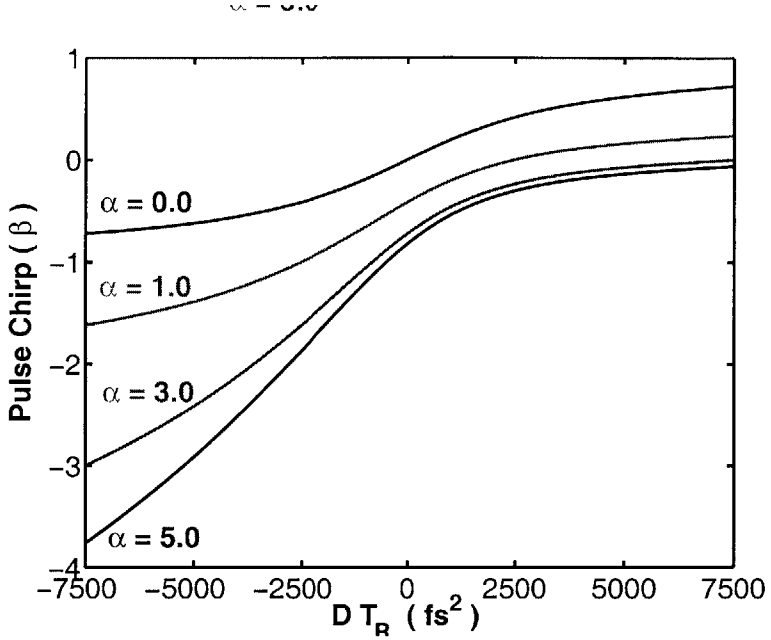

Figure 5-9: The pulse chirp β in an actively mode-locked semiconductor laser is plotted as a function of the dispersion parameter DT_R for different values of the α-parameter for the laser structure shown in Fig. 5-7. The pulse energy is assumed to be 0.15 pJ. The amplitude modulation strength A_M is assumed to $0.1/\tau_p$.

from -0.5 ps^2/cm to -2.0 ps^2/cm [36]. On the other hand, the material dispersion in the SCH regions (see Fig. 2-3 in Chapter 2), where the optical energy is below the material bandgap, is positive and can have values from 0.1 ps^2/cm to 1.0 ps^2/cm [81, 82, 83]. The net dispersion DT_R for the laser in Fig. 5-7 can therefore be in the range -5000 fs^2 to +5000 fs^2 depending upon the device geometry and the confinement factor of the transverse optical mode in each region. The net cavity dispersion in a mode-locked semiconductor laser can also be adjusted by an external dispersion compensator to achieve the dispersion required for minimum timing jitter. The minimum timing jitter obtained this way can be less than the worst case timing jitter by a factor between 2 and 3.

5.6.1 Spectral Densities of the Timing and Frequency Noise

The spectral densities $S_{\delta J}(\omega)$ and $S_{\Delta J}(\omega)$ of the pulse noise operators $\delta\widehat{J}(T)$ and $\Delta\widehat{J}(T)$, respectively, are defined as in Appendix D.5.1. $S_{\delta J}(\omega)$ can be determined by solving (5.57)

in the frequency domain. This yields,

$$\widehat{c}_k(\omega) \;=\; \frac{\widehat{F}_k(\omega)}{j\omega - 2k\lambda_0} \tag{5.83}$$

The spectral density $S_{\delta J}(\omega)$ follows from (5.35) and (D.58),

$$S_{\delta J}(\omega) \;=\; \frac{\tau^2}{4}\int \left[\, \langle \widehat{c}_1(\omega)\, \widehat{c}_1^{\dagger}(\omega')\rangle + \langle \widehat{c}_1^{\dagger}(\omega)\, \widehat{c}_1(\omega')\rangle \,\right] \frac{d\omega'}{2\pi} + (\omega \rightarrow -\omega) \tag{5.84}$$

$$= \frac{\tau^2}{2\, n_o\, \tau_p} \frac{\left[\, 2n_{sp} + (2n_{sp}-1)\,(2\lambda_0 + 2\lambda_0^*)\,\tau_p \,\right]\left(\omega^2 + |2\lambda_0|^2\right)}{\left(\omega^2 - |2\lambda_0|^2\right)^2 + \omega^2\,(-2\lambda_0 - 2\lambda_0^*)^2} \left(1+\beta^2\right)^{3/2} \tag{5.85}$$

$$\approx \left(\frac{n_{sp}}{n_o}\right)\frac{\tau^2}{\tau_p} \frac{\omega^2 + |2\lambda_0|^2}{\left(\omega^2 - |2\lambda_0|^2\right)^2 + \omega^2\,(-2\lambda_0 - 2\lambda_0^*)^2} \left(1+\beta^2\right)^{3/2} \tag{5.86}$$

$$= \left(1+\beta^2\right)^{3/2} \underline{S}_{\delta J}(\omega) \tag{5.87}$$

As a result of the coupling between the pulse timing and frequency noise, the frequency dependence of the timing noise spectral density is that of a second order linear system with the damping constant equal to $(-2\lambda_0 - 2\lambda_0^*)$ and the square of the resonant frequency equal to $|2\lambda_0|^2$. Note that $(1+\beta^2)^{3/2}$ in the expression above is the excess noise factor. The spectral density $\underline{S}_{\delta J}(\omega)$ is defined to be equal to $S_{\delta J}(\omega)$ without the excess noise factor. The spectral density $S_{\delta\Omega}(\omega)$ of the frequency noise $\delta\widehat{\Omega}(T)$ equals $(1+\beta^2)\, S_{\delta J}(\omega)/\tau^4$.

Using (5.53) and (D.58), the expression for the spectral density $S_{\Delta J}(\omega)$ of the timing noise $\Delta\widehat{J}(T)$ becomes,

$$S_{\Delta J}(\omega) \;=\; \frac{\tau^2}{4}\sum_{k,q=0}^{\infty} M_{1k}\, M_{q1} \int \left[\, \langle \widehat{c}_k(\omega)\, \widehat{c}_q^{\dagger}(\omega')\rangle + \langle \widehat{c}_q^{\dagger}(\omega)\, \widehat{c}_k(\omega')\rangle \,\right] \frac{d\omega'}{2\pi} + (\omega \rightarrow -\omega) \tag{5.88}$$

$$= \frac{\tau^2}{2\, n_o\, \tau_p} \sum_{k,q=0}^{\infty} \left\{ \frac{M_{1k}\, M_{qk}\, M_{q1}}{\int dt\, A_q^{*2}(t)\, \int dt\, A_k{}^2(t)} \left[\, 2n_{sp} + (2n_{sp}-1)\,(2k\lambda_0 + 2q\lambda_0^*)\,\tau_p \,\right] \right.$$
$$\left. \times \frac{\left(\omega^2 + kq\, |2\lambda_0|^2\right)}{\left(\omega^2 - kq\, |2\lambda_0|^2\right)^2 + \omega^2\,(-2k\lambda_0 - 2q\lambda_0^*)^2} \right\} \tag{5.89}$$

$$\approx \left(\frac{n_{sp}}{n_o}\right)\frac{\tau^2}{\tau_p} \sum_{k,q=0}^{\infty} \left[\frac{M_{1k}\, M_{qk}\, M_{q1}}{\int dt\, A_q^{*2}(t)\, \int dt\, A_k{}^2(t)} \right.$$
$$\left. \times \frac{\left(\omega^2 + kq\, |2\lambda_0|^2\right)}{\left(\omega^2 - kq\, |2\lambda_0|^2\right)^2 + \omega^2\,(-2k\lambda_0 - 2q\lambda_0^*)^2} \right] \tag{5.90}$$

The series expansion for $S_{\Delta J}(\omega)$ above does not converge for the reasons described in the previous Section. Below, the relation in (5.72) is used to obtain a convergent expansion for $S_{\Delta J}(\omega)$,

$$S_{\Delta J}(\omega) = \frac{\tau^2}{2\,n_o\,\tau_p\,(1+\beta^2)^{3/2}} \sum_{k,q=0}^{N_{max}-1} \left\{ M_{k1}^{-1}\,M_{qk}\,M_{1q}^{-1}\,\left[2n_{sp} + (2n_{sp}-1)\,(2k\lambda_0 + 2q\lambda_0^*)\,\tau_p\right] \times \frac{\left(\omega^2 + kq\,|2\lambda_0|^2\right)}{\left(\omega^2 - kq\,|2\lambda_0|^2\right)^2 + \omega^2\,(-2k\lambda_0 - 2q\lambda_0^*)^2} \right\} \tag{5.91}$$

$$\approx \left(\frac{n_{sp}}{n_o}\right) \frac{\tau^2}{\tau_p\,(1+\beta^2)^{3/2}} \sum_{k,q=0}^{N_{max}-1} \frac{M_{k1}^{-1}\,M_{qk}\,M_{1q}^{-1}\,\left(\omega^2 + kq\,|2\lambda_0|^2\right)}{\left(\omega^2 - kq\,|2\lambda_0|^2\right)^2 + \omega^2\,(-2k\lambda_0 - 2q\lambda_0^*)^2} \tag{5.92}$$

Fig. 5-10 shows the timing noise spectral densities $\underline{S}_{\delta J}(\omega)$, $S_{\delta J}(\omega)$, and $S_{\Delta J}(\omega)$, all normalized to $\underline{S}_{\delta J}(\omega=0)$, for $\beta = 2.0$ and $P_M/A_M = 3.0$. When only the first two eigenfunctions are used in the perturbative expansion, the excess noise factor increases the low frequency timing noise of the pulse by a factor $(1+\beta^2)^{3/2}$ (see (5.87)). Since the noise in different eigenfunctions is correlated, the inclusion of noise contributions from higher order eigenfunctions in $S_{\Delta J}(\omega)$ reduces the low frequency noise and partially compensates the excess noise. Numerical calculations show that $S_{\Delta J}(\omega=0) \approx (1+\beta^2)^{5/8}\,\underline{S}_{\delta J}(\omega=0)$. When $\omega \gg |2\lambda_0|$, the series in (5.92) can be summed exactly,

$$S_{\Delta J}(\omega \gg |2\lambda_0|) = \left(\frac{n_{sp}}{n_o}\right) \frac{\tau^2}{\tau_p\,\omega^2} = \underline{S}_{\delta J}(\omega) \tag{5.93}$$

The above Equation shows that when $\omega \gg |2\lambda_0|$, $S_{\Delta J}(\omega)$ becomes equal to $\underline{S}_{\delta J}(\omega)$ and there is no excess noise. As explained in Appendix D.4, the excess noise results from the non-Hermitian time evolution of the pulse noise, and therefore, at time scales much shorter than $1/|2\lambda_0|$, or at frequencies much larger than $|2\lambda_0|$, the excess noise does not appear. This is also shown in Fig.5-10. The spectral density $S_{\Delta\Omega}(\omega)$ of the frequency noise $\Delta\widehat{\Omega}(T)$ is simply $(1+\beta^2)\,S_{\Delta J}(\omega)/\tau^4$.

5.7 Photon Number and Phase Fluctuations

In Section 5.5, it was mentioned that the dynamical equation for the operator $\widehat{c}_0(T)$ is not damped, and that carrier number fluctuations (or gain fluctuations) must be included in

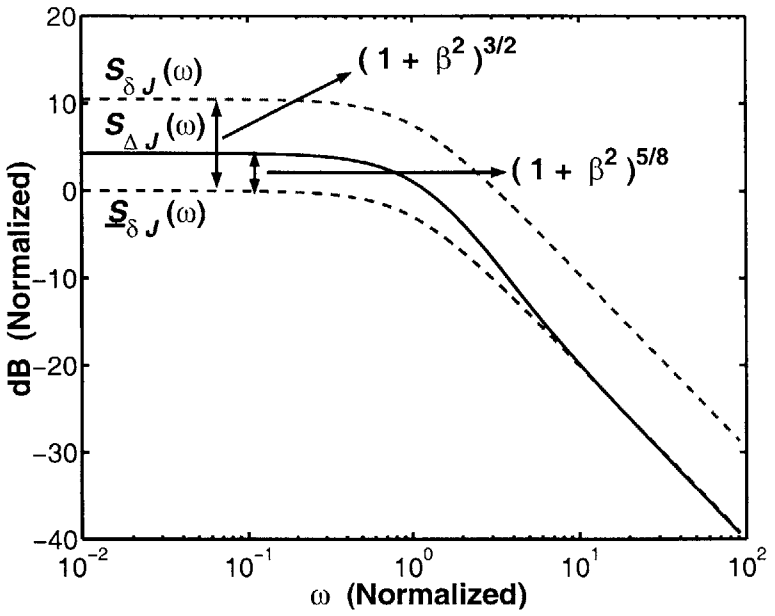

Figure 5-10: The timing noise spectral densities $\underline{S}_{\delta J}(\omega)$, $S_{\delta J}(\omega)$, and $S_{\Delta J}(\omega)$ are shown for $\beta = 2.0$ and $P_M/A_M = 3.0$. The spectral densities in the Figure have been normalized w.r.t. the value of $\underline{S}_{\delta J}(\omega)$ at $\omega = 0$. The frequency ω has been normalized to $|2\lambda_0|$.

the model to determine the pulse photon number and phase fluctuations. Carrier number fluctuations must be incorporated in the model in a way that preserves all the commutation relations. Carrier number fluctuations introduce an additional term,

$$\frac{1}{2}\frac{\partial G}{\partial N}\,(1-j\alpha)\,\Delta\widehat{N}(T)\,\sqrt{n_o}\,A_0(t) \tag{5.94}$$

on the left hand side of the master equation (5.2). The α-parameter, as mentioned earlier, relates the change in the imaginary part of the gain (or the refractive index) to the change in the real part of the gain, and models the refractive index fluctuations which accompany gain fluctuations [1]. Carrier number fluctuations affect only $\widehat{c}_0(T)$,

$$\frac{d\,\widehat{c}_0(T)}{dT} = \frac{(1-j\alpha)}{2\,\tau_{st}\,n_o}\,\Delta\widehat{N}(T) + \frac{\int dt\,\left[\widehat{F}_{SP}(t,T)+\widehat{F}_V(t,T)\right]A_0(t)}{\sqrt{n_o}\int dt\,A_0^2(t)} \tag{5.95}$$

Here, τ_{st} is the carrier stimulated emission lifetime,

$$\frac{1}{\tau_{st}} = \frac{\partial G}{\partial N}\,n_o \tag{5.96}$$

When the non-radiative carrier recombination time τ_{nr} is much smaller than the pulse roundtrip time T_R, a condition true for most semiconductor mode-locked lasers, the equation for the carrier number fluctuations $\Delta\widehat{N}(T)$ is,

$$\begin{aligned}\frac{d\,\Delta\widehat{N}(T)}{dT} &= -\left(\frac{1}{\tau_{nr}}+\frac{1}{\tau_{st}}\right)\widehat{N}(T) \\ &\quad - n_o\sum_{k=0}^{\infty}\left\{\left[\frac{1}{\tau_p}+(\lambda_k-\lambda_0)\right]\widehat{c}_k(T)\int dt\,A_0^*(t)A_k(t)+h.c\right\} \\ &\quad - \sqrt{n_o}\sum_{k=0}^{\infty}\left\{\frac{\int dt\,F_{SP}(t,T)A_k(t)}{\int dt\,A_k^2(t)}\int dt\,A_0^*(t)A_k(t)+h.c\right\} \\ &\quad + \widehat{F}_{pump}(T)+\widehat{F}_{nr}(T) \qquad (5.97)\end{aligned}$$

where $\widehat{F}_{nr}(T)$ models the noise in non-radiative carrier recombination, and $\widehat{F}_{pump}(T)$ models the noise in the pump current. If the pumping process has shot noise then,

$$\langle\widehat{F}_{pump}(T)\,\widehat{F}_{pump}(T')\rangle = R_{pump}\,\delta(T-T') \qquad (5.98)$$

R_{pump} is the average rate at which carriers are pumped into the active region. The correlation function of $\widehat{F}_{nr}(T)$ is,

$$\langle\widehat{F}_{nr}(T)\,\widehat{F}_{nr}(T')\rangle \approx R_{nr}\,\delta(T-T') \qquad (5.99)$$

R_{nr} is the average carrier recombination rate. It can be shown that (5.95) and (5.97), together with (5.57), preserve all the quantum mechanical commutation relations for the operators $\widehat{c}_k(T)$.

5.7.1 Photon Number Fluctuations

The spectral densities $S_{\delta N_p}(\omega)$ and $S_{\Delta N_p}(\omega)$ of the photon number fluctuations $\delta\widehat{N}_p(T)$ and $\Delta\widehat{N}_p(T)$, respectively, are defined as in Appendix D.5.1. Equations (5.95) and (5.97) are easily solved in the frequency domain. The modulation response $H(\omega)$ of the laser is defined as [1],

$$H(\omega) = \frac{\omega_{ro}^2}{\omega_{ro}^2-\omega^2+j\omega\,\gamma} \qquad (5.100)$$

where the laser relaxation oscillation frequency ω_{ro} and the modulation damping constant γ are,

$$\omega_{ro}^2 = \frac{1}{\tau_{st}\,\tau_p} \tag{5.101}$$

$$\gamma = \frac{1}{\tau_{st}} + \frac{1}{\tau_{nr}} \tag{5.102}$$

Equation (5.97) for the carrier number fluctuations is valid only if ω_{ro} and γ are much smaller than $1/T_R$. The photon number noise spectral density $S_{\delta N_p}(\omega)$ can be found by retaining only the terms with $k = 0$ in (5.97). This preserves the equal time commutator $[\widehat{c}_0(T), \widehat{c}_0^{\dagger}(T)]$. The expression for $S_{\delta N_p}(\omega)$ is,

$$\begin{aligned}\frac{S_{\delta N_p}(\omega)}{n_o\,|H(\omega)|^2} &= \frac{\tau_p^2}{n_o}\,(R_{nr} + R_{pump}) \\ &\quad + \tau_p \left[(2n_{sp} - 1)\left(\omega^2 + \frac{1}{\tau_{nr}^2}\right)\tau_{st}^2 + \left(\omega^2 + \gamma^2\right)\tau_{st}^2 \right] \sqrt{1+\beta^2}\end{aligned} \tag{5.103}$$

The first term is the contribution from the non-radiative carrier recombination noise and the noise in the pump current. The second term is the noise contribution from spontaneous emission and vacuum field fluctuations. The term $\sqrt{1+\beta^2}$ in the equation above is the excess noise factor $1/|\int dt\, A_0{}^2(t)|^2$. Just as in the case of the timing noise, the spectral density $\underline{S}_{\delta N_p}(\omega)$ is defined to be equal to $S_{\delta N_p}(\omega)$ but with the excess noise factor $\sqrt{1+\beta^2}$ stripped off,

$$\frac{\underline{S}_{\delta N_p}(\omega)}{n_o\,|H(\omega)|^2} = \frac{\tau_p^2}{n_o}\,(R_{nr} + R_{pump}) + \tau_p \left[(2n_{sp} - 1)\left(\omega^2 + \frac{1}{\tau_{nr}^2}\right)\tau_{st}^2 + \left(\omega^2 + \gamma^2\right)\tau_{st}^2 \right] \tag{5.104}$$

$S_{\Delta N_p}(\omega)$ can be found by solving (5.57), (5.95), and (5.97),

$$\begin{aligned}\frac{S_{\Delta N_p}(\omega)}{n_o} &= \frac{\tau_p^2}{n_o}\,(\,R_{nr} + R_{pump}\,)\,|H(\omega)|^2 \\ &\quad + (2n_{sp} - 1) \sum_{k,q=0}^{\infty} \frac{M_{0k}\,M_{qk}\,M_{q0}}{\int dt\, A_q^{*2}(t)\ \int dt\, A_k{}^2(t)}\, F_{qk}(\omega) \\ &\quad + \sum_{k,q=0}^{\infty} \frac{M_{0k}\,M_{qk}\,M_{q0}}{\int dt\, A_q^{*2}(t)\ \int dt\, A_k{}^2(t)}\, G_{qk}(\omega)\end{aligned} \tag{5.105}$$

$F_{qk}(\omega)$ and $G_{qk}(\omega)$ are expressed in terms of the functions $f_k(\omega)$ and $g_k(\omega)$ where,

$$f_0(\omega) = \tau_{st}\left(j\omega + \frac{1}{\tau_{nr}}\right) H(\omega) \tag{5.106}$$

$$g_0(\omega) = \tau_{st}\,(j\omega+\gamma)\,H(\omega) \tag{5.107}$$

$$f_k(\omega) = -\left(\frac{j\omega+1/\tau_p}{j\omega-2k\lambda_0}\right)H(\omega)+\left(\frac{1/\tau_p}{j\omega-2k\lambda_0}\right) \qquad k\geq 1 \tag{5.108}$$

$$g_k(\omega) = -\left(\frac{2k\lambda_0+1/\tau_p}{j\omega-2k\lambda_0}\right)H(\omega)+\left(\frac{1/\tau_p}{j\omega-2k\lambda_0}\right) \qquad k\geq 1 \tag{5.109}$$

$$F_{qk}(\omega) = \frac{\tau_p}{2}\left[1+(2k\lambda_0+2q\lambda_0^*)\,\tau_p\right]\Big[f_k(\omega)f_q^*(\omega)+(\omega\rightarrow-\omega)\Big] \tag{5.110}$$

$$\approx \frac{\tau_p}{2}\Big[f_k(\omega)f_q^*(\omega)+(\omega\rightarrow-\omega)\Big] \tag{5.111}$$

$$G_{qk}(\omega) = \frac{\tau_p}{2}\Big[g_k(\omega)g_q^*(\omega)+(\omega\rightarrow-\omega)\Big] \tag{5.112}$$

The two series in Equation (5.105) diverge if the magnitude of the pulse chirp is larger than β_c. These series can be replaced by convergent series using (5.72),

$$\begin{aligned}\frac{S_{\Delta N_p}(\omega)}{n_o} &= \frac{\tau_p^2}{n_o}\,(\,R_{nr}+R_{pump}\,)\,|H(\omega)|^2 \\ &\quad+\frac{(2n_{sp}-1)}{\sqrt{1+\beta^2}}\sum_{k,q=0}^{N_{max}-1}M_{k0}^{-1}\,M_{qk}\,M_{0q}^{-1}\,F_{qk}(\omega) \\ &\quad+\frac{1}{\sqrt{1+\beta^2}}\sum_{k,q=0}^{N_{max}-1}M_{k0}^{-1}\,M_{qk}\,M_{0q}^{-1}\,G_{qk}(\omega)\end{aligned} \tag{5.113}$$

The expansion for $S_{\Delta N_p}(\omega)$ in (5.113) converges for all values of the pulse chirp β. The two series in the expression for $S_{\Delta N_p}(\omega)$ in (5.113) can be summed exactly when $\omega\approx 0$, and one obtains,

$$\begin{aligned}\frac{S_{\Delta N_p}(\omega=0)}{n_o} &= \frac{\tau_p^2}{n_o}\,(R_{nr}+R_{pump}) \\ &\quad+\tau_p\left[(2n_{sp}-1)\left(\frac{\tau_{st}}{\tau_{nr}}\right)^2\sqrt{1+\beta^2}\right. \\ &\quad\left.+\frac{\left(\sqrt{1+\beta^2}\frac{\tau_{st}}{\tau_{nr}}+1\right)^2+\sqrt{1+\beta^2}-1}{\sqrt{1+\beta^2}}\right]\end{aligned} \tag{5.114}$$

When $\omega\gg|4\lambda_0|$, a simple analytical expression for $S_{\Delta N_p}(\omega)$, analogous to (5.93), can be obtained,

$$S_{\Delta N_p}(\omega\gg|4\lambda_0|) = \underline{S}_{\delta N_p}(\omega) \tag{5.115}$$

Table 5.1: Parameter Values of a Semiconductor Mode-locked Laser Used in Fig. 5-11

Parameter	Value
Pulse photon number n_o	10^6
Pulse roundtrip time T_R	0.2 ns
Pulse repetition rate $1/T_R$	5.0 GHz
Pulse width τ	5.0 ps
Non-radiative recombination lifetime τ_{nr}	1.0 ns
Stimulated emission lifetime τ_{st}	1.2 ns
Laser relaxation oscillation frequency $\omega_{ro}/2\pi$	300 MHz
Damping frequency $\lvert 2\lambda_0 \rvert/2\pi$	1.8 MHz

Fig. 5-11 shows the spectral densities $S_{\Delta N_p}(\omega)$, $\underline{S}_{\delta N_p}(\omega)$, and $S_{\delta N_p}(\omega)$ for an actively mode-locked semiconductor laser. The values of the laser parameters are given in Table 5.1. R_{nr} and R_{pump} are both assumed to be zero. In semiconductor mode-locked lasers the values of the relaxation oscillation frequency ω_{ro} and the modulation damping constant γ are usually much larger than the value of $|2\lambda_0|$ (see Table 5.1). When only the first two eigenfunctions are used in the perturbative expansion, the excess noise factor increases the low frequency photon number noise of the pulse by a factor $\sqrt{1+\beta^2}$ (see (5.103)). The inclusion of the noise contribution from higher order eigenfunctions in $S_{\Delta N_p}(\omega)$ reduces the low frequency photon number noise and partially compensates the excess noise (see (5.114). At large frequencies, when $\omega \gg |4\lambda_0|$, $S_{\Delta N_p}(\omega)$ equals $\overline{S}_{\delta N_p}(\omega)$, and the excess noise disappears.

5.7.2 Phase Fluctuations

The equation for the pulse phase fluctuations $\delta\widehat{\Theta}(T)$ can be obtained from (5.95) using (5.34),

$$\frac{d\,\delta\widehat{\Theta}(T)}{dT} = -\frac{\alpha}{2\,\tau_{st}\,n_o}\,\Delta\widehat{N}(T) + \frac{1}{2j}\left[\frac{\int dt\,\left(\widehat{F}_{sp}(t,T)+\widehat{F}_V(t,T)\right)A_0(t)}{\sqrt{n_o}\int dt\,A_0^2(t)} - h.c\right] \tag{5.116}$$

The spectral density $S_{\delta\Theta}(\omega)$ can be found from (5.97) and (5.116),

$$\begin{aligned} S_{\delta\Theta}(\omega) &= \alpha^2\,\frac{\tau_p^2}{4\,n_o}\,(\,R_{nr}+R_{pump}\,)\,|H(\omega)|^2 \\ &\quad + \left(\frac{n_{sp}}{n_o}\right)\frac{1}{2\,\tau_p}\left[\frac{1}{\omega^2}+\alpha^2|H(\omega)|^2\left(\frac{1}{\omega^2}+\tau_p^2\right)\right]\sqrt{1+\beta^2} \end{aligned} \tag{5.117}$$

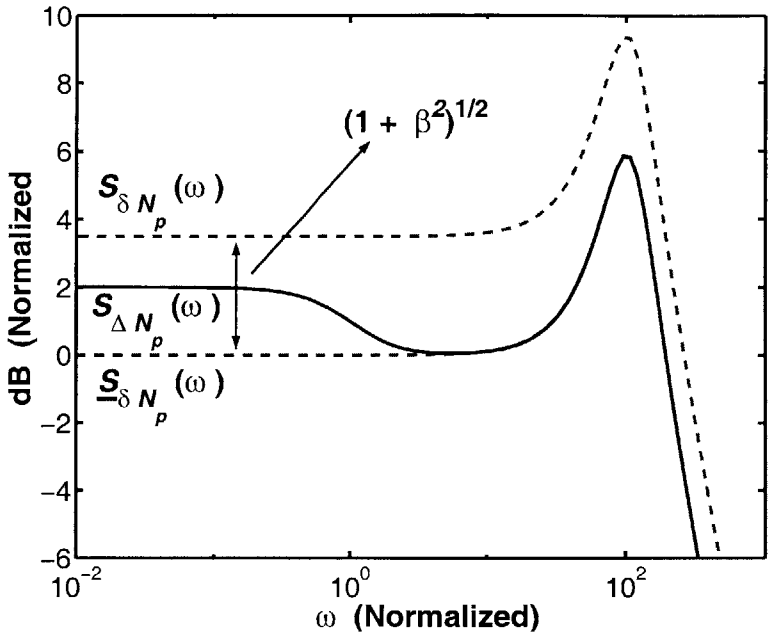

Figure 5-11: The photon number noise spectral densities $S_{\Delta N_p}(\omega)$, $\underline{S}_{\delta N_p}(\omega)$, and $S_{\delta N_p}(\omega)$ are shown for $\beta = 2.0$ and $P_M/A_M = 3.0$ for an actively mode-locked semiconductor laser. The values of the laser parameters are given in Table 5.1. R_{nr} and R_{pump} are both assumed to be zero. The spectral densities in the Figure have been normalized w.r.t. the value of $\underline{S}_{\delta N_p}(\omega)$ at $\omega = 0$. The frequency ω has been normalized to $|4\lambda_0|$. The resonance peak is due to the laser relaxation oscillations.

The factor $\sqrt{1+\beta^2}$ in the above equation is the excess noise factor $1/|\int dt\, {A_0}^2(t)|^2$. The spectral density $\underline{S}_{\delta\Theta}(\omega)$ is defined as equal to $S_{\delta\Theta}(\omega)$ but with the excess noise factor removed,

$$\begin{aligned}\underline{S}_{\delta\Theta}(\omega) &= \alpha^2 \frac{\tau_p^2}{4\,n_o}\,(\,R_{nr} + R_{pump}\,)\,|H(\omega)|^2 \\ &\quad + \left(\frac{n_{sp}}{n_o}\right)\frac{1}{2\,\tau_p}\left[\frac{1}{\omega^2} + \alpha^2|H(\omega)|^2\left(\frac{1}{\omega^2} + \tau_p^2\right)\right] \end{aligned} \tag{5.118}$$

The spectral density $S_{\Delta\Theta}(\omega)$ of the phase noise $\Delta\Theta(T)$ comes out to be,

$$\begin{aligned} S_{\Delta\Theta}(\omega) &= \alpha^2 \frac{\tau_p^2}{4\,n_o}\,(\,R_{nr} + R_{pump}\,)\,|H(\omega)|^2 \\ &\quad + \frac{(2n_{sp}-1)}{n_o}\sum_{k,q=0}^{\infty}\frac{M_{0k}\,M_{qk}\,M_{q0}}{\int dt\, A_q^{*2}(t)\;\int dt\, {A_k}^2(t)}\,U_{qk}(\omega) \\ &\quad + \frac{1}{n_o}\sum_{k,q=0}^{\infty}\frac{M_{0k}\,M_{qk}\,M_{q0}}{\int dt\, A_q^{*2}(t)\;\int dt\, {A_k}^2(t)}\,V_{qk}(\omega) \end{aligned} \tag{5.119}$$

$U_{qk}(\omega)$ and $V_{qk}(\omega)$ are expressed in terms of the functions $u_k(\omega)$ and $v_k(\omega)$ where,

$$u_k(\omega) = \frac{\alpha}{2}\left(1+\frac{2k\lambda_0+1/\tau_p}{j\omega-2k\lambda_0}\right)H(\omega)+\frac{1}{2j}\left(\frac{1/\tau_p}{j\omega-2k\lambda_0}\right) \tag{5.120}$$

$$v_k(\omega) = \frac{\alpha}{2}\left(\frac{2k\lambda_0+1/\tau_p}{j\omega-2k\lambda_0}\right)H(\omega)+\frac{1}{2j}\left(\frac{1/\tau_p}{j\omega-2k\lambda_0}\right) \tag{5.121}$$

$$U_{qk}(\omega) = \frac{\tau_p}{2}\left[1+(2k\lambda_0+2q\lambda_0^*)\,\tau_p\right]\left[u_k(\omega)u_q^*(\omega)+(\omega\rightarrow-\omega)\right] \tag{5.122}$$

$$\approx \frac{\tau_p}{2}\left[u_k(\omega)u_q^*(\omega)+(\omega\rightarrow-\omega)\right] \tag{5.123}$$

$$V_{qk}(\omega) = \frac{\tau_p}{2}\left[v_k(\omega)v_q^*(\omega)+(\omega\rightarrow-\omega)\right] \tag{5.124}$$

The two series in Equation (5.119) diverge if the magnitude of the pulse chirp is larger than β_c. As before, these series can be replaced by convergent series using (5.72),

$$\begin{aligned} S_{\Delta\Theta}(\omega) &= \alpha^2\frac{\tau_p^2}{4\,n_o}\left(R_{nr}+R_{pump}\right)|H(\omega)|^2 \\ &\quad+\frac{(2n_{sp}-1)}{n_o\sqrt{1+\beta^2}}\sum_{k,q=0}^{N_{max}-1}M_{k0}^{-1}\,M_{qk}\,M_{0q}^{-1}\,U_{qk}(\omega) \\ &\quad+\frac{1}{n_o\sqrt{1+\beta^2}}\sum_{k,q=0}^{N_{max}-1}M_{k0}^{-1}\,M_{qk}\,M_{0q}^{-1}\,V_{qk}(\omega) \end{aligned} \tag{5.125}$$

The expansion for $S_{\Delta\Theta}(\omega)$ in (5.125) converges for all values of the pulse chirp β. Analytical expressions for some simple cases can now be obtained. For frequencies much smaller than $|4\lambda_0|$ and the laser relaxation oscillation frequency ω_{ro}, one obtains,

$$S_{\Delta\Theta}(\omega\approx0) = S_{\delta\Theta}(\omega\approx0) = \left(\frac{n_{sp}}{n_o}\right)\frac{(1+\alpha^2)}{2\,\tau_p\,\omega^2}\sqrt{1+\beta^2} \tag{5.126}$$

Unlike pulse timing, frequency, and photon number fluctuations, pulse phase fluctuations at small frequencies exhibit the full excess noise factor $\sqrt{1+\beta^2}$ even when the noise contribution from the higher order eigenfunctions is included. This is because the pulse phase noise $\Delta\widehat{\Theta}(T)$ at small frequencies is dominated by the phase noise contribution from the first eigenfunction since the phase noise contribution from the first eigenfunction is not damped and executes a random walk. This phase diffusion at large time scales can be expressed in

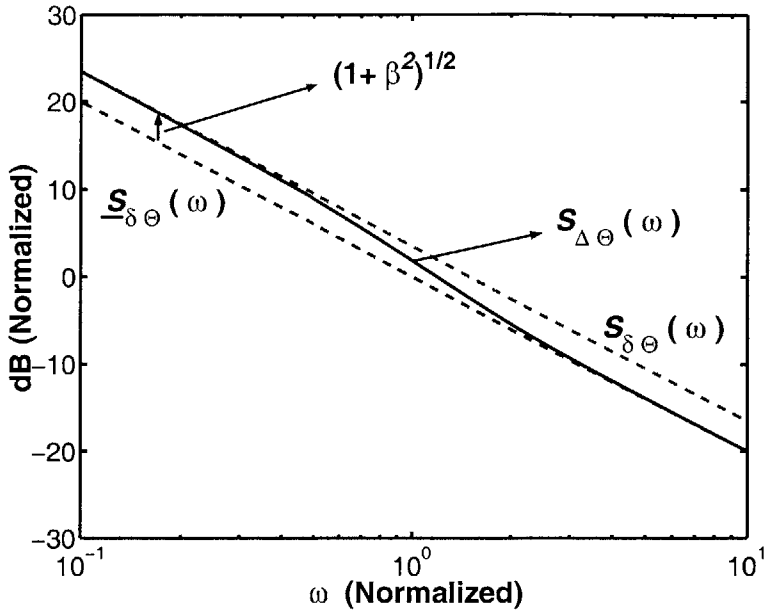

Figure 5-12: The phase noise spectral densities $S_{\Delta\Theta}(\omega)$, $\underline{S}_{\delta\Theta}(\omega)$, and $S_{\delta\Theta}(\omega)$ are shown for $\beta = 2.0$, $P_M/A_M = 3.0$, and $\alpha = 3.0$. The spectral densities in the Figure have been normalized w.r.t. the value of $\underline{S}_{\delta\Theta}(\omega)$ at $\omega = |4\lambda_0|$. The frequency ω has been normalized to $|4\lambda_0|$. The α parameter is assumed to be zero.

the time domain as follows,

$$\langle\,[\,\Delta\Theta(T) - \Delta\Theta(T')\,]^2\,\rangle = \langle\,[\,\delta\Theta(T) - \delta\Theta(T')\,]^2\,\rangle \approx \left(\frac{n_{sp}}{n_o}\right)\frac{(1+\alpha^2)}{2\,\tau_p}\sqrt{1+\beta^2}\;|T-T'| \tag{5.127}$$

When $\omega \gg |4\lambda_0|$, a result similar to (5.93) and (5.115) is obtained,

$$S_{\Delta\Theta}(\omega \gg |4\lambda_0|) = \underline{S}_{\delta\theta}(\omega) \tag{5.128}$$

The excess noise is absent at large frequencies. Fig. 5-12 shows the phase noise spectral densities $S_{\Delta\Theta}(\omega)$, $\underline{S}_{\delta\Theta}(\omega)$, and $S_{\delta\Theta}(\omega)$, all normalized to $\underline{S}_{\delta\Theta}(\omega = |4\lambda_0|)$, for $\beta = 2.0$, $P_M/A_M = 3.0$ and $\alpha = 3.0$. The phase noise spectral density $S_{\Delta\Theta}(\omega)$ at small frequencies shows the full excess noise factor $\sqrt{1+\beta^2}$. At frequencies larger than $|4\lambda_0|$, $S_{\Delta\Theta}(\omega)$ approaches $\underline{S}_{\delta\Theta}(\omega)$, and the excess noise disappears.

5.8 Noise in the Pulses Outside the Laser Cavity

The master equation (5.2) describes the temporal evolution of a single pulse inside the laser cavity as a function of the time variable T. In this section, the noise in the pulse inside the cavity is related to the noise in the pulses coming out of the cavity. The pulses coming out of the laser cavity are more appropriately described by labeling them with a discrete index. A brief review of the discrete time Fourier transforms and the associated noise spectral densities is given in Appendix D.5.2. The field operator of the m-th pulse which comes out of the laser at time $T = mT_R$ is assumed to be $\widehat{\phi}(t, m)$ and it obeys the commutation relation,

$$\left[\widehat{\phi}(t, m), \widehat{\phi}^{\dagger}(t', m)\right] = \delta(t - t') \tag{5.129}$$

The reflected vacuum fluctuations must be included to describe the noise in the pulses coming out of the laser cavity [86]. The photon lifetime τ_p can be expressed in the form,

$$\frac{1}{\tau_p} = \frac{1}{\tau_{pi}} + \frac{1}{\tau_{po}} \tag{5.130}$$

Here, τ_{po} is the lifetime associated with photon loss from the output coupler and τ_{pi} is the lifetime associated with photon loss due to all the other mechanisms. The noise operator for the vacuum fluctuations $\widehat{F}_V(t, T)$ in the master equation (5.2) can be written as,

$$\widehat{F}_V(t, T) = \widehat{F}_{Vi}(t, T) + \widehat{F}_{Vo}(t, T) \tag{5.131}$$

Assuming $n_{th} = 0$, the only non-zero correlations of the noise operators $\widehat{F}_{Vi}(t, T)$ and $\widehat{F}_{Vo}(t, T)$ are as follows,

$$\langle \widehat{F}_{Vi}(t, T)\, \widehat{F}^{\dagger}_{Vi}(t', T') \rangle = \frac{1}{\tau_{pi}}\, \delta(t - t')\, \delta(T - T') \tag{5.132}$$

$$\langle \widehat{F}_{Vo}(t, T)\, \widehat{F}^{\dagger}_{Vo}(t', T') \rangle = \frac{1}{\tau_{po}}\, \delta(t - t')\, \delta(T - T') \tag{5.133}$$

The relation between $\widehat{\phi}(t, m)$ and $\widehat{\phi}(t, T)$ is,

$$\widehat{\phi}(t, m) = \sqrt{\frac{T_R}{\tau_{po}}}\, \widehat{\phi}(t, T = mT_R) - \sqrt{T_R \tau_{po}}\, \widehat{F}_{Vo}(t, T = mT_R) \tag{5.134}$$

The second term on the right hand side represents the reflected vacuum fluctuations. The delta function $\delta(T - T')$ in (5.133) implies that the noise added to the pulse in different roundtrips is uncorrelated. Therefore, the correlation function in (5.133) for equal times must be interpreted as,

$$\langle \widehat{F}_{Vo}(t, T = mT_R)\, \widehat{F}^{\dagger}_{Vo}(t', T' = mT_R) \rangle = \frac{1}{T_R\, \tau_{po}}\, \delta(t - t') \tag{5.135}$$

$\widehat{\phi}(t, m)$ can also be expanded in terms of the functions $A_k(t)$,

$$\widehat{\phi}(t, m) = \sqrt{n'_o}\, A_0(t) + \sqrt{n'_o} \sum_{k=0}^{\infty} \widehat{d}_k(m)\, A_k(t) \tag{5.136}$$

where the average photon number in the output pulse n'_o equals $(T_R/\tau_{po})n_o$. (5.129) and (5.136) give the commutation relations for the operators $\widehat{d}_k(m)$,

$$\left[\widehat{d}_k(m)\, ,\, \widehat{d}^{\dagger}_q(m) \right] = \frac{1}{n'_o}\, \frac{\int dt\, A^*_q(t) A_k(t)}{\int dt\, A^{*2}_q(t)\ \int dt\, A_k{}^2(t)} \tag{5.137}$$

Equations (5.134) and (5.136) give,

$$\widehat{d}_k(m) = \widehat{c}_k(T = mT_R) - \frac{\tau_{po}}{\sqrt{n_o}}\, \frac{\int dt\, \widehat{F}_{Vo}(t, T = mT_R)\, A_k(t)}{\int dt\, A^2_k(t)} \tag{5.138}$$

It can be shown that the expression above satisfies the commutation relation for $\widehat{d}_k(m)$ in (5.137). The operators for the noise in the output pulses can be expressed in terms of $\widehat{d}_k(m)$ if the substitutions $\widehat{c}_k(T) \rightarrow \widehat{d}_k(m)$ and $n_o \rightarrow n'_o$ are made in (5.51)-(5.36). It should be noted that the operators $\Delta\widehat{N}_p(m)$, $\Delta\widehat{\Theta}(m)$, $\Delta\widehat{J}(m)$, $\Delta\widehat{\Omega}(m)$ and $\delta\widehat{N}_p(m)$, $\delta\widehat{\Theta}(m)$, $\delta\widehat{J}(m)$, $\delta\widehat{\Omega}(m)$ for the noise in the output pulses are functions of the discrete index m, and the corresponding noise spectral densities $\Phi_{\Delta N_p}(\omega T_R)$, $\Phi_{\Delta\Theta}(\omega T_R)$, $\Phi_{\Delta J}(\omega T_R)$, $\Phi_{\Delta\Omega}(\omega T_R)$ and $\Phi_{\delta N_p}(\omega T_R)$, $\Phi_{\delta\Theta}(\omega T_R)$, $\Phi_{\delta J}(\omega T_R)$, $\Phi_{\delta\Omega}(\omega T_R)$ are periodic functions of ω with a period $2\pi/T_R$ as shown in Appendix D.5.2.

5.8.1 Timing and Frequency Fluctuations in the Output Pulses

The spectral densities $\Phi_{\delta J}(\omega T_R)$ and $\Phi_{\Delta J}(\omega T_R)$ of the pulse timing noise $\delta\widehat{J}(m)$ and $\Delta\widehat{J}(m)$, respectively, can be determined using the methods described in Section 5.6, and one obtains,

$$\begin{aligned}\Phi_{\delta J}(\omega T_R) &= \frac{1}{T_R}\sum_{m=-\infty}^{\infty} S_{\delta J}\left(\omega - \frac{2\pi m}{T_R}\right) \\ &\quad + \frac{\tau^2}{2\,n_o}\left(1+\beta^2\right)^{3/2}\frac{1}{T_R}\sum_{m=-\infty}^{\infty} R\left(\omega - \frac{2\pi m}{T_R}\right) \\ &\quad + \frac{\tau^2}{2\,n_o'}\left(1+\beta^2\right)^{3/2} \qquad (5.139)\end{aligned}$$

$$\begin{aligned}\Phi_{\Delta J}(\omega T_R) &= \frac{1}{T_R}\sum_{m=-\infty}^{\infty} S_{\Delta J}\left(\omega - \frac{2\pi m}{T_R}\right) \\ &\quad + \frac{\tau^2}{2\,n_o}\frac{1}{T_R}\sum_{m=-\infty}^{\infty} R\left(\omega - \frac{2\pi m}{T_R}\right) \\ &\quad + \frac{\tau^2}{2\,n_o'} \qquad (5.140)\end{aligned}$$

where the function $R(\omega)$ is,

$$R(\omega) = \frac{(2\lambda_0 + 2\lambda_0^*)\left(\omega^2 + |2\lambda_0|^2\right)}{\left(\omega^2 - |2\lambda_0|^2\right)^2 + \omega^2\,(-2\lambda_0 - 2\lambda_0^*)^2} \qquad (5.141)$$

and $S_{\delta J}(\omega)$ and $S_{\Delta J}(\omega)$ are given by the exact expressions in (5.85) and (5.91), respectively. The last two terms on the right hand side in (5.139) and (5.140) are due to the reflected vacuum fluctuations. The mean square value $\langle\delta\widehat{J}^2(m)\rangle$ of the timing noise is,

$$\langle\delta\widehat{J}^2(m)\rangle = T_R\int_{-\pi/T_R}^{\pi/T_R}\frac{d\omega}{2\pi}\,\Phi_{\delta J}(\omega T_R) = \langle\delta\widehat{J}^2(T)\rangle + \frac{\tau^2}{2\,n_o'}\left(1 - \frac{n_o'}{n_o}\right)\left(1+\beta^2\right)^{3/2} \qquad (5.142)$$

and similarly,

$$\langle\Delta\widehat{J}^2(m)\rangle = \langle\Delta\widehat{J}^2(T)\rangle + \frac{\tau^2}{2\,n_o'}\left(1 - \frac{n_o'}{n_o}\right) \qquad (5.143)$$

The reflected vacuum fluctuations make negligible contribution to the mean square timing noise in the output pulses when $|\lambda_0| \ll 1/\tau_p$. The spectral densities $\Phi_{\delta\Omega}(\omega T_R)$ and $\Phi_{\Delta\Omega}(\omega T_R)$ and the mean square values $\langle\delta\widehat{\Omega}^2(m)\rangle$ and $\langle\Delta\widehat{\Omega}^2(m)\rangle$ of the pulse frequency fluctuations are related to the pulse timing fluctuations by a constant factor $\left(1+\beta^2\right)/\tau^4$

(see (5.50).

5.8.2 Photon Number and Phase Fluctuations in the Output Pulses

The spectral density $\Phi_{\delta N_p}(\omega T_R)$ of the pulse photon number noise $\delta\widehat{N}_p(m)$ can be determined using the methods described in Section 5.7, and one obtains,

$$\frac{\Phi_{\delta N_p}(\omega T_R)}{n'_o} = \frac{1}{T_R}\left(\frac{n'_o}{n_o}\right)\sum_{m=-\infty}^{\infty}\frac{S_{\delta N_p}\left(\omega-\frac{2\pi m}{T_R}\right)}{n_o} + \sqrt{1+\beta^2}\left[1-2\frac{\gamma\tau_{st}\tau_p}{T_R}\left(\frac{n'_o}{n_o}\right)\sum_{m=-\infty}^{\infty}\left|H\left(\omega-\frac{2\pi m}{T_R}\right)\right|^2\right] \quad (5.144)$$

where $S_{\delta N_p}(\omega)$ is given in (5.103). A simple expression can be obtained for the mean square photon number fluctuations $\langle\delta\widehat{N}_p^2(m)\rangle$,

$$\frac{\langle\delta\widehat{N}_p^2(m)\rangle}{n'_o} = T_R\int_{-\pi/T_R}^{\pi/T_R}\frac{d\omega}{2\pi}\frac{\Phi_{\delta N_p}(\omega T_R)}{n'_o} \quad (5.145)$$

$$= \left(\frac{n'_o}{n_o}\right)\frac{\langle\delta\widehat{N}_p^2(T)\rangle}{n_o}+\sqrt{1+\beta^2}\left(1-\frac{n'_o}{n_o}\right) \quad (5.146)$$

The second term on the right hand side is due to the reflected vacuum fluctuations and contains the excess noise factor $\sqrt{1+\beta^2}$. The spectral density $\Phi_{\Delta N_p}(\omega T_R)$ of the pulse photon number noise $\Delta\widehat{N}_p(m)$ is,

$$\frac{\Phi_{\Delta N_p}(\omega T_R)}{n'_o} = \frac{1}{T_R}\left(\frac{n'_o}{n_o}\right)\sum_{m=-\infty}^{\infty}\frac{S_{\Delta N_p}\left(\omega-\frac{2\pi m}{T_R}\right)}{n_o} + \left[1-2\frac{\gamma\tau_{st}\tau_p}{T_R}\left(\frac{n'_o}{n_o}\right)\sum_{m=-\infty}^{\infty}\left|H\left(\omega-\frac{2\pi m}{T_R}\right)\right|^2\right] \quad (5.147)$$

where $S_{\Delta N_p}(\omega)$ is given in (5.113). It follows from the expression above that the mean square value $\langle\Delta\widehat{N}_p^2(m)\rangle$ of the photon number fluctuations is,

$$\frac{\langle\Delta\widehat{N}_p^2(m)\rangle}{n'_o} = \left(\frac{n'_o}{n_o}\right)\frac{\langle\Delta\widehat{N}_p^2(T)\rangle}{n_o}+\left(1-\frac{n'_o}{n_o}\right) \quad (5.148)$$

The second term on the right hand side, which is due to the reflected vacuum fluctuations, does not have the excess noise factor.

The spectral densities $\Phi_{\delta\Theta}(\omega T_R)$ and $\Phi_{\Delta\Theta}(\omega T_R)$ of the pulse phase noise $\delta\widehat{\Theta}(m)$ and

$\Delta\widehat{\Theta}(m)$, respectively, are,

$$\Phi_{\delta\Theta}(\omega T_R) = \frac{1}{T_R}\sum_{m=-\infty}^{\infty} S_{\delta\Theta}\left(\omega - \frac{2\pi m}{T_R}\right) + \frac{1}{4\,n_o'}\sqrt{1+\beta^2}\left[1 - \frac{1}{T_R}\left(\frac{n_o'}{n_o}\right)\sum_{m=-\infty}^{\infty} 2\pi\delta\left(\omega - \frac{2\pi m}{T_R}\right)\right] \quad (5.149)$$

$$\Phi_{\Delta\Theta}(\omega T_R) = \frac{1}{T_R}\sum_{m=-\infty}^{\infty} S_{\Delta\Theta}\left(\omega - \frac{2\pi m}{T_R}\right) + \frac{1}{4\,n_o'}\left[1 - \frac{1}{T_R}\left(\frac{n_o'}{n_o}\right)\sum_{m=-\infty}^{\infty} 2\pi\delta\left(\omega - \frac{2\pi m}{T_R}\right)\right] \quad (5.150)$$

where $S_{\delta\Theta}(\omega)$ and $S_{\Delta\Theta}(\omega)$ are given by the exact expressions in (5.117) and (5.125), respectively. The last terms on the right hand side in (5.149) and (5.150) are due to the reflected vacuum fluctuations.

5.9 Pulse Fluctuation Operators and Noise Measurements

Earlier in this Chapter it was emphasized that when the eigenfunctions of the master equation (5.2) are not orthogonal, the operators $\Delta\widehat{N_p}(T)$, $\Delta\widehat{\Theta}(T)$, $\Delta\widehat{J}(T)$, and $\Delta\widehat{\Omega}(T)$ and not the operators $\delta\widehat{N_p}(T)$, $\delta\widehat{\Theta}(T)$, $\delta\widehat{J}(T)$, and $\delta\widehat{\Omega}(T)$, describe the pulse photon number, phase, timing, and frequency fluctuations, respectively. In this Section, we show how the pulse noise operators relate to the measurements of the pulse noise.

5.9.1 Photo-Detector Current Noise Measurements

The most widely used technique for characterizing the photon number and timing fluctuations of pulses from mode-locked lasers is measuring the spectral density of the photo-detector current noise [78, 79, 80, 88]. In this section, it is shown that the photo-detector current noise spectral density is directly related to the spectral densities $\Phi_{\Delta N_p}(\omega T_R)$ and $\Phi_{\Delta J}(\omega T_R)$ of the pulse photon number noise $\Delta\widehat{N_p}(m)$ and the timing noise $\Delta\widehat{J}(m)$, respectively, and not to the spectral densities $\Phi_{\delta N_p}(\omega T_R)$ and $\Phi_{\delta J}(\omega T_R)$ of the noise operators $\delta\widehat{N_p}(m)$ and $\delta\widehat{J}(m)$, respectively. The operator for the photo-detector current is,

$$\widehat{I}(t) = e\sum_{m=-\infty}^{\infty}\widehat{\phi}^{\dagger}(t - mT_R, m)\widehat{\phi}(t - mT_R, m) \quad (5.151)$$

where e is the electron charge, and $\widehat{\phi}(t,m)$ is the field operator for the m-th output pulse from the laser. It is assumed for simplicity that the photo-detector has unit quantum efficiency and an infinitely fast response. Both these assumption do not affect the arguments presented here. (5.151) can be written as,

$$\begin{aligned}\widehat{I}(t) &= en_o' \sum_{m=-\infty}^{\infty} A_0^*(t-mT_R)A_0(t-mT_R) \\ &\quad + e\sqrt{n_o'} \sum_{m=-\infty}^{\infty} \left[A_0^*(t-mT_R)\widehat{\psi}(t-mT_R,m) + h.c\right] \end{aligned} \tag{5.152}$$

The second term in the above equation is the current noise $\Delta\widehat{I}(t)$. The spectral density $S_{\Delta I}(\omega)$ of the current noise is defined in terms of the symmetric time averaged correlation function (see Appendix D.5.1),

$$S_{\Delta I}(\omega) = \lim_{T\to\infty} \frac{1}{T} \int_{-T/2}^{T/2} dt \int_{-\infty}^{\infty} dt' \, \frac{1}{2} \left[\langle \Delta\widehat{I}(t)\, \Delta\widehat{I}(t+t') \rangle + \langle \Delta\widehat{I}(t+t')\, \Delta\widehat{I}(t) \rangle \right] \exp\left(-j\omega\, t'\right) \tag{5.153}$$

After some algebra, (5.153) yields,

$$\begin{aligned} S_{\Delta I}(\omega) &\approx \frac{e^2}{T_R} \Big\{ \Phi_{\Delta N_p}(\omega T_R) + \omega^2 {n_o'}^2 \Phi_{\Delta J}(\omega T_R) \\ &\quad + j\omega\, n_o' \left[\Phi_{\Delta J\, \Delta N_p}(\omega T_R) - \Phi_{\Delta J\, \Delta N_p}(-\omega T_R) \right] \Big\} \end{aligned} \tag{5.154}$$

The spectral density $\Phi_{\Delta J\, \Delta N_p}(\omega T_R)$ is the discrete time Fourier transform of the symmetric cross correlation function between $\Delta\widehat{J}(m)$ and $\Delta\widehat{N}_p(m)$. At small frequencies, $S_{\Delta I}(\omega)$ is proportional to the spectral density $\Phi_{\Delta N_p}(\omega T_R)$ of the pulse photon number fluctuations. Assuming no correlation between the pulse photon number noise and timing noise, the pulse timing noise spectral density $\Phi_{\Delta J}(\omega T_R)$ can be obtained by measuring the current noise spectral density near a large harmonic of the pulse repetition frequency where the photon number noise is negligible. The timing noise spectral density $\Phi_{\Delta J}(\omega T_R)$ can be obtained more reliably by mixing the photo-detector current with a signal from the same RF oscillator that provides the active modulation for the mode-locked laser. In this case, the timing noise is measured relative to the timing (or phase) noise of the RF oscillator. By appropriately adjusting the phase of the signal before mixing it with the photo-detector current, the contribution from the pulse photon number fluctuations can be removed [78, 79, 80].

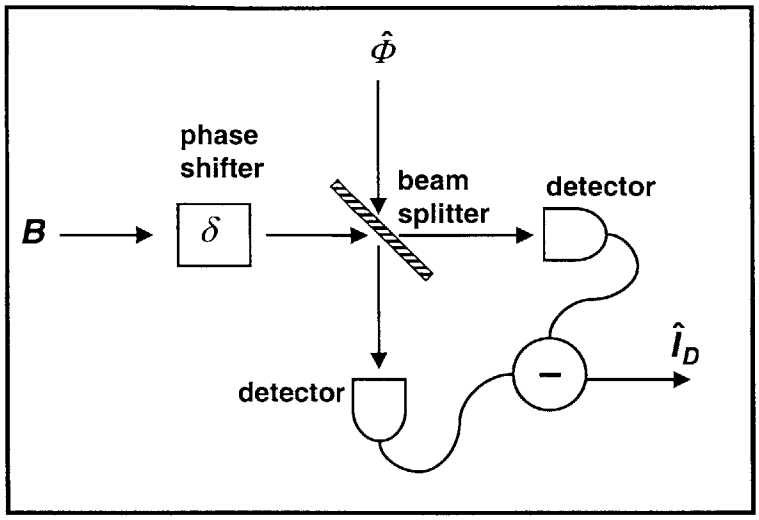

Figure 5-13: Balanced homodyne setup for measuring pulse noise.

5.9.2 Balanced Homodyne Measurements

The noise in the pulse can be measured in principle by homodyning as shown in Fig. 5-13. The scheme shown in Fig. 5-13 can only work in practice if the noise in the local oscillator pulses is much less than the noise in the measured pulses, and if the phase of the local oscillator pulses remains fixed relative to the phase of the pulses being measured. Pulses with large amplitude and envelope $B(t)$ are used as the local oscillator in Fig. 5-13. The local oscillator pulse shape can be tailored to project the desired pulse noise operator. It is assumed that the local oscillator pulses are perfect coherent states and can be treated classically. The operator for the difference current $\widehat{I}_D(t)$ is,

$$\widehat{I}_D(t) = e \sum_{m=-\infty}^{\infty} \left[B^*(t - mT_R)\widehat{\Phi}(t - mT_R, m)\, e^{-j\delta} + B(t - mT_R)\widehat{\Phi}^\dagger(t - mT_R, m)\, e^{j\delta} \right] \tag{5.155}$$

Below, expressions for the low frequency ($|\omega| \ll 2\pi/T_R$) spectral density $S_{I_D}(\omega)$ of the current $\widehat{I}_D(t)$ are given for different cases:

1. $B(t) = \sqrt{n_B} A_0(t)$ and $\delta = 0$

$$S_{I_D}(\omega) \approx \frac{e^2}{T_R} \left(\frac{n_B}{n_o'} \right) \Phi_{\Delta N_p}(\omega T_R) + \frac{4e^2\, n_B\, n_o'}{T_R^2} \sum_{m=-\infty}^{\infty} 2\pi\delta\left(\omega - \frac{2\pi m}{T_R} \right) \tag{5.156}$$

2. $B(t) = \sqrt{n_B}\, t A_0(t)$ and $\delta = 0$

$$S_{I_D}(\omega) \approx \frac{e^2\, n_B\, n_o'}{T_R}\, \Phi_{\Delta J}(\omega T_R) \tag{5.157}$$

3. $B(t) = \sqrt{n_B}\, \partial A_0(t)/\partial t$ and $\delta = \pi/2$

$$S_{I_D}(\omega) \approx \frac{e^2\, n_B\, n_o'}{T_R}\, \Phi_{\Delta\Omega}(\omega T_R) \tag{5.158}$$

5.9.3 Pulse Phase Noise Measurements

Outside the laser cavity, the phase diffusion of the pulses on long time scales follows from (5.127),

$$\langle\, [\, \Delta\Theta(m) - \Delta\Theta(n)\,]^2 \,\rangle = \langle\, [\, \delta\Theta(m) - \delta\Theta(n)\,]^2 \,\rangle \approx D_\Theta\ |m-n|\, T_R \tag{5.159}$$

where the phase diffusion constant D_Θ is,

$$D_\Theta = \left(\frac{n_{sp}}{n_o}\right) \frac{(1+\alpha^2)}{2\,\tau_p}\, \sqrt{1+\beta^2} \tag{5.160}$$

The linewidth of the optical cavity modes, as measured by an optical spectrum analyzer, is directly related to the phase diffusion constant D_Θ. The spectrum $S_{OSA}(\Omega)$ measured by an optical spectrum analyzer is the Fourier transform of the field auto-correlation function,

$$\begin{aligned} S_{OSA}(\Omega) \;=\; & \sum_{m,n=-\infty}^{\infty} \int_{-\infty}^{\infty} ds\, \frac{1}{2} \left[\, \langle \widehat{\phi}^\dagger(t - mT_R, m)\, \widehat{\phi}(t + s - nT_R, n) \rangle \right. \\ & \left. + \langle \widehat{\phi}(t + s - nT_R, n)\, \widehat{\phi}^\dagger(t - mT_R, m) \rangle \,\right] \\ & \times \exp\left\{-j\Omega_o\, [s + (m-n)T_R]\right\} \exp\left(j\Omega\, s\right) \end{aligned} \tag{5.161}$$

where Ω_o is the center optical frequency of the pulse. After some algebra, the above Equation yields,

$$S_{OSA}(\Omega) \;=\; |A_0(\Omega - \Omega_o)|^2 \left(\frac{n_o'}{T_R}\right) \frac{2\sinh\left(\dfrac{D_\Theta T_R}{2}\right)}{\left[2\sinh\left(\dfrac{D_\Theta T_R}{4}\right)\right]^2 + 2\,[1 - \cos\left(\Omega T_R\right)]} \tag{5.162}$$

$$\approx \left|A_0(\Omega-\Omega_o)\right|^2 \left(\frac{n_o'}{T_R^2}\right) \sum_{m=-\infty}^{\infty} \frac{D_\Theta}{\left(\frac{D_\Theta}{2}\right)^2 + \left(\Omega - \frac{2\pi m}{T_R}\right)^2} \tag{5.163}$$

The linewidth of the optical cavity modes is therefore equal to the diffusion constant D_Θ. Note that the full excess noise factor $\sqrt{1+\beta^2}$ contributes to the linewidth of the cavity modes.

5.10 Conclusion

In this Chapter, a theoretical model for the noise in actively mode-locked lasers with amplitude/phase modulation and group velocity dispersion was presented for the first time. While the model presented in this paper has general applicability, it was used to model the noise in semiconductor mode-locked lasers. It was shown that the RMS timing jitter in semiconductor mode-locked can be controlled by a combination of group velocity dispersion and phase modulation. Since phase modulation always accompanies amplitude modulation in semiconductor mode-locked lasers as a result of the non-zero α-parameter, the minimum value of the timing jitter can be controlled by adjusting the net cavity dispersion either by a suitable waveguide design or by an external dispersion compensator. This minimum value of the timing jitter can be less than the worst case timing jitter by a factor greater than 2. It was also shown that semiconductor mode-locked lasers can have less than 50 fs timing jitter at repetition rates of 10 GHz.

Chapter 6

Noise and Correlations in Harmonically Mode-Locked Semiconductor Lasers

6.1 Introduction

In a fundamentally mode-locked laser the active modulation is applied at the cavity round trip frequency, and only a single optical pulse propagates inside the laser cavity. In a laser mode-locked at the N-th harmonic, the active modulation is applied at a frequency N times the cavity round trip frequency, and N different optical pulses propagate inside the laser cavity. The pulse repetition frequency is therefore N times the cavity round trip frequency. Harmonically mode-locked lasers are attractive as sources of high repetition rate optical pulses that can be used in electro-optic sampling, optical analog-to-digital conversion, optical telecommunication systems, and ultra-fast optical measurements [2, 69, 79, 80, 89, 90, 91, 92, 93, 94, 95, 96, 97, 98, 99, 100, 101]. Passive harmonic mode-locking can also be accomplished with suitable laser cavity designs [98, 99, 100, 101].

The noise characteristics of harmonically mode-locked lasers can be much different from those of fundamentally mode-locked lasers. The noise in different pulses inside the laser cavity in a harmonically mode-locked laser can be correlated. The nature and origin of these noise correlations are explained in the next Section. In Chapter 5, it was shown that the photon number noise and the timing noise spectral density functions of mode-locked

lasers can be obtained experimentally from the photo-detector current noise spectral density using Von Der Linde's technique [88]. The noise spectral density functions of fundamentally mode-locked lasers have noise peaks at multiples of the pulse repetition frequency, and therefore there is only one noise peak in a bandwidth equal to the pulse repetition frequency. The noise spectral density functions of harmonically mode-locked lasers can have noise peaks at multiples of the cavity round trip frequency in addition to the noise peaks at multiples of the pulse repetition frequency [79, 90, 91, 96, 102, 103, 104]. Therefore, there can be N different noise peaks in a bandwidth equal to the pulse repetition frequency. The $(N-1)$ additional noise peaks have been called the supermode noise peaks in the literature [79, 90, 91, 96, 102, 103, 104]. Each supermode consists of a set of cavity modes separated from each other by the modulation frequency. Since the cavity mode spacing is N times smaller than the modulation frequency, there are N different supermodes. In actively harmonically mode-locked lasers, the phase of all the cavity modes belonging to the same supermode are locked by the active modulation. It has been suggested in the literature that the supermode noise peaks observed in the noise spectral density functions are related to the beating between different supermodes [96, 102, 103, 104].

In this Chapter, a model for the noise in Harmonically mode-locked lasers is presented. It is shown that the supermode noise peaks in the pulse noise spectral density functions are directly related to the correlations in the noise in different pulses inside the laser cavity. The nature of the correlations in the noise of different pulses inside the laser cavity provides insight into the underlying physics. Noise in pulses in a mode-locked laser can have contributions from several different sources, such as spontaneous emission, vacuum fluctuations, gain fluctuations, and the RF oscillator noise (see Chapter 5). These individual noise contributions can cause different types of noise correlations in the pulses in a harmonically mode-locked laser. For example, the contribution to the pulse timing noise from spontaneous emission and vacuum fluctuations is uncorrelated in different pulses, and the contribution to the pulse timing noise from the phase noise of the RF oscillator is positively correlated in all the pulses since all the pulses in the cavity are driven by the same active modulator. Gain competition in harmonically mode-locked semiconductor lasers can cause negatively correlated photon number fluctuations in different pulses. In addition, inter-cavity reflections that couple energy from one pulse to another can also cause the noise in the pulses to become correlated. Studying the correlations in the noise of different

pulses can therefore provide valuable information about the dynamics inside the laser. It is also shown that the noise correlations among the pulses can be determined exactly from the experimentally measured pulse noise spectral density functions. The information regarding these correlations resides in the distribution of the spectral weight among the N different noise peaks (including the $(N-1)$ supermode noise peaks) which appear in the noise spectral density functions in a bandwidth equal to the pulse repetition frequency.

6.2 Supermodes and Noise Correlations

In a fundamentally mode-locked laser, the pulse repetition rate equals $1/T_R$, where T_R is the cavity round trip time, and the cavity round trip frequency is $\omega_R = 2\pi/T_R$. In a harmonically mode-locked laser, the pulse repetition rate is $1/T_N = N/T_R$, and the cavity round trip frequency is $\omega_N = N\omega_R$. This notation will be used throughout this Chapter. The dominant sources of photon number and timing noise in mode-locked lasers are spontaneous emission and vacuum fluctuations [33, 34]. The spontaneous emission noise, as well as the vacuum fluctuation noise, that goes into different pulses in a harmonically mode-locked laser are independent, and therefore the noise in different pulses is mostly uncorrelated. Correlations in the noise in different pulses can arise in various ways, some of which are described below:

1. *Gain Dynamics:* The gain recovery times in fiber and semiconductor mode-locked lasers can be much longer than the pulse repetition times. Since all the pulses interact with the same gain medium, the noise in different pulses can become correlated. Pulse photon number fluctuations that are positively correlated in all the pulses are damped effectively by the gain medium since the slow gain medium responds to the average energy of the all the pulses. On the other hand, pulse photon number fluctuations that are negatively correlated in the pulses, and do not affect the average power, are not damped by the slow response of the gain medium. As a result, negatively correlated pulse photon number fluctuations can grow causing instabilities and pulse dropouts. Dynamic non-linearities, such as the Kerr effect in fiber lasers, can stabilize harmonically mode-locked operation [92, 108, 109, 110]. When these dynamic non-linearities are small, the pulse photon number fluctuations can become negatively correlated. Numerical simulations of harmonically mode-locked semiconductor lasers

in Ref. [111] indicate negatively correlated photon number fluctuations in the pulses inside the laser cavity.

2. *Optical Fabry-Perot Filters:* Experimental results for harmonically mode-locked lasers with optical Fabry-Perot filters placed inside the laser cavities have been reported in Refs. [103, 112, 113]. If a high-Q Fabry-Perot filter with a free spectral range equal to the pulse repetition frequency ω_N $(= N\omega_R)$ is placed inside a harmonically mode-locked laser cavity then some fraction of the noise in each optical pulse will be transferred to the subsequent pulse because of the Fabry-Perot cavity. As a result, the noise in all the pulses in the laser cavity will become positively correlated. If the free spectral range of the Fabry-Perot cavity is $m\omega_R$, where m is some non-zero integer less than N such that N is a multiple of m, then some fraction of the noise in each pulse is injected into the m-th subsequent pulse. Consequently, the noise in every m-th pulse inside the laser cavity will become positively correlated.

3. *Composite Cavity Harmonically Mode-Locked Lasers:* Recently, experimental results have been reported for the noise spectral densities in composite cavity harmonically mode-locked fiber lasers in Refs. [104, 107]. In these lasers, an all-fiber Mach-Zehnder interferometer with unbalanced arms is inserted into the laser cavity. If the difference in the time taken by the optical pulses to traverse the two arms of the interferometer equals mT_N, where m is some non-zero integer less than N such that N is a multiple of m, then some fraction of the noise in each pulse is injected into the m-th subsequent pulse, and therefore the noise in every m-th pulse will become positively correlated.

4. *RF Oscillator Noise:* In actively harmonically mode-locked lasers all the optical pulses in the laser cavity are driven by the same active modulator. The amplitude and phase noise in the RF oscillator is typically at low frequencies. Therefore, the noise in the pulses coming from the amplitude and/or phase noise of the external RF oscillator is expected to be positively correlated in all the pulses in the laser cavity. This case is considered in greater detail later in the Chapter.

The list above is not meant to be exhaustive, but only intended to provide some concrete examples.

6.3 Noise Spectral Density Functions and Noise Correlations

In Chapter 5, it was shown that the noise in the pulse train coming out of a mode-locked laser is characterized by the noise spectral density functions $\Phi_{\Delta A \Delta B}(\omega T)$, where $\{\Delta A\,,\,\Delta B\}$ stand for any one of the pulse noise fluctuations ΔN_p, $\Delta\Theta$, ΔJ, and $\Delta\omega$, and T is the pulse repetition time. For convenience, it is assumed in this chapter that ΔN_p, $\Delta\Theta$, ΔJ, and $\Delta\omega$ are classical noise variables and not quantum mechanical operators. None of the arguments of this Chapter are affected by this assumption. T equals T_R and T_N in fundamentally and harmonically mode-locked lasers, respectively. The noise spectral density functions are the discrete-time Fourier transforms of the noise correlation functions $R_{\Delta A \Delta B}(n)$ (for details see Appendix D.5.2),

$$R_{\Delta A \Delta B}(n) = \langle \Delta A(n)\, \Delta B(0) \rangle \tag{6.1}$$

$$\Phi_{\Delta A \Delta B}(\omega T) = \sum_{n=-\infty}^{\infty} R_{\Delta A \Delta B}[n]\, \exp\left(-j\omega T\, n\right) \tag{6.2}$$

The discrete index n is used as a label for the n-th optical pulse coming out of the mode-locked laser. From the definition of the noise spectral density functions in (6.2), it is obvious that the noise spectral density functions are periodic in frequency with a period equal to the pulse repetition frequency $2\pi/T$, i.e. $\Phi_{\Delta A \Delta B}(\omega T + 2\pi) = \Phi_{\Delta A \Delta B}(\omega T)$. If the noise spectral density functions $\Phi_{\Delta A \Delta B}(\omega T)$ are known, the noise correlation functions can be found by the inverse Fourier transform [105],

$$R_{\Delta A \Delta B}[n] = T \int_{-\pi/T}^{\pi/T} \frac{d\omega}{2\pi}\ \Phi_{\Delta A \Delta B}(\omega T)\ \exp\left(j\omega T\, n\right) \tag{6.3}$$

It follows from the Equation above that the mean square values, $\langle \Delta A^2 \rangle$, are given as,

$$\langle \Delta A^2 \rangle = R_{\Delta A \Delta A}(0) = T \int_{-\pi/T}^{\pi/T} \frac{d\omega}{2\pi}\ \Phi_{\Delta A \Delta A}(\omega T) \tag{6.4}$$

Note that the full integration bandwidth in (6.4) equals the pulse repetition frequency $2\pi/T$. Below, the noise correlation functions and the noise spectral density functions of fundamentally and harmonically mode-locked lasers are discussed in detail.

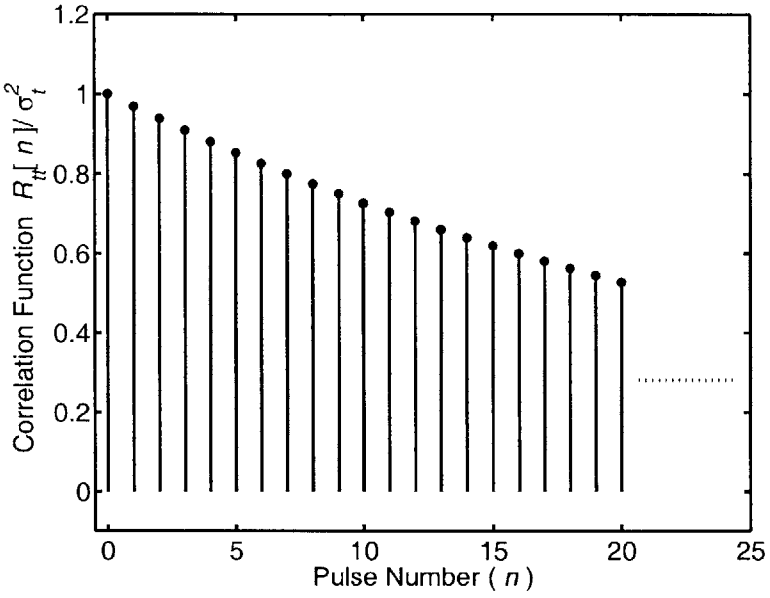

Figure 6-1: The timing noise correlation function $R_{\Delta J \Delta J}(n)$ (normalized to the RMS timing jitter) is plotted for the output pulses from a fundamentally mode-locked laser. T_R is assumed to be 1 nsec. γT_R is 0.01π. The RMS timing jitter is assumed to be 100 fs.

6.4 Fundamentally Mode-Locked Lasers

In a fundamentally mode-locked laser, as shown in Chapter 5, the noise spectral density functions $\Phi_{\Delta A \Delta B}(\omega T_R)$ have identical noise peaks at multiples of the pulse repetition frequency ω_R (for details see Chapter 5). The width of the noise peaks depends on how fast the noise correlation function $R_{\Delta A \Delta B}(n)$ decays with $|n|$. As an example, the pulse timing noise in an actively mode-locked semiconductor laser is discussed below in detail. In order to keep the analysis simple, it is assumed that group velocity dispersion and active phase modulation are both absent. Th effect of dispersion and phase modulation on the timing noise in fundamentally mode-locked lasers is discussed in detail in Chapter 5. In the next Section, the example discussed below will be modified for harmonically mode-locked lasers.

A finite difference equation for the pulse timing noise $\Delta J(n)$ at any location inside the cavity can be derived from the model discussed in Chapter 5(also see Appendix E.1 for details),

$$\Delta J(n+1) - \Delta J(n) = -\gamma T_R \, \Delta J(n) + F(n) \tag{6.5}$$

The above Equation expresses the fact that the pulse timing noise decreases after every

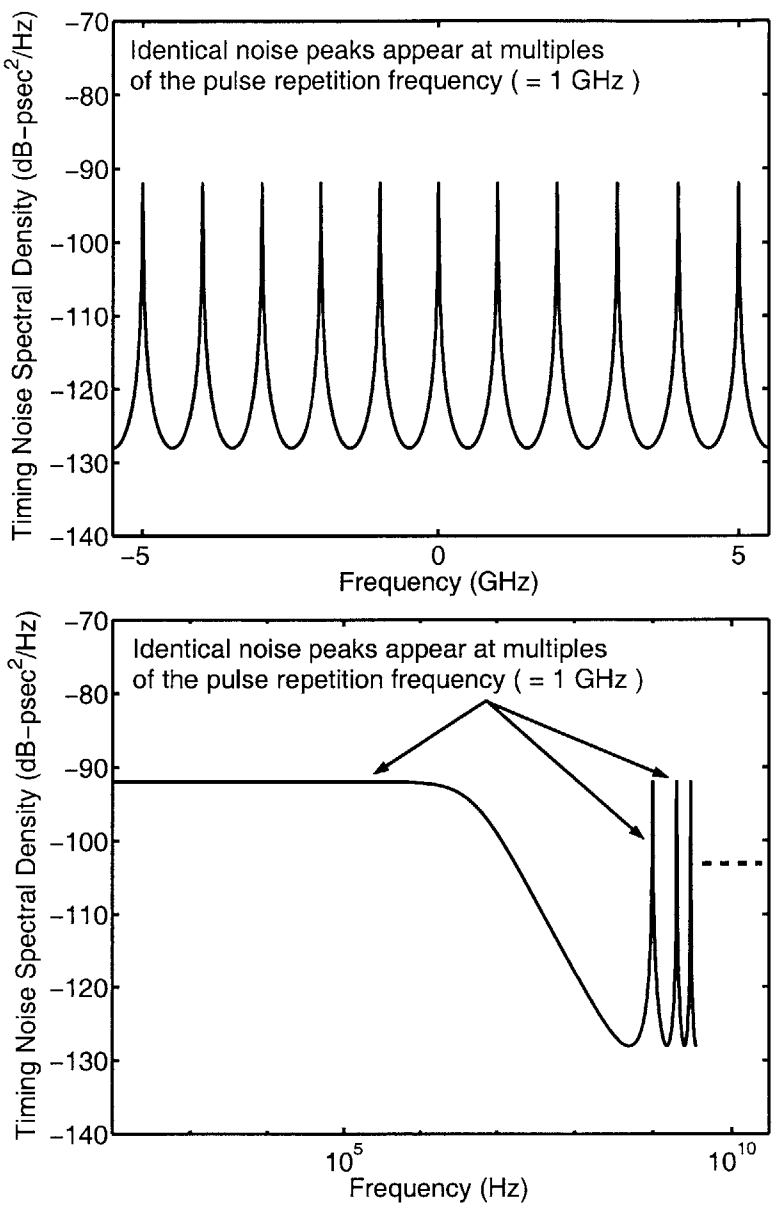

Figure 6-2: The timing noise spectral density $T_R\Phi_{\Delta J\Delta J}(\omega T_R)$ (note the multiplication with T_R to conform to the units used in the literature) is plotted for a fundamentally mode-locked laser on a linear frequency scale and on a log frequency scale. The timing noise spectral density shown corresponds to the timing noise correlation function in Fig. 6-1. The cavity round trip time T_R is 1.0 nsec. γT_R equals 0.01π. The RMS timing jitter is assumed to be 100 fs. The spectral density has identical noise peaks at multiples of the pulse repetition frequency ω_R.

pass through the active modulator. It is assumed that $\gamma T_R \ll 1$ and the pulse timing noise does not change significantly in one round trip. In (6.5), the pulse timing noise has been modeled by a discrete-time finite difference equation instead of a continuous-time differential equation as in Chapter 5. It will become clear in the sections that follow that finite difference equations are much more appropriate for describing the correlations in the noise in different pulses inside the laser cavity in harmonically mode-locked lasers. $F(n)$ in (6.5) represents the contribution from spontaneous emission and vacuum fluctuations added to the pulse timing noise in each round trip. $F(n)$ has the correlation function,

$$\langle F(n)\, F(m)\rangle = D\, \delta_{n,m} \tag{6.6}$$

Expressions for D and γ are given in Appendix E.1. The timing noise correlation function $R_{\Delta J \Delta J}(n)$ for the output pulses can be obtained directly from (6.5) and (6.6), and after a little algebra one obtains,

$$\begin{aligned} R_{\Delta J \Delta J}(n) &= \frac{D}{2\gamma T_R}\,(1-\gamma T_R)^{|n|} \\ &\approx \frac{D}{2\gamma T_R}\, e^{-\gamma T_R |n|} \qquad \text{since } \gamma T_R \ll 1 \end{aligned} \tag{6.7}$$

The mean square timing jitter is,

$$\langle \Delta J^2 \rangle = R_{\Delta J \Delta J}(0) = \frac{D}{2\gamma T_R} \tag{6.8}$$

The correlation function $R_{\Delta J \Delta J}(n)$ is shown in Fig. 6-1 for $T_R = 1.0$ nsec, $\gamma T_R = 0.01\pi$, and $sqrt\langle \Delta J^2 \rangle = 100$ fs. The timing noise spectral density can be obtained from the correlation function using the Fourier transform relation in (6.2),

$$\Phi_{\Delta J \Delta J}(\omega T_R) = \langle \Delta J^2 \rangle \frac{2\gamma T_R}{1 + (1+\gamma T_R)^2 - 2\,(1-\gamma T_R)\cos(\omega T_R)} \tag{6.9}$$

$$\approx \frac{\langle \Delta J^2 \rangle}{T_R} \sum_{n=-\infty}^{\infty} \frac{2\gamma}{(\omega - n\omega_R)^2 + \gamma^2} \qquad \text{since } \gamma T_R \ll 1 \tag{6.10}$$

As expected, the timing noise spectral density has identical noise peaks centered at multiples of the pulse repetition frequency ω_R. The timing noise spectral density is shown in Fig. 6-2 for the correlation function shown in Fig. 6-1, and the values of the parameters are assumed

to be the same as those in Fig. 6-1.

6.5 Harmonically Mode-locked Lasers: Uncorrelated Noise

In this section, it is shown that the supermode noise peaks appear in the noise spectral density functions of harmonically mode-locked lasers when the noise in different pulses inside the laser cavity is uncorrelated. The correlations in the noise in the pulses coming out of the laser cavity at time scales shorter than the cavity round trip time are directly related to the noise correlations in the pulses in the laser cavity. If the noise in the pulses inside the laser cavity is uncorrelated, the correlation function $R_{\Delta A \Delta B}(n)$ for the noise in the output pulses is zero unless the index n is some multiple of the harmonic number N. This is because every N-th output pulse is generated by the same pulse inside the laser cavity after one complete round trip. This observation, without any additional assumptions, leads directly to the supermode noise peaks in the pulse noise spectral density functions, as shown below. From (6.2), the noise spectral density is,

$$\begin{aligned} \Phi_{\Delta A \Delta B}(\omega T_R) &= \sum_{n=-\infty}^{\infty} R_{\Delta A \Delta B}(n) \exp\left(-j\omega T_N n\right) \\ &= \sum_{k=-\infty}^{\infty} R_{\Delta A \Delta B}(Nk) \exp\left(-j\omega T_R k\right) \end{aligned} \tag{6.11}$$

Recall that the noise spectral density functions are by definition periodic in frequency with a period equal to the pulse repetition frequency (which is ω_N in the present case). However, (6.11) shows that when the noise is uncorrelated in the pulses inside the laser cavity, the noise spectral density functions $\Phi_{\Delta A \Delta B}(\omega T_R)$ are periodic in frequency with a period equal to the cavity round trip frequency ω_R. This implies that if the noise spectral density functions have noise peaks located at integral multiples of the pulse repetition frequency ω_N, then between any two such noise peaks there must be $(N-1)$ identical noise peaks located at integral multiples of the cavity round trip frequency ω_R. These additional noise peaks are the supermode noise peaks. Below, this is demonstrated explicitly for the timing noise in a harmonically mode-locked laser.

The finite difference equation for the pulse timing noise in a semiconductor laser mode-locked at the N-th harmonic with uncorrelated timing noise in different pulses inside the

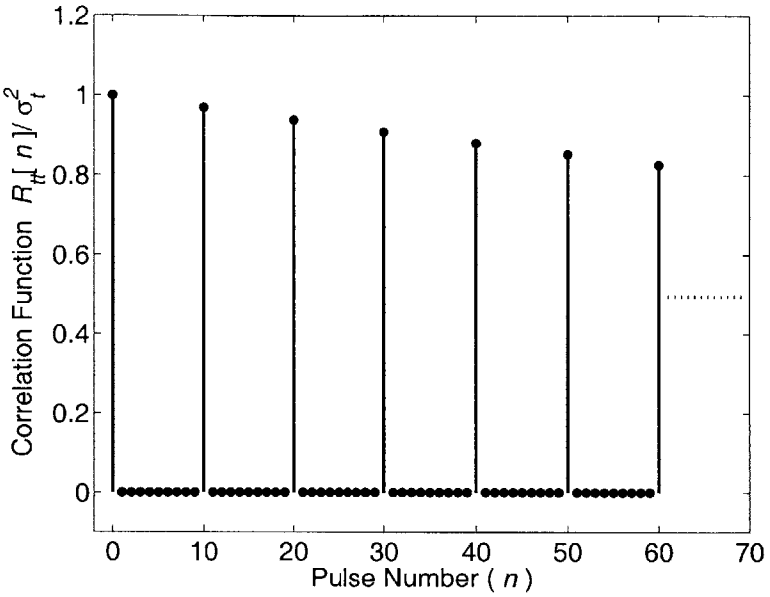

Figure 6-3: The timing noise correlation function $R_{\Delta J \Delta J}(n)$ (normalized to the RMS timing jitter) is plotted for the output pulses from a laser mode-locked at the tenth harmonic ($N = 10$) when the timing noise in different pulses inside the laser cavity is completely uncorrelated. The timing noise in every tenth pulse in the output is correlated. T_R is assumed to be 1 nsec. γT_R is assumed to be 0.01π. The RMS timing jitter is assumed to be 100 fs.

laser cavity is (see Appendix E.1 for details),

$$\Delta J(n+N) - \Delta J(n) = -\gamma_N T_R \, \Delta J(n) + F_N(n) \tag{6.12}$$

Note that $\Delta J(n+N)$ appears on the left hand side of the above Equation. This is because in a harmonically mode-locked laser the n-th pulse at any location in the laser cavity becomes the $(n+N)$-th pulse at the same location after it goes through one complete round trip. In essence, (6.12) is a compact way of writing N separate finite difference equations for the timing noise in N different pulses inside the laser cavity. When $N = 1$, (6.12) reduces to (6.5) for fundamentally mode-locked lasers. The noise source $F_N(n)$ has the correlation function,

$$\langle F_N(n) \, F_N(m) \rangle = D_N \, \delta_{n,m} \tag{6.13}$$

Expressions for D_N and γ_N are given in Appendix E.1. It is assumed that $\gamma_N T_R \ll 1$ and the pulse timing noise does not change significantly in one round trip. The timing noise

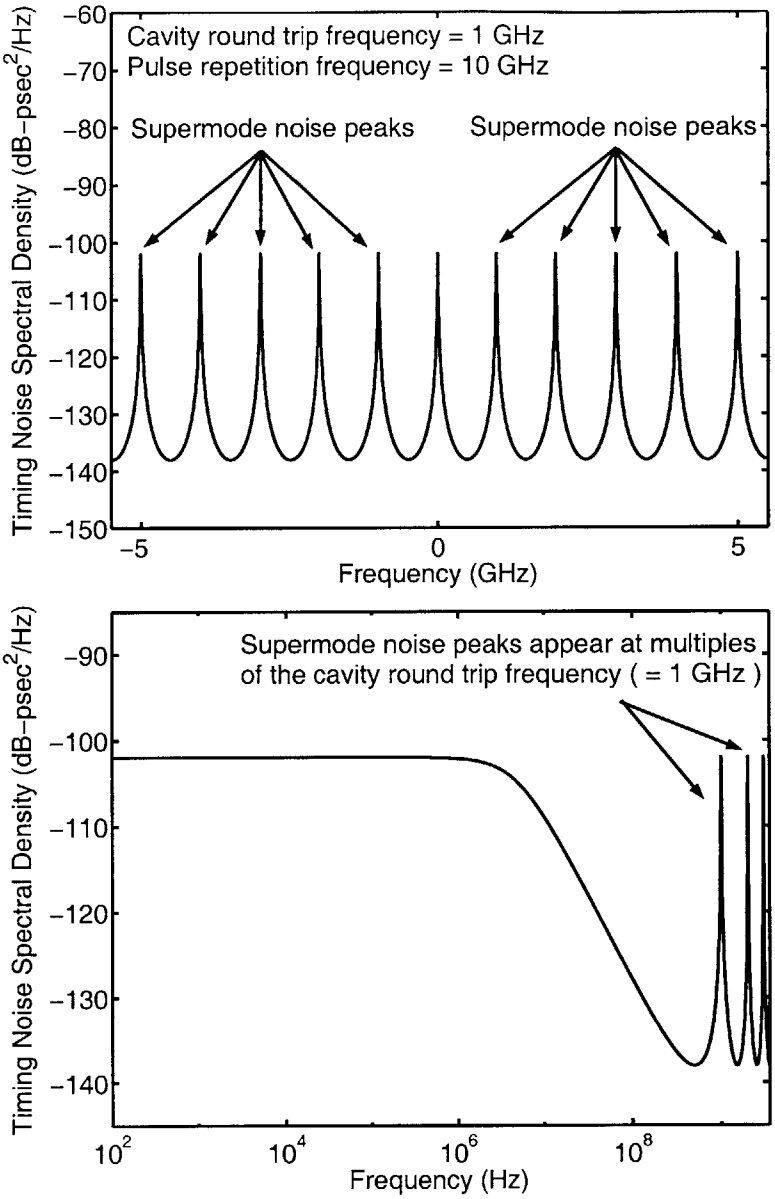

Figure 6-4: The pulse timing noise spectral density $T_N \Phi_{\Delta J \Delta J}(\omega T_N)$ (note the multiplication with T_N to conform to the units used in the literature) is plotted for a laser mode-locked at the tenth harmonic ($N = 10$) on linear and log frequency scales. The timing noise spectral density shown in the Figure corresponds to the timing noise correlation function in Fig. 6-3. T_R is 1.0 nsec. T_N is 0.1 nsec. $\gamma_N T_R$ is assumed to be 0.01π. The RMS timing jitter is assumed to be 100 fs. The timing noise in different pulses inside the laser cavity is assumed to be completely uncorrelated and, consequently, the periodicity of the noise spectral density is reduced from the pulse repetition frequency (10 GHz) to the cavity round trip frequency (1 GHz). Supermode noise peaks appear at multiples of the cavity round trip frequency. All the noise peaks are identical.

correlation function $R_{\Delta J \Delta J}(n)$ for the output pulses follows directly from (6.12) and (6.13),

$$R_{\Delta J \Delta J}(n) = \begin{cases} \dfrac{D_N}{2\gamma_N T_R}\,(1-\gamma_N T_N)^{|n|} \approx \dfrac{D_N}{2\gamma_N T_R}\,e^{-\gamma_N T_N |n|} & \text{if } n \text{ is an integral multiple of } N \\ 0 & \text{otherwise} \end{cases} \tag{6.14}$$

The mean square timing jitter $\langle \Delta J^2 \rangle$ is,

$$\langle \Delta J^2 \rangle = R_{\Delta J \Delta J}(0) = \frac{D_N}{2\gamma_N T_R} \tag{6.15}$$

The timing noise correlation function in (6.14) is shown in Fig. 6-3 for a laser mode-locked at the tenth harmonic ($N = 10$). In Fig. 6-3, $T_R = 1.0$ nsec, $\gamma T_R = 0.01\pi$, and $\sqrt{\langle \Delta J^2 \rangle} = 100$ fs. The timing noise in the output pulses at time scales shorter than the cavity round trip time T_R is uncorrelated. This is because the timing noise in different pulses in the laser cavity is uncorrelated. The timing noise spectral density can be obtained from the correlation function in (6.14) by using the Fourier transform relation in (6.2),

$$\Phi_{\Delta J \Delta J}(\omega T_N) = \langle \Delta J^2 \rangle \frac{2\gamma_N T_R}{1 + (1-\gamma_N T_R)^2 - 2(1-\gamma_N T_R)\cos(\omega T_R)} \tag{6.16}$$

$$\approx \frac{\langle \Delta J^2 \rangle}{N T_N} \sum_{n=-\infty}^{\infty} \frac{2\gamma_N}{(\omega - n\omega_R)^2 + \gamma_N^2} \qquad \text{since } \gamma_N T_R \ll 1 \tag{6.17}$$

The above equation shows that the timing noise spectral density has identical noise peaks at multiples of the cavity round trip frequency ω_R. The noise peaks other than the ones at multiples of the pulse repetition frequency ω_N are the supermode noise peaks. The supermode noise peaks in the timing noise spectral density are a direct consequence of the timing noise being uncorrelated in different pulses inside the laser cavity. The timing noise spectral density function in (6.17) is plotted in Fig. 6-4 for a laser mode-locked at the tenth harmonic ($N = 10$). The values assumed for the parameters are the same as the ones used in generating Fig. 6-3.

Characterization of the Pulse Noise and Integration Bandwidth for the Mean Square Fluctuations

When the noise in different pulses in the laser cavity is uncorrelated, the pulse noise spectral density functions are periodic in frequency with a period equal to ω_R, and the mean square

values for the fluctuations can be obtained by integrating $\Phi_{\Delta A \Delta A}(\omega T_N)$ over a bandwidth equal to ω_R instead of the full bandwidth ω_N,

$$\langle \Delta A^2 \rangle = T_N \int_{-\omega_N/2}^{\omega_N/2} \frac{d\omega}{2\pi} \Phi_{\Delta A \Delta A}(\omega T_N) \tag{6.18}$$

$$= N T_N \int_{-\omega_R/2}^{\omega_R/2} \frac{d\omega}{2\pi} \Phi_{\Delta A \Delta A}(\omega T_N) \tag{6.19}$$

$$\tag{6.20}$$

The integration bandwidth can therefore be reduced to the cavity round trip frequency ω_R provided the result is multiplied by a factor of N.

As discussed in Chapter 5, the noise in optical pulses from mode-locked lasers can be characterized by measuring the spectral density of the photo-detector current noise. In Chapter 5, it is shown that the photo-detector current noise spectral density $S_{\Delta I \Delta I}(\omega)$ is related to the pulse noise spectral densities $\Phi_{\Delta N_p \Delta N_p}(\omega T_N)$ an $\Phi_{\Delta J \Delta J}(\omega T_N)$ as follows,

$$S_{\Delta I \Delta I}(\omega) \approx \frac{e^2}{T_N} \Big\{ \Phi_{\Delta N_p \Delta N_p}(\omega T_N) + \omega^2 {n'_o}^2 \Phi_{\Delta J \Delta J}(\omega T_N) + j\omega n'_o \left[\Phi_{\Delta J \Delta N_p}(\omega T_N) - \Phi_{\Delta J \Delta N_p}(-\omega T_N) \right] \Big\} \tag{6.21}$$

The mean square value for the pulse photon number fluctuations can be determined from the experimentally measured photo-detector current noise spectral density $S_{\Delta I \Delta I}(\omega)$ by integrating over a bandwidth equal to ω_N near $\omega = 0$ where the contribution from the pulse timing fluctuations is expected to be small,

$$\frac{\langle \Delta N_p^2 \rangle \, [measured]}{{n'_o}^2} = \int_{-\omega_N/2}^{\omega_N/2} \frac{d\omega}{2\pi} \frac{S_{\Delta I \Delta I}(\omega)}{I^2} \tag{6.22}$$

$$= N \int_{-\omega_R/2}^{\omega_R/2} \frac{d\omega}{2\pi} \frac{S_{\Delta I \Delta I}(\omega)}{I^2} \tag{6.23}$$

where I is the average photo-detector current and equals en'_o/T_N. Assuming that the pulse photon number fluctuations make small contributions to $S_{\Delta I \Delta I}(\omega)$ near a large harmonic number m of the pulse repetition frequency, the mean square value for the pulse timing fluctuations can be determined as follows,

$$\langle \Delta J^2 \rangle \, [measured] = \int_{(m-1/2)\omega_N}^{(m+1/2)\omega_N} \frac{d\omega}{2\pi} \frac{S_{\Delta I \Delta I}(\omega)}{(\omega I)^2} \tag{6.24}$$

$$= N \int_{m\,\omega_N-\omega_R/2}^{m\,\omega_N+\omega_R/2} \frac{d\omega}{2\pi} \frac{S_{\Delta I \Delta I}(\omega)}{(\omega\, I)^2} \tag{6.25}$$

The supermode noise peaks have been largely ignored in the literature. To the best of the author's knowledge, all the experimental results presented in the literature for the mean square photon number and timing noise of pulses in harmonically mode-locked lasers have left out the contribution to the mean square fluctuations from the supermode noise peaks [79, 90, 91, 93, 94, 97]. When the noise is uncorrelated in different pulses inside the laser cavity, (6.23) and (6.25) show that ignoring the contribution from the supermode noise peaks gives mean square fluctuations that are less than the correct values by a factor of N. The procedure for determining the mean square pulse fluctuations by integrating only over a bandwidth equal to the cavity round trip frequency ω_R and multiplying the result by N is justified only if all the noise peaks are identical. The noise peaks are not identical when the noise in different pulses in the laser cavity is correlated.

6.6 Harmonically Mode-Locked Lasers: Correlated Noise

In the previous section, it was shown that the noise spectral density functions can have N noise peaks in a bandwidth equal to the pulse repetition frequency ω_N. When the noise in different pulses in the cavity is uncorrelated, all the N noise peaks are identical and have the same spectral weight. Here, it is shown that the spectral weights of the different noise peaks are modified when the noise in different pulses is correlated. As mentioned earlier, the noise correlation function $R_{\Delta A \Delta B}(n)$ for the output pulses at time scales shorter than the cavity round trip time (i.e. for $|n| < N$) is a good measure of the noise correlation in pulses inside the laser cavity. For $|n| < N$, $R_{\Delta A \Delta B}(n)$ given by (6.3) can be approximated as,

$$\begin{aligned} R_{\Delta A \Delta B}(n) &= T_N \int_{-\omega_N/2}^{\omega_N/2} \frac{d\omega}{2\pi}\, \Phi_{\Delta A \Delta B}(\omega T_N)\, \exp\left(j\omega\, T_N\, n\right) \qquad (6.26) \\ &\approx \sum_{p=0}^{N-1} \exp\left(j2\pi \frac{p}{N} n\right)\, T_N \int_{(p-\frac{1}{2})\omega_R}^{(p+\frac{1}{2})\omega_R} \frac{d\omega}{2\pi}\, \Phi_{\Delta A \Delta B}(\omega T_N) \\ &= R_{\Delta A \Delta B}[0] \sum_{p=0}^{N-1} W^p_{\Delta A \Delta B}\, \exp\left(j2\pi \frac{p}{N} n\right) \\ &= R_{\Delta A \Delta B}[0]\, C_{\Delta A \Delta B}(n) \qquad (6.27) \end{aligned}$$

where $W^{p}_{\Delta A \Delta B}$ is the spectral weight of the p-th noise peak,

$$W^{p}_{\Delta A \Delta B} = \frac{\int_{(p-\frac{1}{2})\omega_R}^{(p+\frac{1}{2})\omega_R} \frac{d\omega}{2\pi} \; \Phi_{\Delta A \Delta B}(\omega T_N)}{\int_{-\omega_N/2}^{\omega_N/2} \frac{d\omega}{2\pi} \; \Phi_{\Delta A \Delta B}(\omega T_N)} \tag{6.28}$$

and,

$$C_{\Delta A \Delta B}(n) = \frac{R_{\Delta A \Delta B}(n)}{R_{\Delta A \Delta B}[0]} = \sum_{p=0}^{N-1} W^{p}_{\Delta A \Delta B} \; \exp\left(j2\pi \frac{p}{N} n\right) \qquad \text{for } |n| < N \tag{6.29}$$

In deriving (6.27), it is assumed that the complex exponential function in (6.26) is slowly varying with frequency and can be set equal to its value at the center frequency of each noise peak. This approximation is valid for small values of the index n provided the width of each noise peak is much smaller than the separation ω_R of the noise peaks. For most fiber and semiconductor mode-locked lasers this approximation is well justified [79, 80, 90, 91, 93, 94, 97]. The function $C_{\Delta A \Delta B}(n)$ defined above describes the correlations in the noise in different pulses inside the laser cavity. $C_{\Delta A \Delta B}(n)$ satisfies the relations $-1 \leq C_{\Delta A \Delta B}(n) \leq 1$ and $C_{\Delta A \Delta B}[n+N] = C_{\Delta A \Delta B}(n)$. The value of $C_{\Delta A \Delta B}(n)$ gives the correlation, on a scale from -1 to 1, in the noise of any two pulses in the cavity that are separated by $(n-1)$ other pulses. Since the pulse noise spectral densities can be determined experimentally by measuring the spectral density of the photo-detector current noise, the correlations in the noise in different pulses inside the laser cavity can be determined using the result in (6.29). The result in (6.29) shows that $C_{\Delta A \Delta B}(n)$ is equal to the Fourier transform of the spectral weight of all the N noise peaks in $\Phi_{\Delta A \Delta B}(\omega)$ in a bandwidth equal to the pulse repetition frequency ω_N. The following results can be obtained from this Fourier transform relationship :

- Noise peaks in the spectral density near multiples of ω_N will have larger spectral weight if the noise in all the pulses in the laser cavity is positively correlated. As a special case, suppose that the spectral weights of all the supermode noise peaks in $\Phi_{\Delta A \Delta B}(\omega T_N)$ are negligible, and only the noise peaks at multiples of the pulse repetition frequency ω_N have all the spectral weight. It follows from (6.29) that $C_{\Delta A \Delta B}(n) = 1$ for all values of the index n, and the noise is *completely* positively correlated in all the pulses in the laser cavity.

- Noise peaks in the spectral density near odd multiples of $\omega_N/2$ will have larger spectral weight if the noise in the neighboring pulses inside the laser cavity is negatively correlated. For example, suppose that N is even and the supermode noise peaks at odd multiples of $\omega_N/2$ have all the spectral weight. In this case, $C_{\Delta A \Delta B}(n) = (-1)^n$ and the noise is *completely* negatively correlated in the neighboring pulses.

- If all the noise peaks in the spectral density have the same spectral weight, then $C_{\Delta A \Delta B}(n) = 1$ for $n = 0$, and $C_{\Delta A \Delta B}(n) = 0$ for $1 \leq |n| < N$, and the noise is uncorrelated in different pulses inside the laser cavity. This case was also discussed in the last section.

In Ref. [104], experimental results were reported recently for the pulse noise spectral densities of composite cavity harmonically mode-locked fiber lasers. In these lasers, a fraction of each pulse can be injected into the m-th subsequent pulse by an all-fiber Mach-Zehnder interferometer with unbalanced arms placed inside the laser cavity. This is expected to positively correlate the noise in every m-th pulse in the cavity. The noise in any two pulses that are not separated by $(m-1)$ other pulses is expected to remain uncorrelated. When the spectral weights of the noise peaks given in Fig.7 in Ref. [104] for different values of m are used in (6.29), the resulting correlation functions $C_{\Delta A \Delta B}(n)$ confirm these expected noise correlations.

In the last Section, a model for the timing noise in harmonically mode-locked semiconductor laser was presented for the case when the timing noise in the pulses inside the laser cavity was uncorrelated. In this Section, the contribution to the pulse timing noise from the phase noise in the RF oscillator is included. It is shown that since the noise contribution from the RF oscillator is completely positively correlated in all the pulses inside the laser cavity, this noise contribution shows up in the timing noise spectral density only in the noise peaks located at multiples of the pulse repetition frequency Ω_N and not in the supermode noise peaks. On the other hand, the contribution to the timing noise from spontaneous emission and vacuum fluctuations is uncorrelated in different pulses inside the laser cavity and shows up equally in all the noise peaks (including the supermode noise peaks). The electrical signal from the RF oscillator is assumed to be proportional to $\cos[\omega_N(t - \Delta T(t))]$, where $\Delta T(t)$ is the timing noise in the RF oscillator. $\Delta T(t)$ is assumed

to have the correlation function,

$$\langle \Delta T(t)\, \Delta T(t') \rangle = \sigma_{RF}^2 e^{-\kappa |t-t'|} \tag{6.30}$$

which implies that the mean square timing noise of the RF oscillator equals σ_{RF}^2, and the bandwidth of the RF oscillator noise equals $\kappa/2\pi$ Hz. Typically, the phase noise in RF oscillators is mostly at low frequencies [80], and therefore $\kappa \ll \Omega_R$ and the contribution to the pulse timing noise from the phase noise of the RF oscillator is expected to be positively correlated in all the pulses inside the laser cavity. The discrete-time noise variable $\Delta T(n)$ is defined as equal to $\Delta T(t = nT_N)$.

In order to study the correlations in the noise in different pulses, the noise in all the pulses must be included in the model. The finite difference equations for the timing noise introduced earlier are most suitable for this purpose, and allow the noise in all the pulses to be taken into account in a relatively straightforward way. In the presence of phase noise in the oscillator, the finite difference equation for the pulse timing noise become,

$$\Delta J(n+N) - \Delta J(n) = -\gamma_N T_R\, \Delta J(n) + \gamma_N T_R\, \Delta T(n) + F_N[n] \tag{6.31}$$

The above equation is identical to (6.12) except for the term with $\Delta T(n)$. The form of this new term follows from the fact that the pulse cannot be affected by the modulator if $\Delta T(n)$ equals $\Delta J(n)$. It is difficult to solve (6.31) directly but it can easily be solved in the frequency domain using the discrete-time Fourier transform [105], and one obtains the following expression for the pulse timing noise spectral density,

$$\begin{aligned} \Phi_{\Delta J \Delta J}(\omega T_N) &= \frac{1}{\left[1 + (1-\gamma_N T_R)^2 - 2\,(1-\gamma_N T_R)\cos(\omega T_R)\right]} \left\{ D_N \right. \\ &\quad \left. + \sigma_{RF}^2 \frac{\gamma_N^2 T_R^2 \left(1 - e^{-2\kappa T_N}\right)}{\left[1 + e^{-2\kappa T_N} - 2e^{-\kappa T_N}\cos(\omega T_N)\right]} \right\} \qquad (6.32) \\ &\approx \frac{1}{T_N} \sum_{n=-\infty}^{\infty} \frac{2\gamma_N}{(\omega - n\omega_R)^2 + \gamma_N^2} \left[\frac{1}{N} \left(\frac{D_N}{2\gamma_N T_R} \right) \right. \\ &\quad \left. + \frac{\gamma_N\, \sigma_{RF}^2}{2} \sum_{p=-\infty}^{\infty} \frac{2\kappa}{(\omega - p\omega_N)^2 + \kappa^2} \right] \qquad (6.33) \end{aligned}$$

The first term in the square brackets in (6.33) represents the timing noise contribution from spontaneous emission and vacuum fluctuations, and it is identical to the expression given earlier in (6.17). Since the timing noise from spontaneous emission and vacuum fluctuations is uncorrelated in different pulses inside the cavity, its contribution to the timing noise spectral density results in identical noise peaks at multiples of the cavity round trip frequency ω_R. The second term in the square brackets in (6.33) is the noise contribution from the phase noise of the RF oscillator. The noise contribution from the oscillator results in noise peaks at multiples of the pulse repetition frequency ω_N. Since it has been assumed that $\kappa \ll \omega_R$, the phase noise from the RF oscillator does not contribute to the supermode noise peaks. From the discussion above, it follows that the noise contribution from the RF oscillator is completely positively correlated in the pulses inside the laser cavity. This conclusion can be easily tested experimentally by comparing the supermode noise peaks in the timing noise spectral density to the noise peaks at multiples of the pulse repetition frequency. If $\kappa \ll \gamma_N$, (6.33) gives the expected result for the mean square timing jitter upon integration,

$$\langle \Delta J^2 \rangle = \frac{D_N}{2\gamma_N T_R} + \sigma_{RF}^2 \tag{6.34}$$

The first term on the right hand side of the above equation is the mean square timing noise contribution from spontaneous emission and vacuum fluctuations. Fig. 6-5 shows the timing noise spectral density for a laser mode-locked at the tenth harmonic ($N = 10$). The parameter values used in generating these Figures are as follows: $T_R = 1.0$ nsec, $T_N = 0.1$ nsec, $\gamma_N T_R = 0.01\pi$, $\kappa T_R = 2\pi 10^{-5}$, and $\sigma_{RF} = 50$ fs. The RMS contribution to the timing noise from spontaneous emission and vacuum fluctuations is assumed to be 100 fs. Fig. 6-5 shows that the contribution to the timing noise from the phase noise of the RF oscillator does not appear in the supermode noise peaks.

The spectral weights $W^p_{\Delta J \Delta J}$, defined in (6.28), of the noise peaks can be determined for all the N noise peaks in a bandwidth ω_N for the spectral density given in (6.33). Assuming as before that $\kappa \ll \gamma_N$, one obtains,

$$W^p_{tt} = \begin{cases} \dfrac{\frac{1}{N}\left(\dfrac{D_N}{2\gamma_N T_R}\right) + \sigma_{RF}^2}{\langle \Delta J^2 \rangle} & \text{if } p = 0 \text{ i.e. for the noise peaks at multiples of } \omega_N \\ \dfrac{\frac{1}{N}\left(\dfrac{D_N}{2\gamma_N T_R}\right)}{\langle \Delta J^2 \rangle} & \text{if } 1 \le p \le (N-1) \text{ i.e. for all the supermode noise peaks} \end{cases} \tag{6.35}$$

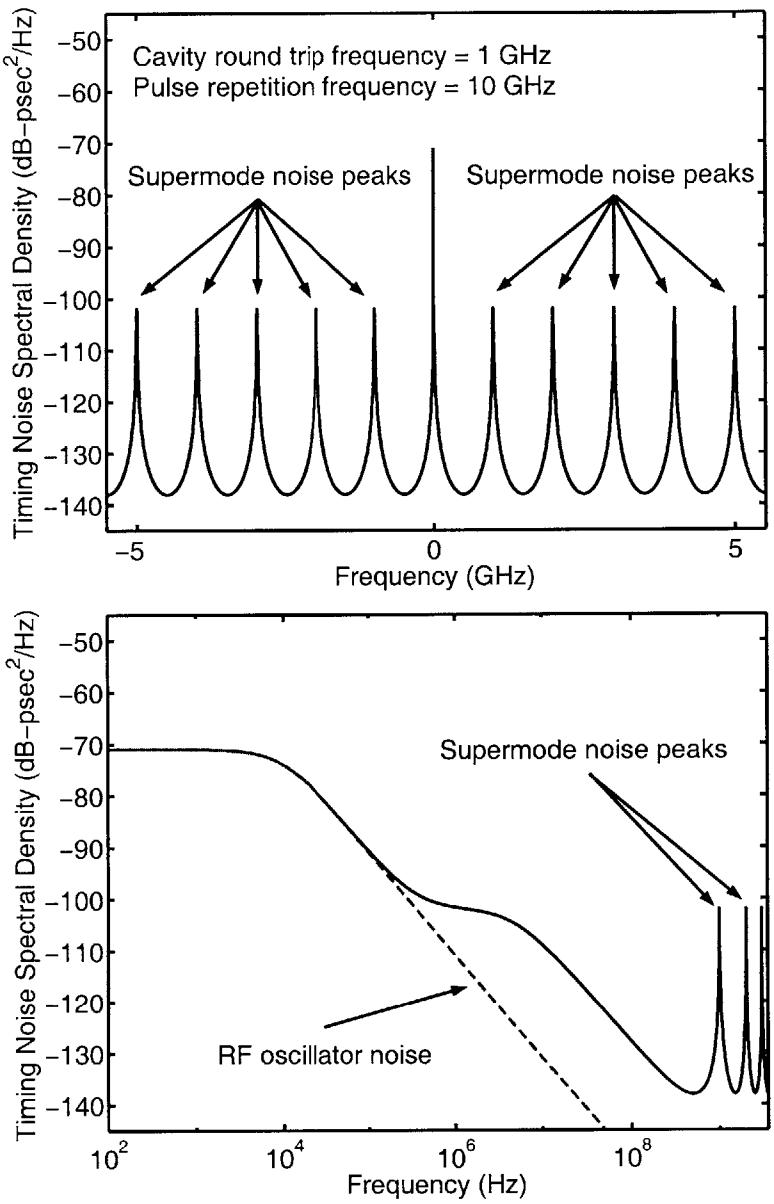

Figure 6-5: The pulse timing noise spectral density $T_N \Phi_{\Delta J \Delta J}(\omega T_N)$ (solid line) is plotted for a laser mode-locked at the tenth harmonic ($N = 10$) in the presence of timing (or phase) noise in the RF oscillator (dashed line) on linear and log frequency scales. T_R is 1.0 nsec. T_N is 0.1 nsec. $\gamma_N T_R$ and κT_R are assumed to be 0.01π and $2\pi 10^{-5}$, respectively. The RMS timing jitter in the RF oscillator is assumed to be 50 fs. The RMS timing jitter contribution from spontaneous emission and vacuum fluctuations is assumed to be 100 fs. The increased noise in the noise peak at $\omega = 0$ is due to the phase noise of the RF oscillator. The Figure shows that the noise contribution form the RF oscillator does not appear in any of the supermode noise peaks. All the supermode noise peaks are identical.

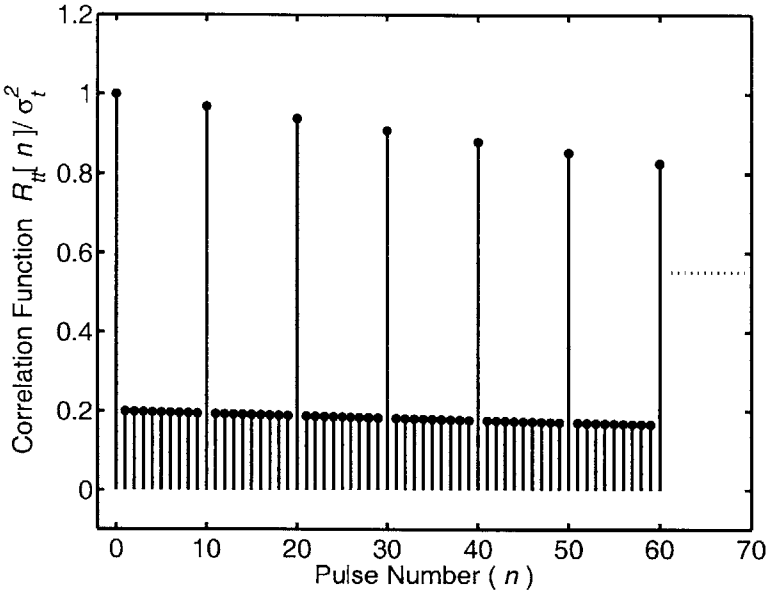

Figure 6-6: The timing noise correlation function $R_{\Delta J \Delta J}(n)$ (normalized to the RMS timing jitter) for the output pulses is shown for a laser mode-locked at the tenth harmonic ($N = 10$) in the presence of phase noise from the RF oscillator. The correlation function corresponds to the timing noise spectral density shown in Fig. 6-5. The timing noise in all the pulses inside the laser cavity is positively correlated, and therefore the timing noise in the output pulses is correlated at time scales shorter than the cavity round trip time.

The correlation function $C_{\Delta J \Delta J}(n)$, defined in (6.29), for the timing noise in different pulses inside the laser cavity can be obtained from the spectral weights of the noise peaks given above, and one gets,

$$C_{\Delta J \Delta J}(n) = \begin{cases} 1 & \text{if } n = 0 \\ \dfrac{\sigma_{RF}^2}{\langle \Delta J^2 \rangle} & \text{if } 1 \leq |n| \leq (N-1) \end{cases} \tag{6.36}$$

This implies that the correlation in the timing noise in different pulses inside the laser cavity is $\sigma_{RF}^2/\langle \Delta J^2 \rangle$. The timing noise correlation function $R_{\Delta J \Delta J}(n)$ for the output pulses can be obtained from the spectral density in (6.33) by using the inverse Fourier transform relation in (6.3). Fig. 6-6 shows the correlation function $R_{\Delta J \Delta J}(n)$, calculated numerically, that corresponds to the noise spectral density shown in Fig. 6-5. The correlation function shows that the timing noise is positively correlated in the output pulses at time scales shorter than the cavity round trip time T_R. The degree of positive correlation is given by the ratio $\sigma_{RF}^2/\langle \Delta J^2 \rangle$, which for the values used in Fig. 6-6 equals $50^2/\sqrt{100^2 + 50^2} = 0.2$.

Characterization of the Pulse Noise and Integration Bandwidth for the Mean Square Fluctuations

Since the pulse noise spectral density functions $\Phi_{\Delta A \Delta B}(\omega T_N)$ are not periodic in frequency with a period equal to Ω_R when the noise in the pulses inside the laser cavity is correlated, the mean square value of the fluctuations can only be determined if the noise spectral density functions $\Phi_{\Delta A \Delta A}(\omega T_N)$ are integrated over the full bandwidth equal to ω_N. It follows that the mean square values of the pulse energy and the timing fluctuations can be determined from the experimentally measured photo-detector current noise spectral density $S_{\Delta I \Delta I}(\omega)$ using (6.22) and (6.24). It should be noted that (6.23) and (6.25) do not hold when the noise in different pulses in the laser cavity is correlated.

6.7 Conclusion

The noise in different pulses inside the laser cavity in harmonically mode-locked lasers is in general correlated, and these noise correlations were shown to be related to the distribution of the spectral weight among the supermode noise peaks in the pulse noise spectral density functions. Models for the timing noise in harmonically mode-locked semiconductor lasers were presented that demonstrated the relationship between the supermode noise peaks and the correlations in the noise of different pulses. Methods to determine the noise correlations from the photo-detector current noise spectral density were also presented. Most experimental results on the noise in harmonically mode-locked lasers that have appeared in the literature have ignored the rich information content in the supermode noise peaks. The analysis presented in this Chapter clearly shows the importance of the supermode noise peaks in understanding the noise dynamics in harmonically mode-locked lasers.

Chapter 7

Conclusions

Theoretical models for the noise and dynamics in different types of semiconductor lasers were presented in this thesis. The main focus was on semiconductor cascade lasers and semiconductor mode-locked lasers. Although noise processes and dynamics in continuous wave and mode-locked semiconductor lasers are of entirely different character, Langevin rate equations were used to model the noise in both types of lasers. In Chapter 4 and Appendix C.1, it was shown that the current noise in electron transport by sequential tunneling in multiple quantum well structures can also be described by Langevin equations. The Langevin equation formalism is the simplest way to analyze fluctuations in systems whose dynamical equations can be linearized around a stable operating point and this was true for all the systems considered in this thesis. The wide range of applicability of the Langevin equation formalism makes it a powerful tool to analyze fluctuations in physical systems.

In this thesis, theoretical models for the current noise and the photon noise in semiconductor cascade lasers were developed and experimentally verified. The modeling of the photon noise in semiconductor cascade lasers required detailed modeling of the current noise in semiconductor lasers. A theory for the current noise in conventional interband semiconductor lasers was developed in Chapter 2. It was shown that the modulation bandwidth of semiconductor lasers can be determined in a non-optical way by measuring their current noise spectral density. The theory for the current noise and photon noise in semiconductor interband cascade lasers was developed in Chapter 3. In cascade lasers, photon emission events in different gain sections were found to be positively correlated. A theory was devel-

oped for the photon noise correlations in multiple cavity cascade lasers and parallel laser arrays, and the experimental results were found to agree well with the theoretical models. The positive correlations in photon emission in cascade lasers result in increased noise in the laser output power. It was shown that in all different types of semiconductor cascade lasers the increased photon noise can be expressed in terms of a scaled external circuit impedance. In Chapter 4, a model for the current noise and the photon noise in intersubband quantum cascade lasers was presented. As in interband cascade lasers, the scaling of the photon noise with the number of cascade sections in quantum cascade lasers can be expressed in terms of a scaled external circuit impedance. Small electron non-radiative lifetime compared to the differential stimulated emission lifetime, and the fact that the contribution to the photon noise from the non-radiative electronic transitions keeps increasing beyond laser threshold, make photon number squeezing difficult, if not impossible, to achieve in quantum cascade lasers.

The results of the work on the photon noise in cascade lasers presented in this thesis show that in both interband and intersubband cascade lasers the increase in the photon noise due to the positive correlations in photon emission in different gain sections is not large enough to overwhelm the improvement in the noise figure of an RF optical link obtained as a result of the increase in the laser differential quantum efficiency. Recall from Chapter 1 that the noise figure NF of an RF optical link is given by the expression,

$$NF = 10\log_{10}\left(1 + \frac{N_a}{GN_i}\right) \tag{7.1}$$

where the link gain G is proportional to the square of the laser differential quantum efficiency. In a link employing a cascade laser, the link gain is proportional to the square of the number N of cascade sections. The noise N_a added by the link contains contribution from the laser noise and the link loss. In Chapter 3 and Chapter 4, it was shown that the increase in the laser noise with the number of cascade sections is negligibly small when the circuit impedance Z_s is much larger than the impedance of the cascade laser, i.e. when $Z_s \gg NZ$, where Z is the impedance of a single cascade section. In this case, the added noise N_a is expected to be dominated by the link loss, and the link noise figure is expected to increase with the number of cascade sections.

The current noise and the photon noise in semiconductor cascade lasers has so far not

been measured experimentally. An important addition to the work presented in this thesis would be the measurement of the noise in different types of cascade lasers and the verification of the scaling relations for the current noise and the photon noise described in Chapter 3 and Chapter 4.

The theory for the noise in semiconductor mode-locked lasers was presented in Chapter 5. In contrast to the previous work in this field, the theoretical model presented in this thesis was fully quantum mechanical and took into account group velocity dispersion, active phase/amplitude modulation, and pulse chirp in a self-consistent way for the first time. It was shown that in the presence of group velocity dispersion and/or active phase modulation the pulse is chirped and has excess noise. The excess noise is related to the degree of non-normality of the pulse roundtrip operator that describes the time evolution of the pulse fluctuations. The contribution of the work presented in this thesis to the field is significant since in most semiconductor mode-locked lasers the roundtrip operator is not normal, and the pulse is highly chirped, because of group velocity dispersion and active phase modulation that accompanies active amplitude modulation as result of the carrier density dependent refractive index (i.e. non-zero α-parameter) in semiconductors. The pulse amplitude, phase, timing, and frequency fluctuations were described by constructing quantum mechanical operators. It was shown that when the roundtrip operator is not normal the pulse fluctuation operators contain noise contributions from all the higher order eigenfunctions of the roundtrip operator. The results obtained from the theoretical model developed showed that the pulse noise is significantly affected by the magnitude of the pulse chirp. Design schemes to achieve less than 50 fs RMS timing jitter in semiconductor mode-locked lasers were also presented. It was shown that in the presence of phase modulation the minimum timing jitter is obtained for a non-zero value of the group velocity dispersion and the pulse chirp.

The theoretical model developed in this work ignored dynamic non-linearities, such as dynamic gain/loss saturation and dynamic self-phase modulation. The main problem in modeling noise in the presence of non-linearities is that the higher order eigenfunctions for the linearized roundtrip operator are not readily available and are also difficult to compute numerically. Approximate results for the pulse timing noise in the presence of dynamic gain/loss saturation but ignoring group velocity dispersion, active phase modulation, and dynamic self-phase modulation were presented in Appendix E. More theoretical work is

required to take into account the non-normal character of the linearized roundtrip operator in the presence of dynamic non-linearities. Although the calculated values of the pulse timing noise in semiconductor mode-locked lasers agree well with the experimental results that have been reported in the literature, the exact relationship which follows from the theoretical model between the pulse timing noise and the cavity dispersion, the phase modulation strength, and the pulse chirp remains to be verified experimentally. Experimental work geared in this direction can also form the basis for future work.

In Chapter 6, the noise in harmonically mode-locked semiconductor lasers was discussed. The supermode noise peaks experimentally observed in the photo-detector current noise spectral density were related to the correlations in the noise in different pulses inside the laser cavity. It was shown that the correlations in the noise of different pulses inside the laser cavity can provide valuable information about the dynamics and the inter-pulse interactions inside the laser cavity. Although many results presented in Chapter 6 agree well with the experimental results obtained in the literature, a full understanding of the inter-pulse interactions and noise correlations in harmonically mode-locked lasers is still lacking and the field remains wide open for future explorations, both theoretical and experimental.

Appendix A

Appendix: Chapter 2

A.1 Noise Spectral Densities and Fano Factors

The noise spectral densities $K_I(\omega)$ and $K_P(\omega)$ for the current noise and the photon noise, respectively, can be computed as follows,

$$K_I(\omega) = \int_{-\infty}^{\infty} \frac{d\,\omega'}{2\pi} \langle \delta I^*_{ext}(\omega)\, \delta I_{ext}(\omega - \omega') \rangle \tag{A.1}$$

$$K_P(\omega) = \int_{-\infty}^{\infty} \frac{d\,\omega'}{2\pi} \langle \delta P^*_{out}(\omega)\, \delta P_{out}(\omega - \omega') \rangle \tag{A.2}$$

Since all the Langevin noise sources are delta correlated in time domain, they will also be delta correlated in frequency domain, and therefore the fluctuations δI_{ext} and δP_{out} in the current and the output power, respectively, will be also be delta correlated in time and frequency domains.

The Fano Factors $F_I(\omega)$ and $F_P(\omega)$ for the current noise and the intensity noise, respectively, are defined as the ratios of the actual noise spectral densities to the noise spectral densities of shot noise, and are given by the relations,

$$F_I(\omega) = \frac{K_I(\omega)}{q\,I} \qquad \text{and} \qquad F_P(\omega) = \frac{K_P(\omega)}{\hbar\Omega_o\, P_{out}} \tag{A.3}$$

The Relative Intensity Noise (RIN) is defined as,

$$\text{RIN} = 10\,\log_{10}\left[\frac{K_P(\omega)}{P^2_{out}}\right] \tag{A.4}$$

A.2 Elements of the Matrix D

Above the laser threshold, the non-zero elements of the matrix $\mathbf{D}$ in (2.26) are given below,

$$\mathbf{D}_{11} = j\omega + \frac{1}{\tau_c} + \frac{1}{\tau_l} \tag{A.5}$$

$$\mathbf{D}_{12} = -\frac{1}{\tau_e} \tag{A.6}$$

$$\mathbf{D}_{13} = 0 \tag{A.7}$$

$$\mathbf{D}_{21} = -\frac{1}{\tau_c} \tag{A.8}$$

$$\mathbf{D}_{22} = j\omega + \frac{1}{\tau_e} + \frac{1}{\tau_{nr}} + \frac{1}{\tau_{st}} \tag{A.9}$$

$$\mathbf{D}_{23} = \frac{1}{\tau_p} \tag{A.10}$$

$$\mathbf{D}_{31} = 0 \tag{A.11}$$

$$\mathbf{D}_{32} = \frac{1}{\tau_{st}} \tag{A.12}$$

$$\mathbf{D}_{33} = j\omega \tag{A.13}$$

A.3 Elements of the Matrix $\mathbf{D}^{-1}$

Above the laser threshold, and for frequencies less than the inverse of the carrier capture time τ_c, the elements of the matrix $\mathbf{D}^{-1}$ are given below,

$$\mathbf{D}_{11} = -\tau_c \left[\left(\frac{j\omega}{\omega_R} \right)^2 + j\omega\,\tau_p \left(1 + \frac{\tau_{st}}{\tau_{nr}} + \frac{\tau_{st}}{\tau_e} \right) - 1 \right] \eta_i\, H(\omega) \tag{A.14}$$

$$\mathbf{D}_{12} = -\left(\frac{j\omega}{\omega_R^2} \right) \frac{\tau_c}{\tau_e}\, \eta_i\, H(\omega) \tag{A.15}$$

$$\mathbf{D}_{13} = \tau_{st} \left(\frac{\tau_c}{\tau_e} \right) \eta_i\, H(\omega) \tag{A.16}$$

$$\mathbf{D}_{21} = -\left(\frac{j\omega}{\omega_R^2} \right) \eta_i\, H(\omega) \tag{A.17}$$

$$\mathbf{D}_{22} = -\left(\frac{j\omega}{\omega_R^2} \right) H(\omega) \tag{A.18}$$

$$\mathbf{D}_{23} = \tau_{st}\, H(\omega) \tag{A.19}$$

$$\mathbf{D}_{31} = \tau_p\, \eta_i\, H(\omega) \tag{A.20}$$

$$\mathbf{D}_{32} = \tau_p\, H(\omega) \tag{A.21}$$

$$\mathbf{D}_{33} = -\left[j\omega + \frac{1}{\tau_{nr}} + \frac{1}{\tau_{st}} + \frac{1-\eta_i}{\tau_e}\right] \frac{H(\omega)}{\omega_R^2} \tag{A.22}$$

where the current injection efficiency η_i, the modulation response function $H(\omega)$, and the relaxation oscillation frequency ω_R are given in (2.5), (2.35), and (2.36), respectively.

A.4 Fabrication of Polyimide Planarized InGaAsP/InP Ridge-Waveguide Lasers

A.4.1 Etch Mask Deposition

1. Coat HMDS (either in an HMDS oven or by spin coating).
2. Spin coat AZ5214 image reversal photoresist at 6000 rpm for 40 seconds.
3. Softbake for 30 minutes at 90 °C in a convection oven.
4. Expose using KS2 MA4 aligner for 25 seconds.
5. Bake on a hot plate at 120 °C for 60 seconds.
6. Flood expose using KS2 MA4 aligner for 180 seconds.
7. Develop for 60 seconds using AZ 422 MIF developer; rinse in DI water for 20 seconds.
8. Descum using O_2 RIE at flow rate of 15 sccm and 10 mTorr chamber pressure for 30 seconds.
9. Etch with BOE (or HF) for 10 seconds; rinse in DI water for 30 seconds.
10. E-beam evaporate 2000 A of Titanium.
11. Liftoff using Acetone; rinse in DI water.

A.4.2 Dry Etching InP/InGaAs/InGaAsP

1. RIE etch InP (or InGaAs or InGaAsP) using a mixture of H_2:CH_4:O_2 with flow rates in the ratio of 20:20:2.5 sccm, 400 DC bias (90-120 Watts RF power), and 5 mTorr chamber pressure. Etch rate is approximately 500 A/min. Additional details can be found in Ref. [55].

A.4.3 Polyimide Coating and Planarization

1. Deposit 800 A to 1200 A thick layer of SiO_2.
2. Spin coat Dupont polyimide adhesion promoter VM652 at 4000 rpm for 40 seconds.
3. Bake on a hot plate at 120 °C for 2 minutes.
4. Spin coat Dupont polyimide PI2560 at 6000 rpm for 60 seconds. Multiple coatings may be required to achieve planarization. After each coating bake for 30 minutes at 170 °C in a convection oven.
5. If a coating gets contaminated, or deformed, strip coating using hot NMP, bake on hot plate 120 °C for 2 minutes, and then coat again.
6. Cure the polyimide by heating in a Nitrogen oven at 380 °C for 20 to 30 minutes. The temperature in the oven must be increased at a rate below 5 °C/min to avoid building stresses in the polyimide film.
7. RIE etch the polyimide using a mixture of O_2:CF_4 with flow rates in the ratio of 15:2 sccm, and 10 mTorr chamber pressure. Determine when planarization has been achieved by examining the sample under a microscope periodically while etching. When nearing completion turn off CF_4 which etches SiO_2.
8. Remove the SiO_2 layer by etching with BOE (or HF) for 15 seconds; rinse in DI water for 30 seconds.

A.4.4 Making Ohmic Contacts

1. Do photolithography on top of the polyimide film using AZ5214 image reversal photoresist as explained in Section A.4.1 above. Do not use HMDS when doing photolithography on a polyimide film.

2. Descum using O_2 RIE at flow rate of 15 sccm and 10 mTorr chamber pressure for 20 seconds.

3. Etch with BOE (or HF) for 10 seconds; rinse in DI water for 30 seconds.

4. E-beam evaporate 50:150:2000 A of Ti:Pt:Au to make the top p-side ohmic contact.

5. Lap the back side of the sample to reduce the sample thickness to 100 μm.

6. Etch the back side with BOE (or HF) for 10 seconds; rinse in DI water for 30 seconds.

7. E-beam evaporate 50:100:500:900:300:2000 A of Ni:Au:Ge:Au:Ni:Au to make the back side ohmic contact.

8. RTA (Rapid Thermal Anneal) the sample in Nitrogen at 380 $^\circ$ for 30 seconds.

Appendix B

Appendix: Chapter 3

B.1 Elements of the Matrix D for a Split Waveguide Laser

Above the laser threshold, the non-zero elements of the matrix $\mathbf{D}$ in (3.40) are given below,

$$\mathbf{D}_{11} = j\omega + \frac{1}{\tau_c} + \frac{1}{\tau_l} \tag{B.1}$$

$$\mathbf{D}_{12} = -\frac{1}{\tau_e} \tag{B.2}$$

$$\mathbf{D}_{13} = 0 \tag{B.3}$$

$$\mathbf{D}_{21} = -\frac{1}{\tau_c} \tag{B.4}$$

$$\mathbf{D}_{22} = j\omega + \frac{1}{\tau_e} + \frac{1}{\tau_{nr}} + \frac{1}{\tau_{st}} \tag{B.5}$$

$$\mathbf{D}_{23} = \frac{1}{\tau_p} \tag{B.6}$$

$$\mathbf{D}_{31} = 0 \tag{B.7}$$

$$\mathbf{D}_{32} = \frac{1}{\tau_{st}} \tag{B.8}$$

$$\mathbf{D}_{33} = j\omega \tag{B.9}$$

Appendix C

Appendix: Chapter 4

C.1 Langevin Equations and Current Noise in Electron Transport by Sequential Tunneling in Resonant Tunneling Diodes

In this Section, it is shown that classical Langevin rate equations can be used to describe the noise in electron transport by sequential tunneling in double barrier resonant tunneling diodes (RTDs). In Refs. [26, 27, 28] it is shown via fully quantum mechanical and clasical master equation approaches that the current noise spectral density in RTDs is given by the formulas,

$$K_I(\omega \ll \Gamma_L, \Gamma_R) = eI_{ext} \frac{\Gamma_L^2 + \Gamma_R^2}{(\Gamma_L + \Gamma_R)^2} \tag{C.1}$$

and

$$K_I(\omega \gg \Gamma_L, \Gamma_R) = eI_{ext} \frac{C_L^2 + C_R^2}{(C_L + C_R)^2} \tag{C.2}$$

where Γ_L and Γ_R are the electron escape rates from the well into the left and right leads, respectively (see Fig. C-1), and C_L and C_R are the capacitances of the left and the right barriers, respectively. (C.1) and (C.2) can be derived using Langevin rate equations. The Langevin equation for the fluctuation δN in the carrier number in the quantum well is,

$$\frac{d\,\delta N}{dt} = \frac{\delta I_L}{e} - \frac{\delta I_R}{e} \tag{C.3}$$

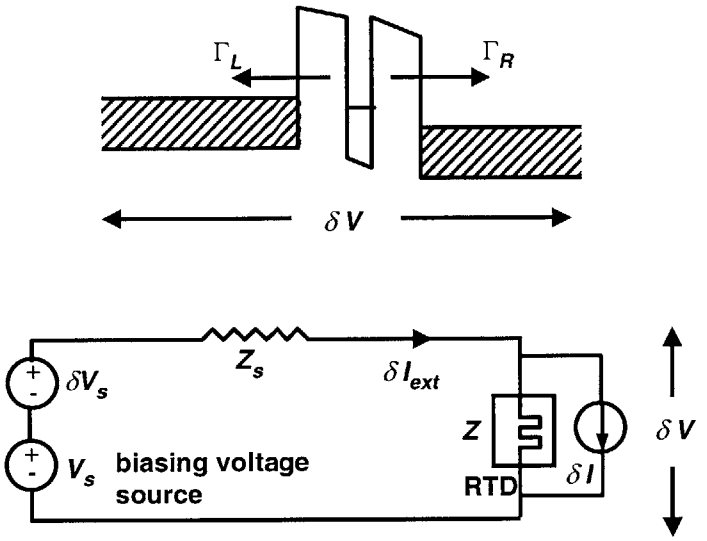

Figure C-1: Current noise model for a double barrier resonant tunneling diode.

where the currents δI_L and δI_R through the left and the right barriers, respectively, are as follows,

$$\frac{\delta I_L}{e} = G_L \frac{\delta V_L}{e} - \delta N \Gamma_L + F_L \tag{C.4}$$

$$\frac{\delta I_R}{e} = G_R \frac{\delta V_R}{e} + \delta N \Gamma_R + F_R \tag{C.5}$$

Here, F_L and F_R are the Langevin noise sources that describes the noise in electron tunneling in the left and the right barriers, respectively, and have the following correlations at small temperatures,

$$\langle F_L(t) F_L(t') \rangle \approx \langle F_R(t) F_R(t') \rangle \approx \frac{I_{ext}}{e} \delta(t - t') \tag{C.6}$$

The potential drops δV_L and δV_R across the left and the right barriers, respectively, are,

$$\delta V_L = \frac{C_R}{(C_L + C_R)} \delta V - \frac{e\,\delta N}{(C_L + C_R)} \tag{C.7}$$

$$\delta V_R = \frac{C_L}{(C_L + C_R)} \delta V + \frac{e\,\delta N}{(C_L + C_R)} \tag{C.8}$$

The current δI_{ext} in the external circuit is,

$$I_{ext} = I_L + C_L \frac{d\,\delta V_L}{dt} \tag{C.9}$$

The constraint imposed by the external circuit is,

$$I_{ext} = \frac{\delta V_s - \delta V}{Z_s} \tag{C.10}$$

The above set of equations can be solved to give

$$\delta I_{ext} = \frac{\delta V_s}{Z_s(\omega) + Z(\omega)} + \frac{Z(\omega)}{Z_s(\omega) + Z(\omega)}\,\delta I(\omega) \tag{C.11}$$

where $\delta I(\omega)$ is given as,

$$\frac{\delta I(\omega)}{e} = \frac{F_L\left(j\omega\frac{C_R}{C} + \Gamma'_R\right) + F_R\left(j\omega\frac{C_L}{C} + \Gamma'_L\right)}{j\omega + \Gamma'_L + \Gamma'_R} \tag{C.12}$$

and $Z(\omega)$ is the impedance of the RTD and is given by the expression,

$$Z^{-1}(\omega) = \frac{(j\omega)^2\,\frac{C_L C_R}{C} + j\omega\left[(\Gamma'_L + \Gamma'_R)\,\frac{C_L C_R}{C} + G_L\frac{C_R^2}{C^2} + G_R\frac{C_L^2}{C^2}\right] + \Gamma'_L G_L\frac{C_R}{C} + \Gamma'_R G_R\frac{C_L}{C}}{j\omega + \Gamma'_L + \Gamma'_R} \tag{C.13}$$

The following definitions have been introduced above,

$$\Gamma'_L = \Gamma_L + \frac{G_L}{C} \tag{C.14}$$

$$\Gamma'_R = \Gamma_R + \frac{G_R}{C} \tag{C.15}$$

$$C = C_L + C_R \tag{C.16}$$

(C.11) shows that a circuit model for the current noise in a RTD can be constructed as shown in Fig.C-1 where a current noise source $\delta I(\omega)$ is attached in parallel with the RTD. The spectral density of the current noise $\delta I(\omega)$ follows from (C.12),

$$K_I(\omega) = eI_{ext}\,\frac{\omega^2\left[\frac{C_L^2 + C_R^2}{(C_L + C_R)^2}\right] + {\Gamma'_L}^2 + {\Gamma'_R}^2}{\omega^2 + (\Gamma'_L + \Gamma'_R)^2} \tag{C.17}$$

It can be seen that (C.17) reduces to (C.1) and (C.2) when $\omega \ll \Gamma'_L, \Gamma'_R$ and when $\omega \gg \Gamma'_L, \Gamma'_R$, respectively. The only difference is that in the low frequency limit (C.1) contains Γ_L and Γ_R and not Γ'_L and Γ'_R. This is because the method used here accounts for the potential fluctuations accompanying the charge density fluctuations inside the RTD whereas (C.1) ignores them.

C.2 Correlations Among the Langevin Noise Sources in QCLs

$$\begin{aligned} WL\,\langle f^j_{32}(t)\, f^q_{32}(t')\rangle &= (R_{3\to 2} + R_{2\to 3})\,\delta_{jq}\,\delta(t-t') \\ &\approx R_{32}(n^j_3, n^j_2)\,\delta_{jq}\,\delta(t-t') \end{aligned} \tag{C.18}$$

$$\begin{aligned} WL\,\langle f^j_{31}(t)\, f^q_{31}(t')\rangle &= (R_{3\to 1} + R_{1\to 3})\,\delta_{jq}\,\delta(t-t') \\ &\approx R_{31}(n^j_3, n^j_1)\,\delta_{jq}\,\delta(t-t') \end{aligned} \tag{C.19}$$

$$\begin{aligned} WL\,\langle f^j_{21}(t)\, f^q_{21}(t')\rangle &= (R_{2\to 1} + R_{1\to 2})\,\delta_{jq}\,\delta(t-t') \\ &\approx R_{21}(n^j_2, n^j_1)\,\delta_{jq}\,\delta(t-t') \end{aligned} \tag{C.20}$$

$$WL\,\langle f^j_{RN}(t)\, f^q_{RN}(t')\rangle = \Gamma^j v_g\, g(n^j_3, n^j_2)\left[(2n_{sp}-1)S_p + \frac{n_{sp}}{WL}\right]\delta_{jq}\,\delta(t-t') \tag{C.21}$$

$$WL\,\langle f^j_{RS}(t)\, f^q_{RS}(t')\rangle = \Gamma^j v_g\, g(n^j_3, n^j_2)\left[(2n_{sp}-1)S_p + \frac{n_{sp}}{WL}\right]\delta_{jq}\,\delta(t-t') \tag{C.22}$$

$$WL\,\langle f^j_{RS}(t) f^q_{RN}(t')\rangle = \Gamma^j v_g\, g(n^j_3, n^j_2)\left[(2n_{sp}-1)S_p + \frac{n_{sp}}{WL}\right]\delta_{jq}\,\delta(t-t') \tag{C.23}$$

$$WL\,\langle F_L(t)\, F_L(t')\rangle = \frac{S_p}{\tau_p}\,\delta(t-t') \tag{C.24}$$

$$\langle F_o(t)\, F_o(t')\rangle = \eta_o\,(h\nu)^2\,\frac{WL\,S_p}{\tau_p}\,\delta(t-t') \tag{C.25}$$

$$\langle F_o(t)\, F_L(t')\rangle = \eta_o\, h\nu\,\frac{S_p}{\tau_p}\,\delta(t-t') \tag{C.26}$$

C.3 Differential Resistance of a QCL

The expression in Equations (4.65) and (4.63) for the differential resistance R_d of a QCL can be put in the form,

$$R_d = \begin{cases} \dfrac{N}{WL}\dfrac{\tau_{in}}{C_{inj}}\,(1+\theta_3'+\theta_2'+\theta_1) & (I < I_{th}) \\ \dfrac{N}{WL}\dfrac{\tau_{in}}{C_{inj}}\,(1+\theta_3+\theta_2+\theta_1) & (I > I_{th}) \end{cases} \tag{C.27}$$

The dimensionless parameters θ_3, θ_3', θ_2, θ_2', and θ_1 that have been used in the above Equation are as follows,

$$\theta_3 = \left(\frac{1}{\tau_{in}}\frac{C_{inj}}{C_3} + \frac{1}{\tau_3}\right)\frac{\tau_{31}\tau_{21}}{(\tau_{21}+\tau_{31})} \quad , \quad \theta_3' = \left(\frac{1}{\tau_{in}}\frac{C_{inj}}{C_3} + \frac{1}{\tau_3}\right)\frac{\tau_{32}\tau_{31}}{(\tau_{32}+\tau_{31})} \tag{C.28}$$

$$\theta_2 = \left(\frac{1}{\tau_{in}}\frac{C_{inj}}{C_2} + \frac{1}{\tau_2}\right)\frac{\tau_{31}\tau_{21}}{(\tau_{21}+\tau_{31})} \quad , \quad \theta_2' = \left(\frac{1}{\tau_{in}}\frac{C_{inj}}{C_2} + \frac{1}{\tau_2}\right)\frac{\tau_{31}\tau_{21}}{(\tau_{32}+\tau_{31})} \tag{C.29}$$

$$\theta_1 = \left(\frac{1}{\tau_{in}}\frac{C_{inj}}{C_1} + \frac{1}{\tau_1}\right)\tau_{out} \tag{C.30}$$

C.4 Elements of Matrix D

The non-zero elements of the matrix **D** are,

$$\mathbf{D}_{11} = j\omega + \frac{1}{\tau_{out}} \quad , \quad \mathbf{D}_{12} = -\frac{1}{\tau_{21}} \quad , \quad \mathbf{D}_{13} = -\frac{1}{\tau_{31}} \tag{C.31}$$

$$\mathbf{D}_{22} = j\omega + \frac{1}{\tau_{21}} + \Gamma v_g\, a\left(S_p + \frac{n_{sp}}{WL}\right) \tag{C.32}$$

$$\mathbf{D}_{23} = -\frac{1}{\tau_{32}} - \Gamma v_g\, a\left(S_p + \frac{n_{sp}}{WL}\right) \tag{C.33}$$

$$\mathbf{D}_{24} = -\mathbf{D}_{34} = -N\,\Gamma v_g\, g(n_3, n_2) \tag{C.34}$$

$$\mathbf{D}_{31} = \frac{1}{\tau_1}\frac{j\omega\,\tau_{in}}{(1+j\omega\,\tau_{in})} \tag{C.35}$$

$$\mathbf{D}_{32} = \frac{1}{\tau_2}\frac{j\omega\,\tau_{in}}{(1+j\omega\,\tau_{in})} - \Gamma v_g\, a\left(S_p + \frac{n_{sp}}{WL}\right) \tag{C.36}$$

$$\mathbf{D}_{33} = j\omega + \frac{1}{\tau_3}\frac{j\omega\,\tau_{in}}{(1+j\omega\,\tau_{in})} + \frac{1}{\tau_{32}} + \frac{1}{\tau_{31}} + \Gamma v_g\, a\left(S_p + \frac{n_{sp}}{WL}\right) \tag{C.37}$$

$$\mathbf{D}_{42} = -\mathbf{D}_{43} = \Gamma v_g\, a \left(S_p + \frac{n_{sp}}{WL} \right) \tag{C.38}$$

$$\mathbf{D}_{44} = j\omega + \frac{1}{\tau_p} - N\,\Gamma v_g\, g(n_3, n_2) \tag{C.39}$$

C.5 Important Elements of Matrix $\mathbf{D}^{-1}$

Above threshold, elements of the matrix $\mathbf{D}^{-1}$ in the limit $\{\tau_2\,,\,\tau_1\} \rightarrow \infty$ are given below. In addition, it is also assumed that $\omega\tau_{in} \ll 1$. If the later condition does not hold then the expressions given below can be corrected by replacing τ_3 by $\tau_3\,(1 + j\omega\,\tau_{in})$.

$$\mathbf{D}_{11}^{-1} = \frac{\tau_{out}}{(j\omega\,\tau_{out} + 1)} \tag{C.40}$$

$$\begin{aligned} \mathbf{D}_{12}^{-1} \;=\; & \tau_{out}\,\tau_p\,\tau_{st} \left\{ (j\omega)^2 \left(1 + \frac{\tau_{in}}{\tau_3}\right) \frac{1}{\tau_{21}} + j\omega \left[\frac{1}{\tau_{st}} \left(\frac{1}{\tau_{21}} + \frac{1}{\tau_{31}} \right) + \frac{1}{\tau_{21}\,\tau_{31}} + \frac{1}{\tau_{21}\,\tau_{32}} \right] \right. \\ & \left. + \frac{1}{\tau_p\,\tau_{st}} \left(\frac{1}{\tau_{21}} + \frac{1}{\tau_{31}} \right) \right\} \frac{\tau_{21}\,\tau_{31}}{(\tau_{21} + \tau_{31})} \frac{H(\omega)}{(j\omega\,\tau_{out} + 1)} \end{aligned} \tag{C.41}$$

$$\begin{aligned} \mathbf{D}_{13}^{-1} \;=\; & \tau_{out}\,\tau_p\,\tau_{st} \left\{ (j\omega)^2 \left(\frac{1}{\tau_{31}}\right) + j\omega \left[\frac{1}{\tau_{st}} \left(\frac{1}{\tau_{21}} + \frac{1}{\tau_{31}} \right) + \frac{1}{\tau_{21}\,\tau_{31}} + \frac{1}{\tau_{21}\,\tau_{32}} \right] \right. \\ & \left. + \frac{1}{\tau_p\,\tau_{st}} \left(\frac{1}{\tau_{21}} + \frac{1}{\tau_{31}} \right) \right\} \frac{\tau_{21}\,\tau_{31}}{(\tau_{21} + \tau_{31})} \frac{H(\omega)}{(j\omega\,\tau_{out} + 1)} \end{aligned} \tag{C.42}$$

$$\mathbf{D}_{14}^{-1} = \tau_{out}\,\tau_{st} \left\{ j\omega \left[\frac{1}{\tau_{21}} \left(1 + \frac{\tau_{in}}{\tau_3}\right) - \frac{1}{\tau_{31}} \right] \right\} \frac{\tau_{21}\,\tau_{31}}{(\tau_{21} + \tau_{31})} \frac{H(\omega)}{(j\omega\,\tau_{out} + 1)} \tag{C.43}$$

$$\mathbf{D}_{21}^{-1} \approx 0; \tag{C.44}$$

$$\mathbf{D}_{22}^{-1} = \tau_p \tau_{st} \left[(j\omega)^2 \left(1 + \frac{\tau_{in}}{\tau_3}\right) + j\omega \left(\frac{1}{\tau_{32}} + \frac{1}{\tau_{31}} + \frac{1}{\tau_{st}} \right) + \frac{1}{\tau_p \tau_{st}} \right] \frac{\tau_{21}\,\tau_{31}}{(\tau_{21} + \tau_{31})} H(\omega) \tag{C.45}$$

$$\mathbf{D}_{23}^{-1} = \tau_p \left[j\omega \left(\frac{\tau_{st}}{\tau_{32}} + 1 \right) + \frac{1}{\tau_p} \right] \frac{\tau_{21}\,\tau_{31}}{(\tau_{21} + \tau_{31})} H(\omega) \tag{C.46}$$

$$\mathbf{D}_{24}^{-1} = \tau_{st} \left[j\omega \left(1 + \frac{\tau_{in}}{\tau_3} \right) + \frac{1}{\tau_{31}} \right] \frac{\tau_{21}\,\tau_{31}}{(\tau_{21} + \tau_{31})} H(\omega) \tag{C.47}$$

$$\mathbf{D}_{31}^{-1} \approx 0; \tag{C.48}$$

$$\mathbf{D}_{32}^{-1} = \tau_p \left(j\omega + \frac{1}{\tau_p}\right) \frac{\tau_{21}\,\tau_{31}}{(\tau_{21} + \tau_{31})} H(\omega) \tag{C.49}$$

$$\mathbf{D}_{33}^{-1} = \tau_p \tau_{st} \left[(j\omega)^2 + j\omega \left(\frac{1}{\tau_{21}} + \frac{1}{\tau_{st}}\right) + \frac{1}{\tau_p \tau_{st}}\right] \frac{\tau_{21}\,\tau_{31}}{(\tau_{21} + \tau_{31})} H(\omega) \tag{C.50}$$

$$\mathbf{D}_{34}^{-1} = -\tau_{st} \left(j\omega + \frac{1}{\tau_{21}}\right) \frac{\tau_{21}\,\tau_{31}}{(\tau_{21} + \tau_{31})} H(\omega) \tag{C.51}$$

$$\mathbf{D}_{41}^{-1} \approx 0 \tag{C.52}$$

$$\mathbf{D}_{42}^{-1} = -\tau_p \left[j\omega \left(1 + \frac{\tau_{in}}{\tau_3}\right) + \left(\frac{1}{\tau_{31}} + \frac{1}{\tau_{32}}\right)\right] \frac{\tau_{21}\,\tau_{31}}{(\tau_{21} + \tau_{31})} H(\omega) \tag{C.53}$$

$$\mathbf{D}_{43}^{-1} = \tau_p \left[j\omega + \left(\frac{1}{\tau_{21}} - \frac{1}{\tau_{32}}\right)\right] \frac{\tau_{21}\,\tau_{31}}{(\tau_{21} + \tau_{31})} H(\omega) \tag{C.54}$$

$$\begin{aligned} \mathbf{D}_{44}^{-1} \;=\; & \tau_p\,\tau_{st} \left\{(j\omega)^2 \left(1 + \frac{\tau_{in}}{\tau_3}\right) + (j\omega) \left[\frac{1}{\tau_{21}} \left(1 + \frac{\tau_{in}}{\tau_3}\right) + \frac{1}{\tau_{31}} + \frac{1}{\tau_{32}} + \frac{1}{\tau_{st}} \left(2 + \frac{\tau_{in}}{\tau_3}\right)\right] \right. \\ & \left. + \left[\frac{1}{\tau_{st}} \left(\frac{1}{\tau_{21}} + \frac{1}{\tau_{31}}\right) + \frac{1}{\tau_{21}\,\tau_{31}} + \frac{1}{\tau_{21}\,\tau_{32}}\right]\right\} \frac{\tau_{21}\,\tau_{31}}{(\tau_{21} + \tau_{31})} H(\omega) \end{aligned} \tag{C.55}$$

where $H(\omega)$ is,

$$\begin{aligned} H(\omega) \;=\; & \frac{1}{\tau_p\,\tau_{st}} \left(\frac{1}{\tau_{21}} + \frac{1}{\tau_{31}}\right) \left\{(j\omega)^3 \left(1 + \frac{\tau_{in}}{\tau_3}\right) \right. \\ & + (j\omega)^2 \left[\frac{1}{\tau_{21}} \left(1 + \frac{\tau_{in}}{\tau_3}\right) + \frac{1}{\tau_{31}} + \frac{1}{\tau_{32}} + \frac{1}{\tau_{st}} \left(2 + \frac{\tau_{in}}{\tau_3}\right)\right] \\ & + j\omega \left[\frac{1}{\tau_{st}} \left(\frac{1}{\tau_{21}} + \frac{1}{\tau_{31}}\right) + \frac{1}{\tau_{21}\,\tau_{31}} + \frac{1}{\tau_{21}\,\tau_{32}} + \frac{1}{\tau_p\,\tau_{st}} \left(2 + \frac{\tau_{in}}{\tau_3}\right)\right] \\ & \left. + \frac{1}{\tau_p\,\tau_{st}} \left(\frac{1}{\tau_{21}} + \frac{1}{\tau_{31}}\right)\right\}^{-1} \end{aligned} \tag{C.56}$$

For small values of ω for which the cubic term in ω in the denominator may be neglected, $H(\omega)$ becomes,

$$H(\omega) = \frac{\omega_R^2}{(\omega_R^2 - \omega^2 + j\omega\gamma)} \tag{C.57}$$

The above approximation will be valid if ω is much less than $1/\tau_{in}$, $1/\tau_{21}$, and $1/\tau_{st}$. In this approximation ω_R and γ are,

$$\omega_R^2 = \frac{\dfrac{1}{\tau_p \tau_{st}} \left(1 + \dfrac{\tau_{21}}{\tau_{31}}\right)}{\left[1 + \dfrac{\tau_{21}}{\tau_{31}} + \dfrac{\tau_{21}}{\tau_{32}} + \dfrac{\tau_{in}}{\tau_3} + \dfrac{\tau_{21}}{\tau_{st}} \left(2 + \dfrac{\tau_{in}}{\tau_3}\right)\right]} \tag{C.58}$$

$$\gamma = \frac{\left[\dfrac{1}{\tau_{st}} \left(1 + \dfrac{\tau_{21}}{\tau_{31}}\right) + \dfrac{1}{\tau_{31}} + \dfrac{1}{\tau_{32}} + \dfrac{\tau_{21}}{\tau_p \tau_{st}} \left(2 + \dfrac{\tau_{in}}{\tau_3}\right)\right]}{\left[1 + \dfrac{\tau_{21}}{\tau_{31}} + \dfrac{\tau_{21}}{\tau_{32}} + \dfrac{\tau_{in}}{\tau_3} + \dfrac{\tau_{21}}{\tau_{st}} \left(2 + \dfrac{\tau_{in}}{\tau_3}\right)\right]} \tag{C.59}$$

Appendix D

Appendix: Chapter 5

D.1 Excess Noise in Linear Systems with Non-orthogonal Eigenvectors

The origin of the excess noise in systems with non-orthogonal eigenvectors can be explained with the help of a simple example. Consider a stable linear system defined in R^2 in which the state vector $\mathbf{V}(T)$, in the presence of a noise source $\mathbf{F}(T)$, obeys the differential equation,

$$\frac{d\mathbf{V}(T)}{dT} = \mathbf{M}.\mathbf{V}(T) + \mathbf{F}(T) \tag{D.1}$$

The matrix $\mathbf{M}$ is not Hermitian, and has two non-orthogonal eigenvectors $\mathbf{e}_1$ and $\mathbf{e}_2$, with corresponding real eigenvalues $-\lambda_1$ and $-\lambda_2$, respectively. The eigenvectors are shown in Fig. D-1a. The angle between the eigenvectors is θ_{12}. The noise source $\mathbf{F}(T)$ is assumed to have the correlation function,

$$\langle\, \mathbf{F}(T)\, \mathbf{F}(T')\, \rangle = \eta \begin{bmatrix} 1 & 0 \\ 0 & 1 \end{bmatrix} \delta(T - T') \tag{D.2}$$

The eigenvectors are not orthogonal but they form a biorthogonal set with the eigenvectors $\mathbf{d}_1$ and $\mathbf{d}_2$ of the adjoint linear system. In the present case, $\mathbf{d}_1$ and $\mathbf{d}_2$ equal $\sigma.\mathbf{e}_2$ and $\sigma.\mathbf{e}_2$, respectively, where the matrix σ is,

$$\sigma = \begin{bmatrix} 0 & -1 \\ 1 & 0 \end{bmatrix} \tag{D.3}$$

The vectors $\mathbf{d}_1$ and $\mathbf{d_2}$ have the property that $\mathbf{d}_1.\mathbf{e}_2 = \mathbf{d}_2.\mathbf{e}_1 = 0$. In the presence of noise, $\mathbf{V}(T)$ can be expanded in terms of the eigenvectors as follows,

$$\mathbf{V}(T) = c_1(T)\mathbf{e}_1 + c_2(T)\mathbf{e}_2 \tag{D.4}$$

The differential equation for the coefficients $c_k(T)$, where $k = 1, 2$, can be obtained by using the eigenvectors of the adjoint system,

$$\frac{d\,\mathbf{c}_k(T)}{dT} = -\lambda_k\,\mathbf{c}_k(T) + \frac{\mathbf{d}_k.\mathbf{F}(T)}{\mathbf{d}_k.\mathbf{e}_k} \tag{D.5}$$

The above equation can be directly integrated to yield,

$$\mathbf{c}_k(T) = \frac{\int_{-\infty}^{T} dT' \exp\left[-\lambda_k\,(T-T')\right]\ \mathbf{d}_k.\mathbf{F}(T')}{\mathbf{d}_k.\mathbf{e}_k} \tag{D.6}$$

The ensemble averages $\langle\, \mathbf{c}_k(T)\,\mathbf{c}_q(T)\,\rangle$, where $k = q = 1, 2$, follow from the noise correlation given in (D.2) above,

$$\langle\, \mathbf{c}_k(T)\,\mathbf{c}_q(T)\,\rangle = \left(\frac{\eta}{\lambda_k+\lambda_q}\right)\frac{\mathbf{d}_k.\mathbf{d}_q}{(\mathbf{d}_k.\mathbf{e}_k)\ (\mathbf{d}_q.\mathbf{e}_q)} = (-1)^{k-q}\left(\frac{\eta}{\lambda_k+\lambda_q}\right)\frac{\cos(\theta_{kq})}{\sin^2(\theta_{12})} \tag{D.7}$$

where θ_{kq} is the angle between $\mathbf{e}_k$ and $\mathbf{e}_q$. The excess noise is described by the multiplicative factor $(1/\mathbf{d}_1.\mathbf{e}_1)^2 = (1/\mathbf{d}_2.\mathbf{e}_2)^2 = 1/\sin^2(\theta_{12})$ and it is a measure of the degree of non-orthogonality of the eigenvectors. If the eigenvectors were orthogonal, θ_{12} would equal $\pi/2$, and there would be no excess noise. Also, (D.7) shows that the noise in different eigenvectors is correlated. If the eigenvectors were orthogonal, such correlations would not exist. The smaller the angle θ_{12} between the eigenvectors, the larger the excess noise and the larger the correlations in the noise in different eigenvectors. Looking at the noise dynamics at different time scales provides a clearer picture of the excess noise. Suppose the system (not driven by $\mathbf{F}(T)$ anymore) is kicked by a noise source $\mathbf{N}$ at time $T = 0$. For $T > 0$, the state $\mathbf{V}(T)$ of the system is $c_1(T)\mathbf{e}_1 + c_2(T)\mathbf{e}_2$, where,

$$c_1(T) = \frac{\mathbf{d}_1.\mathbf{N}}{\mathbf{d}_1.\mathbf{e}_1}\exp\left(-\lambda_1 T\right) \tag{D.8}$$

$$c_2(T) = \frac{\mathbf{d}_2.\mathbf{N}}{\mathbf{d}_2.\mathbf{e}_2}\exp\left(-\lambda_2 T\right) \tag{D.9}$$

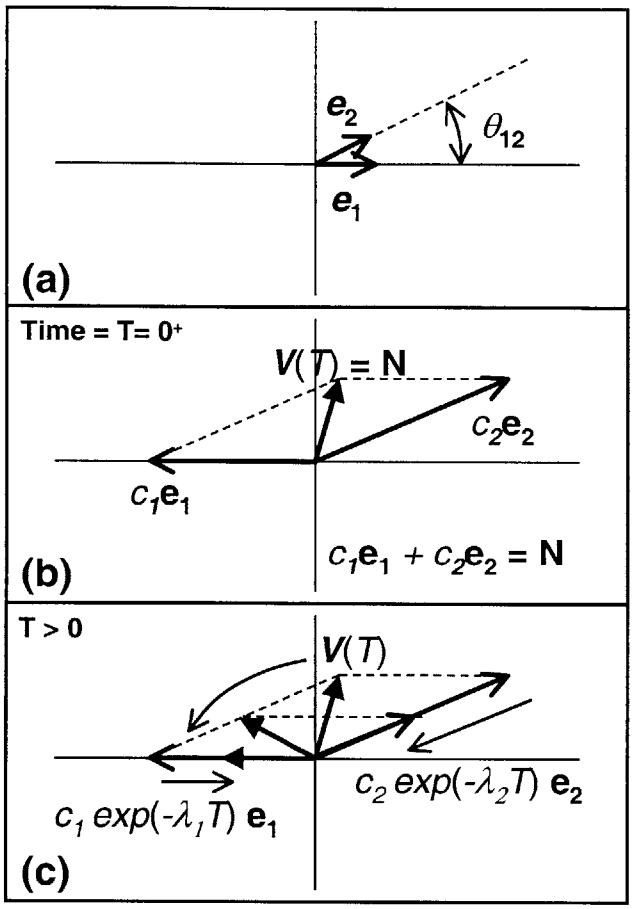

Figure D-1: (a) The two non-orthogonal eigenvectors $\mathbf{e}_1$ and $\mathbf{e}_2$ are depicted. (b) At time $T = 0$, the state $\mathbf{V}(T)$ of the system is $\mathbf{N}$ and there is no excess noise, but the noise in the two eigenvectors is correlated. (c) As time progresses, the noise in eigenvector $\mathbf{e}_2$ decays faster than the noise in eigenvector $\mathbf{e}_1$, and excess noise appears.

At time $T = 0^+$, the noise in the system is just $\mathbf{N}$ and there is no excess noise (see Fig. D-1)b. As time progresses, the noise in the eigenvector $\mathbf{e}_2$, which has the larger (in magnitude) eigenvalue, decays faster than the noise in $\mathbf{e}_1$. For times longer than $1/\lambda_1$, the state of the system may be approximated as $c_1(T)\mathbf{e}_1$ (see Fig. D-1c). The coefficient $c_1(T)$, as shown in (D.8), has the excess noise factor. Therefore, the excess noise, which was absent at short times, appears at time scales longer than the smallest (in magnitude) eigenvalue of the system. At short times, even though the noise in the individual eigenvectors is amplified by the excess noise factor, the noise in different eigenvectors is correlated and as a result of these correlations there is no net excess noise. The excess noise, therefore, results from

the non-Hermitian time evolution of the system. The simple example presented here can be generalized to linear systems defined in higher dimensional complex Hilbert spaces without affecting the essential results.

D.2 Properties of Complex Hermite-Gaussians

The complex Hermite-Gaussians $A_k(t)$ are defined as,

$$A_k(t) = B_k \; H_k\left(\frac{t}{\tau}\sqrt{1+j\beta}\right) \exp\left[-\frac{t^2}{2\tau^2}\,(1+j\beta)\right] \tag{D.10}$$

where B_k is a normalization constant and $H_k(.)$ is the k-th Hermite polynomial [87]. If $A_k(t)$ is normalized such that $\int dt|A_k(t)|^2 = 1$, then B_k is,

$$\frac{1}{B_k^2} = 2^k\, k!\, \sqrt{\pi}\, \tau\, P_k\left(\sqrt{1+\beta^2}\right) \tag{D.11}$$

where $P_k(.)$ is the k-th Legendre polynomial [87]. The following integrals have been used in this paper,

$$\int dt\, A_k^2(t) = \frac{(1-j\beta)^{1/2}}{\sqrt{1+\beta^2}\; P_k\left(\sqrt{1+\beta^2}\right)} \tag{D.12}$$

$$M_{qk} = M_{kq}^* = \int dt\, A_q^*(t)\, A_k(t) = \sqrt{\frac{k!}{q!}}\, \frac{P_{\frac{q+k}{2}}^{\frac{q-k}{2}}\left(\sqrt{1+\beta^2}\right)}{\sqrt{P_q\left(\sqrt{1+\beta^2}\right)\; P_k\left(\sqrt{1+\beta^2}\right)}} \tag{D.13}$$

Here, $P_{\frac{q+k}{2}}^{\frac{q-k}{2}}(.)$ is the associated Legendre function with the following properties,

$$P_{\frac{q+k}{2}}^{\frac{q-k}{2}}(.) = (-1)^{\frac{k-q}{2}}\; \frac{q!}{k!}\, P_{\frac{k+q}{2}}^{\frac{k-q}{2}}(.) \tag{D.14}$$

$$P_k^0(.) = P_k(.) \tag{D.15}$$

D.3 Expansion in an Orthogonal Basis

The perturbation theory for the pulse noise in an actively mode-locked lasers can also be done in an orthogonal basis. One such basis is given by the following set of functions,

$$S_k(t) = D_k \; H_k\left(\frac{t}{\tau}\right) \exp\left[-\frac{t^2}{2\tau^2}\,(1+j\beta)\right] \tag{D.16}$$

where D_k is a normalization constant and $H_k(.)$ is the k-th Hermite polynomial [87]. If $S_k(t)$ is normalized such that $\int dt|S_k(t)|^2 = 1$, then D_k is,

$$\frac{1}{D_k^2} = 2^k\, k!\, \sqrt{\pi}\, \tau \tag{D.17}$$

The functions $S_k(T)$ form an orthonormal set, i.e. $\int dt\, S_q^*(t) S_k(t) dt = \delta_{qk}$. The operator $\widehat{\psi}(t,T)$ can be expanded in this orthonormal basis set,

$$\psi(t,T) = \sqrt{n_o} \sum_{k=0}^{\infty} \widehat{d}_k(T)\, S_k(t) \tag{D.18}$$

where $\widehat{d}_k(T)$ is a quantum mechanical annihilation operator. The operators $\widehat{d}_k(T)$ obey the commutation relation,

$$\left[\widehat{d}_k(T), \widehat{d}_q^{\dagger}(T)\right] = \frac{\delta_{qk}}{n_o} \tag{D.19}$$

The problem with expanding $\widehat{\psi}(t,T)$ in the orthonormal basis $S_k(t)$ is that the functions $S_k(t)$ are not eigenfunctions of the operator $O(t)$ in the master equation (5.2). Consequently, the dynamical equations for the operators $\widehat{d}_k(T)$ obtained by subsituting the orthonormal expansion in the master equation (5.2) results in off-diagonal terms (compare to the simple diagonal dynamical equations for the operators $\widehat{c}_k(T)$ in (5.57) obtained via the eigenfunction expansion). Nevertheless, convergent results can be obtained numerically for the pulse noise without a minimum-error type of expansion (see Appendix D.4 for the minimum-error expansion). Here, the orthonormal expansion is used to prove the result stated in (5.55). Using the orthonormal expansion, the operators for the pulse photon number, phase, timing, and frequency fluctuations become,

$$\Delta\widehat{N}_p(T) = n_o\, \widehat{d}_0(T) + h.c \tag{D.20}$$

$$\Delta\widehat{\Theta}(T) = \frac{1}{2j}\,\widehat{d}_0(T) + h.c \tag{D.21}$$

$$\Delta\widehat{J}(T) = \frac{\tau}{\sqrt{2}}\,\widehat{d}_1(T) + h.c \tag{D.22}$$

$$\Delta\widehat{\Omega}(T) = \frac{j\,(1+j\beta)}{\sqrt{2}\,\tau}\,\widehat{d}_1(T) + h.c \tag{D.23}$$

Note that only the first two functions, $S_0(t)$ and $S_1(t)$, contribute to the pulse photon number, phase, timing, and frequency fluctuations. Also, $S_0(t)$ and $S_1(t)$ are proportional to the first two eigenfunctions, $A_0(t)$) and $A_1(t)$, respectively. The expansion in (D.18) can be written in a more suggestive form,

$$\begin{aligned}\widehat{\psi}(t,T) &= \sqrt{n_o}\left[\left(\frac{\Delta\widehat{N}_p(T)}{2n_o} + j\,\Delta\widehat{\Theta}(T)\right) A_o(t) - \Delta\widehat{J}(T)\,\frac{\partial A_o(t)}{\partial t} - j\,\Delta\widehat{\Omega}(T)\,t\,A_o(t)\right] \\ &\quad + \sqrt{n_o}\sum_{k=2}^{\infty}\widehat{d}_k(T)\,S_k(t)\end{aligned} \tag{D.24}$$

which is the same as (5.55). The terms in the summation in (D.24) consist of perturbations orthogonal to $\Delta\widehat{N}_p(T)$, $\Delta\widehat{\Theta}(T)$, $\Delta\widehat{J}(T)$, and $\Delta\widehat{\Omega}(T)$ since these terms contain noise contributions from only the functions $S_k(T)$ with $k \geq 2$.

D.4 Divergence of the Conventional Perturbative Expansion and the Minimum Error Expansion

The divergence of the perturbative expansion given in (5.70) is best illustrated by studying the noise in a coherent state optical pulse. The pulse in a mode-locked laser is not expected to be a coherent state pulse, but in case of a coherent state pulse exact answers for the mean square pulse fluctuations can be obtained without doing an eigenfunction expansion. Later in this Appendix, a technique to obtain a convergent series expansion for the mean square pulse fluctuations in a mode-locked laser will be presented, and the coherent state case will serve as a check to demonstrate that our technique gives correct answers.

A coherent state pulse is given by the action of the displacement operator on the vacuum state [85],

$$\exp\left[\sqrt{n_o}\int dt\,A_0(t)\widehat{\phi}^{\dagger}(t) - h.c\right]|0\rangle \tag{D.25}$$

The expectation values of the various operators for a coherent state pulse are given be-

low. The time variable T has been suppressed since the operators are assumed to be time independent.

$$\langle\widehat{\phi}(t)\rangle = \sqrt{n_o}\,A_0(t) \quad \langle\widehat{\psi}(t)\rangle = 0 \tag{D.26}$$

$$\langle\widehat{\psi}^\dagger(t)\,\widehat{\psi}(t')\rangle = 0 \quad \langle\widehat{\psi}(t)\,\widehat{\psi}^\dagger(t')\rangle = \delta(t-t') \tag{D.27}$$

The mean square photon number, phase, timing, and frequency fluctuations can be calculated directly using the operator expectation values given above with the relations given in (5.41), (5.42), (5.46), and (5.47), respectively,

$$\langle\Delta\widehat{N}_p^2\rangle = n_o \quad \langle\Delta\widehat{\Theta}^2\rangle = \frac{1}{4\,n_o} \tag{D.28}$$

$$\langle\Delta\widehat{J}^2\rangle = \frac{\tau^2}{2\,n_o} \quad \langle\Delta\widehat{\Omega}^2\rangle = \frac{1}{2\,\tau^2\,n_o}\left(1+\beta^2\right) \tag{D.29}$$

If $\widehat{\psi}(t)$ for a coherent state pulse is expanded in terms of the complex Hermite-Gaussians, as in (5.29), then the following expectation values are obtained,

$$\langle\widehat{c}_k\rangle = \langle\widehat{c}_k^\dagger\rangle = \langle\widehat{c}_k^\dagger\,\widehat{c}_q\rangle = \langle\widehat{c}_k\,\widehat{c}_q\rangle = \langle\widehat{c}_k^\dagger\,\widehat{c}_q^\dagger\rangle = 0 \tag{D.30}$$

$$\langle\widehat{c}_k\,\widehat{c}_q^\dagger\rangle = \frac{1}{n_o}\,\frac{\int dt\,A_q^*(t)A_k(t)}{\int dt\,{A_k}^2(t)\;\int dt\,A_q^{*2}(t)} \tag{D.31}$$

The mean square pulse fluctuations can also be calculated using the expectation values given in (D.30) and (D.31) with the relations given in (5.51)-(5.54). The resulting series can be summed exactly using the completeness relation for the eigenfunctions given in (5.25). For example, for the mean square timing noise of a coherent state pulse one obtains,

$$\langle\Delta\widehat{J}^2\rangle = \frac{\tau^2}{2\,n_o}\sum_{k,q=0}^{\infty} M_{1k}\,M_{qk}\,M_{q1}\,\frac{1}{\int dt\,{A_k}^2(t)\;\int dt\,A_q^{*2}(t)} \tag{D.32}$$

$$= \frac{\tau^2}{2\,n_o}\sum_{k,q=0}^{\infty}\int dt\,A_1^*(t)A_k(t)\int dt\,A_q^*(t)A_1(t)\,\frac{\int dt\,A_q^*(t)A_k(t)}{\int dt\,{A_k}^2(t)\;\int dt\,A_q^{*2}(t)} \tag{D.33}$$

$$= \frac{\tau^2}{2\,n_o} \tag{D.34}$$

The series in (D.32) is similar to the one in (5.70) and does not converge. Fig. D-2 shows the results obtained for the mean square timing fluctuations $\langle\Delta\widehat{J}^2\rangle$ (normalized to the exact value $\tau^2/2n_o$) when only N_{max} eigenfunctions are included in the perturbative expansion

(i.e. only terms with $k, q < N_{max}$ are included in the summation in (D.32)). When the pulse chirp $|\beta|$ is small, the series in (D.32) converges. When $|\beta|$ is large, the series does not converge, and diverges exponentially as more eigenfunctions are included in the perturbative expansion. The largest terms in the series are the diagonal ($k = q$) terms. From the properties of the eigenfunctions $A_k(t)$ given in Appendix D.2, the ratio of two successive diagonal terms can be calculated,

$$\lim_{k\to\infty} \frac{\left|\int dt\, A_1^*(t) A_{k+2}(t)\right|^2}{\left|\int dt\, A_{k+2}^2(t)\right|^2} \frac{\left|\int dt\, A_k^2(t)\right|^2}{\left|\int dt\, A_1^*(t) A_k(t)\right|^2} \approx \beta^2 \left(|\beta| + \sqrt{1+\beta^2}\right)^2 \tag{D.35}$$

The perturbative expansion diverges when $|\beta| > \beta_c$, where the critical value β_c is determined by setting $\beta\left(|\beta| + \sqrt{1+\beta^2}\right)$ equal to unity. This yields $\beta_c = 1/\sqrt{3} \approx 0.577$. This critical value was found in reference [84] in the general context of series expansions using complex Hermite-Gaussians. Numerical calculations confirm the value of $1/\sqrt{3}$ for β_c. Since $\langle \Delta \widehat{J}^2 \rangle$ for a coherent state pulse is not infinite, it follows that when N_{max} becomes infinitely large, the off-diagonal ($k \neq q$) terms in the series in (D.32) suppress the divergence coming from the diagonal ($k = q$) terms. The physical significance of this result is that when $|\beta| \geq \beta_c$, the noise in different eigenfunctions is highly correlated, and these noise correlations suppress the divergence provided an infinite number of eigenfunctions are included in the perturbative expansion. Similar conclusions can be drawn for the mean square frequency fluctuations in a coherent state pulse. $\langle \Delta \widehat{J}^2(T) \rangle$ for a pulse in an actively mode-locked laser is given by the series in (5.70). In contrast to the series in (D.32), completeness relation for the eigenfunctions cannot be used to sum the series in (5.70). In general, a series of the type,

$$\sum_{k,q=0}^{\infty} F_{qk} \frac{M_{pk}\, M_{qk}\, M_{qp}}{\int dt\, A_q^{*2}(t)\ \int dt\, {A_k}^2(t)} \tag{D.36}$$

where F_{qk} ($= F_{kq}^*$) decays only algebraically as k, q become large, will diverge exponentially when $|\beta| > \beta_c$. Below, a technique to obtain convergent expansions for series of the type (D.36) is presented.

D.4.1 Minimum-Error Series Expansion

In reference [84], it was shown that an arbitrary complex function $f(t)$ can be expressed in a convergent series of the form $\sum_{k=0}^{N_{max}-1} a_k A_k(t)$ by choosing the values of the coefficients

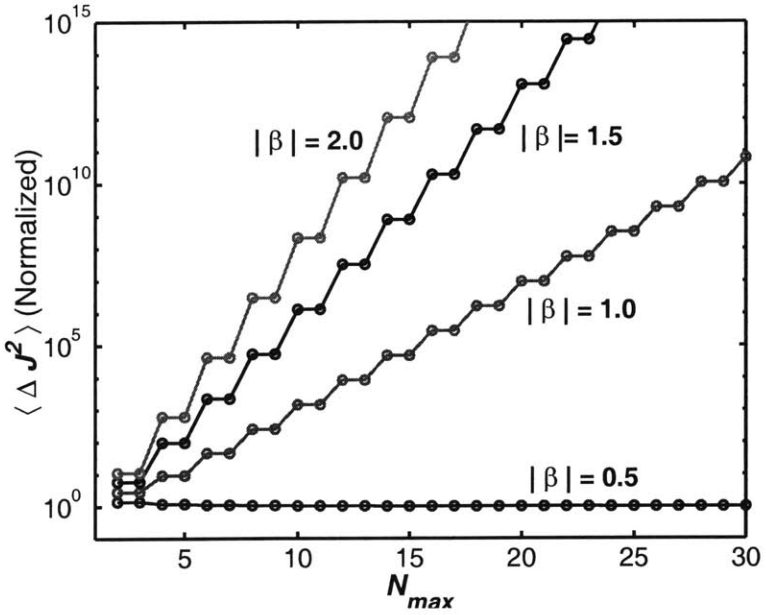

Figure D-2: Mean square timing noise $\langle \Delta \widehat{J}^2 \rangle$ for a coherent state optical pulse calculated using (D.32), normalized to the exact result $\tau^2/2n_o$, is plotted as a function of the number of eigenfunctions N_{max} used in the perturbative expansion. The perturbative expansion diverges when the pulse chirp $|\beta|$ becomes larger than $\beta_c = 1/\sqrt{3}$. The steps appear because only the odd numbered eigenfunctions contribute to the timing noise.

a_k such that the mean square error,

$$\int dt \left| f(t) - \sum_{k=0}^{N_{max}-1} a_k A_k(t) \right|^2 \tag{D.37}$$

is minimized. The expansion obtained this way was shown to have much better convergence properties than the one in which a_k is obtained by projecting the function $f(t)$ onto the basis vectors $A_k(t)$,

$$a_k = \frac{\int dt A_k(t) f(t)}{\int dt A_k^2(t)} \tag{D.38}$$

Here, the minimum error expansion is used to obtain a convergent series from the divergent series in (D.36). A new operator $\Delta \widehat{Q}_p(T)$ is defined as follows,

$$\Delta \widehat{Q}_p(T) = \int dt\, A_p^*(t) \widehat{\psi}(t,T) + h.c = \sum_{k=0}^{\infty} M_{pk}\, \widehat{c}_k(T) + h.c \tag{D.39}$$

A series of the form (D.36) is generated when the mean square value of the operator $\Delta\widehat{Q}_p(T)$ is evaluated and if one assumes that (compare with (5.60), (5.61) and (D.31)),

$$\langle \widehat{c}_k(T)\, \widehat{c}_q^{\dagger}(T)\rangle + \langle \widehat{c}_q^{\dagger}(T)\, \widehat{c}_k(T)\rangle = F_{qk}\ \frac{M_{qk}}{\int dt\, A_q^{*2}(t)\ \int dt\, A_k{}^2(t)} \tag{D.40}$$

The field operator $\widehat{\psi}(t,T)$ can also be expanded using the eigenfunctions of the adjoint operator $O^{\dagger}(t)$,

$$\psi(t,T) = \sqrt{n_o} \sum_{k=0}^{\infty} \widehat{b}_k(T)\, A_k^*(t) \tag{D.41}$$

In terms of the operators $\widehat{b}_k(T)$, the expression for $\Delta\widehat{Q}_p(T)$ is simply,

$$\Delta\widehat{Q}_p(T) = \widehat{b}_p(T) \int dt\, A_p^{*2}(t) + h.c \tag{D.42}$$

We assume that the field $\widehat{\psi}(t,T)$ is known exactly in terms of the operators $\widehat{c}_k(T)$. The operators $\widehat{b}_k(T)$ need to be expressed in terms of the field $\widehat{\psi}(t,T)$ when the summation in (D.41) is restricted to only N_{max} eigenfunctions. If the value of N_{max} is finite, the resulting solution can only be approximate, and this approximation will be considered good if the solution converges as N_{max} becomes large. For a given N_{max}, the optimal $\widehat{b}_k(T)$ is chosen to minimize the mean square error,

$$\int dt \left[\widehat{\psi}^{\dagger}(t,T) - \sqrt{n_o} \sum_{k=0}^{N_{max}-1} \widehat{b}_k^{\dagger}(T)\, A_k(t)\right] \left[\widehat{\psi}(t,T) - \sqrt{n_o} \sum_{k=0}^{N_{max}-1} \widehat{b}_k(T)\, A_k^*(t)\right] \tag{D.43}$$

which gives,

$$\sqrt{n_o} \sum_{k=0}^{N_{max}-1} \widehat{b}_k(T) \int dt\, A_k^*(t) A_q(t) \;=\; \int dt\, A_q(t) \widehat{\psi}(t,T) \tag{D.44}$$

$$\sum_{k=0}^{N_{max}-1} M_{kq}\, \widehat{b}_k(T) \;=\; \widehat{c}_q(T) \int dt\, A_q^2(t) \tag{D.45}$$

Inverting the matrix relation in the above Equation gives the desired result,

$$\widehat{b}_k(T) = \sum_{q=0}^{N_{max}-1} M_{qk}^{-1}\, \widehat{c}_q(T) \int dt\, A_q^2(t) \tag{D.46}$$

Therefore, the expectation value $\langle \widehat{b}_k(T)\, \widehat{b}_q^{\dagger}(T) \rangle$ becomes,

$$\langle \widehat{b}_k(T)\, \widehat{b}_q^{\dagger}(T) \rangle = \lim_{N_{max}\to\infty} \sum_{p,r=0}^{N_{max}-1} M_{pk}^{-1} \int dt\, A_p^2(t)\, \langle \widehat{c}_p(T)\, \widehat{c}_r^{\dagger}(T) \rangle \int dt\, A_r^{*2}(t)\, M_{qr}^{-1} \tag{D.47}$$

Using (D.39), (D.40), (D.42), and (D.47), one obtains,

$$\begin{aligned}
\langle\, \Delta \widehat{Q}_p^2(T)\, \rangle &= \sum_{k,q=0}^{\infty} M_{pk}\, M_{qp} \left[\langle \widehat{c}_k(T)\, \widehat{c}_q^{\dagger}(T) \rangle + \langle \widehat{c}_q^{\dagger}(T)\, \widehat{c}_k(T) \rangle \right] && \text{(D.48)} \\
&= \sum_{k,q=0}^{\infty} F_{qk}\, \frac{M_{pk}\, M_{qk}\, M_{qp}}{\int dt\, A_q^{*2}(t)\ \int dt\, {A_k}^2(t)} && \text{(D.49)} \\
&= \left| \int dt\, A_p^2(t) \right|^2 \left[\langle \widehat{b}_p(T)\, \widehat{b}_p^{\dagger}(T) \rangle + \langle \widehat{b}_p^{\dagger}(T)\, \widehat{b}_p(T) \rangle \right] && \text{(D.50)} \\
&= \lim_{N_{max}\to\infty} \left| \int dt\, A_p^2(t) \right|^2 \sum_{k,q=0}^{N_{max}-1} F_{qk}\, M_{kp}^{-1}\, M_{qk}\, M_{pq}^{-1} && \text{(D.51)}
\end{aligned}$$

Thus, one obtains the important relation,

$$\sum_{k,q=0}^{\infty} F_{qk}\, \frac{M_{pk}\, M_{qk}\, M_{qp}}{\int dt\, A_q^{*2}(t)\ \int dt\, {A_k}^2(t)} = \lim_{N_{max}\to\infty} \left| \int dt\, A_p^2(t) \right|^2 \sum_{k,q=0}^{N_{max}-1} F_{qk}\, M_{kp}^{-1}\, M_{qk}\, M_{pq}^{-1} \tag{D.52}$$

Below, it is shown that the series on the right hand side of the above equation converges. Using (D.32) and (D.52), the mean square timing noise for a coherent state pulse is,

$$\begin{aligned}
\langle \Delta \widehat{J}^2 \rangle &= \frac{\tau^2}{2\, n_o} \sum_{k,q=0}^{\infty} M_{1k}\, M_{qk}\, M_{q1}\, \frac{1}{\int dt\, {A_k}^2(t)\ \int dt\, A_q^{*2}(t)} && \text{(D.53)} \\
&= \lim_{N_{max}\to\infty} \frac{\tau^2}{2\, n_o} \left| \int dt\, A_1^2(t) \right|^2 \sum_{k,q=0}^{N_{max}-1} M_{k1}^{-1}\, M_{qk}\, M_{1q}^{-1} && \text{(D.54)} \\
&= \lim_{N_{max}\to\infty} \frac{\tau^2}{2\, n_o}\, \frac{M_{11}^{-1}}{(1+\beta^2)^{3/2}} && \text{(D.55)}
\end{aligned}$$

Fig. D-3 shows the mean square timing fluctuations of a coherent state pulse calculated using (D.55), normalized to the exact value $\tau^2/2n_o$, as a function of N_{max}. As N_{max} becomes large, M_{11}^{-1} rapidly converges to $(1+\beta^2)^{3/2}$, and $\langle \Delta \widehat{J}^2 \rangle$ converges to $\tau^2/2n_o$.

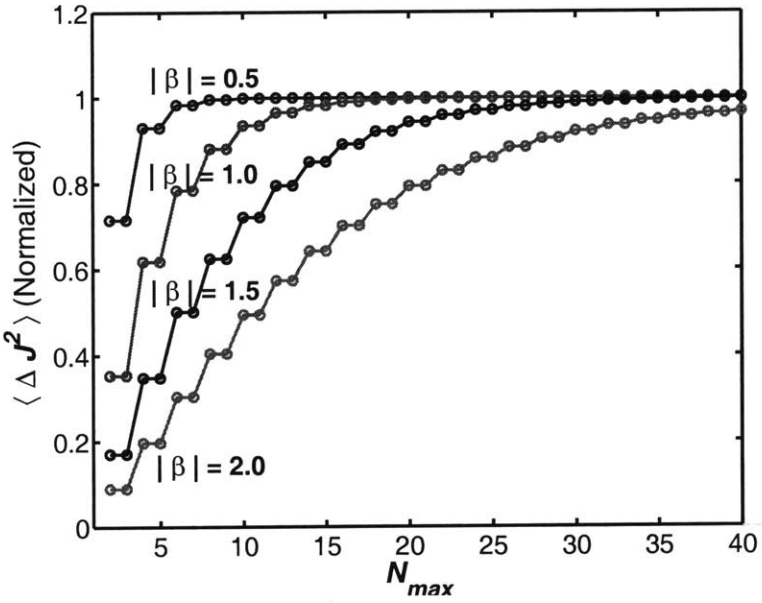

Figure D-3: Mean square timing noise $\langle \Delta \widehat{J}^2 \rangle$ of a coherent state optical pulse calculated using (D.55), normalized to the exact result $\tau^2/2n_o$, is plotted as a function of the number of eigenfunctions N_{max} used in the expansion. The result converges for all values of the pulse chirp. The steps appear because only the odd numbered eigenfunctions contribute to the timing noise.

D.5 Fourier Transforms and Noise Spectral Densities

The properties of the continuous time and discrete time Fourier transforms and the corresponding noise spectral densities are briefly reviewed here.

D.5.1 Continuous Time Fourier Transform and Noise Spectral Densities

The Fourier transform of a zero mean noise operator $\widehat{W}(T)$ is defined as,

$$\widehat{W}(\omega) = \int dt\, \widehat{W}(T)\, \exp\left(-j\omega\, T\right) \tag{D.56}$$

The inverse Fourier transform is,

$$\widehat{W}(T) = \int_{-\infty}^{\infty} \frac{d\omega}{2\pi}\, \widehat{W}(\omega)\, \exp\left(j\omega\, T\right) \tag{D.57}$$

The spectral density $S_W(\omega)$ of $\widehat{W}(T)$ is defined as the Fourier transforms of the symmetric correlation function,

$$S_W(\omega) = \int_{-\infty}^{\infty} ds\, \frac{1}{2}\, \left[\, \langle \widehat{W}(T)\, \widehat{W}(T+s)\rangle + \langle \widehat{W}(T+s)\, \widehat{W}(T)\rangle \,\right] \exp\left(-j\omega\, s\right) \tag{D.58}$$

It is assumed in the definition above that the correlation function is stationary and, therefore, independent of the time variable T. It follows from the definition of $S_W(\omega)$ that the mean square value $\langle \widehat{W}^2(T)\rangle$ of the fluctuations is,

$$\langle \widehat{W}^2(T)\rangle = \int_{-\infty}^{\infty} \frac{d\omega}{2\pi}\, S_W(\omega) \tag{D.59}$$

D.5.2 Discrete Time Fourier Transforms and Noise Spectral Densities

The discrete time Fourier transform $\widehat{W}(\omega T_R)$ of a zero mean noise operator $\widehat{W}(m)$, which is a function of the discrete index m, is defined as,

$$\widehat{W}(\omega T_R) = \sum_{m=-\infty}^{\infty} \widehat{W}(m)\, \exp\left(-j\omega\, T_R\, m\right) \tag{D.60}$$

$\widehat{W}(\omega T_R)$ is periodic in ω with a period $2\pi/T_R$. The inverse Fourier transform is,

$$\widehat{W}(m) = T_R \int_{-\pi/T_R}^{\pi/T_R} \frac{d\omega}{2\pi} \widehat{W}(\omega T_R) \exp(j\omega T_R m) \tag{D.61}$$

The spectral density $\Phi_W(\omega T_R)$ of $\widehat{W}(m)$ is defined as the discrete time Fourier transform of the symmetric correlation function,

$$\Phi_W(\omega T_R) = \sum_{m=-\infty}^{\infty} \frac{1}{2} \left[\langle \widehat{W}(n)\, \widehat{W}(n+m) \rangle + \langle \widehat{W}(n+m)\, \widehat{W}(n) \rangle \right] \exp(-j\omega T_R m) \tag{D.62}$$

It is assumed in the definition above that the correlation function is stationary and, therefore, independent of n. The spectral density $\Phi_W(\omega T_R)$ is periodic in ω with a period $2\pi/T_R$. It follows from the definition of $\Phi_W(\omega T_R)$ that the mean square value $\langle \widehat{W}^2(m) \rangle$ of the fluctuations is,

$$\langle \widehat{W}^2(m) \rangle = T_R \int_{-\pi/T_R}^{\pi/T_R} \frac{d\omega}{2\pi} \Phi_W(\omega T_R) \tag{D.63}$$

If $\widehat{W}(m)$ equals $\widehat{W}(T = mT_R)$ then the following relationships hold,

$$\widehat{W}(\omega T_R) = \frac{1}{T_R} \sum_{m=-\infty}^{\infty} \widehat{W}\left(\omega - \frac{2\pi m}{T_R}\right) \tag{D.64}$$

$$\Phi_W(\omega T_R) = \frac{1}{T_R} \sum_{m=-\infty}^{\infty} S_W\left(\omega - \frac{2\pi m}{T_R}\right) \tag{D.65}$$

In addition, if $\widehat{W}(T)$ varies significantly only over time scales much larger than T_R than for $|\omega| < 2\pi/T_R$,

$$\widehat{W}(\omega T_R) = \frac{1}{T_R} \widehat{W}(\omega) \tag{D.66}$$

$$\Phi_W(\omega T_R) = \frac{1}{T_R} S_W(\omega) \tag{D.67}$$

and,

$$\langle \widehat{W}^2(m) \rangle = T_R \int_{-\pi/T_R}^{\pi/T_R} \frac{d\omega}{2\pi} \Phi_W(\omega T_R) = \int_{-\pi/T_R}^{\pi/T_R} \frac{d\omega}{2\pi} S_W(\omega) = \langle \widehat{W}^2(T) \rangle \tag{D.68}$$

Appendix E

Appendix: Chapter 6

E.1 Finite Difference Equations for Pulse Timing Noise in Fundamentally and Harmonically Mode-Locked Semiconductor Lasers

In Chapter 6, models for the pulse timing noise in the absence of dispersion and active phase modulation were presented for fundamentally and harmonically mode-locked semiconductor lasers. In this Appendix, the derivation of the discrete-time finite difference equations for the pulse timing noise in (6.5) and (6.12) are explained in more detail. The models discussed below are simple since increasing the complexity of the model does not affect the nature of the conclusions in Chapter 6. It is assumed that there is no dispersion in the cavity, and active phase modulation is also assumed to be absent. However, in contrast to the model presented in Chapter 5, dynamic gain and/or loss saturation is included. The time domain pulse perturbation theory presented in Chapter 5 for actively mode-locked semiconductor lasers is used here. The master equation that describes the slow time evolution of the amplitude $\phi(t,T)$ of a pulse in an actively mode-locked semiconductor laser in the absence of dispersion and active phase modulation is,

$$\frac{\partial \phi(t,T)}{\partial T} = \frac{j\nu}{T_R} + \frac{B}{2}\frac{\partial^2 \phi(t,T)}{\partial t^2} + \frac{1}{2}\left[G(t) + g_m(t) - L(t)\right]\phi(t,T) \tag{E.1}$$

$$+ F_{sp}(t,T) + F_v(t,T) \tag{E.2}$$

where the time variable T describes the pulse evolution over time scales longer than the cavity round trip time T_R. ν is the phase shift acquired by the pulse in one round trip. $G(t)$ is the gain. Because of dynamic gain saturation in semiconductor lasers [36], $G(t)$ is assumed to be a function of the time-dependent pulse intensity. For simplicity, dynamic self-phase modulation that accompanies dynamic gain saturation in semiconductor lasers is also ignored [36]. $L(t)$ is the loss and is also assumed to be a function of the time-dependent pulse intensity because of dynamic loss saturation (i.e. slow saturable absorption). $g_m(t)$ describes the time dependent gain because of the active modulation. $g_m(t)$ equals $A_M\left[\cos\left(\omega_N t\right)-1\right]$, where ω_N is the modulation frequency. B describes the effect of the finite gain bandwidth (or filter bandwidth). $F_{sp}(t,T)$ and $F_v(t,T)$ represent the noise sources for spontaneous emission and vacuum fluctuations, respectively, and their correlation functions are given in Chapter 5.

Fundamentally Mode-locked Lasers

For a fundamentally mode-locked laser ($N=1$), the modulation frequency ω_N equals the cavity round trip frequency ω_R. The steady state pulse is obtained by solving the non-linear master equation in the absence of noise. It is assumed that the steady state pulse amplitude is $\sqrt{n_o/\tau}\,A(t/\tau)$, where n_o is the number of photons in the pulse, and τ is the pulse width. $A(t/\tau)$ is real and is normalized such that $\int_{-\infty}^{\infty}dx\,A^2(x)=1$. In the presence of noise, $\phi(t,T)$ may be expanded as,

$$\begin{aligned}\phi(t,T) \;\approx\; & \sqrt{\frac{n_o}{\tau}}A\left(\frac{t}{\tau}\right)+\sqrt{\frac{n_o}{\tau}}\left[\frac{\Delta N_p(T)}{2n_o}A\left(\frac{t}{\tau}\right)+j\Delta\Theta(T)\,A\left(\frac{t}{\tau}\right)\right.\\ & \left.-\Delta J(T)\,\frac{dA}{dt}-j\Delta\Omega(T)\,(t-t_o)A\left(\frac{t}{\tau}\right)\right]\end{aligned} \tag{E.3}$$

where $\Delta N_p(T)$, $\Delta\Theta(T)$, $\Delta J(T)$, and $\Delta\Omega(T)$ are the pulse amplitude, phase, timing, and frequency fluctuations, respectively. The temporal position t_o of the steady state pulse is defined by the Equation, $\int_{-\infty}^{\infty}dt\,(t-t_o)A^2(t/\tau)=0$. In the presence of dynamic gain and/or loss saturation, the pulse position t_o does not coincide with the peak gain in the active modulator [36]. The expansion in (E.3) ignores the fluctuations that distort the pulse shape. The equation for the pulse amplitude (phase) fluctuations can be obtained by substituting the expansion in (E.3) in the master equation, and projecting out the pulse amplitude (phase) fluctuations by multiplying both sides of the resulting equation by

$A(t/\tau)$, integrating, and keeping the real (imaginary) part. The pulse timing (frequency) fluctuations can be projected out by multiplying both sides by $dA(t/\tau)/dt$, integrating, and keeping the real (imaginary) part. This yields,

$$\frac{d\,\Delta J(T)}{dT} = -\gamma \Delta J(T) + F(T) \tag{E.4}$$

where γ is given by the expression,

$$\begin{aligned}
\gamma &= \frac{1}{2}\frac{\int_{-\infty}^{\infty} dt\, \frac{dg_m(t)}{dt} A(t/\tau) \frac{dA(t/\tau)}{dt}}{\int_{-\infty}^{\infty} dt\, \frac{dA(t/\tau)}{dt}\frac{dA(t/\tau)}{dt}} \\
&= \frac{A_M}{2}\omega_R^2 \tau^2 \left\{ -\frac{\int_{-\infty}^{\infty} dx\; x\, A(x)A'(x)}{\int_{-\infty}^{\infty} dx\, A'(x)A'(x)} \right\} \qquad \text{(E.5)} \\
&= \frac{A_M}{2}\omega_R^2 \tau^2 \left\{ \frac{1}{2\int_{-\infty}^{\infty} dx\, A'(x)A'(x)} \right\} \qquad \text{(E.6)}
\end{aligned}$$

(E.6) follows from (E.5) since the integral $\int_{\infty}^{\infty} dx\; xA(x)A'(x)$ equals $-1/2$ for any arbitrary pulse shape. If the pulse shape is approximately gaussian, the expression in the curly brackets in (E.6) equals unity. The correlation function for the noise source $F(T)$ is approximately given by the expression,

$$\langle F(T)F(T')\rangle = \frac{\tau^2}{2n_o}\left[(2n_{sp}-1)\langle G\rangle + \langle L\rangle\right] \left\{ \frac{1}{2\int_{-\infty}^{\infty} dx\, A'(x)A'(x)} \right\} \delta(T-T') \tag{E.7}$$

where $\langle G\rangle$ is the total average gain in the steady state, $\langle L\rangle$ is the total average loss, and n_{sp} is the spontaneous emission factor which takes into account the incomplete inversion of the gain medium [1]. In the steady state, since the gain $\langle G\rangle$ equals the loss $\langle L\rangle$, (E.7) can be simplified,

$$\langle F(T)F(T')\rangle = \left(\frac{n_{sp}}{n_p}\right)\langle L\rangle\, \tau^2 \left\{ \frac{1}{2\int_{-\infty}^{\infty} dx\, A'(x)A'(x)} \right\} \delta(T-T') \tag{E.8}$$

Assuming that $\gamma T_R \ll 1$, (E.4) can be discretized,

$$\Delta J(n+1) - \Delta J(n) = -\gamma T_R \, \Delta J(n) + F(n) \tag{E.9}$$

The discrete-time noise variable $\Delta J(n)$ is the timing noise in the pulse after the n-th round trip. The noise source $F(n)$ represents the total timing noise added to the pulse in one round trip,

$$F(n) = \oint dT \; F(T) \tag{E.10}$$

and has the correlation function,

$$\langle F(n) \, F(m) \rangle = D \, \delta_{n,m} \tag{E.11}$$

where D equals,

$$D = \left(\frac{n_{sp}}{n_p} \right) \langle L \rangle \, T_R \, \tau^2 \left\{ \frac{1}{2 \int_{-\infty}^{\infty} dx \, A'(x) A'(x)} \right\} \tag{E.12}$$

The expression for the mean square timing Jitter in a fundamentally mode-locked laser was given in (6.8),

$$\langle \Delta J^2 \rangle = \langle \Delta J^2(n) \rangle = \frac{D}{2 \gamma T_R} \tag{E.13}$$

Using the values of γ and D given above, one obtains,

$$\langle \Delta J^2 \rangle = \left(\frac{n_{sp}}{n_p} \right) \langle L \rangle \, \frac{1}{A_M \omega_R^2} \tag{E.14}$$

Note that the loss $\langle L \rangle$ can be related to the photon lifetime τ_p in the laser cavity, $\langle L \rangle = 1/\tau_p$. The analysis for the timing noise presented here assumed dynamic gain and/or loss saturation. The mean square timing jitter is found to be independent of the pulse shape and the pulse width. This is not true for the timing noise spectral density which depends on the pulse shape and the pulse width through γ (see (6.10) and (E.6)). The model for the pulse timing noise presented here is not applicable when the pulse is chirped and its amplitude is described by a complex function. The pulse can acquire a chirp in the presence of dispersion, active phase modulation, or dynamic self-phase modulation.

Harmonically Mode-locked Lasers

A laser mode-locked at the N-th harmonic has N pulses propagating inside the laser cavity. Some additional assumptions are required before the model presented above for fundamentally mode-locked lasers can be used for harmonically mode-locked lasers. In the noiseless steady state, all the pulses are assumed to be identical. Any departure from this steady state is considered noise. The steady state is assumed to be stable in the sense that the pulse energy and timing fluctuations are damped and do not become very large (this implies no pulse dropouts). The pulse fluctuations are assumed to be stationary. In the steady state, each pulse is assumed to obey the noiseless master equation. The steady state amplitude of each pulse is assumed to be $\sqrt{n_o/\tau_N}B(t/\tau_N)$, where τ_N is the pulse width, and n_o is the number of photons in each pulse. $B(t/\tau_N)$ is real and is normalized such that $\int_{-\infty}^{\infty}dx\,B^2(x) = 1$.

If the timing fluctuations in different pulses are assumed to evolve completely independently, finite difference equation for the timing noise in each pulse can be obtained in the same as for fundamentally mode-locked lasers. It should be pointed out here that the photon number fluctuations in different pulses cannot be assumed to evolve independently since all the pulses interact with the same gain (and loss) medium whose recovery time can be much longer than the pulse repetition time. For the timing fluctuations, assuming independent evolution, the N separate finite difference equations for the timing noise in N different pulses can be written in the compact form shown below,

$$\Delta J(n+N) - \Delta J(n) = -\gamma_N T_R\,\Delta J(n) + F_N(n) \tag{E.15}$$

where γ_N is,

$$\gamma_N = \frac{A_M}{2}\omega_N^2\tau_N^2\left\{\frac{1}{2\int_{-\infty}^{\infty}dx\,B'(x)B'(x)}\right\} \tag{E.16}$$

The noise source $F_N(n)$ represents the total timing noise added to each pulse in one round trip, and has the correlation function,

$$\langle F_N(n)\,F_N(m)\rangle = D_N\,\delta_{n,m} \tag{E.17}$$

where D_N is,

$$D_N = \left(\frac{n_{sp}}{n_o}\right) \langle L \rangle T_R \tau_N^2 \left\{ \frac{1}{2\int_{-\infty}^{\infty} dx\, B'(x)B'(x)} \right\} \tag{E.18}$$

The expression for the mean square timing Jitter in a harmonically mode-locked laser was given in (6.15),

$$\langle \Delta J^2 \rangle = \langle \Delta J^2(n) \rangle = \frac{D_N}{2\gamma_N T_R} \tag{E.19}$$

Using the values for γ_N and D_N given above, one obtains,

$$\langle \Delta J^2 \rangle = \left(\frac{n_{sp}}{n_p}\right) \langle L \rangle \frac{1}{A_M \omega_N^2} \tag{E.20}$$

The loss $\langle L \rangle$ is related to the photon lifetime τ_p in the laser cavity, $\langle L \rangle = 1/\tau_p$. As in the fundamentally mode-locked case, the mean square timing jitter is found to be independent of the pulse shape and the pulse width, but the timing noise spectral density depends on both the pulse width and the pulse shape through γ_N (see (6.17) and (E.16)). When a fundamentally mode-locked laser is harmonically mode-locked by increasing the modulation frequency from ω_R to ω_N, (E.14) and (E.20) show that the mean square timing jitter decreases as long as the pulse energy, the modulation strength, and the cavity round trip loss do not change. Also, the pulse shape and the pulse width may or may not change depending upon whether the dominant pulse shaping mechanism is dynamic gain and/or loss saturation or active modulation.

Bibliography

[1] L. A. Coldren, S. Corzine,*Diode Lasers and Photonic Integrated Circuits*, John Wiley and Sons, NY (1995).

[2] P. W. Juodawlkis, J. C. Twichell, G. E. Betts, J. J. Hargreaves, R. D. Younger, J. L. Wasserman, F. J. O'Donnell, K. G. Ray, R. C. Williamson, "Optically sampled analog-to-digital converters," Trans. Mirowave Theory and Tech. **49**, 1840-1853 (2001).

[3] C. Cox, H. Roussell, R. J. Ram, R. J. Helkey, "Broadband, directly modulated analog fiber link with positive intrinsic gain and reduced noise figure," International Topical Meeting on Microwave Photonics, Princeton, October 1998.

[4] S. G. Ayling, D. R. Wight, M. B. Allenson, K. P. Hilton, G. W. Smith: "Intrinsically matched 50 Ohm laser arrays with greater than 100% quantum efficiencies for optically coupled transistors and low loss fibre optic links," SPIE Photonics West '98, Optoelectroncs '98: Laser Diode Applications IV; Conf. No. 3285B-Paper 36.

[5] S. G. Ayling, D. R. Wight, M. B. Allenson, K. P. Hilton, G. W. Smith: "Novel integrated laser devices with greatly enhanced quantum efficiency and intrinsic RF matching for low loss, broad band opto-microwave applications," Microwave Photonics '98, October 1998.

[6] J. T. Getty, O. Buchinsky, R. A. Salvato, B. Mason, L. A. Coldren, "Enhanced differential efficiency with monolithic, series-connected, segmented ridge lasers," Proceedings Annual Meeting of the IEEE Lasers and Electro-Optics Society'1999, IEEE Press, NJ (1999).

[7] L. J. Olafsen, E. H. Aifer, W. W. Bewley, C. L. Felix, J. R. Meyer: "Near room temperature mid-infrared interband cascade laser," App. Phys. Lett. **72**, 2370-2372 (1998).

[8] J. P. van der Ziel, W. T. Tsang, "Integrated multi-layer GaAs lasers separated by tunnel junctions," App. Phys. Lett. **41**, 499-501 (1982).

[9] J. Ch. Garcia, E. Rosencher, Ph. Collot, N. Luarent, J. Guyaux, B. Vinter, J. Nagle: "Epitaxially stacked lasers with Esaki junctions: A bipolar cascade laser," App. Phys. Lett. **71**, 3752-3754 (1997).

[10] S. G. Patterson, G. S. Petrich, R. J. Ram, L. A. Kolodzjieski, "Room temperature, continuous wave operation of a bipolar quantum cascade laser," Elect. Lett. **35**, 395-397 (1999).

[11] J. K. Kim, S. Nakagawa, E. Hall, L. Coldren, "Near room temperature continuous wave operation of multiple active region 1.55 μm vertical cavity lasers with high differential efficiency," Appl. Phys. Lett. **77**, 3137-3139 (2000).

[12] J. Faist, F. Capasso, C. Sirtori, D. L. Sivco, A. L. Hutchinson, A. Y. Cho, "Vertical transition quantum cascade laser with Bragg confined excited state," Appl. Phys. Lett. **66**, 538-540 (1995).

[13] J. Faist, F. Capasso, C. Sirtori, D. L. Sivco, A. L. Hutchinson, A. Y. Cho, "Continuous wave operation of a vertical transition quantum cascade laser above T=80 K," Appl. Phys. Lett. **67**, 3057-3059 (1995).

[14] C. Sirtori, J. Faist, F. Capasso, D. L. Sivco, A. L. Hutchinson, S. N. G. Chu, A. Y. Cho, "Continuous wave operation of midinfrared (7.4-8.6 μm) quantum cascade lasers up to 110 K temperature," Appl. Phys. Lett. **68**, 1745-1747 (1996).

[15] C. Sirtori, J. Faist, F. Capasso, D. L. Sivco, A. L. Hutchinson, A. Y. Cho, , "Pulsed and continuous-wave operation of long wavelength infrared ($\lambda \approx 9.3$ μm) quantum cascade lasers," IEEE J. Quantum Electron. **33**, 89-93 (1997).

[16] J. Faist, A. Tredicucci, F. Capasso, C. Sirtori, D. L. Sivco, J. N. Baillargeon, A. L. Hutchinson, "High-power continuous-wave quantum cascade lasers," IEEE J. Quantum Electron. **34**, 336-343 (1998).

[17] C. Sirtori, P. Kruck, S. Barbieri, P. Collot, J. Nagle, "GaAs/$Al_xGa_{1-x}As$ quantum cascade lasers," Appl. Phys. Lett. **73**, 3486-3488 (1998).

[18] C. Gmachl, J. Faist, F. Capasso, C. Sirtori, D. L. Sivco, A. Y. Cho, "Long-wavelength (9.5-11.5 μm) microdisk quantum-cascade lasers," IEEE J. Quantum Electron. **33**, 1567-1573 (1997).

[19] C. Gmachl, F. Capasso, A. Tredicucci, D. L. Sivco, "Noncascaded intersubband injection lasers at $\lambda \approx 7.7$ μm," Appl. Phys. Lett. **73**, 3830-3832 (1998).

[20] C. Gmachl, F. Capasso, J. Faist, A. L. Hutchinson, A. Tredicucci, D. L. Sivco, J. N. Baillargeon, S. N. G. Chu, A. Y. Cho, "Continuous-wave and high-power pulsed operation of index-coupled distributed feedback quantum cascade laser at $\lambda \approx 8.5$ μm," Appl. Phys. Lett. **72**, 1430-1432 (1998).

[21] A. Tredicucci, F. Capasso, C. Gmachl, D. L. Sivco, A. L. Hutchinson, A. Y. Cho, J. Faist, G. Scamarcio, "High-power inter-miniband lasing in intrinsic superlattices," Appl. Phys. Lett. **72**, 2388-2390 (1998).

[22] A. Tredicucci, F. Capasso, C. Gmachl, D. L. Sivco, A. L. Hutchinson, A. Y. Cho, "High performance interminiband quantum cascade lasers with graded superlattices," Appl. Phys. Lett. **73**, 2101-2103 (1998).

[23] A. Tredicucci, C. Gmachl, F. Capasso, D. L. Sivco, A. L. Hutchinson, A. Y. Cho, J. Faist, G. Scamarcio, "Long wavelength superlattice quantum cascade lasers at $\lambda \approx 17$ μm," Appl. Phys. Lett. **74**, 638-640 (1999).

[24] G. Strasser, S. Gianordoli, L. Hvozdara, W. Schrenk, K. Unterrainer, E. Gornik, "GaAs/AlGaAs superlattice quantum cascade lasers at $\lambda \approx 13$ μm," Appl. Phys. Lett. **75**, 1345-1347 (1999).

[25] C. Gmachl, H. M. Ng, A. Y. Cho, "Intersubband absorption in degenerately doped GaN/AlGaN coupled double quantum wells," Appl. Phys. Lett. **79**, 1590-1592 (2001).

[26] Y. M. Blanter, M. Buttiker, "Transition from sub-Poissonian to super-Poissonian shot noise in resonant quantum wells," Phys. Rev. B **59**, 10217-10226 (1999).

[27] J. H. Davies, P. Hyldgaard, Selman Hershfield, J. W. Williams, "Classical theory for shot noise in resonant tunneling," Phys. Rev. B **46**, 9620-9633 (1992).

[28] G. Iannaccone, M Macucci, B. Pellegrini, "Shot noise in resonant-tunneling structures," Phys. Rev B **55**, 4539-4550 (1997).

[29] Y. Yamamoto, S. Machida, "High-impedance suppression of pump fluctuation and amplitude squeezing in semiconductor lasers," Phys. Rev. A **35**, 5114-5130 (1987).

[30] D. J. Derickson, R. J. Helkey, A. Mar, J. R. Karin, J. G. Wasserbauer, J. E. Bowers, "Short pulse generation using multisegment mode-locked semiconductor lasers," IEEE J. Quantum Electron. **28**, 2186-2202 (1992).

[31] J. E. Bowers, P. A. Morton, A. Mar, S. W. Corzine, "Actively mode-locked semiconductor lasers," IEEE J. Quantum Electron. **25**, 1426-1439 (1989).

[32] R. H. Walden, "Analog-to-Digital Converter Survey and Analysis," IEEE J. Selected Areas in Communication **17**, 539-550 (1999).

[33] H. A. Haus, A. Mecozzi, "Noise of mode-locked lasers," IEEE J. Quantum Electronics **29**, 983-996 (1993).

[34] H. A. Haus, M. Margalit, C. X. Yu, "Quantum noise of a mode-locked laser," J. Optical Soc. America B **17**, 1240-1256 (2000).

[35] D. R. Hjelme, A. R. Mickelson, Theory of timing jitter in actively mode-locked lasers," IEEE J. Quantum Electronics **28**, 1594-1606 (1992).

[36] F. Rana, R. J. Ram, "Noise and timing jitter in active and hybrid mode-locked semiconductor lasers," Proceedings CLEO'2001, 6-7 (2001).

[37] F. Rana, R. J. Ram, "Excess Noise in Non-Hermitian Mode-Locked Laser Systems," To be presented at CLEO'2002 in May 2002.

[38] E. Goobar, A. Karlsson, G. Bjork, P-J. Rigole, "Quantum correlated light beams and Sub-Poissonian electrical partition noise in parallel and serics coupled semiconductor light emitters," Phys. Rev. Lett., Jan. 1993, 70, pp. 437-440.

[39] P. J. Edwards, G. H. Pollard, "Quantum noise correlated operation of electrically coupled semiconductor light emitters," Phys. Rev. Lett., Sep. 1992, 69, pp. 1757-1760.

[40] G. Bjork, "Generation of intensity correlated twin beams using series coupled semiconductor lasers," Phy. Rev. A, June 1992, 45, pp. 8259-8267.

[41] K. Petermann, "Laser Diode Modulation and Noise," Kluwer, Netherlands (1991).

[42] J. Kim, Y. Yamamoto, "Theory of noise in p-n junction light emitters," Phys. Rev. B **55**, 9949-9959 (1997).

[43] Y. Yamamoto, H. A. Haus, "Effect of of electrical partition noise on squeezing in semiconductor lasers," Phys. Rev. A **45**, 6596-6604 (1992).

[44] F. Rana, R. Ram, "Photon noise and correlations in semiconductor cascade lasers," Appl. Phys. Lett. **76**, 1083-1085 (2000).

[45] F. Rana, S. G. Patterson, R. Ram, "Noise in semiconductor cascade lasers," Proceedings Integrated Photonics Research'1999 (1999).

[46] F. Rana, "Current noise, photon number fluctuations and squeezing in quantum cascade lasers," Proceedings IEEE LEOS Annual Meeting'1999 (1999).

[47] F. Rana, R. Ram, "Current Noise in Semiconductor Lasers," Proceedings IEEE LEOS Summer Topical'2001 (2001).

[48] K. Y. Lau in "Quantum Well Lasers," P. S. Zory (Editor), Academic Press, New York (1993).

[49] G. P. Agrawal, N. K. Datta, "Long Wavelength Semiconductor Lasers," Van Nostrand Reinhold, New York (1993).

[50] S. Machida, Y. Yamamoto, "Observation of amplitude squeezing from semiconductor lasers by balanced direct detectors with a delay line," Optics Lett. **14**, 1045-1047 (1989).

[51] Y. Yamamoto, S. Machida, W. H. Richardson, "Photon number squeezed states in semiconductor lasers," Science **255**, 1219-1224 (1992).

[52] J. A. Brum, G. Bastard, "Resonant carrier capture by semiconductor quantum wells," Phys. Rev. B **33**, 1420-1423 (1986).

[53] H. Schneider, K. V. Klitzing, "Thermionic emission and gaussian trasnport of holes in GaAs/AlGaAs multiple quantum well structure," Phys. Rev. B **38**, 6160-6165 (1988).

[54] S. L. Chuang, *Physics of Optoelectronic Devices*,Wiley, NY (1995).

[55] M. H. Lim, *Development of X-ray lithography and nanofabrication techniques for III-V optical devices*, Doctor's Thesis, Department of Electrical Engineering and Computer Science, Massachusetts Institute of Technology, Cambridge (2002).

[56] P. Mayer, *Current Fluctuations in Semiconductor Devices*, Master's Thesis, Department of Electrical Engineering and Computer Science, Massachusetts Institute of Technology, Cambridge (2002).

[57] C. W. Gardiner, "Quantum Noise," Springer Verlag, New York (1996).

[58] T. Martin, R. Landauer, "Wave-packet approach to noise in multichannel mesoscopic systems," Phys. Rev. B **45** , 1742-1755 (1992).

[59] M. Buttiker, "Scattering theory of current and intensity noise correlations in conductors and wave guides," Phys. Rev. B **46**, 12845-12507 (1992).

[60] J. Faist, F. Capasso, C. Sirtori, D. L. Sivco, A. L. Hutchinson, A. Y. Cho, "Laser action by tuning oscillator strength," Nature **387**, 777-782 (1997).

[61] J. Faist, F. Capasso, C. Sirtori, D. L. Sivco, D. L. Hutchinson, M. S. Hybertsen, A. Y. Cho, "Quantum cascade lasers without intersubband population inversion," Phys. Rev. Lett. **76**, 411-414 (1996).

[62] C. Gmachl, F. Capasso, A. Tredicucci, D. L. Sivco, R. Kohler, A. L. Hutchinson, A. Y. Cho, "Dependence of the device performance on the number of stages in quantum-cascade lasers," IEEE J. Selected Topics Quantum Electronics **5**, 808-816 (1999).

[63] A. Wacker, A-P. Jauho, "Microscopic modelling of perpendicular electronic transport in doped multiple quantum wells," Physica Scripta **T69**, 321-324 (1997).

[64] C. W. Gardiner, "Handbook of Stochastic Methods," Springer Verlag, New York (1996).

[65] F. Rana, "Current noise, photon number fluctuations and squeezing in quantum cascade lasers," Proceedings IEEE LEOS Annual Meeting'1999 (1999).

[66] P. D. Yoder, K. Gartner, W. Fichtner, "A generalized Ramo-Shockley theorem for classical to quantum transport at arbitrary frequencies," J. Appl. Phys. **79**, 1951-1954 (1996).

[67] N. Mustafa, L. Pesquera, L. Cheung, K. A. Shore, "Terahertz bandwidth prediction for amplitude modulation response of unipolar intersubband semiconductor lasers," IEEE Photonics Tech. Lett. **11**, 527-529 (1999).

[68] S. Inoue, H. Ohzu, S. Machida, Y. Yamamoto, "Quantum correlation between longitudinal-mode intensities in a multimode squeezed semiconductor laser," Phys. Rev. A **46**, 2757-2765 (1992).

[69] T. G. Ulmer, M. C. Gross, K. M. Patel, J. T. Simmons, P. W. Juodawlkis, "160-Gb/s optically time-division multiplexed link with all-optical demultiplexing," IEEE J. Lightwave Technology **18**, 1964-1977 (2000).

[70] H. A. Haus, Y. Lai, "Quantum theory of soliton squeezing: a linearized approach," J. Opt. Soc. Am. B **7**, 386 (1990).

[71] L. A. Jiang, M. E. Grein, H. A. Haus, E. P. Ippen, "Noise of mode-locked semiconductor lasers," J. Select. Quantum Electronics **7**, 159-167 (2001).

[72] H. A. Haus, "A theory of forced mode locking," IEEE J. Quantum Electronics **11** , 323-330 (1975).

[73] E. Zeidler, *Applied Functional Analysis*, Springer-Verlag, NY (1995).

[74] K. Petermann, "Calculated spontaneous emission factor for double-heterostructure injection lasers with gain-induced waveguiding," IEEE J. Quantum Electronics **15**, 566-570 (1979).

[75] H. A. Haus, S. Kawakami, "On the 'excess spontaneous emission factor' in gain-guided laser amplifiers," IEEE J. Quantum Electronics **21**, 63-69 (1985).

[76] A. E. Siegman, "Excess spontaneous emission in non-Hermitian optical systems. I. Laser amplifiers," Phys. Rev. A **39**, 1253-1263 (1989).

[77] A. E. Siegman, "Excess spontaneous emission in non-Hermitian optical systems. II. Laser oscillators," Phys. Rev. A **39**, 1264-1268 (1989).

[78] D. J. Derickson, P. A. Morton, J. E. Bowers, "Comparison of timing jitter in external and monolithic cavity mode-locked semiconductor lasers," Appl. Phs. Lett. **59**, 3372-3374 (1991).

[79] A. Braun, J. H. Abeles, C. M. DePriest, P. J. Delfyett Jr., "10-GHz ultralow-noise optical sampling stream from a semiconductor diode ring laser," IEEE Photonics Tech. Lett. **13**, 1109-1111 (2001).

[80] J. J. Hargreaves, P. W. Juodawlkis, J. J. Plant, J. P. Donnelly, J. C. Twichell, Proceedings Annual Meeting of the IEEE Lasers and Electro-Optics Society 2001.

[81] K. E. Hall, G. Lenz, E. P. Ippen, "Femtosecond time domain measurements of group velocity dispersion in diode lasers at 1.5 μm," IEEE J. Lightwave Tech. **10**, 616-619 (1992).

[82] K. Naganuma, H. Yasaka, "Group delay and α-parameter measurement of 1.3 μm semiconductor traveling wave optical amplifier using the interferometric method," IEEE J. Quantum Electronics **27**, 1280-1287 (1991).

[83] A. P. Bogatov, A. E. Boltaseva, A. E. Drakin, M. A. Belkin, V. P. Konyaev, "Anomalous dispersion, differential gain, and dispersion of the α factor in InGaAs/AlGaAS/GaAS strained quantum well semiconductor lasers," Semiconductors **34**, 1207-1213 (2000).

[84] A. Kostenbauder, A. E. Siegman, "Eigenmode expansions using biorthogonal functions: complex-valued Hermite-Gaussians," J. Opt. Soc. America B **14**, 1780-1790 (1997).

[85] D. F. Walls, G. J. Milburn, *Quantum Optics*, Springer Verlag, NY (1994).

[86] Y. Yamamoto, S. Machida, O. Nilsson, "Amplitude squeezing in a pump-noise-suppressed laser oscillator," Phys. Rev. A **34**, 4025-4042 (1986).

[87] C. E. Pearson, *Handbook of Applied Mathematics*, Van Nostrand Reinhold Co., NY, 1974.

[88] D. Von Der Linde, "Characterization of the noise in continuously operating mode-locked lasers," J. Appl. Phys. B **39**, 201-217 (1986).

[89] M. F. Becker, D. J. Kuizenga, A. E. Siegman, "Harmonic mode locking of the Nd:YAG laser," IEEE J. Quantum electronics **8**, 687-693 (1972).

[90] T. Yilmaz, C. M. DePriest, P. Delfyett Jr., "Complete noise characterisation of external cavity semiconductor laser hybridly modelocked at 10 GHz'," Elec. Letts. **37**, 1338-1339 (2001).

[91] C. M. DePriest, P. Delfyett Jr., J. H. Abeles, A. Braun, "Ultrahigh-stability photonic sampling streams from an actively-modelocked semiconductor diode ring laser," Proceedings of the Conference on Lasers and Electro-Optics'2001, OSA Technical Digest, Washington DC (2001).

[92] M. Horowitz, C. R. Menyuk, T. F. Carruthers, I. N. Duling, "Theoretical and experimental study of harmonically modelocked fiber lasers for optical communication systems," IEEE J. Lightwave Tech. **18**, 1565-1574 (2000).

[93] T. R. Clark, T. F. Carruthers, P. J. Mathews, I. N. Duling III, "Phase noise measurements of ultrastable 10 GHz harmonically modelocked fibre laser," Elec. Letts. **35**, 720-721 (1999).

[94] T. R. Clark, T. F. Carruthers, I. N. Duling III, P. J. Mathews, "Sub-10 femtosecond timing jitter of a 10-GHz harmonically mode-locked fiber laser," Proceedings of the Optical Fiber Communication Conference'1999, IEEE Press, NJ (1999).

[95] M. Nakazawa, E. Yoshida, Y. Kimura, "Ultrastable harmonically and regeneratively modelocked polarisation-maintaining erbium fibre ring laser," Elec. Letts. **30**, 1603-1605 (1994).

[96] M. Nakazawa, K. Tamura, E. Yoshida, "Supermode noise suppression in a harmonically modelocked fibre laser by selfphase modulation and spectral filtering," Elec. Letts. **32**, 461-463 (1996).

[97] E. Yoshida, M. Nakazawa, "Measurement of timing jitter and pulse energy fluctuation of a PLL regeneratively mode-locked fiber laser," IEEE Photonics Tech. Letts. **11**, 548-550 (1999).

[98] A. B. Grudinin, S. Gray, "Passive harmonic mode locking in soliton fiber lasers," J. Opt. Soc. America B **14**, 144-154 (1997).

[99] J. F. Martins-Filho, E. A. Avrutin, C. N. Ironside, J. S. Roberts, "Monolithic multiple colliding pulse mode-locked quantum-well lasers, experiment and theory," IEEE J. Select. Topics in Quantum Electronics **1**, 539-552 (1995).

[100] T. Shimizu, I. Ogura, H. Yokoyama, "860 GHz rate asymmetric colliding pulse modelocked diode lasers," Elec. Letts, **33**, 1868-1869 (1997).

[101] D. A. Yanson, M. W. Street, S. D. McDougall, I. G. Thayne, J. H. Marsh, E. A. Avrutin, "Ultrafast harmonic mode-locking of monolithic compound-cavity laser diodes incorporating photonic-bandgap reflectors," IEEE J. Quantum Electronics **38**, 1-11 (2001).

[102] X. Shan, D. M. Spirit, "Novel method to suppress noise in harmonically modelocked erbium fibre lasers," Elec. Letts. **29**, 979-981 (1993).

[103] Private communication with P. Delfyett Jr., School of Optics, U. of Central Florida, USA.

[104] O. Pottiez, O. Deparis, R. Kiyan, M. Haelterman, P. Emplit, P. Megret, M. Blondel, "Supermode noise of harmonically mode-locked erbium fiber lasers with composite cavity," IEEE J. Quantum Electronics **38**, 252-259 (2002).

[105] A. V. Oppenheim, A. S. Willsky, I. T. Young, "Signals and Systems," Parentice Hall, NJ (1983).

[106] D. J. Derickson, P. A. Morton, J. E. Bowers, "Comparison of timing jitter in external and monolithic cavity mode-locked semiconductor lasers," Appl. Phs. Letts. **59**, 3372-3374 (1991).

[107] N. Onodera, "Supermode beat suppression in harmonically mode-locked erbium-doped fiber lasers with composite cavity structure," Elec. Letts. **33**, 962-963 (1997).

[108] H. A. Haus, A. Mecozzi, "Long term storage of a bit stream of solitons," Optics Letts. **17**, 1500-1502 (1992).

[109] M. Horowitz, C. R. Menyuk, "Analysis of pulse dropout in harmonically mode-locked fiber lasers by use of the Lyapunov method," Optics Letts. **40**, 40-42 (2000).

[110] M. Horowitz, C. R. Menyuk, T. F. Carruthers, I. N. Duling III, "Pulse dropout in harmonically mode-locked fiber lasers," IEEE Photonics Tech. Letts. **12**, 266-268 (2000).

[111] A. J. Lowery, I. W. Marshall, "Numerical simulations of 1.5 μm actively mode-locked semiconductor lasers including dispersive elements and chirp," IEEE J. Quantum Electronics **27**, 1981-1989 (1991).

[112] J. S. Wey, J. Goldhar, G. L. Burdge, "Active harmonic modelocking of an erbium fiber laser with intracavity Fabry-Perot filters," IEEE J. Lightwave Tech. **15**, 1171-1180 (1997).

[113] G. T. Harvey, L. F. Mollenauer, "Harmonically mode-locked fiber ring lasers with an internal Fabry-Perot stabilizer for soliton transmission," Optics Letts. **18**, 107-109 (1993).